Direction Reconstruction in the SNO+ Liquid Scintillator Phase with 2.2 g/L PPO

by

Chloe Laurence Lefebvre

A thesis submitted to the
Graduate Program of Physics, Engineering Physics, and Astronomy
in conformity with the requirements for
the degree of Doctor of Philosophy

Queen's University
Kingston, Ontario, Canada
June 2026

Copyright © Chloe Laurence Lefebvre, 2026

Abstract

The current generation of ton-scale neutrino detectors are filled with liquid scintillators. These feature near instantaneous rise times with impressive light yield. While this is beneficial to energy resolution, the use of these fast, isotropic scintillators implies the loss of early Cherenkov radiation which entails forfeiting directionality in solar neutrino interaction identification. That is, unless timing resolution of these detectors allows for the separation of the early Cherenkov light from the prompt scintillation light. While solar fluxes have been broadly studied over the last decades, they remain difficult to probe in lower energy ranges. For $0\nu\beta\beta$ experiments, ^{8}B ν_e are the predominant irreducible background in the region of interest. In both cases, whether solar neutrinos be signal or background, using directionality to identify them in hard to reach regions would be extremely valuable.

This thesis explores the possibility of reclaiming directional Cherenkov radiation in the SNO+ detector, located 2 km underground in a mine near Sudbury, Ontario, during its scintillator phase. The dataset studied is comprised of the livetime accumulated during the phase in which the detector was filled with 780 tonnes of linear alkylbenzene as the solvent base in which the fluor 2,5-diphenyloxazole was dissolved at a concentration of 2.2 g/L. The methodology applied is that introduced by the Borexino collaboration and named Correlated Integrated Directionality. This thesis

transposes the concepts to the SNO+ detector and data. In the energy region beyond 5 MeV, 81 ± 3 ^{8}B ν_e solar event candidates out of an expected 83 from solar flux calculations are identified through directional reconstruction which stands as a proof of concept of directionality in large liquid scintillator experiments. Its application in the wider regions yields 175^{+43}_{-56}(stat.) $\pm$ 76(syst.) solar candidate events out of an expected 103 in a space counting 1303 total events for energies extending down to 2.5 MeV. Despite limitations in livetime and radiopurity, this thesis shows that the CID methodology can be applied to the SNO+ detector to extract directional information from the ^{8}B ν_e solar signal.

Acknowledgments

...comme mille millions d'univers.

As tradition rightly dictates, my foremost thanks are owed to my supervisor Mark Chen without whose guidance and insight this thesis would not have been possible. I am also deeply grateful to Alex Wright for the time and interest he so generously invested in discussions that helped shape this analysis. I also extend my thanks to all professors, postdoctoral fellows, research scientists and students having contributed to the excellence of the SNO+ Queen's group.

SNO+ would not be kept afloat without all the valuable members from each of its participating institutions. Any SNO+ Collaboration publication will list contributors more extensively and precisely than I could hope to. No analysis would be feasible without the dedication of the individuals maintaining the infrastructure on and off site to collect and process data. No analysis could be carefully carried out without the expertise with which the collaboration analysis framework continues to be developed. No analysis would bear fruit without the constant effort invested in all other analyses underway that it may both draw from and inform. Thank you in particular to all the teams and individuals at SNOLAB who have made my time at site not only possible, but enjoyable, and hopefully productive.

To the colleagues I'd go so far as to call friends who paved the way before and alongside me, from Queen's, Andy Anderson, Anthony Allega, Jasmine Corning, Jamie Grove, Hector Hawley Herrera, Brian Krar, Colin Moore, Debbie Morris, James Page, Serena Ricetto, Sara Stickley, Gary Sweeney, Benjamin Tam and Shengzhao Yu, from the UK, Daniel Cookman, Katharine Dixon and Gulliver Milton: "I don't know half of you half as well as I should like, and I like less than half of you half as well as you deserve". Thank you for all your help with the work itself, but also for your help in taking a break from it.

À mes amis, merci de m'avoir rappelé que la vie continue en dehors de la thèse. Merci d'avoir gardé les souvenirs que nous partageons depuis longue date vivants et proches à ma mémoire. Rien n'est plus précieux à mes yeux.

Finalement, à toi, papa, et à maman, de haut, merci. Merci, tout simplement. Et merci, infiniment. Je n'aurais pas eu l'opportunité de poursuivre mon intérêt pour ce domaine sans votre support inconditionnel. Votre dévoument, votre détermination et votre amour ont été et seront toujours pour moi une source d'inspiration. Je vous aime comme mille millions d'univers.

Statement of Originality and Disclosure of Use of Artifical Intelligence

The work presented in this thesis was made possible by all the past and current members of the SNO+ collaboration each having their part in building and maintaining this detector and its physics program. This includes gathering data through detector maintenance and operation, processing data as well as keeping up to date a working analysis framework. More broadly, this work builds upon years of extraordinary advancements in the field of particle astrophysics and the author does not claim any theoretical or experimental concepts alluded to and employed as original. The analysis and writing are original to the author.

The author used AI tools during their research for the purpose of writing a python script tasked with converting text files with event information into skimmed text files with runID and GTID pairs that were used to generate a third text file in the format required for downloading the data from these runs from the computing grid used by the collaboration. AI tools were not used in the writing process of this thesis.

Chapter 2 presents a review of neutrino physics in the context of developing theories for physics beyond the Standard Model through the search for neutrinoless double beta decay. As such, this chapter draws on decades of knowledge built by the international physics community and appropriate references are attributed throughout the

text.

Chapter 3 is dedicated to the design of the SNO+ detector, in particular its focus on enabling this rare event search through background mitigation and resolution improvement. Credit for this work directly concerns the author's collaborators and is appropriately referenced throughout.

Chapter 4 concerns the optical properties of the SNO+ scintillator cocktail. The author inherited the quality assurance program from Benjamin Tam, and led it through the addition of bis-MSB from coordinating loading operations to carrying out all *in situ* measurements of its optical properties necessary for the development of the optical model by the author's collaborators for the next analysis phase.

Chapter 5 details the main analysis portion of this thesis, and is therefore developed and applied by the author. The methodology is inspired by that of the Borexino collaboration and draws on its two relevant publications to adapt it to the SNO+ detector. Though explicitly referenced where relevant, a summary of external contributions will be restated. Solar fluxes were adapted and scaled to the purposes of this analysis from updated calculations from Ana Sofia Inacio and Joan Kladnik. The background tag list of ^{212,214}BiPo and ^{208}Tl was compared against that independently obtained by Gulliver Milton. The energy systematics related to the corrected energy reconstruction were taken from a calculation by Daniel Cookman. The solar event set used as a data subset to validate the performance of the algorithm was provided by Ana Sofia Inacio. The second set of background suppressing cuts was developed by Daniel Cookman for his ^{8}B solar oscillation analysis.

Contents

Abstract i

Acknowledgments iii

Statement of Originality and Disclosure of Use of Artifical Intelligence v

Contents vii

List of Tables x

List of Figures xii

List of Acronyms xviii

Chapter 1: Introduction 1

Chapter 2: Neutrino Physics 6
2.1 Neutrinos within the Standard Model . . . 7
2.2 Neutrinos without the Standard Model . . . 12
2.2.1 The Solar Neutrino Problem . . . 12
2.2.2 Neutrino Oscillations . . . 18
2.2.3 Neutrino Masses . . . 28
2.2.4 Neutrinoless double beta decay . . . 33

Chapter 3: The SNO+ experiment 42
3.1 The Detector . . . 43
3.2 Physics Goals . . . 44
3.3 Mitigating Backgrounds . . . 47
3.3.1 Cosmogenics and Shielding . . . 50
3.3.2 Radioactivity and the Purification Systems . . . 54
3.4 Calibrating the Detector Response . . . 75
3.4.1 Optical Calibrations . . . 75

3.4.2 Radioactive Sources . . . 77
3.4.3 Electronic Calibrations . . . 78
3.5 Aquiring Data . . . 80
3.5.1 PMTs . . . 81
3.5.2 Triggering . . . 83
3.6 Processing Data . . . 86
3.7 Simulating Data . . . 88
3.8 Reconstructing Data . . . 90
3.9 Characterising Surviving Backgrounds . . . 92

Chapter 4: Liquid Scintillator 99
4.1 Propagating Light . . . 99
4.1.1 Cherenkov Radiation . . . 102
4.1.2 Scintillation Light . . . 105
4.1.3 Characterising Light . . . 109
4.2 Enhancing the Scintillator . . . 118
4.2.1 LAB . . . 121
4.2.2 PPO . . . 127
4.2.3 BHT . . . 129
4.2.4 Bis-MSB . . . 131
4.2.5 Te&co . . . 144

Chapter 5: Directionality in Liquid Scintillator 147
5.1 Directionality . . . 148
5.2 Correlated Integrated Directionality . . . 148
5.3 Designing the methodology . . . 154
5.3.1 Sun Direction . . . 155
5.3.2 Timing . . . 157
5.3.3 Position Reconstruction . . . 159
5.3.4 Energy Reconstruction . . . 164
5.3.5 Building the Probability Density Functions . . . 168
5.3.6 Modeling the Fit . . . 169
5.4 What If . . . 182
5.4.1 Validating the algorithm . . . 184
5.4.2 Fitting the Model . . . 190
5.4.3 Improving the Selection . . . 200

Chapter 6: Conclusion 212

Bibliography 215

Appendix A: Bis-MSB deployment campaign **242**

List of Tables

2.1 Measured values of the neutrino oscillation parameters. 25

3.1 Measured values of some of the most prevalent backgrounds in SNO+. 50

3.2 Concentration of the components of the SNO+ scintillator cocktail. . 74

3.3 Coincidence cut values used in the tagging algorithms of the prominent backgrounds to this analysis. 96

4.1 Summary table of available QA tests. 123

4.2 Summary table of QA metrics for each bis-MSB loading batch. 135

5.1 Summary table of MC sets produced. 155

5.2 Energy regions determined by the LLR obtained from an extended LL fit over the energy distributions of ^{8}B and ^{208}Tl MC sets aimed at isolating the ^{208}Tl peak. 172

5.3 Summary of the parameters making up the signal and background PDF models. 177

5.4 Summary table of fit results of the optimisation of number of hit PMTs to include in final PDFs. 189

5.5 Summary table of solar selection cuts used by [103]. 190

5.6 Summary table of fit results of the optimisation of number of hit PMTs taken from the solar set. 191
5.7 Summary table of selection cuts applied to MC distributions and datasets. 192
5.8 Summary table of updated selection cuts by [74] applied to the PPO Gold dataset with the aim of improving background rejection. 203
5.9 Expected and fitted events for different energy and fiducial volume regions with lesser backgrounds. 205

A.1 Reference table for Bis-MSB loading metrics as reported during underground activities. 243

List of Figures

2.1 The table of fundamental subatomic SM particles organised by families and generations. Inspired by figure found in [187]. 8

2.2 Common neutrino interactions. 10

2.3 A pion decay. 10

2.4 Solar neutrino energy spectrum. 13

2.5 The *pp* and CNO cycles. 14

2.6 Status of the measured neutrino fluxes. 16

2.7 Depiction of the two possible neutrino mass hierarchies. 29

2.8 β decays in nuclei with an even atomic mass A. 34

2.9 (a) $2\nu\beta\beta$ decay (b) $0\nu\beta\beta$ decay. 35

2.10 Predictions on $m_{\beta\beta}$ from oscillations as a function of the lightest neutrino mass. 36

2.11 Leading $0\nu\beta\beta$ decay isotopes. 37

2.12 Illustration of the broad $2\nu\beta\beta$ peak with respect to the narrower and rarer $0\nu\beta\beta$ peak. 39

2.13 Sensitivies of current and projected neutrino experiments. 40

3.1 Depiction of the SNO+ detector. 44

3.2 Contributing backgrounds and spectrum plot for the $0\nu\beta\beta$ half-life of 8×10^{25} years for SNO+'s 0.5% Te loaded phase. 46
3.3 Main decays in the Uranium-238 chain 48
3.4 Main decays in the Thorium-232 chain. 49
3.5 Expected muon flux for the current neutrino experiments with respect to the depth of the laboratories housing them. 51
3.6 A typical muon event in LAB as captured by xsnoed. 54
3.7 Normalised energy reconstruction of the simulated flux of potentially problematic cosmogenic isotopes. 55
3.8 Schematic of the scintillator plant and its main connections to the AV, UPW, Master Solution preparation and tellurium processing plants. . . . 64
3.9 Schematic of the master solution preparation plant. 69
3.10 Transit time probability distribution measured by SNO and recoordinated with SNO+ specific values through the `RAT` simulation software. . 79
3.11 Schematic of the photomultiplier tubes. 82
3.12 Schematic of the DAQ system for SNO+. 84
3.13 Wavelength dependent quantum efficiencies measured by SNO for four types of R1408 Hamamatsu PMTs. 86

4.1 A Cherenkov cone forming in the wake of a particle traveling faster than light ($v > c/n$) in a medium of refractive index n. 103
4.2 Different notations and representations of the benzene ring. 108
4.3 Jablonski diagram of π orbitals. 109
4.4 Light yield of SNO+ AV and bench top LAB+PPO compared to published measurements. 111

4.5 Absorption spectra of LAB samples. 113
4.6 Redshift over time of energy transfers between scintillator components to bring emitted photons to the longer wavelengths where they may align with the PMT response curve. 120
4.7 The SNO+ experimental phases. 121
4.8 Chemical structure of LAB. 122
4.9 Density readings of the SNO+ LAB. 125
4.10 Absorption and emission spectra for LAB, PPO and bis-MSB as simulated by RAT. 126
4.11 Apbsorption spectra taken from 1 cm and 10 cm path lengths of pure LAB. 128
4.12 Chemical structure of PPO. 129
4.13 Chemical structure of BHT. 130
4.14 Chemical structure of bis-MSB. 131
4.15 Measured observed light yield for various combinations of PPO and bis-MSB in LAB by the JUNO collaboration. 133
4.16 AV concentrations of bis-MSB recorded for every sample taken during recirculation after loading the third batch. 137
4.17 AV absorption spectra of following every bis-MSB batch addition alongside AV spectra for every scintillator stage. 138
4.18 Absorption and attenuation lengths for the 2.2 g/L PPO and 2.2 g/L PPO + BHT + 2.2 mg/L bis-MSB SNO+ scintillator cocktails. 142
4.19 Cyclohexane dilutions of the AV scintillator from April 2022 (2.2 g/L PPO) and from December 2023 (2.2 g/L PPO + 2.2 mg/L bis-MSB). . . 143

4.20 The RAT optical model for the enhanced scintillator phase LAB + 2.2 g/L PPO + BHT + 2.2 mg/L bis-MSB. 144

5.1 Angular distribution for MC events of ^{7}Be and ^{210}Bi showing a clear peak in the solar signal and fit results of the CID data. 152
5.2 Schematic of a solar event interaction in the detector. 153
5.3 Time residuals distributions of signal MC for all hit PMTs in every triggered event. 158
5.4 Timing profiles of all hit PMTs and the reconstructed timing distribution of their corresponding event vertex. 159
5.5 Five first hit PMTs for every simulated ^{8}B MC event with Cherenkov or scintillation processes enabled within the full detector volume and a 2 m fiducial volume. 160
5.6 Five first hit PMTs for every simulated ^{8}B MC event with Cherenkov or scintillation processes enabled within the full detector volume. 162
5.7 Truth and fitted vertex positions for a few events within the Cherenkov and scintillation ^{8}B MC sets. 165
5.8 Mapping between corrected energy, energy, corrected nHits and cleaned nHits for ^{8}B ν_e and ^{208}Tl MC sets. 167
5.9 Energy distributions for the MC simulation sets of four solar neutrino channels and the ^{208}Tl background. 170
5.10 Fit results for all three energy regions from 0.7 LLR as defined in table 5.2 where the 2D PDFs are constructed as products in RooFit. 173

5.11 Normalised $\cos\theta_\odot$ distributions for ^{8}B and ^{208}Tl MC sets with their parametrised function fitted to best match the shape of the binned PDFs and representation of the constraints set on the shape parameters. 175
5.12 An example of the ensemble test results for the model function determination obtained by fitting functions to the ^{8}B and ^{208}Tl MC sets. 177
5.13 CID workflow schematic. 185
5.14 Time residual profile of the first 50 calibrated hit PMTs of all 83 events in the solar set. 187
5.15 $\cos\theta_\odot$ distribution and density plot of the time residuals with respect to $\cos\theta_\odot$ for the solar events as selected by the cuts in table 5.7. 193
5.16 Visual representation of the designed algorithm for five events randomly selected from the solar set. 194
5.17 Energy spectrum of all triggered events within the PPO phase for the basic selection cuts. 195
5.18 Event position on a normalised (ρ, z) projection of the AV for all triggered events within the PPO phase for the basic selection cuts. 196
5.19 Constrained fit result of the $\cos\theta_\odot$ distribution of the 5 first PMT hits for the (2.0, 2.8) MeV region. 197
5.20 Constrained fit result of the $\cos\theta_\odot$ distribution of the 5 first PMT hits for the $0\nu\beta\beta$ decay ROI region. 198
5.21 $\cos\theta_\odot$ and time residuals density plots of all triggered events within the PPO phase for the basic selection cuts and presented for every month. 200

5.22 PMT occupancy flat maps of the first 20 hit PMTs of every triggered event in the PPO gold period. 201
5.23 Energy profile of the full (2.5, 14) MeV region with additional cuts. 204
5.24 Constrained fit result of the $\cos\theta_{\odot}$ distribution of the 5 first PMT hits for the (2.5, 14.0) MeV energy region as stacked and normalised histograms. 206
5.25 Constrained fit result of the $\cos\theta_{\odot}$ distribution of the 5 first PMT hits for the (5.0, 14.0) MeV energy region. 207
5.26 Constrained fit result of the $\cos\theta_{\odot}$ distribution of the 5 first PMT hits for the combined (2.5, 2.8) and (4.6, 14.0) MeV energy region. 208
5.27 Constrained fit result of the $\cos\theta_{\odot}$ distribution of the 5 first PMT hits for the (2.8, 4.6) MeV energy region. 209
5.28 Constrained fit result of the $\cos\theta_{\odot}$ distribution of the 5 first PMT hits for the (2.5, 2.8) MeV energy region. 210

Acronyms

`RATDB` Reactor Analysis Tool Data Base. 87–89, 91, 186

`RATDS` Reactor Analysis Tool Data Structure. 87

AmBe Americium-Beryllium. 75, 77, 211

AMELLIE Attenuation Module. 76

AV Acrylic Vessel. 43, 47, 53, 56–62, 67, 69, 73, 83, 85, 90, 91, 93–95, 111, 118, 120–122, 124, 127, 130, 132–136, 139, 157–159, 161, 163, 164, 166, 168, 186, 190, 193

BD 1,2-butanediol. 72, 73, 120, 145

BEH Brout-Englert-Higgs. 8

BHT Butylated hydroxytoluene. 68, 70, 71, 122, 129, 130, 137

bis-MSB 1,4-Bis(2-methylstyrl)benzene. 42, 61, 67, 68, 70, 71, 90, 97, 122, 126, 131–134, 136, 137, 139, 141, 145, 211, 242

BNL Brookhaven National Laboratory. 9

CC Charged Current. 9, 15, 17, 18, 23, 24, 32

CERN Conseil Européen pour la Recherche Nucléaire. 11

CID Correlated and Integrated Directionality. 148, 149, 151, 153, 183, 184, 186, 188, 190, 195, 196, 198–200, 202, 203, 205, 206, 210, 211

CLR Closed Loop Recirculation. 73, 139

CP Charge Parity. 19–22, 24, 25, 41

DAQ Data Acquisition. 85, 86

DDA N,N-Dimethyldodecylamine. 71, 73, 74, 120, 145

DONUT Direct Observation of the NuTau. 9

DUNE Deep Underground Neutrino Experiment. 24

ECA Electronic Calibrations. 75, 78, 87

EDF Energy Density Functional. 37

ELLIE Embedded LED/Laser Light Injection Entity. 75, 76, 87

ES Elastic Scattering. 9, 15, 17

FEC Front End Card. 84

FRET Förster (or fluorescence) Resonance Energy Transfer. 115, 116, 128

GT Global Trigger. 85, 87

GTID Global Trigger Identification Number. 85, 87

HTiO Hydrous Titanium Oxide column. 67

IBD Inverse β Decay. 48, 77, 110

IBM-2 Interacting Boson Model-2. 37

ICPMS Inductively Coupled Plasma Mass Spectrometry. 70, 72

ITR In-Time Ratio. 92, 202, 203

JUNO Jiangmen Underground Neutrino Observatory. 27, 132

KamLAND Kamioka Liquid Scintillator Antineutrino Detector. 27, 60, 88, 121

KMPS Kock Modular Process Systems. 60

LAB Linear Alkylbenzene. 42, 43, 47, 57, 59, 61–63, 65–69, 71–73, 75, 77, 80, 88, 92, 96, 107, 111, 115, 118, 121, 122, 124, 127–134, 141, 145, 148, 163, 168, 182, 183, 209, 211

LHC Large Hadron Collider. 151

LL Log-Likelihood. 110, 170–172, 178–181

LLR Log-Likelihood Ratio. 171, 180, 198, 204, 205

LSSM Large-Scale Shell Model. 37

MC Monte Carlo. 88–90, 118, 132, 136, 139, 149–151, 154, 157, 161, 164, 166, 168–172, 174, 185, 186, 188, 192, 205

MSW Mikheyev, Smirnov, Wolfenstein. 18, 23

MTC/A Master Trigger Card / Analog. 84, 85

MTC/D Master Trigger Card / Digital. 85

NC Neutral Current. 9, 15–18, 23, 32

NOνA Neutrinos at the Main Injector Off-axis ν_e Appearance. 26

OWL Outward Looking PMT. 43, 53, 87, 88, 154, 202

PC Pseudocumene. 121, 148, 151

PCA PMT Calibrations. 75, 79

PDF Probability Density Functions. 89, 91, 150, 151, 159, 161, 166, 169, 172–174, 176, 178–180, 185, 188–190, 198, 208

PDG Particle Data Group. 24

PED pedestal. 78, 79

PFA/PTFE Fluoropolymer. 72

PHFB Projected Hartree-Fock-Bogoliubov. 37

PMNS Pontecorvo, Maki, Nakagawa and Sakata. 19–22, 24, 25, 29, 35

PMT Photomultiplier Tube. 43, 47, 53, 56, 58, 59, 61, 75, 76, 78–92, 94, 98, 103, 111, 119, 131, 144, 149–151, 153, 154, 157–159, 163, 164, 166–169, 184, 186–190, 199, 201, 202, 211

PMTIC PMT Interface Card. 83

PP Polypropylene. 72

PPO 2,5-diphenyloxazole. 42, 47, 68–71, 80, 90, 96, 111, 115, 124, 126–129, 131, 132, 134, 137, 141, 145, 148, 150, 154, 161, 163, 168, 169, 182–184, 186, 191, 193, 199, 200, 202, 209, 211

PSUP PMT Support structure. 43, 47, 53, 56, 62, 78, 80, 81, 91, 94, 157, 159, 163, 186

PTFE Polytetrafluoroethylene. 134

QA Quality Assurance. 63, 122, 124, 126, 127, 135, 139, 141, 242

QCD Quantum Chromodynamics. 24

QED Quantum Electrodynamics. 24

QRPA Quasi-particle Random Phase Approximation. 37

ROI Region of Interest. 40, 45, 47, 56, 57, 59, 70, 92, 93, 96, 147, 192, 196

SDS Safety Data Sheet. 121

SM Standard Model. 7–9, 12, 24, 30–32, 39

SMELLIE Scattering Module. 76, 77

SMS Source Manipulator System. 75

SNEWS Supernova Early Warning System. 28

SNO Sudbury Neutrino Observatory. 7, 15, 17, 18, 43, 56, 57, 60, 76, 81, 86, 89, 155, 157

SNP Solar Neutrino Problem. 12, 15, 23

SNU Solar Neutrino Unit. 15

SSM Standard Solar Model. 12, 15, 17, 18, 182

STF Surface Transfer Facility. 122

Super-K Super-Kamiokande. 7, 17, 18

T2K Tokai to Kamioka. 26

TAC Time-to-Amplitude Converter. 79, 83, 85

TeA Telluric Acid. 70–73, 120, 145

TeBD Tellurium Butanediol. 71–74, 145

TELLIE Timing system. 76, 79

UI Universal Interface. 60, 75

UPW Ultrapure Water. 43, 53, 56–61, 64, 67–69, 71–73, 94, 133, 163

URM Umbilical Retrieval Mechanism. 75

UTC Coordinated Universal Time. 155

XRF X-Ray Fluorescence Spectrometry. 72

Chapter 1

Introduction

Into Thin Air

J. Krakauer

Experimental particle physics enjoyed a boom during the XX^{e} century. Observation by observation, the Standard Model of Particle Physics emerged as the leading theory putting order in the quantum world and the forces that govern it. In spite of its extraordinary success this past century, a few unanswered questions arising from measurements yet unaccounted for are causing it to come apart at the seams. In 2015, the Sudbury Neutrino Observatory and Super Kamiokande were jointly awarded the Nobel Prize for their independent reporting of neutrino flavour mixing in 2001-2002 and 1998 respectively, most commonly explained by oscillation theories that are not accommodated for by the Standard Model framework. While this implies the massive nature of neutrinos, it does not provide the mechanism by which they acquire this mass, their absolute value or even their ordering between flavours. Detecting the ultra-suppressed neutrinoless double beta decay would constitute a significant advancement in that direction. In astroparticle physics, the effort invested in constructing experiments capable of this observation is at the foreground as it is one of

the rare phase spaces within the grasp of current day technologies.

One such experiment is the SNO+ liquid scintillator detector in Canada. This thesis seeks to contribute to the efforts of this collaboration through the recovery of directional information in a medium that is lauded for the promptness of its isotropic light propagation. Since Cherenkov radiation encodes the direction of the particle creating it, the separation of Cherenkov radiation from this isotropic scintillation light would provide an additional discriminant in the identification of solar neutrino events. Neutrinos produced during the fusion processes within the Sun's core are useful in measuring neutrino oscillation parameters. Their identification is obstructed at lower energies where radioactive backgrounds are abundant. The retrieval of directional information in a scintillator medium would provide a distinct advantage in discerning solar signal from non-directional backgrounds from common radioactive decay chains. On the other hand, solar events are themselves irreducible backgrounds in the energy region of interest to neutrinoless double beta decay analyses. In this case, directionality would help suppress solar backgrounds in the search for the interaction SNO+ was designed to observe.

While there is currently interest in hybrid detectors that would benefit from the energy resolution of liquid scintillator while maintaining directional discrimination power, these are a part of a new generation of neutrino experiments and employ an event-by-event analysis method based on timing profiles of scintillation and Cherenkov light unavailable to large pure scintillator detectors.

SNO+ itself was an accidental and unconventional hybrid detector during the partial fill period of April till October 2020. 365 tonnes of linear alkylbenzene doped with 0.6 g/L of 2,5-diphenyloxazole sat atop ultrapure water; the interface lying 75 cm

above the equator. Timing profiles were derived from ^{214}BiPo pair tagging, sufficient to characterize the scintillation light yield. Separation in these profiles for Cherenkov and scintillation light enabled a selection of 37 solar events, statistically inline with the expected 40 from flux predictions at the given exposure. This was SNO+'s first observation of event-by-event directionality outside of the water phase [12, 151]. While this result has been replicated internally using complementary techniques, the extension of this methodology to the full scintillator phase has proven unsuccessful as of yet, despite several independent efforts. This thesis is focused on continuing the pursuit of directionality in scintillator, but will do so following an approach inspired by the success of the Borexino collaboration.

The Borexino collaboration is the first and only ton-scale liquid scintillator experiment to have reported a directional measurement of solar neutrino signal. The Correlated and Integrated Directionality method [9] compiles the position of the earliest collected light of every event as they are read by the photomultiplier tubes surrounding the detector. Light propagation in Borexino's medium is expected to allow for a few nanoseconds during which instantaneous Cherenkov light is emitted along the direction of the interaction before isotropic scintillation light takes over the remaining event time window. As a statistical method, directional significance is expected to be built by collecting the early light of every event over a vast livetime. It also stands that the expected solar flux must be statistically significant with respect to the accepted radioactive background rate of the experiment. Borexino applied their methodology to the sub-MeV energy range of their data to extract their most precise measurement of CNO solar neutrinos [28].

By design, Correlated and Integrated Directionality relies on the precision of timing resolution, as well and energy and position reconstruction, to correctly discern early Cherenkov radiation from scintillation light. Its success is also dependent on the radiopurity of the scintillation medium for the directional solar distribution to be distinguishable from the isotropic background produced by radioactive decays. SNO+ does not have the radiopurity to probe the [0.85, 1.29] MeV neutrino energy region targeted by Borexino for its measurement. However, the SNO+ 2.2 g/L PPO-loaded full scintillator period has sufficient livetime to allow a measurement of ^{8}B solar neutrinos of which the directional information could be extracted for as low as 2.5 MeV. If proven successful, the method can be retuned for the optics of the tellurium-loaded scintillator as a background rejection tool for the neutrinoless double beta decay analysis.

Chapter 2 introduces the theoretical foundations of neutrino physics. The focus is laid on some important results in the field and how they shaped modern theories governing neutrino interactions beyond the Standard Model of particle physics. Chapter 3 lays bare the challenge all neutrino detectors face: contending with particle interactions producing signatures in the region where the extremely rare event of neutrinoless double beta decay is predicted to be observed. The discussion on backgrounds exposes the design choices from the location to the materials used on SNO+. Conversion from a photoelectric signal to a reconstructed event, through a discussion on electronics hardware and data processing, is described to emphasize that background suppression is an active part of data taking and data analysis. The physics and chemistry of the SNO+ liquid scintillator are the subject of chapter 4.

The current status of the liquid scintillator with *in* and *ex situ* measurements of its optical properties are reported. The methodology and results of the directional analysis on ^{8}B solar neutrinos constitute the focus of chapter 5. This is the first correlated integrated directional analysis performed on the fully loaded scintillator phase of the SNO+ experiment.

Chapter 2

Neutrino Physics

Foundation

- I. Asimov

This chapter lays out a non-exhaustive review of the key properties of the neutrino and how it came to be theorised and empirically observed. Focus is put on the ramifications their existence and uniqueness have on physics beyond the Standard Model. This chapter concludes with an overview of neutrinoless double beta decay, the elusive signature the SNO+ detector was designed and commissioned to investigate.

When Cowan and Reines answered Pauli's neutrino postulate as the carrier of missing energy in nuclear β decay in "Dear radioactive ladies and gentlemen" [152] with an observation of inverse beta decay through the production of $\bar{\nu}_e$ created alongside positrons in their soberly titled "The Neutrino" radiogram [164], the existence of the neutrino was cemented. The questions surrounding its mass, flavour, production, decay modes and interaction mechanisms, spin, and magnetic moment remained unanswered.

The stability of the Standard Model of particle physics hinges on the resolution of these questions. The bulk of the Standard Model of physics was developed during

the 1970s as physicists aimed to put order in the so-called particle zoo. To this day, it remains one of the most successful models, with experiments continuing to publish observations and measurements confirming its theories. However, vast areas of particle physics remain unexplained, and therefore modern experiments and detectors aim to breach physics beyond the Standard Model to search for anomalies, aspiring to fill its gaps and inconsistencies. The Sudbury Neutrino Observatory (SNO) [57] and Super-Kamiokande (Super-K) [111] were jointly awarded the Nobel Prize in 2015 for providing the first empirical observation of such physics beyond the Standard Model through their measurement of neutrino oscillations, a process which can only occur if neutrinos have mass, a feature which is not accounted for in the Standard Model. The newest generation of neutrino experiments is probing the neutrinoless double beta decay region of interest, the observation of which would determine the Majorana nature of neutrinos and provide insight on the absolute neutrino mass.

2.1 Neutrinos within the Standard Model

As an elementary particle with spin $\frac{1}{2}$, neutrinos belong to the lepton family of the Standard Model (SM). They come in three flavours derived from the three generations: e, μ, τ and their interactions with other particles from the SM are governed only by the weak force, as they have no electric charge or colour by which to interact electromagnetically or strongly. Gravity also exerts its pull on neutrinos though it, regrettably, is not accounted for in the SM.

The SM of particle physics classifies known elementary particles according to their characteristics and the interactions by which they are governed through the fundamental forces excluding gravity. Though it densely fills out a page in its complete

formulation, the Lagrangian of the SM can be written as

$$\mathcal{L} = -\frac{1}{4}F_{\mu\nu}F^{\mu\nu} + i\bar{\psi}D\psi + \psi_i y_{ij}\psi_j\delta + h.c. + |D_\mu\delta|^2 - V(\delta) \tag{2.1.1}$$

according to [192]. The first term is the gauge-field kinetic representation of mediators, excluding the Higgs boson. The second term contains the kinetic electromagnetic, weak and strong interactions between mediators and matter, again excluding the Higgs boson. The third and fourth terms describe matter and mediator couplings with the Brout-Englert-Higgs (BEH) field respectively. BEH is the mechanism by which particles (and antiparticles in the case of the hermitian conjugate on the Yukawa coupling) obtain their mass. The fifth and last term represents the potential of the BEH field describing the Higgs boson self-interactions. It is common to organise the particles within the SM in a table such as in 2.1. While neutrinos are dubbed an

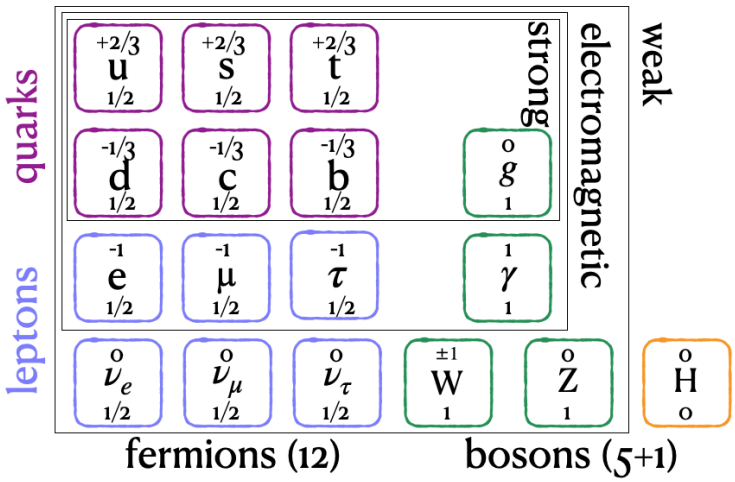


Figure 2.1: The table of fundamental subatomic SM particles organised by families and generations. Inspired by figure found in [187].

"elusive" particle, it is not for their scarcity. In fact, they are the most abundant massive[a] subatomic particles uninterruptedly showered on Earth by solar fusion. What is incontrovertibly rare is the occurrence of an interaction between neutrinos and other particles that leaves a signature detectable by modern day technology.

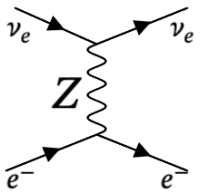
The Feynman diagrams of common neutrino processes are illustrated in figure 2.2. These include Neutral Current (NC) interactions such as Elastic Scattering (ES) through Z and Charged Current (CC) interactions. [156, 187]

Neutrinos fit in the SM as massless, spin-half, 3-generation leptons: ν_e, ν_μ and ν_τ that interact via the weak and gravitational forces. They are therefore expected to obey the quantum electrodynamical rules to which leptons are bound. As a matter of fact, in 1934, Enrico Fermi drew the 4-fermion vertex including a neutrino[b] upon which he would base his theory of weak interactions [126, 85]. With a despairingly small β decay cross section in the phase space attainable at the time, it took over 20 years for Cowan and Reines to experimentally confirm the particle's existence.

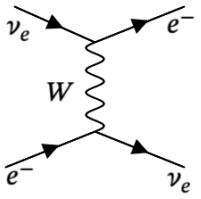
Almost ten years later, at the Brookhaven National Laboratory (BNL) in 1962, Lederman, Shwartz and Steinberger used a sychrotron beam to produce pion decays to leptons and neutrinos such as those in figure 2.3. With a spark chamber placed behind a wall meant to stop electrons, only muon and muon neutrinos could be detected. They were [76]. The third generation neutrino, the τ neutrino produced alongside the heaviest lepton, would not be observed until 2000 by the Direct Observation of the NuTau (DONUT) collaboration which used the Tevatron in Fermilab to reach collision energies sufficient to produce charm meson decays [117].

[a] Though this qualification is necessary to maintaining the veracity of this statement, it must be ignored until section 2.2.

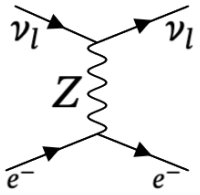
[b] Fermi's 4-point interaction is no more than the weak hadronic CC interaction mediated by a boson, a β decay, found in figure 2.2h.



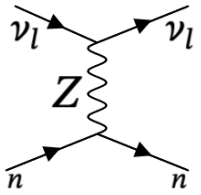
(a) ES via neutral Z exchange



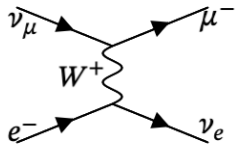
(b) ES via charged W exchange



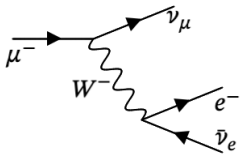
(c) Leptonic NC



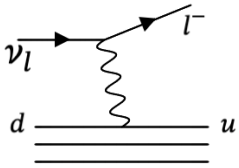
(d) Hadronic NC



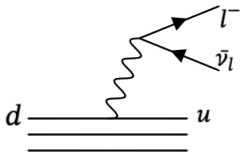
(e) CC via W^+



(f) CC via W^-



(g) Hadronic CC



(h) β decay

Figure 2.2: Common neutrino interactions.

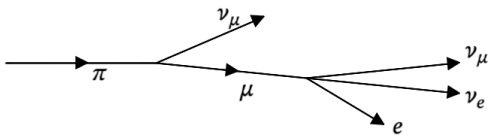


Figure 2.3: A pion decay.

While conservation of parity, the invariance under space inversion, was a building block of the strong and electromagnetic processes, β decays and other weak interactions seemed to provide no such evidence of parity conservation. In 1956, Lee and Yang proposed a series of experiments allowing the observation of parity conservation or violation in weak interactions [123]. A year later, the β decay of polarized ^{60}Co was investigated by Wu, who found that the electrons were emitted mainly in the opposite direction to that of the polarized Co nucleus [195]. If parity had been conserved, no such asymmetry would have been observed. Independently, Lederman published his own result on the same day as Wu, following his observation of parity violation in pion and muon decays. [35]

This new understanding of the weak force through parity violation led Landau [120], Salam [171], Lee and Yang [122] to postulate the two-component neutrino theory, in which the neutrino is a massless particle with helicity[c] and a Hamiltonian field not invariant under spatial inversion.

Another year elapsed until the two-component neutrino theory was generalised to a more universal weak theory by Gell-Mann and Feynman [86], and Marshak and Sudarshan [178]. The Hamiltonian of the weak force then included both right and left-handed fields of all fermions broadening the two-component neutrino theory to a universal weak interaction theory. Observation of the electron decay of the pion at the Conseil Européen pour la Recherche Nucléaire (CERN) facility in 1958 [83] gave credence this generalised model at the time.

Years later, in 1976, detection of elastic scattering by Reines [165] through the

[c]Helicity can be thought of as the projection of the spin onto the direction of momentum. A particle is right-handed if its spin is aligned with its linear momentum and left-handed in the case where they are opposite.

vector of reactor antineutrinos further solidified the already-established Glashow-Weinberg-Salam Standard Model. So far, neutrinos as described fit in the SM perfectly. Perfectly, except for a pesky discrepancy compiled by the Homestake experiment in 1964.

2.2 Neutrinos without the Standard Model

Within the phase space presently available to experimental physicists, neutrino theory offers several probes to physics beyond the standard model. The weight of the observation that warranted the SNO and Super-Kamiokande collaborations a Nobel prize can be understood by diving into the ramifications of a previous observation by the Homestake experiment.

2.2.1 The Solar Neutrino Problem

The Homestake experiment [78], a radiochemical experiment which induced the neutrino capture on chlorine, was commissioned in 1964 to measure the solar neutrino flux. The expected neutrino flux, shown in figure 2.4, is predicted by the Standard Solar Model (SSM) [23, 26]. The *pp* chain and the CNO cycle, critical processes in the SSM, are shown in figure 2.5. Homestake was the first to report the solar ^{8}B neutrino flux, thus providing a direct observation of solar nuclear reactions in the Sun. However, the result was approximately one third of what was expected. This unforeseen deficit was to be henceforth known as the infamous Solar Neutrino Problem (SNP). The decay of ^{8}B, specifically the last β decay found in figure 2.5, has historically been the solar fusion reaction most accessible to experiments given its energy range. As shown in figure 2.4, the main hydrogen burning process, referred

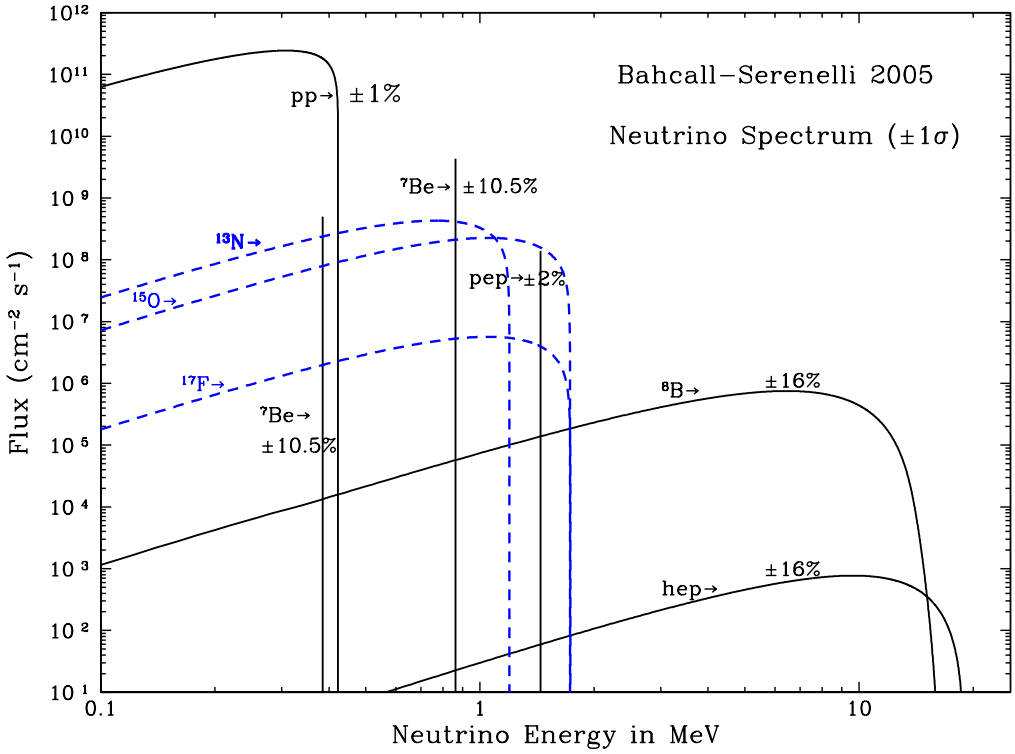


Figure 2.4: Solar neutrino energy spectrum according specifically to the BP04 solar model. Flux depicted by spectra are presented in neutrinos per $\mathrm{cm}^{-2}\mathrm{s}^{-1}\mathrm{MeV}^{-1}$ and line sources in neutrinos per $\mathrm{cm}^{-2}\mathrm{s}^{-1}$. The CNO flux is in blue. Figure made available at [108].

to as the *pp* chain, is confined by the low binding energy of the deuteron, at 2.2 MeV, which sets the upper limit on the energy the neutrino can carry away upon production in the first reaction in figure 2.5 [24]. Therefore, though the flux of the *pp* chain is the highest, the energy threshold required to observe neutrinos carrying 0.5 MeV is more difficult to reach; the right choice of target isotope, such as gallium, rendered experiments SAGE [2] and GALLEX [96] sensitive to it. The ^{8}B spectrum offers a wider energy range though its lower expected flux imposes a longer livetime on

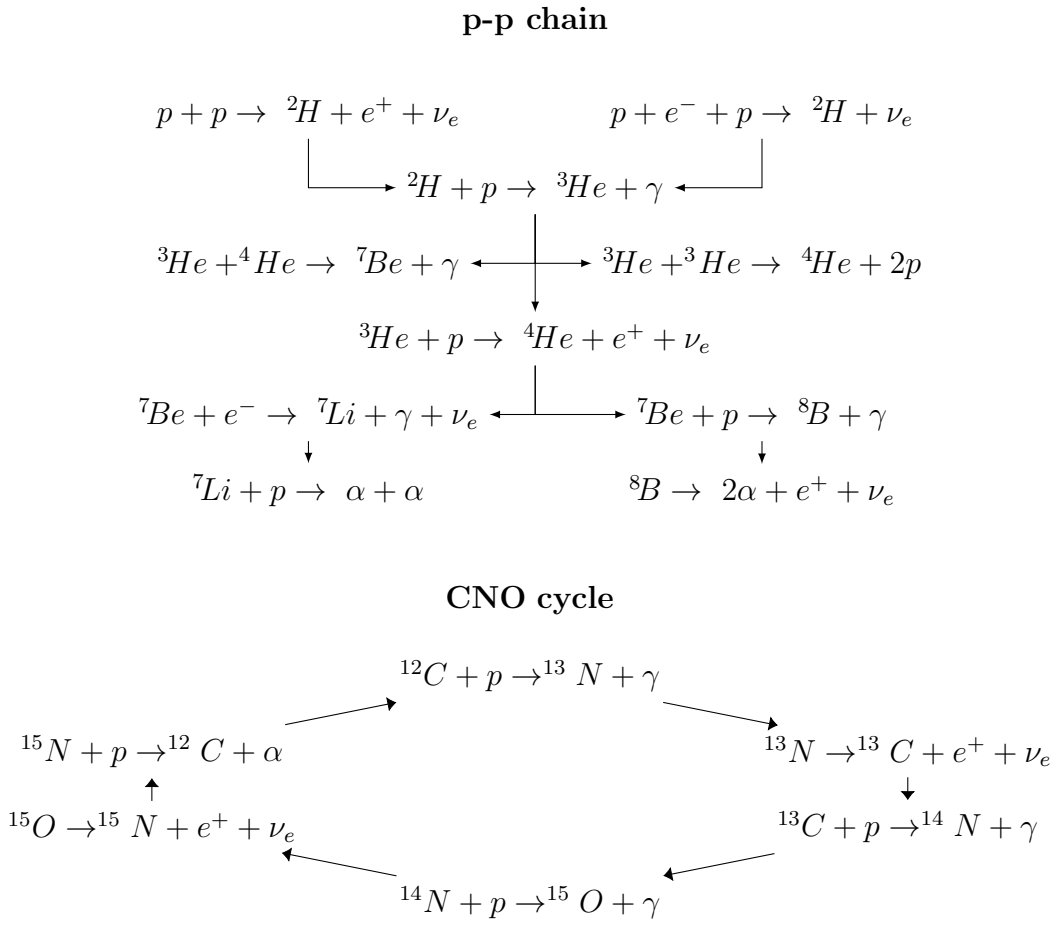


Figure 2.5: The *pp* and CNO cycles.

experiments.

The Homestake experiment, led by Ray Davis Jr., puts in practice the detection principle centered around the neutrino capture process Pontecorvo postulated in 1946 [158]. Homestake employed 520 tonnes of chlorine comprised of approximately one quarter of its target isotope ^{37}Cl to monitor the production and subsequent decay rates of the ^{37}Ar nuclei. This argon nucleus is produced alongside neutrinos in the

solar fusion reaction part of the *pp* chain $^{37}\mathrm{Cl} + e \rightarrow ^{37}\mathrm{Ar} + \nu_e$. Counted over 20 years of livetime in the Homestake chlorine detector, the average reported argon rate corresponded to 2.55 ± 0.25 Solar Neutrino Unit (SNU) [50], while the SSM calculations scaled to the configuration of the Homestake chlorine detector according to Bahcall and Ulrich had predicted a rate of 7.9 ± 2.6 (3σ) SNU [25].

Furthermore, SAGE [1] and GALLEX [95] also probed the ^{7}Be, the *pp* and *pep* fluxes through the use of the gallium isotope ^{71}Ga. Over the subsequent decades, water based Cherenkov detectors searching for electron neutrinos through ES on electrons, such as Kamiokande-II [100], also aimed to shed light on the longstanding SNP. With an energy threshold of around 5 MeV, these large Cherenkov detectors are sensitive to ^{8}B solar neutrinos. Though all neutrino flavours undergo NC scattering, electron neutrinos remain favoured because of the additional CC interaction allowed. Results reported by these two complementary detection techniques varied due to the sensitivity to muon and tau flavoured neutrinos, which contribute to the cross section through a NC interaction. Consistently, however, the observed solar neutrino flux returned a measurement below the predicted rate. Figure 2.6 summarises these results against the predicted theoretical solar neutrino flux while accounting for the different energy thresholds and target materials of these detectors.

The SNO experiment, informed by the deficit of solar electron neutrinos consistently reported by experiments previously mentioned, was designed to measure the total solar neutrino flux. The use of heavy water (D_2O) as the target medium allows for solar neutrinos to be probed down to 5 MeV through three separate processes. The CC interaction with the deuteron is only sensitive to the ν_e flux, while all flavours of neutrinos can interact with it via the NC interaction. The CC interaction

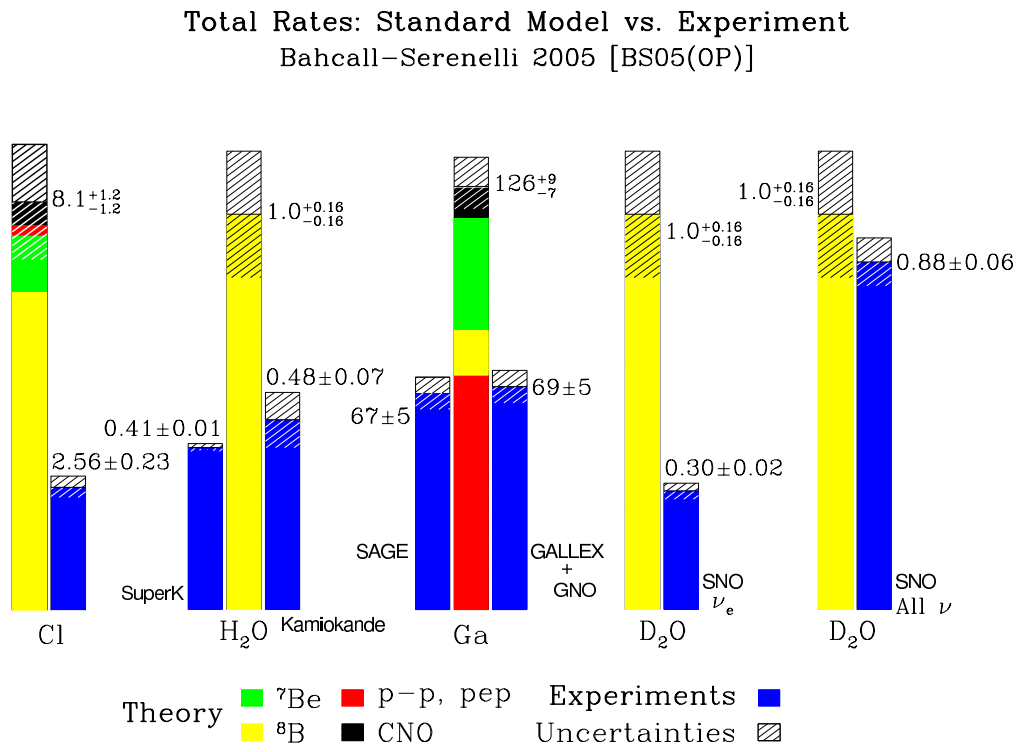


Figure 2.6: Status of the measured neutrino fluxes in different experiments compared to the SSM BS05(OP) predicted rates. Figure made available at [108].

$\nu_e + D \rightarrow e + p + p$ produces an outgoing electron with a signature Cherenkov ring. On the other hand, the neutron produced through NC, $\nu_{e,\mu,\tau} + D \rightarrow \nu_{e,\mu,\tau} + p + n$, will eventually be recaptured via the $n + {}^2_1\mathrm{H} \rightarrow {}^3_1\mathrm{H} + \gamma$ reaction. The gamma is released with a characteristic delayed 6.25 MeV energy, which will continuously produce electrons in a Cherenkov cone through Compton scattering as it passes through the detector. A Cherenkov cone will be recorded by the detector as a directional ring with a radius vastly smaller than that of the detector itself. Elastic scattering, depicted in the upper Feynman diagrams of figure 2.2, is also sensitive to all three flavours,

though the cross section for ν_e is the largest by a factor of about six [144].

In other words, a weak isotropic signal opposing the ν direction is the signature of a charged current electron; while a Cherenkov cone correlated with the Sun's direction is the signature of a scattered electron. Event directionality with respect to the position of the Sun provided the necessary separation power to distinguish ES events from CC and NC events. CC and NC fluxes were separated throughout three data taking phases in SNO.

The second phase introduced NaCl into the heavy water to make use of the higher neutron capture cross section of ^{35}Cl. THe burst of gamma rays produced results in more Cherenkov light per neutron capture. The multiple gamma rays also allowed for an isotropy parameter to separate CC and NC interactions independent of their energies. The third phase was tasked with further boosting the NC sensitivity of SNO. An array of low-background ^{3}He proportional counters were deployed. These collected the neutrons liberated by NC interactions on D_2O [14]. In 2002, SNO reported a ν_e flux of $1.8 \times 10^{-6}\text{cm}^{-2}\text{s}^{-1}$ from the CC signal [160]. The total neutrino flux inferred through the NC signal was $5.1 \times 10^{-6}\text{cm}^{-2}\text{s}^{-1}$, the excess indicating contributions from the solar ν_μ and ν_τ fluxes. This result was finally consistent with the SSM predictions and explained the original deficit reported by the Homestake experiment and all subsequent experiments sensitive only to ν_e. SNO's joint NC and CC flux measurement attested to neutrino flavour mixing over long distances. Super-K showed concurring evidence though the measurement of atmospheric ν_μ originating from atmospheric pion decays as seen in figure 2.3 [101]. SNO and Super-K were jointly awarded the 2015 Nobel Prize for advancements in the field of astroparticle physics through the study and measurement of neutrino flavour mixing.

So, which theory correctly describes the quantum mechanical effect by which a neutrino changes lepton number as it propagates? A well tried model is the Mikheyev, Smirnov, Wolfenstein (MSW) mechanism [137, 193, 138]. The MSW effect describes neutrino oscillations in which an electron neutrino transitions to a heavier muon or tau neutrino state. Because muons and tau leptons are far more massive than electrons, the energy required for their production is high and their channels are heavily suppressed in CC interactions, with high cross sections through NC. They are therefore viable candidates for the "missing signal" underlined by Homestake's reported ^{8}B neutrino flux accounting for only a third of the expected rate predicted by the SSM. The MSW effect, discussed in a later section, of resonant neutrino flavour conversion in the Sun provides constraints on neutrino mixing parameters and relative neutrino masses.

2.2.2 Neutrino Oscillations

The neutrino oscillation mechanism requires the neutrinos to have mass. Therefore, the observation of this process by Super-K and SNO firmly placed the neutrino in a land ruled by hypothesis rather than theory, Beyond the Standard Model. Therefore, for the remainder of this discussion, neutrinos will be assumed to be light[d], relativistic[e] particles coupling to the electroweak gauge bosons.

2.2.2.1 in Vacuum

Flavour mixing is a process that occurs because the mass eigenstates of the neutrinos are not related to their flavour eigenstates through an identity matrix, but

[d] $E_\nu \approx |\vec{p_\nu}|$, where as usual the naturalised units $c = 1$ are employed.
[e] $m_\nu \ll |\vec{p_\nu}|$

rather the Pontecorvo, Maki, Nakagawa and Sakata (PMNS) matrix comprised of three mixing angles θ_{12}, θ_{23}, and θ_{13} parametrising the mixing of mass eigenstate, as well as a complex Charge Parity (CP) violating phase δ that is a well observed phenomenon in weak interactions[133]. In quantum mechanics, this superposition of the weak eigenstates to the mass eigenstates can be written as

$$|\nu_i\rangle = \sum_{j=1}^{3} U_{i,j}|\nu_j\rangle \tag{2.2.1}$$

$$\begin{pmatrix} \nu_e \\ \nu_\mu \\ \nu_\tau \end{pmatrix} = \begin{pmatrix} U_{e1} & U_{e2} & U_{e3} \\ U_{\mu 1} & U_{\mu 2} & U_{\mu 3} \\ U_{\tau 1} & U_{\tau 2} & U_{\tau 3} \end{pmatrix} \begin{pmatrix} \nu_1 \\ \nu_2 \\ \nu_3 \end{pmatrix}. \tag{2.2.2}$$

In this notation, it is easy to see that each neutrino flavour state propagates as a linear superposition of the three mass eigenstates. As they travel through space and matter, an interaction may occur and cause a collapse of the wave function which may incur flavour mixing. It is also apparent that the oscillation process requires neutrino masses, or more accurately $|\Delta m_{ij}|^2 = m_i^2 - m_j^2$, to be non-zero. The PMNS matrix can be factored in terms of three two-flavour oscillation matrices with parameters sensitive to neutrinos of three origins: atmospheric, reactor and solar. Solving the Schrödinger equation with a plane wave solution[f] allows the evolution of a neutrino state in vacuum to be expressed as

$$|\nu_i\rangle = \sum_{j=1}^{3} U_{i,j}^{*}|\nu_j\rangle, \qquad |\nu_j\rangle = \sum_{i=e,\mu,\tau} U_{i,j}|\nu_i\rangle \tag{2.2.3}$$

[f] As opposed to the more correct, more tedious wave packet treatment found in [90]. Within the ultrarelativistic limit where $|\vec{p}| \approx E$, plane waves with definite momenta encapsulate the behaviour of light neutrinos.

in the flavour and mass bases related by the the PMNS matrix:

$$U = \begin{pmatrix} c_{12}c_{13} & s_{12}c_{13} & s_{13}e^{-i\delta} \\ -s_{12}c_{23} + c_{12}s_{23}s_{13}e^{i\delta} & c_{12}c_{23} + s_{12}s_{23}s_{13}e^{i\delta} & -s_{23}c_{13} \\ s_{12}s_{23} + c_{12}c_{23}s_{13}e^{i\delta} & -c_{12}s_{23} + s_{12}c_{23}s_{13}e^{i\delta} & c_{23}c_{13} \end{pmatrix} \tag{2.2.4}$$

$$= \begin{pmatrix} 1 & 0 & 0 \\ 0 & c_{23} & s_{23} \\ 0 & -s_{23} & c_{23} \end{pmatrix} \begin{pmatrix} c_{13} & 0 & s_{13}e^{-i\delta} \\ 0 & 1 & 0 \\ -s_{13}e^{-i\delta} & 0 & c_{13} \end{pmatrix} \begin{pmatrix} c_{12} & s_{12}0 & \\ -s_{12} & c_{12} & 0 \\ 0 & 0 & 1 \end{pmatrix}, \tag{2.2.5}$$

where the abbreviations $c_{ij}, s_{ij} = \cos\theta_{ij}, \sin\theta_{ij}$ have been used to denote the projections of the mixing angles between the weak interaction eigenstates and the mass eigenstates. In other words, these represent the dimensionless phases of the mass eigenstates. The CP violating phase is kept in the PMNS matrix because it is governed by the weak force, subject to CP violation. Time (T), charge (C) and parity (P) symmetry would affect neutrino oscillations in the following manner:

$$T : \nu_i \to \nu_j \xrightarrow{\hat{\mathrm{T}}} \nu_j \to \nu_i \tag{2.2.6}$$

$$CP : \nu_i \to \nu_j \xrightarrow{\hat{\mathrm{C}}\hat{\mathrm{P}}} \bar{\nu}_i \to \bar{\nu}_j \tag{2.2.7}$$

$$CPT : \nu_i \to \nu_j \xrightarrow{\hat{\mathrm{C}}\hat{\mathrm{P}}\hat{\mathrm{T}}} \bar{\nu}_j \to \bar{\nu}_i \tag{2.2.8}$$

The distinction between these transformations becomes relevant through the complex imaginary phase δ that appears in certain elements of the PMNS matrix. In the absence of this complex phase, the PMNS matrix would be real and CP symmetry would be conserved. As it stands, this phase changes sign in CP conjugation, and

can produce differences between the probabilities of a neutrino oscillation process and its CP-transformed counterpart. Consequently, a non-zero δ provides a source of CP violation in neutrino oscillations which remain completely insensitive to the additional phases that would arise if neutrinos were Majorana particles[g].

The oscillation probabilities are then defined in terms of the flavours of the charged leptons produced in the weak interactions and the relevant PMNS matrix elements. The probability of a neutrino oscillating between some $\alpha = e, \mu, \tau$ and $\beta = e, \mu, \tau$ flavour eigenstates after traveling a distance L through vacuum is given by

$$\begin{aligned} P(\alpha \to \beta) &= |\langle \nu_\beta | \Psi(\vec{x}, t) \rangle|^2 \\ &= |\langle \nu_\beta | \nu_\alpha \rangle|^2 \\ &= |\langle \nu_\beta | \sum_{i=1}^{3} U_{\alpha i} | \nu_i \rangle|^2. \end{aligned} \tag{2.2.9}$$

Referring back to equation 2.2.3 and applying approximations for ultra-relativistic neutrinos of energy E and momentum p traveling a distance L over a time t: $t \approx L$ and $p \approx E$

$$E_{i,j} = \sqrt{m_{i,j}^2 + p_{i,j}^2} \approx p_{i,j} + \frac{m_{i,j}^2}{2p_{i,j}} \approx E + \frac{m_{i,j}^2}{2E}, \tag{2.2.10}$$

where it as also assumed the neutrinos in the initial and final state had the same energy. The probability can then be taken as

$$P(\alpha \to \beta) = \left| \sum_{i=1}^{3} U_{\alpha i}^* U_{\beta i} e^{-i \frac{m_i^2}{2E} L} \right|^2 \tag{2.2.11}$$

[g]Which entails that neutrino oscillation experiments remain blind to the Dirac or Majorana nature of neutrinos.

$$
\begin{aligned}
&= \left|U^*_{\alpha1}U_{\beta1}e^{-i\delta_1} + U^*_{\alpha2}U_{\beta2}e^{-i\delta_2} + U^*_{\alpha3}U_{\beta3}e^{-i\delta_3}\right|^2 \\
&= \sum_{i,j} U^*_{\alpha i}U_{\beta i}U_{\alpha j}U^*_{\beta j}e^{-i\frac{m_i^2}{2E}L} \\
&= \delta_{\alpha\beta} - 4\sum_{i>j}\mathfrak{Re}(U^*_{\alpha i}U_{\beta i}U_{\alpha j}U^*_{\beta j})\sin^2\left(\frac{\Delta m^2_{ij}L}{4E}\right) \\
&\pm 2\sum_{i>j}\mathfrak{Im}(U^*_{\alpha i}U_{\beta i}U_{\alpha j}U^*_{\beta j})\sin\left(\frac{\Delta m^2_{ij}L}{2E}\right),
\end{aligned}
\tag{2.2.12}
$$

where Δm^2_{ij} is the difference in mass squared between mass eigenstates i and j and $\delta_{\alpha\beta}$ comes from using the unitary relation $UU^\dagger = 1$ so that $\sum_i U_{\alpha i}U^*_{\beta i} = \delta_{\alpha\beta}$ [90]. The imaginary terms associated with the Dirac phase contribute with opposite signs to neutrino and antineutrino oscillation probabilities, hence giving rise to CP violation. As will be addressed in section 2.2.3.2, the additional phases that would arise were neutrinos Majorana particles would cancel out in the oscillation probabilities, rendering neutrino oscillations insensitive to these Majorana phases.

What stands out from equation 2.2.11 is that the oscillation probability is only non-zero if neutrinos carry mass. Moreover, they are precluded from carrying the same mass from the Δm^2_{ij} term.

Due to approximations, the survival probability of neutrino flavours can be drastically simplified as hinted at in the factored form of the PMNS matrix shown in equation 2.2.6. This is possible due to the fact that θ_{13} is small and $\Delta m_{12} \ll \Delta m_{23}$ which will be addressed in section 2.2.3. The remaining isolated parameters are accessible through different experimental techniques. For example, constraints on θ_{13} can be imposed by short baseline reactor antineutrino experiments, θ_{23} by atmospheric neutrino experiments, and θ_{12} by solar neutrino experiments and long-baseline reactor experiments [15]. A classical example of such a simplification of the survival

probability of a neutrino flavour in vacuum is commonly written as

$$\begin{aligned} P(\nu_e \to \nu_e) &= 1 - P((\nu_e \to \nu_{\mu,\tau})) \\ &= 1 - \frac{1}{2}\cos^4\theta_{13}\sin^2\theta_{12}\left(1 - \cos\left(\frac{\Delta m^2_{21}}{2E}L\right)\right) \\ &- \frac{1}{2}\sin^2\theta_{13}\left(1 - \cos\left(\frac{\Delta m^2_{31}}{2E}L\right)\right) \\ &- \frac{1}{2}\sin^2\theta_{12}\sin^2 2\theta_{13}\left(\cos\left(\frac{\Delta m^2_{31}}{2E}L\right) - \cos\left(\frac{\Delta m^2_{21} + \Delta m^2_{31}}{2E}L\right)\right) \end{aligned} \quad (2.2.13)$$

Applying the condition $\frac{\Delta m^2}{2E}L \ll 1$ further simplifies the survival probability expression to

$$P(\nu_e \to \nu_e) = \cos^4\theta_{13}\left(1 - \sin^2 2\theta_{12}\sin^2\left(\frac{\Delta m^2_{21}}{4E}L\right)\right) + \sin^4\theta_{13}. \quad (2.2.14)$$

2.2.2.2 in Matter

The case of oscillations in vacuum can be expanded to propagation in matter by introducing the previously-mentioned MSW effect which accounts for the coherent forward scattering of neutrinos on leptons via the weak force. This effect alters the oscillation parameters and can significantly enhance flavour conversion. An effective potential that differs among flavours is generated as neutrinos travel through matter, thereby modifying the oscillation behaviour relative to that in vacuum. Propagations through matter require the introduction of an effective mass term to the neutrino mass to account for neutrino interactions. This effective mass term differs from the other neutrino flavours for the electron neutrino because, as mentioned in the SNP discussion, electron neutrinos are sensitive to CC as well as NC, thus implying that they interact differently with matter than their flavour counterparts. This additional

potential energy term gained from the possibility of CC interactions introduces a different "effective mass" for electron neutrinos traveling through a medium of varying density. The survival probability for two-flavour mixing can be rewritten as

$$P(\alpha \to \beta) = \sin^2(2\theta_{\text{eff}}) \sin^2\left(\frac{\Delta m^2_{\text{eff}}}{4E}\right), \tag{2.2.15}$$

where the effective mass difference and effective mixing angle due to matter effects depend on the potential induced by matter on a neutrino flavour which is related to the distance and time traveled. From equation 2.2.15, it can be seen that the survival probability depends on the neutrino energy E, the mixing angle θ_{eff}, and the neutrino mass splitting Δm^2_{eff}.

2.2.2.3 Status of Oscillation Parameters

As previously mentioned, different types of neutrinos and the detection methods used to measure them provide limits on the six PMNS matrix parameters. Table 2.1 summarises the current best global fit of the oscillation parameters as quoted in the 2022 Particle Data Group (PDG) release [194].

While the CP violating phase δ remains unknown, accelerator-based long-baseline experiments such as the Deep Underground Neutrino Experiment (DUNE) [54] and Hyper-Kamiokande [161] aim to perform this measurement as their main physics goal. Such importance is warranted given that Quantum Electrodynamics (QED) and Quantum Chromodynamics (QCD) interactions are known to conserve C and P separately. In turn, only the weak force is left within the SM to account for the excess of matter over antimatter in the Universe through CP violation. Neutrino oscillations incur charge, parity and time symmetry violation. Indeed, if CP were

Observable	**Oscillation Parameter**	**Value $\pm 1\sigma$**	**Experiment(s)**
solar ν, long baseline $\bar{\nu}$, accelerator ν	θ_{12}	35°	Homestake [78], GALLEX/GNO [110], SAGE [58], SuperK [67], SNO [57], Borexino [69]
	Δm^2_{21}	$(7.5 \pm 0.2) \times 10^{-5}$ eV^2	Homestake [78], GALLEX/GNO [110], SAGE [58], SuperK [67], SNO [57], Borexino [69], KamLAND [70]
atmospheric ν	θ_{23}	45°	MINOS/MINOS+ [56], T2K [68], NOνA [7], SuperK [66], IceCube [55]
	Δm^2_{32}	$(2.3 \pm 0.1) \times 10^{-5}$ eV^2	MINOS/MINOS+ [56], T2K [68], NOνA [7], SuperK [66], IceCube [55]
short baseline ν, accelerator ν	θ_{13}	10°	DayaBay [52], DoubleChooz [53], RENO [116], T2K [3]
accelerator ν	δ		T2K [68], NOνA [7]

Table 2.1: Measured values of the neutrino oscillation parameters from global fit to solar, atmospheric, reactor and accelerator data.

conserved, the oscillation probabilities from one neutrino flavour to the other would be such that $P(\alpha \to \beta) = P(\beta \to \alpha)$. However, since this computation involves taking the complex conjuguate of the PMNS matrix elements, it would hold true only if these elements were real, eliminating the imaginary terms. Keeping this complex CP violating phase in the PMNS matrix allows for the possibility of CP violating effects in neutrino oscillations.

Populating the oscillation parameter phase space is synonymous with probing neutrino interactions spanning over three orders of magnitude in energies from solar neutrinos, atmospheric neutrinos, reactor antineutrinos, geoneutrinos, accelerator neutrinos and supernova neutrinos.

Solar neutrinos Solar neutrinos arise from the fusion reactions taking place within the core of the Sun and contribute mostly to θ_{12} and Δm^2_{21} through the production of electron neutrinos oscillating to other flavours –or not– during their 1 AU ($\sim 1.5 \times 10^6$ km) voyage toward Earth.

Atmospheric neutrinos When cosmic rays carrying energies of $\mathcal{O}(10^5 - 10^{17})$ MeV [16] travel through the Earth's atmosphere, interactions with atomic nuclei induce hadronic showers producing pions which further decay into atmospheric neutrinos predominantly through the muon channel

$$\pi^{\pm} \to \mu^{\pm} + \nu_{\mu}^{(-)} \to e^{\pm} + 2\nu_{\mu}^{(-)} + \nu_{e}^{(-)}.$$

Atmospheric neutrinos contribute, along with accelerator neutrinos, to the θ_{23} and Δm^2_{32} oscillation parameters. Because the sign of Δm^2_{32} has not been determined of yet, both $m_1 < m_2 < m_3$ and $m_2 > m_1 > m_3$ are allowed. This is dubbed the mass hierarchy problem with the former being referred to as the normal hierarchy and the latter, the inverted hierarchy θ_{23} can be measured by long baseline neutrino oscillation experiments such as the Neutrinos at the Main Injector Off-axis ν_e Appearance (NOνA) and Tokai to Kamioka (T2K).

Reactor antineutrinos Nuclear reactors are a perk to particle physics as nearby (on a neutrino travel scale) detectors capture the electron antineutrinos emanating from the β decays of nuclear fission. These constitute a sustained and easily monitored signal as, by design, the reactor core provides a source that is fixed in location and tracks its production rate closely. Additionally, informed by the nuclear fuel in use,

the expected energy spectrum of the antineutrino flux is also well known. Reactor experiments are distinguished between short and long baseline based on whether they aim to measure first or subsequent oscillation minima. They are situated either ∼2 km or over ∼100 km away from their nuclear reactor. Short baseline experiments probe θ_{13} while long baseline experiments probe the θ_{12} oscillation parameter. While the Kamioka Liquid Scintillator Antineutrino Detector (KamLAND) previously held the most precise measurement of Δm^2_{21} [4], SNO+ recently put out its own competitive measurement of $(7.58^{+0.18}_{-0.17}) \times 10^{-5}\text{eV}^2$ and $\sin^2\theta_{12}$ of 0.308 ± 0.013 [5] in parallel to Jiangmen Underground Neutrino Observatory (JUNO)'s result of $\Delta m^2_{21} = (7.50 \pm 0.12) \times 10^{-5}\text{eV}^2$ and $\sin^2\theta_{12} = 0.3092 \pm 0.0087$ [6].

Geoneutrinos Geoneutrinos arise from radioactive decays occurring within the Earth's mantle and crust. ^{40}K primarily, as well as isotopes in the ^{238}U and ^{232}Th chains, include β decays where the antineutrino emitted is dubbed "geoneutrino". They provide an insight into the abundance of radioactivity underneath the surface of the Earth which is likely the predominant (∼50-100%) source of geothermal energy or radiogenic heat [87]. The geological area where SNO+ is located has been extensively studied. The uniformity of the Earth's crust in that region constrains the expected geoneutrino signature, making their detection fairly straightforward.

Accelerator neutrinos Proton beams are accelerated and aimed at a target made of a material whose main decay upon interaction of protons with the target nuclei produce hadronic showers. These are accompanied by subsequent pion and muon decays involving neutrinos similar to figure 2.3. The choice of magnetic field allows to narrow these into a beam of neutrinos or antineutrinos. Oscillation analyses rely

on the distance of travel L/E. It is controlled by placing a detector near the source and another further away to measure flux. This allows a window into θ_{23} and Δm^2_{32}. Furthermore, δ_{CP} is attainable due to the ability of these detectors to switch from neutrino to antineutrino beams.

Supernova neutrinos As a star undergoes a supernova explosion, the heavy elements composing our universe are released alongside bursts of neutrinos. Though it has been discussed that fusion processes occurring within the core of a star emit neutrinos, supernovae expel a neutrino flux superior to its production throughout its life during a mere ∼10 second period [44]. The Supernova Early Warning System (SNEWS) [176], a global network of detectors, has been set up by neutrino physicists to be triggered upon a sudden influx of neutrinos. As a testament to how far technology has come, neutrino experiments are expected to record several 10^3 events compared to the combined 24 events recorded across three detectors in 1987 upon the supernova SN 1987A in the Large Magellanic Cloud [130]. In a way, supernovae mimic a point source, emitting neutrinos of all three flavours at a fixed point in space and time.

2.2.3 Neutrino Masses

No direct neutrino mass measurements have been carried out. The overall neutrino mass scale cannot be constrained by neutrino oscillation experiments because the survival probabilities depend on differences of the squared masses. This dependency entails that only upper limits on these parameters can be set. The mass of the lightest neutrino has been constrained to $\lesssim 0.1\,\text{eV}$ [80] determined by studying the endpoint of the tritium β decay spectrum. Other model-dependent limits can be obtained

from cosmology that constrain the masses of relic neutrinos from the Big Bang to $\sum_{i=1}^{3} m_{\nu_i} \lesssim 1\,\text{eV}$ [125].

Two mass hierarchies arise from the PMNS matrix being parametrised in differences of the squares of neutrino masses. In the 'normal'[h] hierarchy $m_3 > m_2$, while in the 'inverted' hierarchy $m_3 < m_2$ [162]. While experimental technologies have not yet reached the required sensitivity to solve the mass hierarchy dilemma, some results do provide useful constraints and simplifications. The observation of neutrino flavour mixing resulted in the condition that $\Delta m^2_{21} \ll |\Delta m^2_{32}|$ [31, 88], which reasonably implies that $|\Delta m^2_{31}| \approx |\Delta m^2_{32}|$ since the mass splittings are correlated via $\Delta m^2_{21} + \Delta m^2_{32} - \Delta m^2_{31} = 0$ as illustrated in figure 2.7[i]. The experimental sensitivity required to determine the sign of $\Delta m^2_{32,31}$ are not yet attainable, hence the absolute value[j]. This renders neutrinos lighter by a factor of 10^6 and 10^9 than electrons and

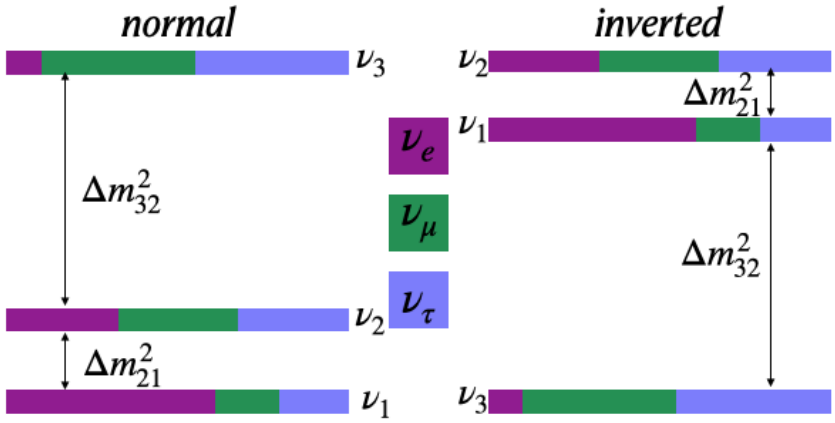


Figure 2.7: Depiction of the two possible neutrino mass hierarchies where the three neutrino flavours are combinations of the three mass eigenstates. The scales of $m_3 > m_2$ and $m_2 > m_3$ are arbitrary.

tau leptons, respectively. In the case where neutrinos are Dirac particles, like all the

[h] Deemed such as it follows the hierarchy of other lepton generations.
[i] The mass numbering is arbitrary. The oscillation results gives $\Delta m^2_{solar} \ll |\Delta m^2_{atmospheric}|$.
[j] This is at the heart of the mass ordering question: $m_2 < m_3$ or $m_2 > m_3$?

other fermions, the Yukawa coupling to the Higgs fields would be surprisingly small ($\mathcal{O}(10^{-12})$). The Yukawa coupling for neutrinos is a symptom of how light neutrinos are compared to the other fermions of the Standard Model rather than a framework to explain this discrepancy. If it were to persist, this gap between fermion masses would indicate an upper energy limit at which the SM is valid. However, the Seesaw mechanism discussed in section 2.2.3.3 provides a solution to this large gap by introducing a Majorana mass term in the Lagrangian, making the neutrinos their own antiparticles.

2.2.3.1 Dirac neutrinos

To accommodate massive neutrinos, a mass term must be introduced in the SM Lagrangian. This can be achieved through the same mechanism as for up-type quarks using the conjugate Higgs doublet. It follows that after spontaneous symmetry breaking, the gauge invariant Dirac mass term for the neutrino is given by

$$\mathfrak{L}_D = -m_D(\overline{\nu}_R\nu_L + \overline{\nu}_L\nu_R). \tag{2.2.16}$$

This in turn allows for right-handed chiral neutrinos capable of coupling with the electroweak bosons in the processes used in experiments to observe neutrino oscillations. It remains however that they are far lighter than any other fermions, thus hinting at another possible mass generating mechanism. [187, 90]

2.2.3.2 Majorana neutrinos

An alternate addendum to the SM Lagrangian takes the form of

$$\mathfrak{L}_{\mathfrak{M}} = -\frac{1}{2}M(\bar{\nu}_R^C\nu_R + \bar{\nu}_R\nu_R^C) \tag{2.2.17}$$

representing right-handed neutrino fields as well as left-handed antineutrino fields. This Majorana mass term respects the local gauge invariance of the SM which dictates that right-handed neutrinos and left-handed antineutrinos should transform as singlets under gauge transformations. An additional feature, or complication, arises from the Majorana mass term and takes the shape of an allowed direct coupling between a particle and an antiparticle which naturally violates charge conservation; unless they carry null charge as the only solution to avoiding this complication. A Majorana neutrino would be its own antiparticle. By definition, a right-handed neutrino would be indistinguishable from a left-handed antineutrino. [142]

2.2.3.3 The Seesaw mechanism

The lightness of Majorana neutrinos requires further theoretical stretches and gymnastics. For light particles, helicity and chirality manifest in similar ways causing the light Majorana neutrino to be stuck in a single chirality state. It is possible to construct a Lagrangian for the combined Dirac and Majorana masses by introducing a right-handed chiral neutrino field ν_R^C.

$$\mathfrak{L}_{DM} = -\frac{1}{2}(\bar{\nu}_L\bar{\nu}_R^C)\begin{pmatrix} 0 & m_D \\ m_D & M \end{pmatrix}\begin{pmatrix} \nu_L^C \\ \nu_R \end{pmatrix} + h.c. \tag{2.2.18}$$

If the Majorana mass M is far greater than the Dirac mass m_D, then a light neutrino state ν and a heavy neutrino state N will have masses

$$|m_\nu| \approx \frac{m_D^2}{M} \text{ and } m_N \approx M. \tag{2.2.19}$$

Taking the eigenvalues of the mass matrix, these can be expressed as

$$m_\nu = (\nu_L + \nu_L^C) - \frac{m_D}{M}(\nu_R + \nu_R^C) \tag{2.2.20}$$

for the light neutrino state, and

$$m_N = (\nu_R + \nu_R^c) + \frac{m_D}{M}(\nu_L + \nu_L^c) \tag{2.2.21}$$

for the heavy neutrino state [187]. The Seesaw mechanism works in such a way that the Dirac mass term of the neutrino can be of the same order of magnitude as that of other fermions by allowing their Majorana mass to be of the order of $M \sim 10^{11}$ GeV. The couplings of the light neutrinos to the weak CC would be similar to those of the SM. The massive neutrino state, being almost entirely right-handed, would not allow it to participate in the weak CC or NC interactions. As is, the SM uses a singlet Langrangian to describe weak interactions implying that ν_R is inert or sterile. An extension to the SM introduces a Higgs triplet that allows ν_R and $\bar{\nu}_L$ to couple to Z^0 and $W^\pm$ bosons. This Majorana extension would introduce mechanisms necessary for neutrino mass generation, and neutrino flavour oscillation. [154]

For the Seesaw mechanism hypothesis to be confirmed, it would require direct observation of the neutrinos being Majorana. The most promising probe for this lies

in the observation of the $0\nu\beta\beta$ decay.

2.2.4 Neutrinoless double beta decay

The most common radioactive decays can be classified according to the particles they emit: alpha (a helium nucleus α), beta (electrons β^- or positrons β^+) or gamma (high energy photon γ) decays. To follow conservation rules, beta decays involve the production of neutrinos in both the β^- and β^+ modes which are

$$n \rightarrow p + e^- + \bar{\nu}_e \tag{2.2.22}$$

$$p \rightarrow n + e^+ + \nu_e \tag{2.2.23}$$

respectively, which can also be more generally written as

$$(Z, A) \rightarrow (Z + 1, A) + e^- + \bar{\nu}_e. \tag{2.2.24}$$

This highlights the idea that single β decays can be energetically unfavourable, making it forbidden or at least strongly suppressed for many isotopes because the mass of its products, the daughter particle and the electron, exceeds that of the mother particle. Therefore, double β decays must occur in the form of

$$(Z, A) \rightarrow (Z + 2, A) + 2e^- + 2\bar{\nu}_e. \tag{2.2.25}$$

Mass parabolas and the allowed decay channels they offer are illustrated in figure 2.8.

The two neutrino double β decay ($2\nu\beta\beta$) was introduced by Goeppert-Mayer in

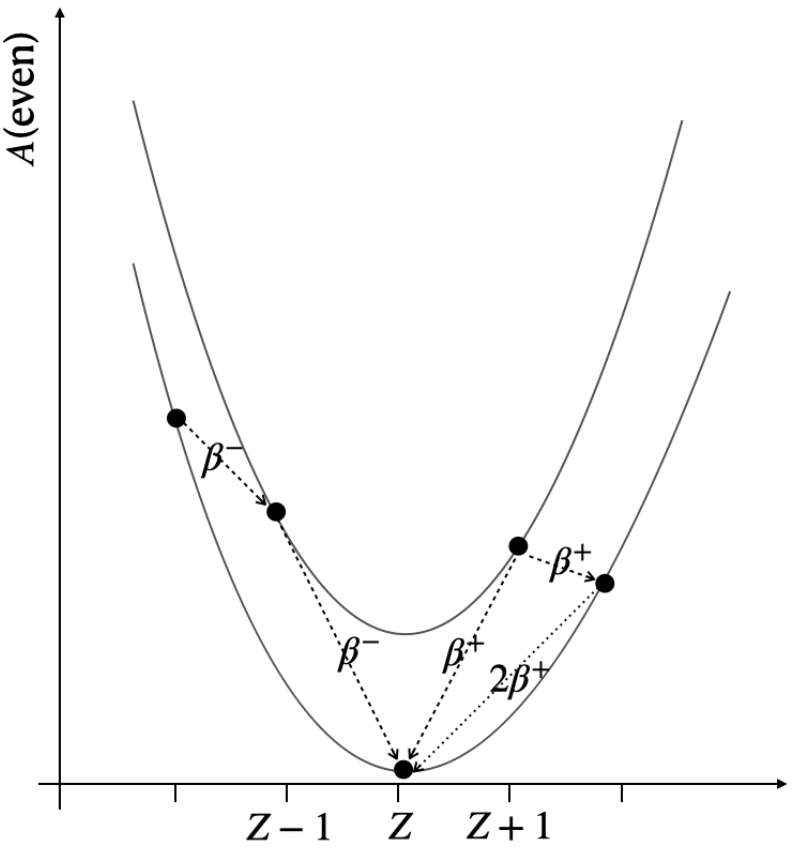
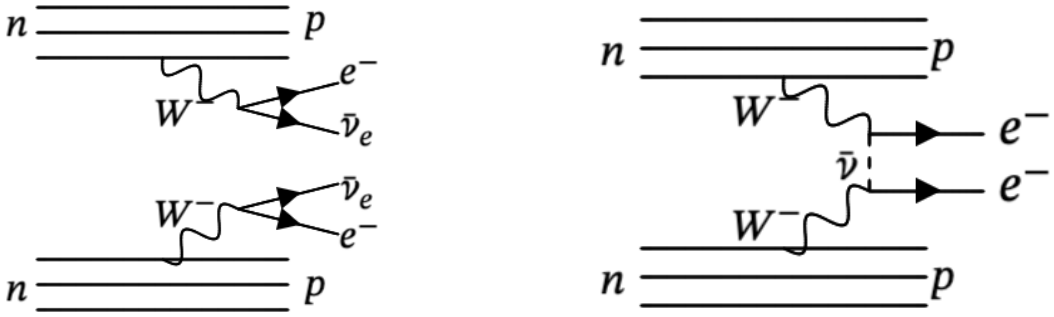


Figure 2.8: β decays in nuclei with an even atomic mass A. The progression along the mass parabolas denote radioactive decays, resulting in the integer addition or subtraction of their atomic number Z. In the case of an odd atomic mass A, the mass parabolas would be superimposed. The double β decay takes place when the single channel is energetically unfavourable and is only a feature of nuclei with even A.

1935 [91]. The half life of nuclei undergoing $2\nu\beta\beta$ are of the order of $10^{18} - 10^{21}$ years. Because part of the energy is carried away by the antineutrinos, it is observed as a spectrum ending at $\mathcal{Q}_{\beta\beta}$ [157].

If neutrinos are Majorana particles, there is the possibility of a $2\nu\beta\beta$ decay becoming the lepton number violating neutrinoless double beta decay ($0\nu\beta\beta$) through the annihilation of the neutrinos. This would occur through the exchange of a virtual

Majorana neutrino flipping its helicity to conserve momentum, and would present a distinct cross section from $2\nu\beta\beta$. The Feynman diagrams for these processes can be found in figure 2.9. This is the case where the $\mathcal{Q}$-value of the decay is exactly $\mathcal{Q}_{\beta\beta}$.



(a) (b)

Figure 2.9: (a) $2\nu\beta\beta$ decay (b) $0\nu\beta\beta$ decay.

The ease of discovery of this process is also correlated to the mass hierarchy. The $0\nu\beta\beta$ rate is proportional to the effective electron neutrino Majorana mass

$$m_{\beta\beta} = \left| \sum_{i=1}^{3} U_{ei}^{e} m_i \right|, \tag{2.2.26}$$

which includes the PMNS mixing matrix element U_{ei}^{e} relating to the electron neutrino [187]. The relation between the mass eigenstates and the squared mass differences that arise from expanding the matrix elements allow for both mass orderings. Because the effective mass cannot be parametrised in terms of a fixed neutrino mass eigenstate, large phase spaces of the $|m_{\beta\beta}|$ exist in areas beyond the sensitivity of current technologies, as illustrated in figure 2.10[k]. However, the inverted mass ordering puts $0\nu\beta\beta$ just within the grasp of modern day technology. [32]

[k] Colloquially referred to as a lobster plot.

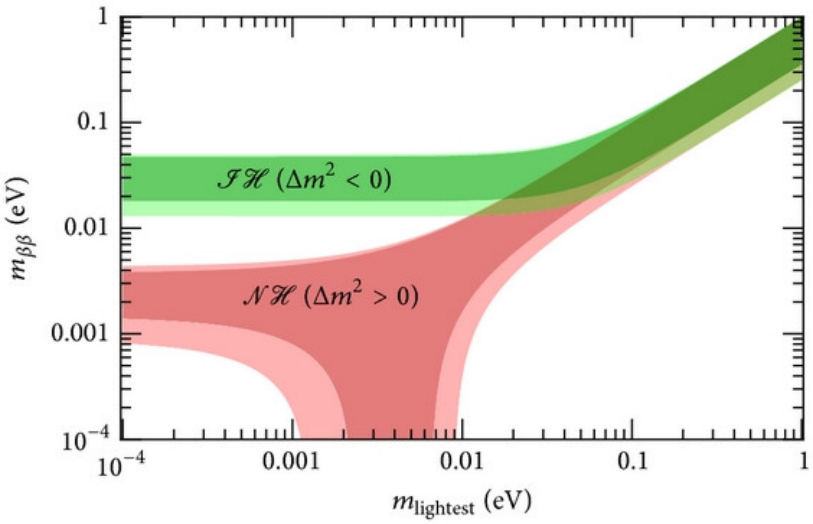


Figure 2.10: Predictions on $m_{\beta\beta}$ from oscillations as a function of the lightest neutrino mass in both the normal ($\mathcal{NH}$) and inverted ($\mathcal{IH}$) hierarchy cases where Δm^2 is defined as $m_3^2 - \frac{m_1^2+m_2^2}{2}$. Uncertainties on the oscillation parameters are taken into account in the shaded regions corresponding to 3σ uncertainty. Figure from [79].

The calculation of the nuclear matrix element assumes a further estimate known as the closure approximation. Under the conjecture according to which the exchanged virtual neutrino is vastly more energetic than the excitation energy that precipitates the decay, the cross section of the $0\nu\beta\beta$ decay is expressed as

$$\Lambda^{0\nu} = \frac{1}{T_{1/2}^{0\nu}} = G^{0\nu}(\mathcal{Q}, Z)|M^{0\nu}|^2 \frac{|m_{\beta\beta}|^2}{m_e^2} \tag{2.2.27}$$

$$T_{1/2}^{0\nu} = G^{0\nu}|M^{0\nu}|^2 (\frac{m_{\beta\beta}}{m_e})^2, \tag{2.2.28}$$

where $G^{0\nu}(\mathcal{Q}, Z)$ is a phase space integral unique to each isotope and reported for common $0\nu\beta\beta$ candidates alongside their half-lives $T_{1/2}^{0\nu}$. Calculating the matrix elements, and therefore $T_{1/2}^{0\nu}$, is non-trivial. As most many-body problems, they employ

numerical methods and assumptions. Figure 2.11 shows the combined results of the most common approaches for several approaches: Quasi-particle Random Phase Approximation (QRPA) [41, 174], the Energy Density Functional (EDF) method [169, 170], the Projected Hartree-Fock-Bogoliubov (PHFB) approach [163], the Interacting Boson Model-2 (IBM-2) [27] and the Large-Scale Shell Model (LSSM) [136].

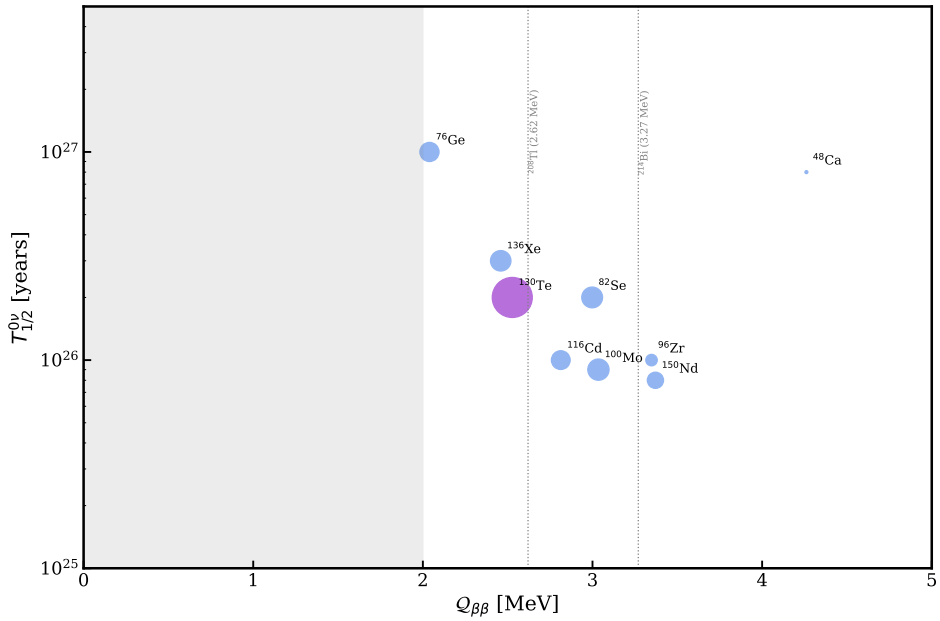


Figure 2.11: Leading $0\nu\beta\beta$ isotopes are plotted in the ($\mathcal{Q}_{\beta\beta}$, $T^{0\nu}_{1/2}$) space with their natural abundance reflected in their marker size. Some pervasive background sources are included such as the 2.6 MeV γ produced by external ^{208}Tl and ^{222}Rn manifesting through the endpoint of ^{214}Bi, their $\mathcal{Q}$-value represented as vertical dotted lines. Isotopes lying in the shaded region below 2 MeV are omitted as this region is both challenging to access and flooded backgrounds. Values for energy and abundance collected from [109]; values for half-life are taken as an average of the calculations by models listed above. The half-life assumes a hypothetical value for $m_{\beta\beta}$ and selected nuclear matrix elements, also from [109]. The tellurium isotope chosen by SNO+ is in purple.

With $\mathcal{Q}_{\beta\beta}$ being a calculable value for all nuclei, the choice of target isotope needs to present a $\mathcal{Q}_{\beta\beta}$ in an energy region attainable to experimental physics techniques. Figure 2.11 shows the leading candidates. The expected number of events within the $\mathcal{Q}_{\beta\beta}$ region is given by

$$N_{\beta\beta} = \ln(2)\frac{N_A}{W}\left(\frac{a\epsilon}{T^{0\nu}_{1/2}}\sqrt{\frac{Mt}{B\Delta E}}\right) \begin{cases} N_A := \text{Avogadro's number} \\ W := \text{target molar mass} \\ a := \text{isotope abundance} \\ \epsilon := \text{detection efficiency} \\ M := \text{isotope deployed mass} \\ t := \text{experiment livetime} \\ B := \text{background proportion} \\ \Delta E := \text{detector energy resolution} \end{cases} \tag{2.2.29}$$

which highlights all the considerations that go into both detector design and isotope choice. Figure 2.12 highlights the experimental intricacies of detecting this already rare process, as the region of interest is crowded with overwhelming backgrounds. As such, resolving the narrow $0\nu\beta\beta$ peak from the wide $2\nu\beta\beta$ spectrum requires precise detector resolution. Beyond the practical background suppression strategies that will be covered in chapter 3, the choice of isotope itself offers a non-negligible handle on maximising the signal ($0\nu\beta\beta$) to background ($2\nu\beta\beta$) ratio

$$\frac{S}{B} \propto \left(\frac{\mathcal{Q}_{\beta\beta}}{\Delta E}\right)^6 \frac{T^{2\nu}_{1/2}}{T^{0\nu}_{1/2}}. \tag{2.2.30}$$

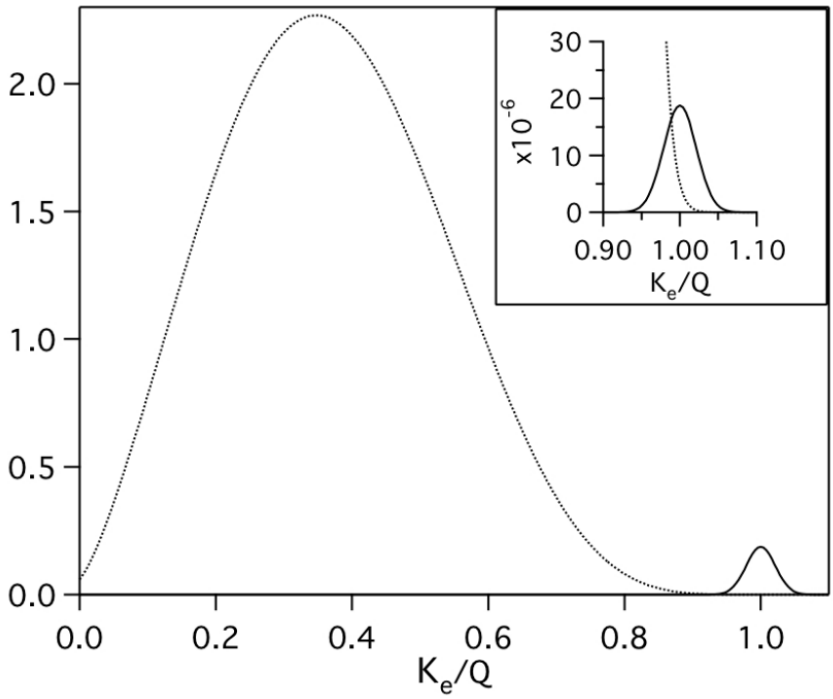


Figure 2.12: Illustration of the broad $2\nu\beta\beta$ peak with respect to the narrower and rarer $0\nu\beta\beta$ peak. The inlay is meant to emphasize the overlap between the two spectra due to the tail of $2\nu\beta\beta$. Figure adapted from [18].

Experiments then fine tune their design around boosting the S/B ratio by manipulating as many parameters as feasible: the enrichment of isotopes pushes their abundance above natural levels, increasing the isotope doping levels of the active target within the detection medium, enlarging the active volume, employing state-of-the-art detector technologies, novel analysis strategies, and purification methods; all of which are the subject of chapter 3.

Figure 2.13 presents the sensitivities of current and projected neutrino experiments. Fully exploring the inverted hierarchy phase space in search of $0\nu\beta\beta$ would either confirm the Majorana nature of neutrinos, allow a direct mass measurement, open particle physics to a multitude of theories beyond the SM, or impose more

stringent limits on the inverted mass hierarchy scenario and the Majorana nature of neutrinos.

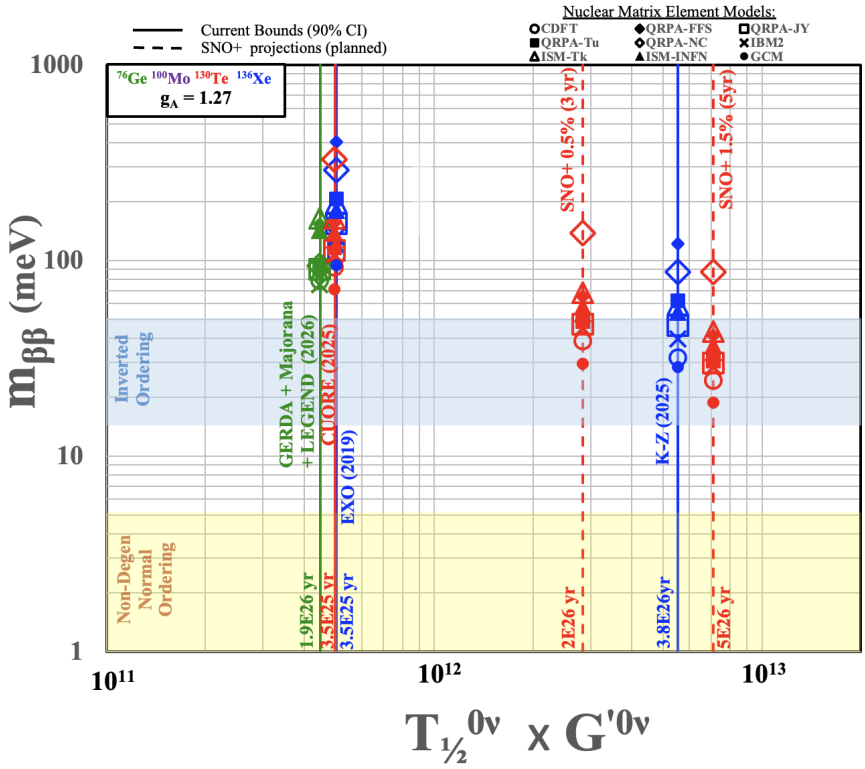


Figure 2.13: Running (solid) and near-term projected (dashed) sensitivities of $0\nu\beta\beta$ experiments with the inverse hierarchy phase space shaded. Figure from [38].

2.2.4.1 SNO+'s choice

SNO+'s choice of the tellurium (Te) isotope balances lower backgrounds through a $\mathcal{Q}_{\beta\beta}$ value above most radioactive decays within the uranium and thorium chains[1]. It also features a long $2\nu\beta\beta$ half-life compared to the candidate isotopes in figure

[1]With $\mathcal{Q}_{\beta\beta}$ >2 MeV, the Region of Interest (ROI) lies beyond most of the solar neutrino sources except ^{8}B which, although a nuisance in the search for the process the SNO+ detector was commissioned, is worth studying in itself if only in the ongoing scintillator phase in preparation to the Te phase.

2.11 without compromising the expected $0\nu\beta\beta$ cross section. It also boasts relative ease and safety of deployment as well as natural abundance and cost. The high natural abundance of ^{130}Te renders its enrichment unnecessary compared to other isotopes.

This chapter closes with several open questions in neutrino physics. What is the absolute neutrino mass? Which is the correct mass hierarchy? What is δ_{CP} and could CP violation in the lepton sector explain the matter versus antimatter imbalance unaccounted for by CP violation in the quark sector? And the question that could be the key to answering them all: are neutrinos Majorana or Dirac particles? A few large scale detectors, including SNO+, are poised to seek the answers to these questions.

Chapter 3

The SNO+ experiment

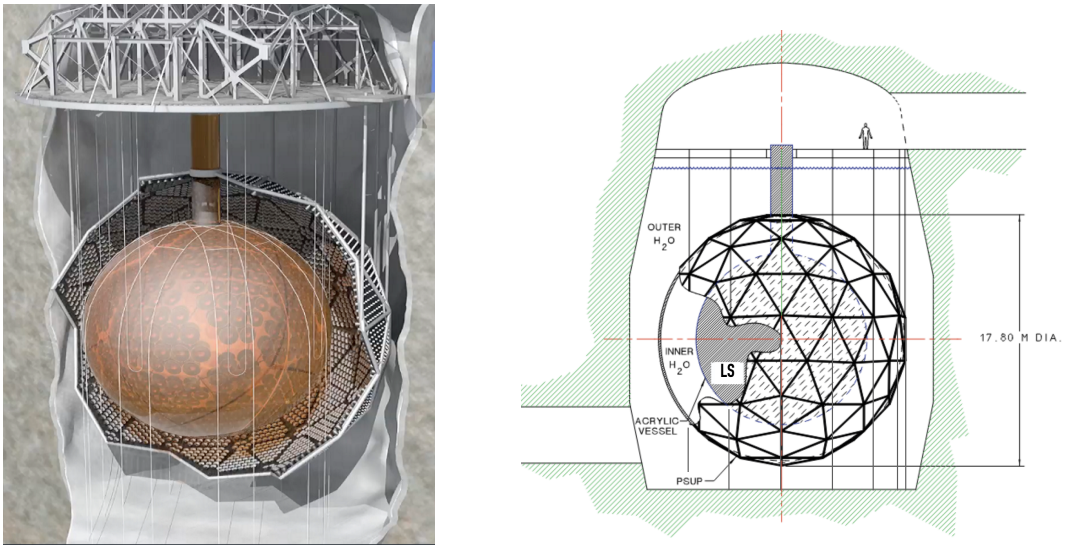
Do [PMTs] Dream of Electric Sheep?

- P.K. Dick

As of April 29$^{\text{th}}$ 2022, the SNO+ experiment has successfully loaded its liquid scintillator into the acrylic vessel. Having already produced interesting physics in its previous ultrapure water phase operating as a Cherenkov detector, SNO+ is now operating in its enhanced scintillator phase with 2.2 g/L 2,5-diphenyloxazole (PPO) and 2.2 mg/L 1,4-Bis(2-methylstyrl)benzene (bis-MSB) wavelength shifting fluors dissolved in 780 tons of Linear Alkylbenzene (LAB). While the main physics goal of this experiment is the search for $0\nu\beta\beta$ decay, signatures for low energy solar neutrinos, geoneutrinos, reactor antineutrinos, supernova neutrinos and antineutrinos as well as exotic physics have been undertaken [59, 62, 63] or anticipated. Tellurium loaded LAB features as SNO+'s next and final phase that is entirely dedicated to the measurement of $0\nu\beta\beta$ decay.

3.1 The Detector

The SNO+ detector is located 2 km underground in a cavity reserved by the active Creighton mine for SNOLAB, and situated on the periphery of Lively, Ontario. Inheriting most of its infrastructure and electronics from its predecessor SNO, the SNO+ detector was upgraded to accommodate LAB in place of of heavy water as its target medium. The practical realities of the less dense medium lead to the most significant structural upgrade from SNO to SNO+: the addition of hold-up and hold-down Tensylon ropes. These were necessary to accommodate the buoyancy from filling the 12 m diameter Acrylic Vessel (AV) with LAB as it floats in its Ultrapure Water (UPW) filled cylindrical cavity, required to absorb the background radiation emitted from the surrounding rock. As can be seen from the artistic rendering in figure 3.1, over nine thousand (9362) inward facing Photomultiplier Tube (PMT)s line the geodesic stainless steel PMT Support structure (PSUP) surrounding the AV. Because SNO+ is an optical detector relying on the capture of photons emitted from the energy deposition of particle interactions within the liquid scintillator, PMTs were selected due to their high sensitivity to light and configurability to adapt to the shape of the detector in a way that provides optimal coverage and high resolution. Just under one hundred (91) Outward Looking PMT (OWL)s are used as cosmic-ray muon vetos for the expected 3-per-hour rate of muons traversing the 2 km rock overburden. The neck is the sole access point to the detector infrastructure. It connects the AV to the deck sitting on top of the UPW cavity as a sort of floating lid. Any and all practical operations ranging from target medium filling to calibration source deployment go through the neck. Four PMTs sitting at the junction of the neck and the AV sphere are angled upwards to monitor events occurring within the neck volume. [65]



(a) (b)

Figure 3.1: (a) Artistic rendering of the SNO+ detector and cavity. Illustrated are the deck, neck, PSUP and PMT array, hold-down and hold-up rope system, and AV. (b) Detector schematics of the main hardward features. Figure upgraded from [71].

This chapter aims to give an overview of the SNO+ detector, and how its entire design revolves around enabling it to attain its physics goals. This brings about discussions centered on the hardware, processing plants for the detector medium[a] from the perspective of tackling the challenge of ridding a very crowded signal region of noise and background events; as well as the journey of an event from scintillation light to data files fit for physics analysis.

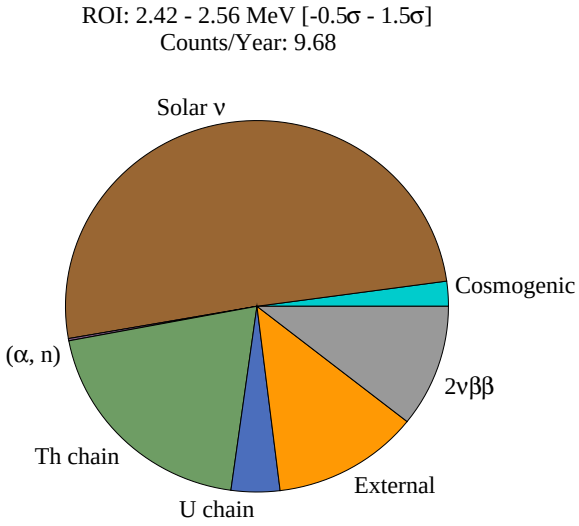
3.2 Physics Goals

In the search for neutrinoless double beta decay, the expression 'finding a needle in a haystack' is a gross understatement. Experiments such as SNO+ push modern

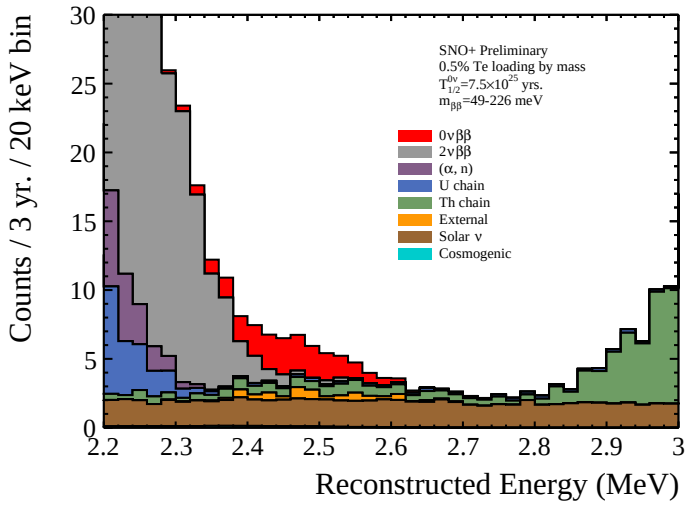
[a]The optics are kept for the chapter 4.

day technology in their search for ever improving designs, be they in electronics and hardware for resolution, chemistry for the development of an optical medium maximising interaction cross sections, engineering for the construction of purification and process systems, materials for shielding, etc.

The ROI of $0\nu\beta\beta$ decay for ^{130}Te is defined as [-0.5-1.5] σ around $Q_{\beta\beta}(^{130}\text{Te}) = 2.53\,\text{MeV}$ [189]. The number of expected events given a 3 tonne isotope loading within the 780 tonne active medium, taking into account a fiducial volume of 3.3 m, can be calculated to be 13.4 events per year. This leaves a background budget of 9.68 counts per year allowing for a signal extraction with sufficient statistical significance as determined by a counting analysis of contributing backgrounds with the same conditions. The remaining backgrounds are expected to be dominated by the flat ^{8}B electron neutrino solar flux, as well ^{130}Te $2\nu\beta\beta$ decay backgrounds. Contributing backgrounds and the spectrum plot for ^{130}Te at 0.5% loading can be found in figure 3.2. Only an improved energy resolution would provide a solution to discriminating from the $2\nu\beta\beta$ decay background. As for the flat solar flux from ^{8}B electron neutrinos, other means, like directionality, the subject of this thesis, could provide a good distinction. Nevertheless, there exist a slew of background sources that detector design, purification and tracking methods are equipped to tackle.



(a)



(b)

Figure 3.2: Contributing backgrounds (top) and spectrum plot for the $0\nu\beta\beta$ half-life of 8×10^{25} years (bottom) for SNO+'s 0.5% Te loaded phase as projected by simulated Monte Carlo sets. Figure from [143].

3.3 Mitigating Backgrounds

SNO+ classifies its backgrounds in two broad categories: internal and external. External backgrounds include radioactive decays or nuclear interactions originating from trace radioactive impurities in the surrounding rock, water, as well as matter from the AV, the hold-down or hold-up rope system, the PSUP, and the PMTs themselves. Internal backgrounds are the products of radioactive decays or nuclear reactions of events occurring with particles of the target material. Internal background rates are therefore related to the components of the liquid scintillator cocktail.

Internal or external, a majority of backgrounds existing within the ROI are the daughters of natural radioactivity within the ^{238}U and ^{232}Th decay chains. The chains are illustrated in figures 3.3 and 3.4, while the main isotopes of nuisance to SNO+ are summarised in table 3.1 which lists backgrounds in the LAB+PPO SNO+ scintillator phase and their status. From the ^{238}U chain, ^{214}Bi, $^{234\mathrm{m}}$Pa, ^{210}Tl have $\mathcal{Q}$ values within the $0\nu\beta\beta$ decay ROI; ^{214}Bi, ^{210}Bi and ^{210}Tl appear throughout the wide spectrum of interest to solar neutrino analyses. As for the ^{232}Th chain, the isotopes detrimental to both solar and $0\nu\beta\beta$ decay analyses are therefore ^{212}Bi, ^{212}Po and ^{208}Tl. All the isotopes listed are relatively short-lived, which means they could be expected to fully decay away within a matter of days. However, this is not the case and their rate is sustained due to the radioactivation of atoms within this chain prompted by radon ingress – a subject that will resurface with undeterred perseverance throughout this chapter.

Nuclear reactions involving atoms of the target material are also susceptible to generating backgrounds which interfere with the ROIs for different SNO+ analyses. Alpha particles from ^{210}Po interacting with the scintillator produce neutrons, via

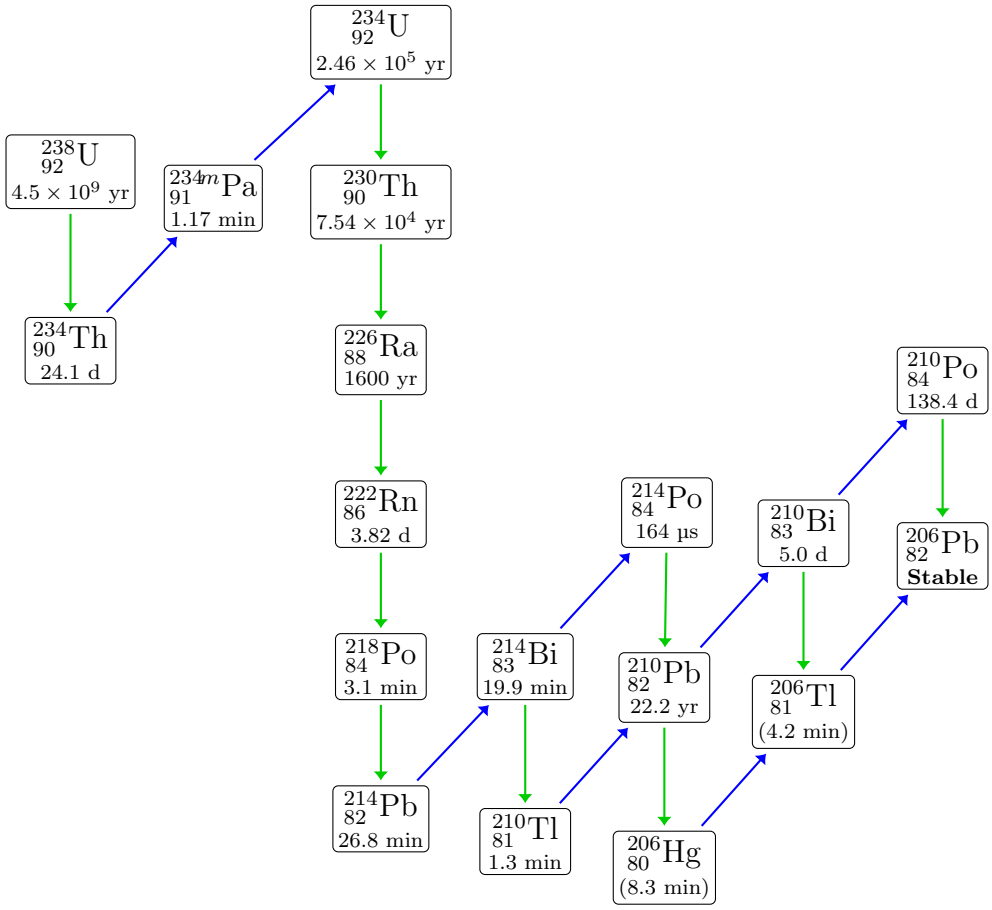


Figure 3.3: Main decays in the Uranium-238 chain where α and β decays are represented with green or blue arrows respectively.

(α, n) reactions, with the energy signature of the Inverse β Decay (IBD) tied to $\bar{\nu}$ reactions.

Internal target levels of the backgrounds from the two main decay chains ^{238}U and ^{232}Th are of the order of 10^{-17} g/g. The rate can be assessed *in situ* through the analysis method of coincidence tagging. ^{212}Bi-^{212}Po and ^{214}Bi-^{214}Po pairs (^{212,214}BiPo) are produced via β and α decays, respectively, that occur within relatively short set time windows tied to the half lives of the daughter isotopes. A good understanding of the scintillator properties allows one to set radial windows between pairs produced

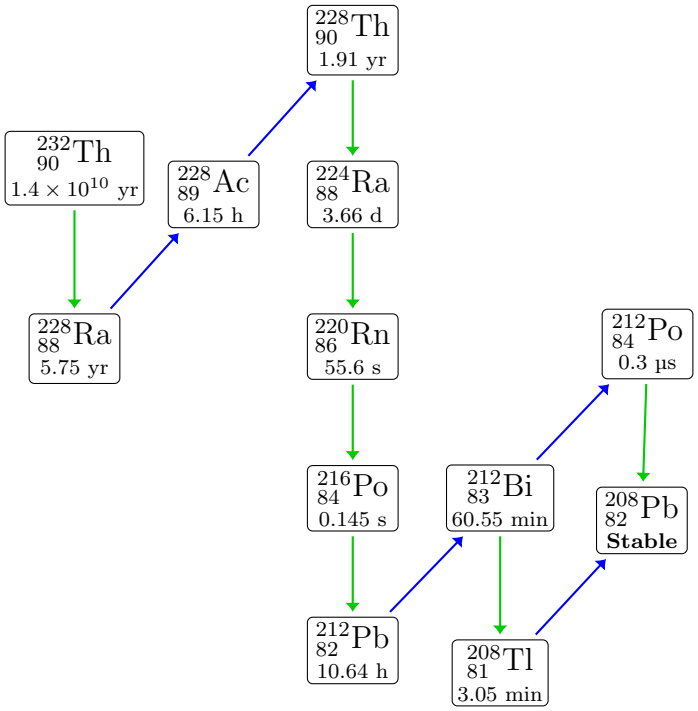


Figure 3.4: Main decays in the Thorium-232 chain where α and β decays are represented with green or blue arrows respectively.

by certain calibration sources, though this does not apply to BiPos, informed by the expected distance traveled through scintillator of a particle carrying a certain energy. The radial cuts for BiPos are set to ensure events are matched as the only position differences should arise from position reconstruction error. The target 10^{-17} g/g rate corresponds to 3 counts per day of ^{208}Tl, the α decay of ^{212}Bi from the ^{232}Th chain, and 9 counts per day of ^{214}Bi and ^{212}Bi from the ^{238}U chain. As will be discussed in this section, ^{222}Rn ingress from operations and ambient environment play a role in sustaining if not increasing this rate.

Internal ^{238}U (780T)	**target** $[\times 10^{-17} g/g]$	**measured** $[\times 10^{-17} g/g]$	**decays/year**
^{214}Bi	1.6	4.32	13224
^{214}Po	1.6	4.32	13224
^{210}Tl	1.6	4.32	3
^{210}Po	4.15×10^{-7}	?	1.12×10^{9}
Internal ^{232}Th (780T)	**target** $[\times 10^{-17} g/g]$	**measured** $[\times 10^{-17} g/g]$	**decays/year**
^{212}Bi	0.68	5.29	3381
^{212}Po	0.68	5.29	3381
^{208}Tl	0.36	5.29	1902
External		**measured** $[\times 10^{-10} g/g]$	**decays/year**
Internal ropes (45.2g)	^{214}Bi	2.8	4966
	^{210}Tl	2.8	1.04
	^{212}BiPo	2.0	743
	^{208}Tl	2.0	418
Hold-down ropes (222.09kg)	^{214}Bi	0.47	4.06×10^{6}
	^{210}Tl	0.47	853
	^{212}BiPo	2.27	4.13×10^{6}
	^{208}Tl	2.27	2.32×10^{6}
Hold-up ropes (45.7kg)	^{214}Bi	0.47	8.34×10^{5}
	^{210}Tl	0.47	175
	^{212}BiPo	2.27	8.5×10^{5}
	^{208}Tl	2.27	4.78×10^{5}
Cavity water (1634T)	^{214}Bi	0.00206	1.32×10^{8}
	^{210}Tl	0.00206	2.77×10^{4}
	^{212}BiPo	0.00052	6.96×10^{6}
	^{208}Tl	0.00052	3.92×10^{6}
AV (32.53T)	^{214}Bi	0.01	1.28×10^{7}
	^{210}Tl	0.01	25284
	^{212}BiPo	0.01	2.67×10^{6}
	^{208}Tl	0.01	1.50×10^{6}
PMTs (9456)	^{214}Bi	10^{6}	3.27×10^{11}
	^{210}Tl	10^{6}	7.8×10^{7}
	^{212}BiPo	10^{6}	7.8×10^{10}
	^{208}Tl	10^{6}	4.4×10^{10}

Table 3.1: Measured values of some of the most prevalent backgrounds in SNO+, listed per source. Rarer isotopes of concern such as Kr and Ar are not included. Values taken from [129].

3.3.1 Cosmogenics and Shielding

The Earth's surface is bombarded with any and all particles as it spins through our solar system. Cosmic rays hurtle muons – the most pervasive of offenders originating from cosmic rays as they are the only ones capable of traveling to significant depths underground – at a rate of one per square centimeter per minute at sea level. As they continue to undergo ionisation and radiative processes underground, fluxes of photons, electrons and hadrons are to be expected. As for the Sun, it spews a flux

of 65 to 100 billion neutrinos per square centimeter per second. In other words, a common astroparticle physics outreach fun fact is that this is equivalent to the rate of neutrinos going through one's thumb per second.

Boasting such rates and broad energy spectra, these particles would engulf the elusive $Q_{\beta\beta}$ of $0\nu\beta\beta$ no matter the choice of isotope. $0\nu\beta\beta$ decay experiments, more broadly neutrino experiments, seek refuge from these particle showers under mountains in Italy (Borexino, COBRA, CUORE, CUPID, GERDA, LEGEND, XENON) and China (Daya Bay, JUNO), in mines in Japan (KamLAND-Zen) and Canada (SNO, SNO+), or in tunnels in France (NEMO, SuperNEMO). Figure 3.5 places these national laboratories on the axis of their total muon flux as determined by their equivalent vertical overburden.

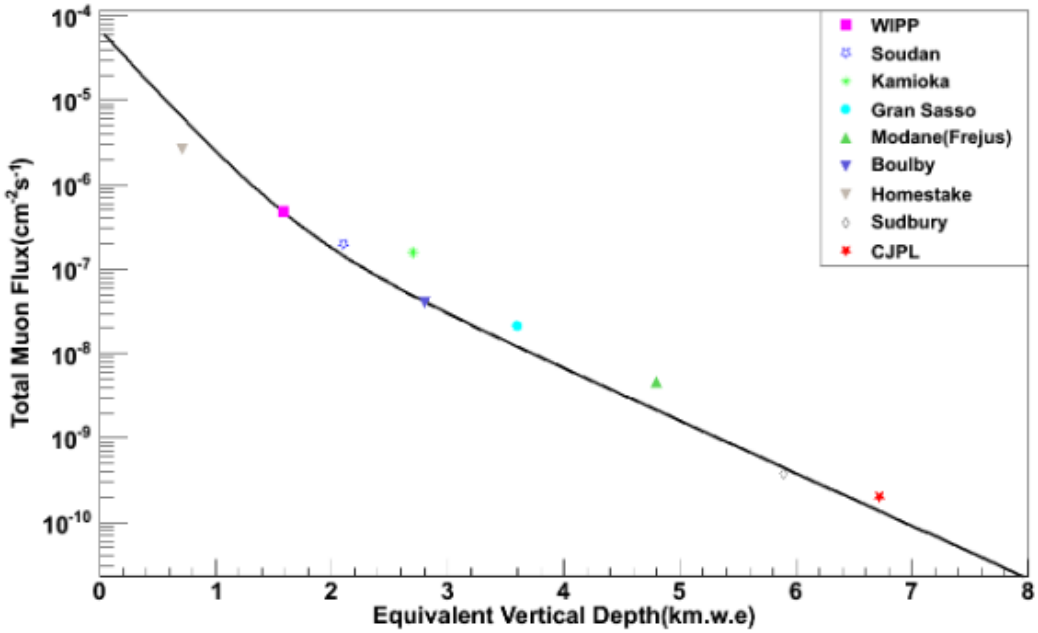


Figure 3.5: Expected muon flux for the current neutrino experiments with respect to the depth of the laboratories housing them. Figure from [49]. SNO+ sits at an equivalent vertical depth of 6 km w.e..

Air showers of cosmic radiation include all stable charged particles and nuclei generated when they interact with products of solar winds upon entering the atmosphere [30]. Reaching the Earth's atmosphere are primarily hydrogen and helium nuclei, which then interact with atmospheric particles. The resulting charged mesons ($\pi^{\pm}, K^{\pm}$) will produce muons and neutrinos after their secondary decays, while eletrons and photons arise from the further decay of neutral mesons (π^0). Produced primarily just before entering the troposphere, muons lose about 2 GeV through ionisation, leaving them with, on average, 4 GeV upon reaching the ground. Their vertical intensity is the relevant figure of merit for underground experiments. The larger the incidence angle, the less depth is traveled for the same increments of stopping power. The vertical intensity depends on the kinetic energy they carry, but is on average $70\,\mathrm{m^{-2}s^{-1}sr^{-1}}$. For comparison, the vertical intensity of electrons and photons of energies in the GeV range is $0.2\,\mathrm{m^{-2}s^{-1}sr^{-1}}$, with nucleons are on the same order of magnitude. The incidence angle must also be accounted for in detectors which have chosen mountains as their lairs. The calculation of the effective overburden must account for the vertical depth as well as the penetration power of muon fluxes with lower incidence angles. Therefore, SNO+'s first line of defense is its 2092 m flat norite rock overburden.

Indeed, the muon spectrum can be described as

$$\frac{dN_\mu(X)}{dE_\mu} = \frac{dN_\mu}{dE_{\mu,0}}\frac{dE_{\mu,0}}{dE_\mu} = \frac{N_\mu}{dE_{\mu,0}}e^{bX} \tag{3.3.1}$$

where $E_{\mu,0} = (E_\mu + \epsilon)e^{bX} - \epsilon$ represents the energy of a muon upon its production in the atmosphere [30]. E_μ is its energy after penetrating a rock of depth X, and is uniquely defined by the ratio ϵ of the ionisation loss over the fractional energy loss by

radation processes (*Bremsstrahlung*, pair production and photonuclear interactions). The atmospheric neutrinos produced alongside these muons share a similar high-energy signature, and are expected to keep within a tight cone around the muon track. In high energy physics, this is known as a jet.

Additional shielding has been layered onto the detector to further protect it from the continuous muon flux. The 34 m tall cylindrical cavity housing the AV and its 8.9 m radius surrounding PSUP are filled with 7000 tonnes of UPW. Once the norite, UPW and mine air shields, as well as the geographical location and elevation from sea level of the site are considered, the incoming muon rate is effectively suppressed to a mere $3.31^{\pm 0.01(\text{stat})}_{\pm 0.09(\text{sys})} \times 10^{-10}$ muons per square centimeter per second [71] or 0.286 ± 0.009 muons per square meter per day [65].

While an additional 3 m of water may seem irrelevant compared to the rock overburden corresponding to a 6010 m water equivalent in the previous calculation, it must be noted that the advantage lies in the OWLs arrayed on the PSUP. These allow for the implementation of a directionality-based external muon veto. In conjunction with an energy based cut, any muons surviving their journey through cosmos and norite are effectively identified and rejected from any analysis. Furthermore, a time window following a muon, or any other high energy event, lighting up the detector, as can be seen in figure 3.6, allows for a quick detector cooldown before PMTs start recording further events, thus avoiding the potential pileup following such a high energy event as a muon scintillating through SNO+. A 20 s time window is implemented to discard any spallation induced from cosmogenic isotopes. Despite the significant rate reduction, 68.9 ± 1.8 muons per day are still expected to penetrate the SNO+ target material [11]. Highly energetic, muons are likely to interact with nuclei of the liquid

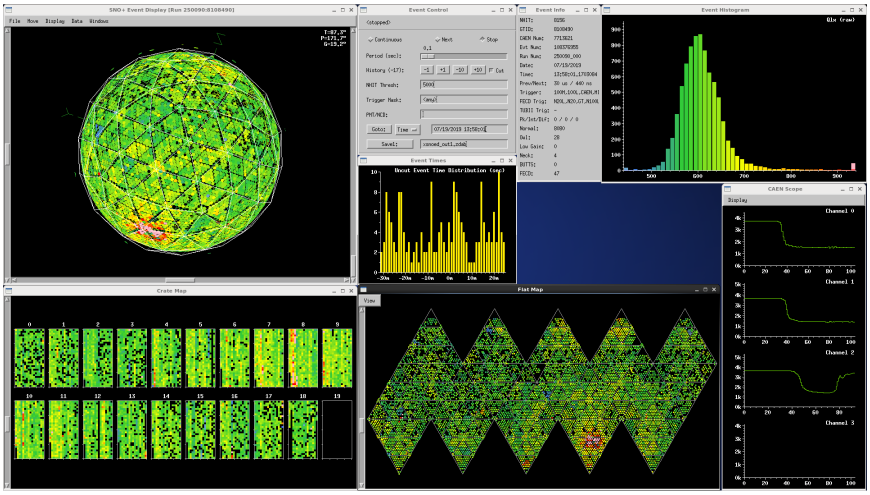


Figure 3.6: A typical muon event in LAB as captured by xsnoed, a GUI used by detector operators. Hit distributions can be seen on a histogram, through summed charge pulses over hit PMTs, on a spherical model of the detector, on a flat map projection and on a crate map of the SNO+ electronics.

scintillator and spallate. Cosmogenically activated isotopes span the energy range of all SNO+ physics goals; of particular note are those in figure 3.7 originating from muon interaction with ^{130}Te nuclei and with energies overlapping with the $\mathcal{Q}_{\beta\beta}$, and with a half-life rendering them impossible to "wait out" at above 20 days.

3.3.2 Radioactivity and the Purification Systems

While this unique combination of natural and human designed shielding does an impressive job of suppressing cosmogenic backgrounds, additional sources of radioactive backgrounds must be contended with for the success of SNO+'s physics goals. Overlooking any man-made radiation emanating from nuclear energy or medical facilities, naturally occurring environmental background radiation is far from negligible. Radioactive elements are found naturally in rocks, in the air, in water, almost everywhere – including the human body. Elements have half lives spanning from fractions

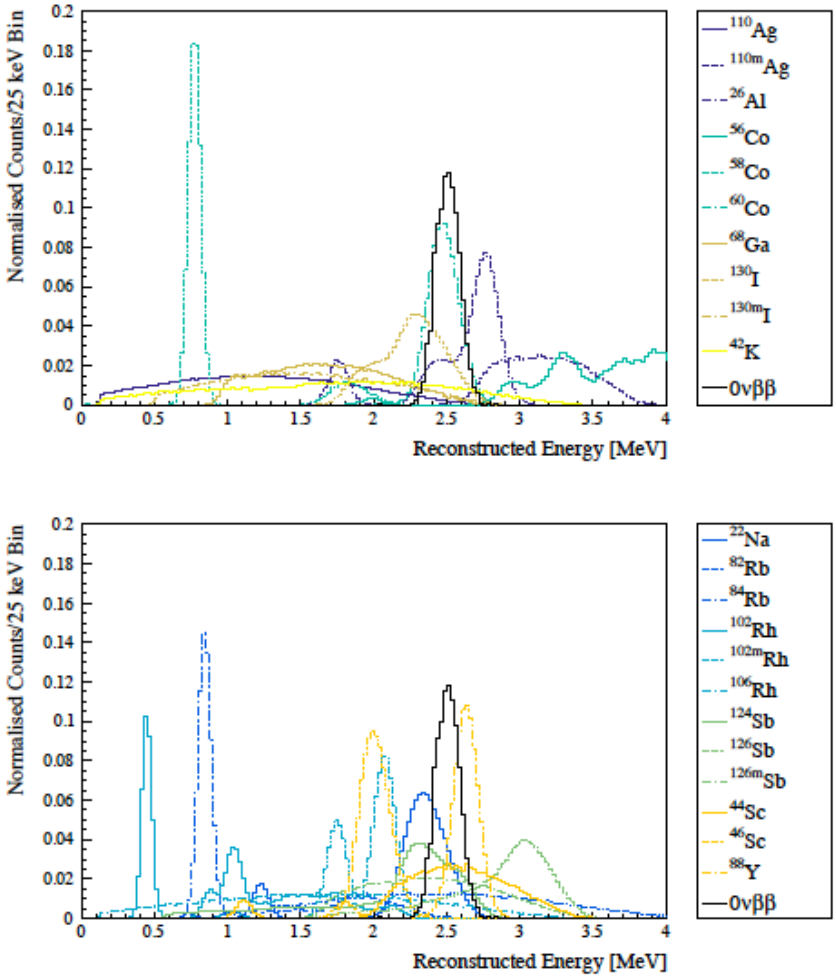


Figure 3.7: Normalised energy reconstruction of the simulated flux of potentially problematic cosmogenic isotopes. In black is the $0\nu\beta\beta$ peak at $\mathcal{Q}_{\beta\beta} = 2.527\,\text{MeV}$ for the Te isotope. Figure from [118].

of seconds to several billions of years. Unstable nuclei have positive $\mathcal{Q}$-values allowing them to spontaneously undergo radiative decays, during which a daughter particle is released with a signature kinetic energy until they reach a stable state. Every isotope has its specific half-life, the time required for half of a given quantity of this isotope to have decayed away, ranging from 10^{24} to 10^{-23} seconds. The steps an isotope takes until reaching its stable state forms a decay chain. The most straightforward way

to reduce background radiation is to hack into the abundance of all airborne particulates. To this effect, SNOLAB is a class-2000 clean room facility meaning 2000 is the upper limit of how many 0.5 μm diameter or larger particles per cubic foot are tolerated. For reference, the ambient air we're exposed to would be of class 2 million. Particle counters nearer the "seams" of the detector, i.e. on the deck clean room, monitor the space within a class-200 to further contain contamination in proximity to the target material.

3.3.2.1 The Cavity and Water Systems

^{238}U and ^{232}Th are both naturally occurring, relatively abundant isotopes that decay into daughters populating the $0\nu\beta\beta$ decay ROI. Unfortunately, norite, which absorbs much of the cosmic radiation flux, does contribute to ^{238}U and ^{232}Th backgrounds rate. The UPW-filled cavity comes back into play. Since one of its functions is to reduce background radiation, it is first and foremost important to not have it, itself, be a significant contributor to radiation. The choice of material is paramount and was devised for SNO. Material testing taking into account coating nature, layers, thickness, tensile strength, adhesion, resistance to varying temperatures and humidity settled on the choice of a dual coating of Urylon polyurethane as best for reducing airborne radon particles. More than two were applied in a well ventilated environment to avoid trapping of dust while drying and to obtain a smooth, thick seal. [94]

The PSUP and its PMTs are also sources of external backgrounds against which the cavity water provides some shielding. With the PSUP sitting almost 3 m from the AV wall, just under 1700 tonnes of water fill that gap called the inner cavity and the remaining 5700 tonnes live between the PSUP and the cavity walls. The rope

net is another structure to be accounted for. Vectran ropes suspended from the deck were installed for SNO to hold up the AV when it was filled with D_2O, aptly dubbed "heavy water" as its greater density would cause it to have had a tendency to sink in the UPW filled cavity. These were replaced by tensylon ropes which provides a lower activity rate. Futhermore, a set of hold-down ropes anchored in the floor of the cavity loop over the top of the AV sphere in a net arranged around the neck was added to counteract the inevitable buoyancy of a LAB-filled AV sitting in a UPW-filled cavity. [34]

As for the AV, acrylic was put through series of test bench experiments to determine the expected leaching rates. Studies of (α,n) counts within the detector are a good indicator of the residual concentration levels of ^{222}Rn daughters, specifically ^{210}Po, embedded in the AV walls. Exposed to mine air (123 Bq/m^3 ^{222}Rn) during its construction, the AV walls leach radioisotopes. Following the decay chain in figure 3.3, ^{210}Pb with a half-life of 22.2 years will accompany signal throughout SNO+'s active data taking years. Ridding the AV walls of radioactivity could not have been achieved by any standard measure of typical cleaning as ionic deposits embed themselves ~100 nm into the material. While ^{210}Pb does not have a $\mathcal{Q}$-value infringing on the $0\nu\beta\beta$ ROI, its daughters ^{210}Bi and ^{210}Po at the end of the decay chain represent non negligible and constant backgrounds for various analyses. At a slighlty "worse" case than the planned operating environment, the leaching rate of $(1.05^{+0.18}_{-0.19}) \times 10^{-3}$ of ^{210}Po events per day in the acrylic was measured in 18°C water. This represents the equivalent of 0.40 Bq/m^3 after one year of exposure of the acrylic to UPW. In scintillator kept at similar temperatures, this rate is reduced by a factor of ten. The implementation of a fiducial volume cut in analyses reduces the active volume but

is an effective way of discounting external radiation from the detector structure and components.

Water naturally absorbs radiation. The UPW plant was equipped with a recirculation and purification system. There has already been discussion on the use of UPW as shielding against cosmic rays, radiation from norite and mine activities, as well as intrinsic residual backgrounds in the PMT array and cavity wall materials.

To begin with, SNOLAB sources its water through VALE directly from Lively municipal water. Pre-treatment of municipal water to get it to comply to the status of UPW requires it to undergo several chemical purification techniques. First, water is distilled by being run through resins which absorb cations, then through resins which absorb anions. This ion exchange removes mostly salts in the case of municipal water. Particulates larger than 0.1 μm are subsequenty caught in a sediment filter. This includes any organic or inorganic particulates that can be expected from municipal water. Remaining smaller organics are dealt with by an active charcoal filter. Finally, reverse osmosis traps surviving chemical elements and bacteria on the pressurised side of the membrane while allowing the solvent, water molecules, to pass. [65]

A characteristic to having municipal water sent 6800 feet underground is that the travel to higher pressures aerates the liquid. Trapped air bubbles contain one of the main radioactive background culprits: ^{222}Rn. An additional step in the water treatment plant is thus de-aeration. Degassing lowers O_2 levels by 1000 which results in a reduction by a factor of 50 the ^{222}Rn contamination introduced by UPW. [65]

Maintained at an inhospitable 12°C to keep bacteria propagation at bay, insulate the AV from the surrounding norite reaching temperatures of 40°C at this depth, combat the PMT dark rate by specifically by lowering the risk of thermoionic emission

though, as discussed, UPW also shields against radioactive decays and cosmic rays both contributors to PMT dark rates, minimise tension in the AV hold-down and hold-up ropes, and decrease the creation of convection currents of liquid scintillator if breaking equilibrium with the temperature at which the AV is maintained, the cavity can be recirculated through a processing plant that draws from the outer cavity and reinjects it in the inner cavity delimited by the AV walls and the PSUP. Distinct from the potable water treatment plant, the recirculation loop focuses on stripping water of radon carrying oxygen, filtering trace contaminants leaching from the detector structure it surrounds and cooling. This is achieved, in turn, through a UV filter to non-chemically neutralize bacteria and microorganisms, an ion exchanger for radiochemical impurities, degassing to tackle radon ingress, reinjection of N_2 to repressurise the water, a set of filters to catch any remaining suspended particulates, and a heat exchanger unit to cool the water back down before returning it to the cavity. The purification system described reaches $\mathcal{O}(10^{-15})$ g/g U or Th equivalent. [65]

This purification loop required amending following higher levels of U than acceptable during the water phase. Further down the decay chain, ^{214}Bi events indicated that radioactivity due to the U chain were of the order of 10^{-14} g/g. While the diffusion time through the neck filled with still LAB is longer than the 3.8 days half-life of ^{222}Rn, the shorter intermediate decays and the short 19.9 minutes ^{214}Bi half-life, this ^{222}Rn daughter with an energy placing it within the $0\nu\beta\beta$ ROI would decay away in the neck before reaching the AV, it has been observed to make its way into the active fiducial volume of the AV through convection along the walls. Furthermore, the longer lived ^{222}Rn daughters drown low energy solar neutrino signals, specifically

CNO and pep. The acceptable limit was set to 650 decays per day in the upper region of the Universal Interface (UI). The radon from the laboratory air alone reads out as 123 Bq/m^3, a nuisance which cannot be eliminated.

3.3.2.2 The Cover Gas System

Thus ensued the commissioning of the new cover gas system. Indeed, inherited from the SNO infrastructure is a flow-through system allowing the circulation of 5 L/min ^{2}N in the headspace above the UPW level in the cavity. As this proved insufficient because Rn is far more soluble in scintillator compared to water, SNO+ developed a sealed cover gas system during its water phase designed around the headspace above the scintillator level in the AV neck. Both systems rely on nitrogen flushing which is set to allow for an oxygen concentration of no more than 2 ppm and water concentration of 3 ppm. In the new sealed system, three bags attached to the UI allow for up to 360 L of expansion to be filled with nitrogen and acclimitise to any pressure differences introduced by mine activities that could compromise the structural integrity of the AV. The radon monitor connected to the cover gas system has a sensitivity of $\mathcal{O}(1)$ mBq/m^3 and reports a reduction factor of $\sim 2\times10^{-4}$ in radon concentration compared to the ambient air circulating throughout the rest of the SNOLAB facility. [65]

Finally, UPW also finds its uses in several stages, such as solvent-solvent extraction and steam stripping. These are two of the functions of the liquid scintillator plant built by Kock Modular Process Systems (KMPS) custom for SNO+'s needs and informed by the purification techniques deployed with success by Borexino (also designed by KMPS) and KamLAND. Though the growth in expertise has translated to improved

performance of all systems, the approach of liquid scintillators, purification systems and PMT readout apparatus dates all the way back to the days of Cowan and Reines. While the UPW plant was the sole plant required for SNO+'s water phase and assured the filling and recirculation of 905 tonnes of UPW in the AV, the scintillator plant with a few tellurium treatment plants that will be discussed later was poised to take over for SNO+'s subsequent phases.

3.3.2.3 The Scintillator Plant

Most extensive of the SNO+ plants is the scintillator plant. Its lines sprawl from the AV to a dedicated closed off section of the LAB ∼20 m away from the neck of the AV and spans three levels. A series of lines connect vessels, columns, tanks, heat exchangers, valves, pumps and filters charged with circulating LAB through subsystems with specific aims. Distillation is required to remove U, Th and K contamination while improving the optical clarity of the LAB. Gas stripping removes Rn, Ar, Kr and O_2 contamination. While recirculation through the plant should also reduce Rn concentrations and eliminate leached Ra, Po, Bi and Pb from the AV materials, the unfortunate reality is that radon ingress incurred by recirculation involving a leaky column in the plant, although mitigated by the cover gas system, is dealt with by tracking its Bi and Po daughter decays throughout the detector volume. Lack of foresight during the bis-MSB loading phase led to Ar exposure from the liquid N_2 plant, which will require a full turnover of the scintillator volume through the plant. The stripping column has been designed to handle a 150 LPM flow rate (8000 kg/h of LAB), meaning the operation could take place in 100 hours. At the time of writing, it is yet to be seen how many multiples of the theoretical turnover time will be required

to accomplish this while complying with operational and logistical restrictions.

Purchased from CEPSA Química Bécancour Inc, formerly Petresa now Moeve Global, PETRELAB 500-Q C11 LAB was shipped to site on trucks and stored on surface in a stainless steel storage tank awaiting transfer to the underground facility in preparation for the bulk fill. LAB is alkynated benzene presenting a long carbon chain of varying length (a blend of C10-C13) presenting positional isomers. Isomers, molecules sharing a molecular formula but bonding in different arrangements, are positional if their functional group (double bonded carbon atoms, in the case of alkenes) can occupy different positions in the carbon chain. While the properties of LAB will be discussed in chapter 4, this section will focus on how the plants have been designed to purify the liquid scintillator both to meet optical property requirements and also as a vital step in mitigating backgrounds.

Transport underground was arranged by decanting the LAB received by road tanker trucks from CEPSA and stored in a 70 ton surface storage tank into rail tankers fitted to VALE's Creighton Mine specific cage and rail dimensions. Once the two 60 ton underground storage tanks, the largest holding vessels – bar the AV – connected to the scintillator plant, were filled with these individual LAB rail car shipments, the LAB underwent a series of purification treatments to meet the chemical specifications required by the SNO+ physics program. These are distillation, water extraction and stripping. Their impact on background mitigation and broad engineering specificities are the focus of these subsequent sections.

Common to all components of the scintillator plant, the first concern is with the materials employed – a dilemma already discussed with respect to the AV, cavity and PSUP. To avoid any radioactive contaminants leaching into the scintillator as

it flows through the plant, all piping is made of electropolished 316 L stainless steel to ensure compatibility with organic solvents including LAB. Compatibility tests also identified PTFE and glass as materials meeting operational requirements while maintaining cleanliness standards; these populate the shelves of Quality Assurance (QA) instruments in the chemistry laboratories. Further tests were commissioned to check that these properties extended to all doping stages of the SNO+ cocktail [65]. The entirety of the system is kept under vacuum to preserve an air leak tightness below 10^{-6} mbar$\cdot$ L/s throughout, thus limiting any radon ingress from the ambient air [89]. Whenever this seal is broken for repairs or replacement of constituents, the plant is required to undergo a recommissioning phase to re-establish the cleanliness standards. This entails several rounds of flushing out the pipes and vessels exposed to air with distilled LAB, and sampling along key points on the lines. The sampled scintillator is submitted to QA tests developed to assess the levels of contamination within the material.

The purification plant is outfitted with three in-line columns, any combination of which can be chosen for the path to recirculate LAB. They are the distillation column (C-100), the solvent-solvent water extraction column (C-200), and the gas stripping column (C-300). They are depicted in the plant schematic in figure 3.8. A more straightforward yet vital component of the purification plant are the series of filters set to catch the larger impurities suspended in the scintillator. Their porosity and placement varies according to their use case.

Multistage Distillation Centuries of experimentation with distilleries of the alcoholic nature and more recently with oil refineries have made multistage distillation a very customisable process. The multistage distillation plant plays a critical role in

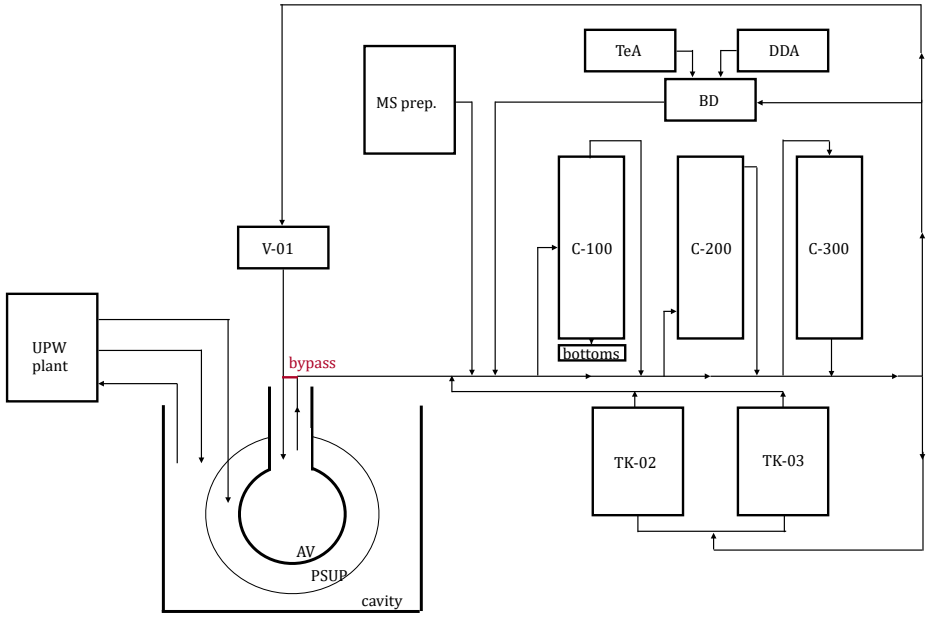


Figure 3.8: Schematic of the scintillator plant and its main connections to the AV, UPW, Master Solution preparation (MS prep.) and tellurium processing plants (TeA, DDA and BD). Omitted for clarity are connections between the UPW plant and the TeA purification plant as well as between the UPW plant and the water extraction column for the purpose of rinsing. In red above the AV neck is the bypass line to allow the plant to run in CLR. V-01 is the header tank. TK-02 and TK-03 are the 60 tonnes storage tanks.

assuring the optical clarity of the liquid scintillator. The scintillator is vapourised in a boiler and injected midway through the first column. This incoming stream is the flux. Assuming the flux is kept at a temperature higher than that at which the column has been heated, as the vapourised scintillator travelling up in the column condenses into the purified product, leaving the lower volatility "bottoms" rich in contaminants to collect at the lower end of the column where they are drained. A heat exchanger allows for rapid cooling of the purified product, which can be reintroduced into the now relatively higher temperature column to flow down. This is called the reflux.

Reflux stripping, or steam distillation, therefore exploits the difference in volatilities between contaminants and the solvent they are dissolved in. Heavier contaminants are collected in the bottoms while the product is purified upon recondensation.

The distillation process is entirely reliant on the difference in volatility of the contaminants and the solvent. Otherwise separation could not occur without immediate revaporisation. When the liquid and gaseous phases are brought to equilibrium inside the tower, the separation efficiency is tied to the molar flow rate of the phases within the system such that the split fraction, SF, of the backgrounds found in the scintillator can be represented as

$$SF = \frac{n_{\text{dist}}}{n_{\text{feed}}}$$

where n_{dist} is the molar flow rate of the first purified product from the column and n_{feed} is the molar flow rate of the feed LAB before distillation [172]. Therefore, it is especially effective for any heavy metals such as Ra, Th, Po, Pb, Bi and K dissolved in LAB.

The SNO+ plant utilises perforated trays to multiply the vapour-liquid interaction phases. This multistage distillation process was designed to handle low volatility contaminants such as heavy metals, which are predominant for SNO+. Rn is mitigated through stripping or upstream by the cover gas system that attempts to limit its ingress.

Distillation also improves optical clarity of a scintillator exposed to air and thus harboring any oxidized organic molecules such as carboxyl groups. As these have lower volatility than mineral oil, they will be pulled out in the refining process. An optimal distillation column will minimise the loss of solvent (LAB) in the bottoms.

While it would be chemically most effective to operate in the opposite regime, this is generally achieved by maintaining low pressures and high temperatures in the column to keep the gaseous and liquid phases in equilibrium. The feed and reflux loops can be extended to additional in-line columns to maximise refinement and stripping. LAB's boiling point range is 278-314 °C, putting it close to its auto ignition point of 300 °C. The system is therefore kept under vacuum. Minimising the differential pressure (vacuum kept at 20 Torr) allows the system to operate at lower temperatures (242 °C nominal) yet still obtaining the required separation stages between different solvent phases for distillation within the column [89]. While these can be adjusted, generally the distillation column operates just above 200 °C and the stripping column around 100 °C. Feed and reflux rates are adjusted according to the purification objectives for the scintillator.

However, the efficiency of the heat exchanger limits operations, as well as feed and reflux power. Distillation is ideal for an undoped liquid scintillator. SNO+'s physics goals required the development of a scintillator cocktail combining chemical reagents to optimise its energy resolution, longevity and radiopurity requirements. The pitfall of distillation is then apparent when run on such a mixture, as opposed to pure LAB, where it will by default run the risk of separating out the solutes from the solvent. While these can be recuperated from the bottoms, they will not come without the contaminants.

Water extraction Beyond being a possible conductor for free radicals from U, Th, Ra, K and Pb leaching into the detector as well as a suspension medium for fine particulates, water itself murkens the optical properties of LAB. LAB is injected at the bottom of a column while water is injected at the top. In this application, heavier

hydrophilic contaminants including water molecules themselves suspended in the less dense scintillator flowing upwards will bond with the water flowing downwards. To maximise efficiency, the SNO+ water extraction column is outfitted with 22 stacked stages in which the solvents are swirled to increase surface contact. The water employed in the water extraction system, once cooled through a heat exchanger, must go through stages of decontamination before being fed back into the UPW processing plant. Ra, Th and Pb are removed by a Hydrous Titanium Oxide column (HTiO), as well as the usual radon degassing. Any suspended LAB is caught in filters. C-200 was never used. [89]

Stripping LAB exiting the AV always undergoes stripping before returning to the AV to rid it of high vapour pressure impurities and residual humidity. This is done in the gas stripping column in which gaseous nitrogen rises through the counter current of LAB. Nitrogen strips the scintillator of Rn, Kr and Ar. It also rids it of trapped oxygen. Finally, as mentioned earlier, it dries the scintillator of residual suspended humidity. The opposing currents interact in stages to maximise stripping. Steam stripping, not yet put to practice for the experiment though the plant is capable of it, separates volatile organic compounds and dissolved gases from the scintillator by injecting steam into the bottom of a column in which the scintillator flows downwards. Because nitrogen must be shipped underground in dewars[b], this steam stripping system aims to minimise the nitrogen feed rate while maintaining efficiency. This is a balancing act, as stripping efficiency obviously depends on the purity of the stripping gas, and N_2 is known to contain traces of Rn and Kr. An option for future steam

[b]The switch to SNOLAB-supplied nitrogen during bis-MSB addition doubled the experiment's background target levels.

stripping operations could be to diminish the proportion of N_2 used with respect to the steam which is purified through the UPW plant prior to use in the stripping process. Though this was taken into account during the design process of the stripping column, the Kr content of the SNOLAB-supplied liquid nitrogen was not verified. With the UPW plant equipped to strip Rn from water, the steam supply is heated to boiling temperatures under vacuum making it dry and effective at removing 95% Rn and 99% O_2 at a rate of 10 kg/h alongside a 3 kg/h nitrogen feed. [65]

Backgrounds such as Ra and Pb are suppressed by water extraction. Metal scavenging columns employ a different method to capture these isotopes in addition to Bi, a recurring daughter in the main background decay chains clouding the ROI of several SNO+ analyses. These columns were never used.

Loading through Master Solution Mixing Pure distilled LAB is only the first ingredient of the second phase of the SNO+ experiment. The fluor PPO must be incorporated into the cocktail to bring the light yield within the ideal spectral response for the Hamamatsu photomultiplier tubes. The enhanced scintillator cocktail was also enriched two years later with Butylated hydroxytoluene (BHT), an antioxidant, and bis-MSB, a wavelength shifter, to prepare for eventual Te loading. In general, reagents are purchased in powder form and loaded via different means. PPO and BHT were introduced as a powder to the scintillation plant, while the bis-MSB powder was mixed into a slurry with pure LAB before being carried underground. Loading campaigns operate in stages where the added quantities are tracked by batch[c]. A section of the plant is dedicated to batch preparation. Preparation of the master solution cannot

[c]BHT is the only additive having required a single batch due to the limited mass incorporated in the cocktail.

be done in-line with the distillation loops for the straightforward reason that the volatility of the fluors would cause them to separate from the LAB. Therefore a concentrated master solution must be prepared in a series of mixing vessels, then diluted by being injected in the columns within a closed loop before finally being fed into the AV recirculation loop. Figure 3.9 illustrates this section of the plant.

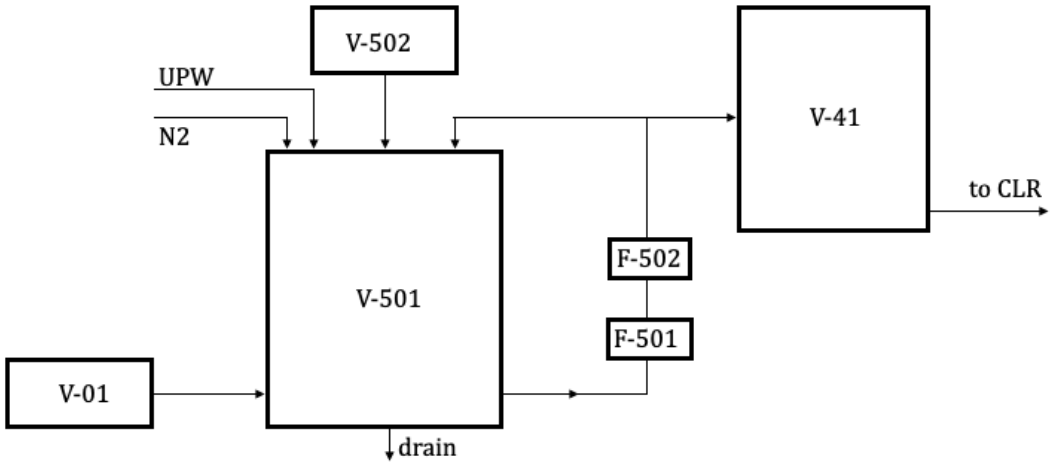


Figure 3.9: Schematic of the master solution preparation plant. The mixing vessel, V-501, can be filled with plant distilled, AV scintillator or TK-02 scintillator. Additives are introduced through the header tank, V-502. The concentrate solution once mixed and rudimentarily purified can be transferred back to the scintillator plant through the storage tank, V-41.

As purchased from Perkin-Elmer, PPO contains trace amounts of K and other insoluble particulates. The powder is loaded into V-501, the main mixing vessel, filled with pure, distilled or AV LAB to the desired concentration. V-501 is equipped with an agitator to roughly homogenise the solution. The mixture then undergoes a series of nitrogen sparges by simple pump purging. A UPW line allows for water extraction within V-501 as well. As this does not compare with the columns dedicated to these tasks, the draining of the resulting interface layer is done manually. The cleaned

solution then moves to V-41, the storage vessel upstream from the recirculation loop, through 5 μm and 0.2 μm filters to catch suspended water droplets leftover from the water extractions or other remaining contaminants. This master solution preparation plant was reused for BHT and bis-MSB loading. Unlike the PPO fill, the concentrate product was not flash distilled and the bottoms were not drained.

3.3.2.4 Tellurium Plants

The quest to suppress backgrounds linked to tellurium begins prior to the purification plants. As was discussed in section 2.2.4, the choice of isotope itself is strongly motivated by the purity of its $Q_{\beta\beta}$ region. ^{130}Te presents a hypothesized $0\nu\beta\beta$ decay at 2.53 MeV [189], away from the low energy region crowded by solar neutrinos or the bulk of common ^{212,214}BiPo events. The most bothersome event classes remain to be ^{208}Tl and ^{8}B νs, for which improved energy resolution and careful coincidence tagging strategies rely on to discriminate from the yearly 13.4 expected signal event rate [189].

While the target loading is a 1.5% concentration by mass of natural Te in the scintiallator cocktail, the initial deployment aims for 0.5% corresponding to 1.3 tonnes of the isotope itself. Before considering purification plants, the tellurium, shipped as Telluric Acid (TeA) ($Te(OH)_6$) purchased from ABSCO, has been cooling in the SNOLAB underground facility to allow contamination from cosmogenic sources to decay away. Among isotopes activated by cosmogenic spallation that manifest within the $0\nu\beta\beta$ ROI are ^{22}Na, ^{60}Co, ^{110m}Ag, ^{88}Y and ^{124}Sb [128]. The 302 barrels have lain in a removed drift of the underground laboratory, mostly undisturbed save a test batch, since 2015. Inductively Coupled Plasma Mass Spectrometry (ICPMS)

analysis on dissolved TeA crystals yields the abundance of the usual impurities of concern, namely U and Th. This method was used to ascertain the limits purification plants involved in both background suppression and the basic chemical consideration of forming a compound stably, homogeneously soluble in LAB presenting optical characteristics with longevity extending beyond the experiment's scientific program, must reach for the viability of the program [139].

Tellurium loading is a more chemically involved process compared to the dissolution of fluors (PPO, bis-MSB) and stabilisers (BHT) touched on previously. To keep the target isotope stably suspended in the cocktail, three dedicated plants come into play: the N,N-Dimethyldodecylamine (DDA) plant, the Tellurium Butanediol (TeBD) and the TeA plant. Only with the product of these plants, a complex known as TeA-TeBD-DDA, can the target isotope be stably suspended in the scintillator mixture while avoiding chemical instabilities such as crashing out of the solute and yellowing. The TeA and TeBD plants are situated in the underground laboratory while the DDA plant has been built and commissioned in the clean room surface facility at SNOLAB.

The TeA plant purifies the cooled down crystals, removing remaining isotopes from cosmic ray spallation as well as U and Th chain daughters. TeA, formed by oxidising the Te metalloid with six free electrons, can bind with up to six hydroxyl (-OH) groups rendering it soluble in water. The TeA plant is outfitted with a recrystallisation tank that receives the crystals in powder form. The vessel is heated, agitated and filled with UPW in which tellurium crystals are dissolved. The solution is filtered to remove insoluble particulate contamination. 70% nitric acid HNO_3 (pH $\sim$3) is also used to facilitate recrystallisation which is also possible through cooling as the solubility of

TeA in water is dependent on both pH and temperature. The resulting 10% TeA aqueous solution sits at pH ∼3.5 [19].

Recrystallised TeA is heavier than the residual contaminated process water which is drained to acid waste tanks. Informed by preliminary test bench results from [98], the acid and thermal recrystallisations, filtration and UPW rinsing achieved the target levels of ^{22}Na, ^{60}Co, ^{110m}Ag, ^{88}Y and ^{124}Sb as ascertained through ICPMS counting and X-Ray Fluorescence Spectrometry (XRF) tracing. ^{212,214}BiPo coincidence counting also confirmed target rates of U and Th chain daughters.

As usual, extensive care must be taken in the choice of material for the construction of the chemical plant. Polypropylene (PP) and Fluoropolymer (PFA/PTFE) are compatible with TeA and minimise heavy metal leaching upon contact. This goes for the TeBD plant as well.

However, as was underlined in some purification methods above, what is water soluble is likely immiscible with SNO+'s organic mineral oil based liquid scintillator. This incompatibility is the first difficulty to overcome in the process of tellurium loading. This is achieved by the addition of 1,2-butanediol (BD), an organic compound presenting two hydroxyl groups and a carbon tail. Before being combined with the aqueous TeA, BD is to be purified by multistage distillation. The scintillator plant and its distillation column (C-100) is suitable for this purpose. BD will attach to up to two of the six hydroxyl groups in TeA to form CH_3O_2 groups, further increasing the acidity. While TeBD can be dissolved in LAB at room temperature, trace amounts of water have been shown to cause it to precipitate out and for the TeA crystals to reform. This is due to the fact that the presence of water molecules can cause the synthesis of TeA + BD → TeBD + H_2O (condensation) to undergo the

opposite reaction (hydrolysis). The precursor to the final tellurium compound destined to loading is heated and nitrogen sparged to promote condensation and create an LAB soluble complex. The LAB in the AV is kept dry to maintain optical clarity. Acceptable humidity levels have been set to 200 ppm because 300 ppm will cause immediate crashing out of TeBD from the scintillator cocktail. However, it should be noted that standard levels are closer to 60 ppm (an order of magnitude higher than the ∼5 ppm achievable by the scintillator plant). The threat of hydrolysis brought on by the increasing of humidity levels from the acrylic itself or a slow leak from the UPW cavity[d] is too important for TeBD to be loaded as is, even at its most advantageous ratio. The addition of DDA stabilises this reaction to form a TeA-diol compound suitable for solubilisation in mineral oil.

The DDA plant is responsible for the addition of DDA to the TeBD-LAB cocktail. The tertiary amino group in DDA bonds with one of the remaining TeBD hydroxyl groups to form a long hydrocarbon tail which offers bonding options to the LAB molecules thus making it soluble. DDA itself will be purified on surface in the DDA still employing thin-film distillation.

The diol plant is the final phase in synthesizing the tellurium into a compound stably soluble in LAB. It will combine the purified TeA and BD at a 3:1 ratio [134]. During this process prone to hydrolization instead of the desired condensation, drying is achieved through partial vacuum in combination with heat, as well as nitrogen sparging. TeBD will be combined with scintillator LAB at a 1:1 ratio in the TeBD synthesis plant. The product will then be redirected to the scintillator plant operating in Closed Loop Recirculation (CLR) mode to be further dissolved. DDA can be incorporated directly to the AV as a neutraliser and therefore stabliser as the last

[d] Which may be no more than a seismic shudder away.

stage before the concentrated TeBD batch is passed back on to the scintillator plant for deployment to the detector. [185]

DDA is set to increase the light yield by at least 15% [65] depending on the tellurium concentration of the cocktail by countering quenching effects of the isotope in the scintillator.

The ratios of the different components of the scintillator cocktail have been extensively tested (and continue to be) in a series of tests known as the Thousand Sample Tests. Mixtures of varying concentrations are submitted to different combination methods, torture tests and contrasting environments. Results are controlled at set points in time upon which options are discarded and others left to continue to push their longevity until the next checkpoint. It is therefore with a combination of background purity requirements, engineering restrictions, chemical limitations and optical characteristics in mind that the liquid scintillator cocktail has been developed to fit SNO+'s unique physics targets. The concentration of each component can be found in table 3.2.

LAB	780±12 tonnes
PPO	2.2 g/L
Bis-MSB	2.2 mg/L
BHT	5.4 mg/L
TeBD	0.5% by mass (1.5, 3)
DDA:TeBD	0.25:1 molar

Table 3.2: Concentration of the components of the SNO+ scintillator cocktail. Those yet to be added are italicised.

The optics of the liquid scintillator are the subject of chapter 4.

3.4 Calibrating the Detector Response

While this discussion has focused on radioactive isotopes being a nuisance, they can also – when in a controlled environment – offer an opportunity to tune the detector energy and position resolution *in situ*. SNO+ has an array of calibration methods including radioactive sources such as the Americium-Beryllium (AmBe) source, hardware systems such as Electronic Calibrations (ECA) and PMT Calibrations (PCA), and optical sources through light pulsing such as the Embedded LED/Laser Light Injection Entity (ELLIE) systems and the Laserball. Radioactive sources provide a known emission spectrum used to calibrate the energy reconstruction algorithms efficiency. Optical sources are used to characterise the optical properties of the scintillator, namely the light yield, absorption and scattering coefficients, as well as PMT timing.

3.4.1 Optical Calibrations

As has been the theme throughout this chapter, the hardware designed for deploying optical and radioactive sources is constructed through the compatibility of materials with LAB and methods of background mitigation. This refers to the Source Manipulator System (SMS), which is comprised of the umbilical used to tether and lower sources on the z axis, the Umbilical Retrieval Mechanism (URM), source encapsulations themselves, the side ropes and side rope manipulation system to move sources on the x and y axes, and calibration guide tubes for calibration sources deployed in the external water cavity. In general, the UI is kept under the cover gas system to minimise radon ingress from calibration operations.

The Laserball The crown jewel of optical calibration sources is the Laserball which is being deployed at the time of writing. However common such a deployment was during the SNO operating days, it is a rare occurrence in SNO+ due to higher radiopurity requirements in the scintillator[e]. The Laserball, outfitted with an optical fibre bundle, was designed as a point-like source producing light at well-defined wavelength then used to compare against the detector response. Comparing Laserball datasets allows for PMT timing offset monitoring. It also provides a metric for the angular response of the detector as it monitors the degradation of the PMT reflectors over time.

The ELLIE Systems The Embedded LED/Laser Light Injection Entity came about as an alternative to the Laserball that did not involve exposing SNO+ to the pesky backgrounds associated with source deployments. ELLIE is a coalition of three singular role systems: the Attenuation Module (AMELLIE) set to determine attenuation length measurements of the scintillator, the Timing system (TELLIE) set to monitor PMT timing offsets along with gain and charge response using photon time-of-flight, and the Scattering Module (SMELLIE) set to determine scattering cross sections of the scintillator as a function of scattering angle or photon wavelength. AMELLIE offers an alternative to spectrophotometry of benchtop samples to monitor changes in the attenuation properties of the scintillator [140]. TELLIE, designed to fine tune the synchronisation of timing across the PMT array as well as calibrating energy reconstruction by correctly tuning the gain and charge of PMT response to signal as a function of wavelength, also helps tune the angular response of PMTs in

[e]As will be made apparent during the discussion on systematics uncertainties, this is quite a shame for the purpose of this analysis influenced by the angular response of the PMTs.

a similar manner to moving physical optical sources at different positions within the detector [146]. SMELLIE aims to take advantage of the well understood Rayleigh scattering process to study the differences between scattering cross sections in LAB compared to absorption and re-emission effects [73].

3.4.2 Radioactive Sources

Radioactive calibration sources are γ emitters rather than α or β sources to limit radioactive contamination within the detector. They are chosen to span the energy range relevant to SNO+ event searches from 0.1 MeV to 10 MeV [65]. At the time of writing, the only deployed radioactive source used in the scintillator phase has been the AmBe calibration source due to its relevance to the reactor antineutrino analysis the collaboration recently published [63]. ^{241}Am undergoes an α decay with an 84.6% branching ratio. The resulting α particle is absorbed by ^{9}Be to produce a neutron via

$$^{241}\mathrm{Am} \rightarrow ^{237}\mathrm{Np} + \alpha; \tag{3.4.1}$$

$$^{9}\mathrm{Be} + \alpha \rightarrow ^{12}\mathrm{C} + \mathrm{n}. \tag{3.4.2}$$

The first excited state of ^{12}C emits a 4.4 MeV γ with a 60% branching ratio. As for the neutron, it emits a 2.2 MeV γ upon undergoing neutron capture on hydrogen. These prompt and delayed γ signals mimic the IBD reaction used in reactor antineutrino analyses. Naturally, the AmBe source also offers energy calibration points at the γ emission energies (2.2 MeV and 4.4 MeV) with the former overlapping with the $0\nu\beta\beta$ ROI. ^{237}Np is a stable isotope at a half life on the order of millions of years and is therefore considered an acceptable background byproduct to the target material.

However, additional encapsulation shielding was required to absorb the 59.5 keV γ emitted alongside the alpha decay of ^{241}Am. [140]

Not deployed in SNO+'s scintillator phase, though of interest to any directionality analysis, is the ^{16}N source. As a gamma emitter, it is of particular use for studying the PMT angular resolution response. The detector angular response is modeled through the theoretical geometry of electron scattering generating Cherenkov light and knowledge of the geometric structure of the PSUP. Single Compton interactions occurring from the momentum transfer of a ^{16}N gamma to an electron generate the source position. PMT hits can then be compiled to determine angular resolution. Source position uncertainties can be mitigated by excluding large radial distances and lower energy Compton scatters. [64], [102]

Ironically, another radioactive calibration source is the *in situ* rate of some of the better known and sustained rate backgrounds discussed throughout this chapter. ^{212,214}BiPo pairs, ^{208}Tl, ^{210}Po and ^{14}C all present established spectra which can be used to calibrate SNO+'s energy response. The method of tagging these events will be discussed in section 3.9.

3.4.3 Electronic Calibrations

Electronics calibrations are run as hardware performance diagnostics. ECAs scan each channel to set its discriminator threshold above the dark hits rate as well as monitor general health of these channels. ECAs can be run in two modes. The first calculates the charge pedestals of each channel. This refers to the the DC offset between integrated charge measured in each channel when a forced discriminator pedestal (PED) signal is fired followed 150 ns later by a PULGT signal. Varying

the time offset between sending the PED and PULGT signals helps link the Time-to-Amplitude Converter (TAC) values to the recorded hits per PMT. The timing resolution is so crucial for SNO+ that differences in PMT cable lengths is accounted for and calibrated through this process by the PCAs, because each issued global trigger will take a unique time to travel the length of its cable to each channel.

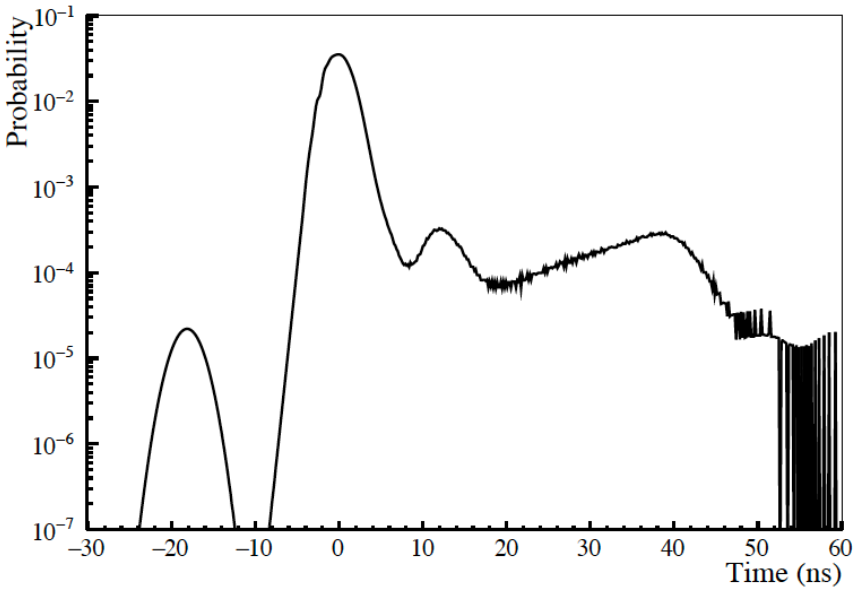


Figure 3.10: Transit time probability distribution measured by SNO and recoordinated with SNO+ specific values through the `RAT` simulation software. The prompt peak can be seen at the expected 0 ns. The standard deviation of the prompt peak was measured to be 1.577 ns. A peak corresponding to pre-pulsing can be seen around -18 ns which occurs when a photon hits the dynode stack in reverse order. The late (at 10 ns) and double (at 40 ns) pulsing peaks are due to photoelectrons backscattering off the dynode stack. Figure taken from [151].

Another minute timing effect is the dependence on the amplitude of the charge pulse to the rapidity of a threshold to be triggered, known as the time walk effect [45], [107]. These two considerations can be measured by the optical calibration sources, notably TELLIE and the Laserball. The objective of these calibrations to the

nanosecond level of precision is to attenuate these effects so as to have the scintillator decay time[f] and PMT transit time spread[g], that is the time taken for a photon arriving on the photocathode to register on the anode through a signal pulse, dominate them [13]. The transit time distribution can be found in figure 3.10. Synchronising the PMT timing with some regularity is key in keeping the time-of-flight based position reconstruction accurate. Electronic calibration results are applied to the timing and charge pulse information recorded in raw data files before these are processed and recorded to raw data files before being processed into more readable formats for physics analyses. [114]

3.5 Aquiring Data

Now that the rate of undesirable events has been minimised through physical means, it is time for electronics to convert scintillation light into analysable data. Though the optics of scintillation will be left to the subsequent chapter, it is sufficient to mention for the purpose of this discussion that scintillation light occurs when electrons in the LAB benzene ring de-excite, a luminescent phenomenon, following ionisation from an incident particle. Once light in the form of photons travels through scintillator, acrylic and water – or only through water for muon events in the cavity picked up by outward facing PMTs - it reaches a PMT embedded in the PSUP. Assuming the PMT is still active, it will convert the photon input into a pulse charge.

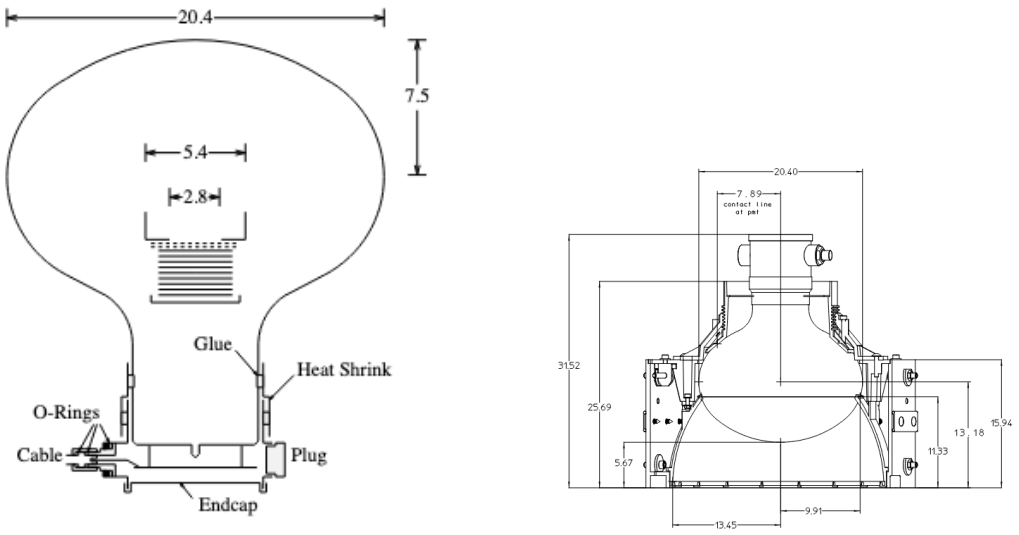
[f] Anticipated around 4.6 ns in LAB+PPO.
[g] Measured around 1.577 ns.

3.5.1 PMTs

SNO+'s 9362 PMTs, of which 8459[h] have not irremediably fallen to water damage, pressure or high-voltage incidents, are 8" Hamamatsu R1408 photomultiplier tubes inherited and refurbished from SNO, for which a schematic is included in figure 3.11 [71]. Each PMT acts as an independent photon detector. The photons reaching the photocathode below the glass housing are transformed into a photoelectron through the photoelectric effect. The initial photoelectron is directed down the dynode series via a constant supply of high-voltage, where the photoelectrons are multiplied upon striking each dynode surface. The signal is magnified when the number of electrons emitted multiplies with each secondary impact on a dynode. The increase in gain incurred by this multiplication effect is the signal registered by the anode at the base of each PMT. The two main variables extracted from this process for event reconstruction are the signal pulse and transit time.

A crucial consideration for all analyses in increasing the phase space and resolution of the detector is the coverage. The 92-face geodesic PSUP outfitted with all these PMTs only offers fractional coverage in terms of surface occupied by the photocathodes on which photons accumulate. Each PMT is therefore equipped with a 27 cm diameter concentrator. The reflective petals attached around the PMT as seen in the schematic in figure 3.11 increase the total photocoverage from 31 to 54% [71], though these values were determined for SNO. Since then, the concentrators have aged and the number of fatally damaged PMTs has increased. The lack of modeling of the effect of dulled concentrators on the optical model of the detector poses a serious consideration regarding systematic uncertainties for this analysis, though five PMTs

[h] ∼2000 channels are waiting on fixes underground to be brought back online as of November 10th, 2025 according to the Minard online monitoring page.



(a) (b)

Figure 3.11: Schematics of the photomultiplier tubes from [71]. Dimensions are in cm. (a) PMT and waterproof encapsulation filled with silicone gel as manufactured by Hamamatsu. The dynode stacks are represented by the horizontal lines. The endcap is flexible to allow for thermal expansion. (b) PMT with attached concentrator.

have been installed with their concentrator petals removed to compare efficiency in light collection to aging concentrators. Deployment of the laserball also allows for the characterisation of the concentrators' light collection efficiency as a function of incident angle; in other words, the PMT angular response [37]. At the time of this analysis, the laserball has only recently been deployed in the enhanced scintillator phase for the first time since the water phase, and the PMT angular response implemented in SNO+'s scintillator optical model is yet to be informed by this critical set of calibration data. This is another consideration for sources of systematic uncertainty for this particular analysis. In addition, four PMTs are arranged around the base of the neck to help veto events occurring within the neck volume, many of which are pervasive backgrounds such as ^{214}BiPo events incurred by radon ingress.

3.5.2 Triggering

In the discussion on backgrounds, the 'dark rate' from PMTs refers to the baseline current flowing through the anode while it is kept at high voltage. Dark noise being registered as a single photoelectron hit that surpasses pedestal trigger thresholds is a background that can only be mitigated (though never eliminated) by rejecting events with low hits, the value itself being decided by analysis coordination campaigns.

Signal collected in each PMT under the guise of photoelectrons travels along cables feeding into a PMT Interface Card (PMTIC) lodged in its dedicated slot in one of 19 crates sitting on the SNO+ deck area. PMTICs process incoming pulses from PMTs through daughterboards equipped with discrimators programmed with the different threshold values. If the signal registered by a hit PMT surpasses its set threshold, the same cable maintaining the high voltage on the anode at ∼1.7-2.1 keV [71] transmits the charge pulse to the front-end electronics. Here, the signal stored on a temporary cache awaits a global trigger during a set time window before the cache is cleared to accommodate further incoming signal. The PMT hit signal is recorded following a TAC. This timing information is therefore converted into three distinct charge values:

- QHL - charge high gain, long integration window
- QHS - charge high gain, short integration window
- QLX - charge low gain, long or short integration window.

Simultaneously, two high (20 ns) and low (100 ns) gain square pulses are issued for each hit. These are the N20 and N100 triggers. A photon traveling the entire diameter of the AV is expected to have a time of flight of 86 ns, hence the choice of N100 as the main trigger for SNO+. Charge information is collected through the ESUM (high or

low gain options) trigger pulse. Trigger pulses are forwarded to the Front End Card (FEC) of the crate where the analog pulse is summed over every active channel.

In an analysis hinging on counting and time-ordering PMT hits such as is the subject of this thesis, it must be noted that the threshold set to record a hit is set to ∼25% of the average charge deposited by a single electron; a quantity individually determined for each PMT anode through electronic calibrations as discussed in section 3.4.3. This amounts to sacrificing a fraction of real photoelectron hits. In simulations, single photoelectrons can be counted and dark noise mimicking a photoelectron hit can be discriminated. It will become apparent in section 5.3 however, that the 'dark rate' will be a background source appearing as unphysically early light.

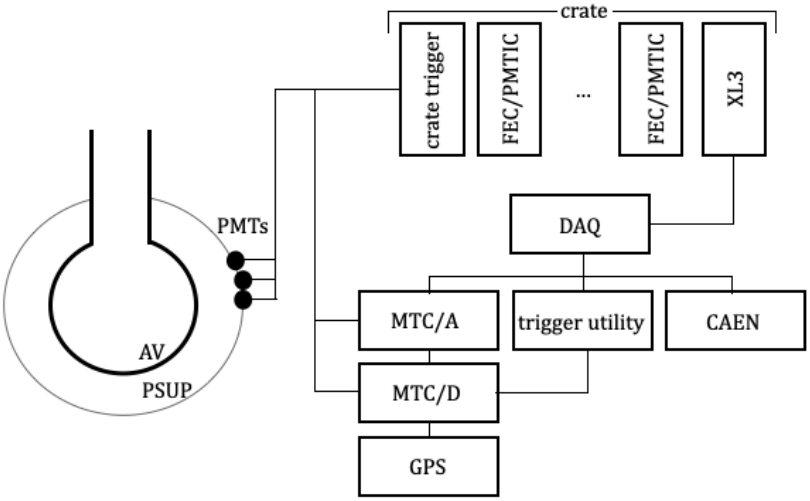


Figure 3.12: Schematic of the DAQ system for SNO+.

The Master Trigger Card / Analog (MTC/A) collects and sums surviving triggers over crates. The resulting pulse amplitude corresponds to the proportion of hit PMTs during the 100 ns window in the case of the N100 trigger, or the total charge collected over all PMTs in the case of the ESUMHI signal. Encoded in the MTC/A are several

adjustable discriminators with their set thresholds. The number of hit PMTs encoded as a threshold value is determined by the optical properties of the current medium within the AV in the case of physics data taking. They can also accordingly be set for the type of calibration data being commissioned. Assuming any of these are reached, the MTC/A sends a pulse to the Master Trigger Card / Digital (MTC/D) to issue a Global Trigger (GT). This signals all crates to permanently encode timing and charge information recorded by hit PMTs during that triggered event. Then follows a 420 ns dead time window during which no GT can be issued regardless of discriminator thresholds on the MTC/A being reached. Information of hit PMTs 180 ns before the GT, identified by Global Trigger Identification Number (GTID), is bundled with that of the subsequent 220 ns make up the event window and are recorded as a single event.

Data Acquisition (DAQ) ends with the XL3 cards responsible for reading out digitised events from the DAQ hardware to SNO+ servers where software takes over data processing. Passed on in the event structure are therefore TAC and charge information for each hit PMT. Transferred additionally are the waveforms provided by the CAEN digitizer, the timing information from the 50 MHz MTC/D clock used to time order events within runs (20 ns resolution), as well as the GPS central clock used to determine time of day. The builder packages raw data, PMT charge, timing information and trigger settings, in `.ZDAB` files passed onto a grid host where it can be processed in the hopes of becoming usable physics data. Simultaneously, hardware settings linked to runs are recorded on a PgSQL database.

The efficiency of the PMTs in converting photons into charge pulses is well characterised for this model as illustrated in figure 3.13. The quantum efficiency[i] of PMTs

[i]This is the probability for a photon having reached the anode to generate a photoelectron.

as a function of wavelength becomes a factor in the optical considerations taking place in the development of the liquid scintillator cocktail which is the subject of the next chapter.

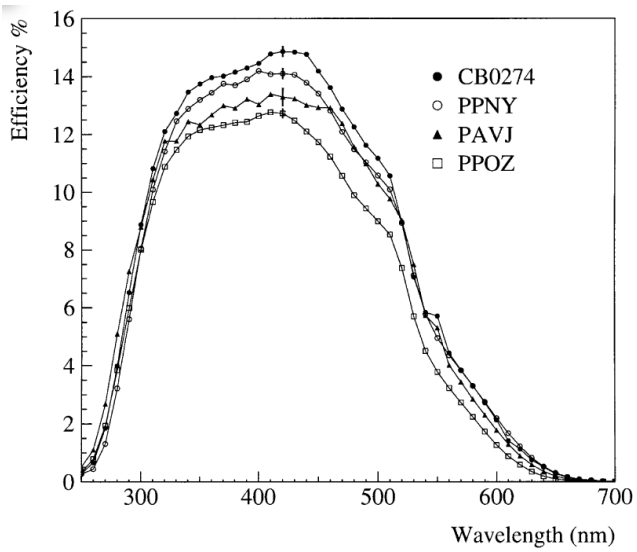


Figure 3.13: Wavelength dependent quantum efficiencies measured by SNO for four types (listed) of R1408 Hamamatsu PMTs. Figure taken from [37].

Another interesting issue specific to electronics arises from none other than the Earth's magnetic field which influences the PMT gains. A set of compensation coils were added to dampen its effect on the detector's DAQ system. [65]

A simplified schematic of the SNO+ electronics following their upgrades and refurbishments from the SNO days is presented in figure 3.12.

3.6 Processing Data

Runs are organised in a nominal, though not strictly enforced, one hour time period and categorised by run type and data quality standards. Run types include physics, maintenance during detector repair, unusual deck or plant activity, or during

abnormal detector read-out monitoring, or calibrations using internal or external sources or ECAs and the ELLIE specific systems, and during the repositioning of deployed sources. Runs also record onsite activities relevant to data quality as well as detector state. Run lists compiled for SNO+'s different physics goals rely heavily on these markers, specifically detector state which is recorded in run tables. Moreover, run selection includes an assortment of criteria that physics runs are tested against to be sorted into Gold, Silver, Bronze or Nickel lists, or discarded. A number of sanity checks are performed on raw data before processing to filter out unusable data. Among these are trigger clock jumps, as well as muon and muon follower events, characterised by high energy and OWL PMT hits.

Once the preliminary processing is completed on `.ZDAB`s, selected runs with their information saved in run tables on a PgSQL server are passed on to the Reactor Analysis Tool Data Base (`RATDB`) to be formatted as either Reactor Analysis Tool Data Structure (`RATDS`) `ROOT` files or `nTuple ROOT` files. `RATDS` files will have additional processing applied such as PMT electronic calibrations, but `nTuple` files are heavily pared down by going through the full set of RAT reconstruction algorithms and saving only commonly used physical quantities to trees, such as event time and position as opposed to hit, charge and trigger information, and common classifier results to trees. Run and GT identification numbers (RunID and GTID) are written to `nTuples` in case upstream information must be queried from the `RATDB`. Because this analysis relies on timing information for hit PMTs and time residual calculations for all hits per event, the heavier `RATDS` files are required.

`RAT` handles everything that is not a raw event trigger from the detector. It is a powerful software tool designed to accommodate infrastructure needs arising

with experiments growing in scope and length. This software also bolsters a `Geant4` and `GLG4sim` based simulation tool for detector geometry and particle interactions producing optical photons in liquid scintillator, as well as the customizable and programmable framework required both for Monte Carlo (MC) and data analysis. It calls upon run tables stored on the PgSQL server to coherently reconstruct events from raw trigger information in the case of data analysis. MC production sets can be generated to mimic detector state and geometry thanks to `RATDB` in run-by-run simulations.

3.7 Simulating Data

The simulation software is designed to output MC sets in a structure and format identical to collected data such that both may be analysed and compared using `RAT`. Physics events are simulated through generators. Generators manage particle type, flux, energy and initial vertex position. From this initial event, `Geant4` then goes down the chain of interactions as they would occur within the SNO+ medium and geometry [191]. For example, external backgrounds would be modeled from their entry point in the cavity, tracked through water, triggering any OWLs where applicable, and tracked through LAB; the deposited energy is then picked up by PMTs triggered by the optical photons produced from the simulated interaction. `Geant4`, widely used in all fields of particle physics, provides the structure for electromagnetic and hadronic interactions for any and all isotopes. It generates MC datasets in line with any physics theory system. `GLG4sim` was originally developed by and for KamLAND and handles propagation of optical photons and their light emission mechanisms, be they Cherenkov or scintillation.

Because the simulation software is integrated with RAT's dynamic database (RATDB), not only the geometry of the detector structure is taken into account but also the run-by-run electronics specific characteristics. This allows for photons to interact with the detector material following Probability Density Functions (PDF)s closest to what the detector state would enable. RAT also accepts the optical model developed with the input of *in* and *ex situ* measurements determining intrinsic scintillation properties such as absorption and scattering lengths. All of this equips SNO+ simulations with physically sound light propagation behaviour where photons are emitted, scattered and absorbed within the target material.

As for the PMT response, calibration results are fed to the simulation software such that the production of photoelectrons on the dynode follow an efficiency representative of the detector at any given time. It should be noted that the concentrator response and efficiency is not one such a calibration value provided to the simulation software. Instead, a "grey disk" approximation is employed where the diameter surrounding the PMTs is modelled as a flat disk instead of the petal-like conic configuration of the concentrators. However, absorption and reflection probabilities with respect to wavelength and incident angle are modeled on the concentrator calibrations from SNO. Triggers themselves are also subject to simulation details such as the trigger window length and the loss incurred by dark noise.

It then follows that MC datasets are produced and saved in the same format as live data acquired by the detector hardware with the addition of *"Truth"* information used to validate analysis models. Collaboration-approved Monte Carlo production datasets are centrally generated for common background and signal sources to harmonise Data/MC comparisons for various analyses. However, it is both commonplace

and possible to generate specific simulation sets with user defined features.

3.8 Reconstructing Data

Raw PMT hit timing and gain information must be converted to physical quantities for analysis. Pulse amplitude and number of hits allows for vertex energy, position and time reconstruction, which form the basis of event analysis. This event reconstruction hinges on electronics and optical calibration data, making it dependent on the medium with which the AV is filled. Position and timing reconstruction starts with the counting of the number of PMTs hit by a photon. Timing distributions and their tuning to the MC model are vital. Events occurring near the center of a scintillator filled AV will record PMT hits distributed isotropically around the sphere with similar time of flight[j]. Conversely, interactions near the AV wall will record PMT hits on a wider time range as light disperses through the volume of the detector.

`ScintFitter` is the reconstruction algorithm developed for the scintillator target medium; it has been updated to reflect the different PPO and bis-MSB loading phases. `ScintFitter` assumes point-like, single electron interactions that travel in straight lines for position and time reconstruction. Time residuals are key in position reconstruction and are defined as

$$t_{\text{residual}} = t_{\text{PMT}} - t_{\text{flight}} - t_{\text{event}}, \tag{3.8.1}$$

where t_{PMT} is the recorded hit time of a PMT, t_{flight} corresponds to the total transit time of a photon in a straight line through scintillator in the AV, then through water

[j]...in principle. The basis of this thesis is to extract early Cherenkov light in scintillator. Perhaps, the concluding sentence of this work will challenge this statement.

to the PMT array following a refraction at the media interface which is ignored, and t_{event}, sometimes denoted t_0, refers to the reconstructed event time. In addition to the interface refraction, the misalignment between the AV and PSUP centroids, known as the 'AV offset' is taken into account when calculating the distance traveled at any given time in both media. This is an example of another run dependent value stored in RATDB tables. Other effects accounted for in the timing PDFs are internal reflections. Timing distributions are produced from raw data and are compared against PDFs generated run-by-run. Minimising the integrated t_{residual} of an event is the method by which the event position and time are reconstructed.

Energy reconstruction makes use of the number of hit PMTs and the instrinsic optical properties of liquid scintillator. `nHits` are mapped to energy and depend on the scintillator's light yield and absorption length. Because β particles (2.5 MeV electrons) are used to simulate the energy response, heavier α particles, more prone to quenching effects in the scintillator, will be reconstructed with lower energies. Additionally, `nHits` weaken as an energy proxy on the higher end of the spectrum - though the effect starts being visible as low as 2 MeV- given that there is a saturation point to the proportionality of recorded photoelectrons per hits registered by a PMT per event. While the charge information could quantify the incident number of photoelectrons, it is discounted because of how unreliable and difficult to calibrate the reading is. Both `nHits` and energy corrections are applied based on simulations to account for the multiplicity of photoelectrons per PMT in higher energy events.

Both position and energy reconstruction will be revisited in the context of this analysis in section 5.3.3 and 5.3.4, respectively, and are only introduced here to provide the context necessary to defining the ultimate background rejection method that

is event identification.

With these physical quantities extracted from raw data, additional information can be added to the `ROOT nTuples`. In particular, classifiers utilise time residual distributions, timing profiles, energy, radial separation, etc. to provide likelihood ratios of event types as in

$$\log\mathcal{L}_{\alpha\beta} = \log P_{\alpha} - \log P_{\beta} \tag{3.8.2}$$

$$\log\mathcal{L}_{\text{in window}^{212,214}BiPo} = \log P_{0\nu\beta\beta} - \log P_{^{212,214}BiPo} \tag{3.8.3}$$

where the likelihood of a type of event is taken to be its difference with another type of event. Examples of such classifiers are the In-Time Ratio (ITR), multisite and $\alpha - \beta$ classifiers. The ITR classifier helps distinguish early light from PMT noise through time residual profiles. The multisite classifier employs timing and topological signatures to separate events with single site energy deposits, such as solar ^{8}B ν_e, compared to events depositing energy in multiple sites across the detector. These are usually tagged via coincidence methods with specific ΔR and Δt.

3.9 Characterising Surviving Backgrounds

After all efforts have been put into designing the cleanest LAB environment, purifying the target medium and selecting the isotope maximizing $0\nu\beta\beta$ decay cross sections, there remain backgrounds to be contended with. It is then time to turn to analysis techniques to distinguish these backgrounds from signal.

The electron scatter of solar ^{8}B electron, and $2\nu\beta\beta$ products in the tail of the decay spectrum, are known to appear in the $0\nu\beta\beta$ decay ROI. However, for the remainder

of this section, the emphasis will be placed on backgrounds to the ^{8}B solar signal. Though surprises in the background rate cannot be definitively ruled out until SNO+ has been tellurium loaded and data taking commenced, the background model for the $0\nu\beta\beta$ ROI has been the subject of many studies including the "target out" analysis [180] and other sensitivity studies [118, 102].

Event rates are reported in Bq or g/g by using the abundance equation

$$A_{Bq} = \frac{m}{m_A} N_A \frac{\ln 2}{T_{1/2}}, \tag{3.9.1}$$

where N_A is Avogadro's number, m/m_A is the mass (event count) of the isotope over its atomic mass corresponding to the number of moles and $T_{1/2}$ is the isotope's half life.

With the rate of ^{238}U and ^{232}Th maximally reduced by purification techniques, the efficiency of event reconstruction can be put to use by tracking the rate of ^{212,214}Bi-Po pairs in the detector. The ^{212,214}Bi-Po pair and ^{208}Tl rates are assumed to represent g/g the levels of ^{238}U and ^{232}Th in the detector under the assumption of secular equilibrium. This is achieved because the half lives of ^{238}U and ^{232}Th, the progenitors of their decay chains, are several orders of magnitude longer than that of the second most long lived isotope in their respective decay chains. Therefore, it can then be assumed that decay rates are constant and equal along the chain. It should be noted that abnormal contributions of isotopes along the chain will break this secular equilibrium as is the case with ^{222}Rn ingress from the laboratory environment and plant operations.

External backgrounds reconstructing within the AV are eliminated by reducing the fiducial volume. Any events reconstructed beyond a certain set radius from the center

of the AV are discarded. For analyses benefiting from steady signal rates, such as solar ones, this radial cut can be quite stringent and therefore effective at eliminating external backgrounds without overly compromising the amount of signal events. The $0\nu\beta\beta$ analysis has chosen a 3.3 m fiducial volume to quote its expected event rate per year as in figure 3.2. External ^{208}Tl from UPW, the ropes lattice, the PSUP and the AV produces a 2.6 MeV γ with a Compton scatter length of 10 cm in water and 26 cm in undoped scintillator. This represents a significant background for solar analyses that usually probe larger fiducial volumes of 5.5 m. In the particular case of this analysis, it will be important to exclude all externals as, producing radiation near the AV walls, they will produce the scintillation light first to reach the PMTs which is problematic for reconstruction as will be illustrated in section 5.3.3.

After fiducial volume cuts have been applied to reduce the occurrence of external backgrounds, an analysis method referred to as coincidence tagging is employed. It profits from the high energy α decay of a short lived ^{212,214}Po atom having β decayed from its ^{212,214}Bi mother. Referring back to figure 3.3, the ^{214}Bi isotope has two decay modes. It can α decay to ^{210}Tl or β decay to ^{214}Po, but, with a branching ratio of $> 99\%$ to 0.021%, the β decay is predominant and a common *in situ* gauge of Rn levels in the detector [129]. The method of coincidence tagging involves finding the ^{214}Po event with a quenched energy value of $\sim$0.9 MeV and "looking back" for the^{214}Bi event with a $\mathcal{Q}$-value of 3.27 MeV within a window corresponding to the ^{214}Po half life of 164 μs and an infinitesimal and irresolvable travel distance. The time window is extended to account for timing resolution. The narrower peak of the Po event is the reason why coincidence algorithms tend to search first for this delayed event before looping back through previous events to identify its corresponding prompt Bi

partner.

As for the ^{232}Th chain in figure 3.4, the same analysis principle and method applies with the α decay from ^{212}Bi to ^{208}Tl having a branching ratio of 36% compared to 64% for the β decay to ^{212}Po. The search starts with identifying the ^{208}Tl or ^{212}Po delayed event with $\mathcal{Q}$-values of 6.21 and 8.95 MeV, respectively, then looping back for its ^{212}Bi partner within a window associated with the ^{208}Tl or ^{212}Po half lives of 3 mins and 0.3 μs. With its high $\mathcal{Q}$-value, ^{208}Tl is expected to be the most pervasive source of background across all analyses.

Pile-up plagues event windows when distinct β and α decay products occur within less than 400 ns of each other. Because the SNO+ trigger window is 400 ns, these will be reconstructed as one in the same event time window instead of as two separate triggered events. The combined pile-up event will feature the sum of the $\mathcal{Q}$-values of both decays. Likelihood classifiers have been developed to pick out Bi-Po pile-up events. They take advantage of the difference in time residual profiles of background pile-up events compared to $0\nu\beta\beta$ events. Later scintillator pulses from α decays and step difference in energy deposit when it occurs, result in shape differences in these profiles [189]. This is the distinction between in- and out-of-window events, where the former refers to coincidences occurring within the same event trigger window, and the latter to a decay with the Bi and Po decays occurring in separate windows.

Additionally, (α,n) reactions constitute a non-negligible background to the $0\nu\beta\beta$ search and are also identified with coincidence tagging. When an α, primarily ^{210}Po nuclei leached from the AV surface into the scintillator, is absorbed by a nucleus, it emits a neutron alongside its daughter nucleus. In SNO+, common occurrences of

(α,n) interactions are

$$\alpha + {}^{13}\mathrm{C} \rightarrow {}^{16}\mathrm{O} + n$$
$$\alpha + {}^{18}\mathrm{O} \rightarrow {}^{21}\mathrm{Ne} + n.$$

The prompt and delayed signature between the α decay and subsequent neutron capture are sufficiently removed in time ($\sim$220 μs) and distance to be classified through coincidence tagging algorithms.

The standard window cuts for coincidence tagging in LAB+PPO for notable background searches are listed in table 3.3.

	E_{prompt} [MeV]	$E_{delayed}$ [MeV]	ΔT [ns]	ΔR [m]	FV [m]	classifier cuts
^{214}BiPo	[1.3, 3]	[0.7, 1]	[500, 2×10^6]	<1	<5.5	0.1<ITR<0.35
^{212}BiPo	[0.5, 4]	[0.9,1.5]	<800	<1	<5.5	0.1<ITR<0.35
^{212}Bi^{208}Tl	[0.5, 4]	[2.75, 5.25]	[3×10^5, 7.56×10^8]	<1	<5.5	LL<-2

Table 3.3: Coincidence cut values used in the tagging algorithms of the prominent backgrounds to this analysis. ΔT, ΔR and classifier cut values are determined for LAB+PPO. FV refers to the fiducial volume.

As is evidenced in the simulated background spectra from figure 3.2, the $0\nu\beta\beta$ of ^{130}Te lies away from most sources of contamination besides solar ^{8}B neutrinos, ^{208}Tl, ^{214}Bi and $2\nu\beta\beta$ products known to smear into the $0\nu\beta\beta$ decay ROI. Spectra below the ROI have been simulated to illustrate isotopes hindering lower energy solar neutrino analyses. For this analysis focusing on extracting the directional information of the ^{8}B solar neutrino flux, the ^{8}B signal is inundated at energies below 2.5 MeV. Of those, notably is the 1.16 MeV β decay of ^{210}Bi. Though the subsequent α decay to ^{210}Po has a $\mathcal{Q}$ value of 5.4 MeV, quenching effects within the scintillator shift the ^{210}Po peak to lower energies.

Cosmogenically activated ^{39}Ar enters the detector through plant operations. With $\mathcal{T}_{1/2} = 269$ years, its influence on signal purity is directly correlated with its ingress in the scintillator. As was touched on, ^{39}Ar contaminated nitrogen was used for sparging during the bis-MSB loading campaign, causing a notable increase through a 0.585 MeV β decay [190]. Present in the atmosphere as a byproduct of nuclear fission, ^{85}Kr ($\mathcal{T}_{1/2}$) mostly (99.57%) β decays to ^{85}Rb with $\mathcal{Q} = 0.687$ MeV. ^{85}Kr demonstrates the importance of keeping plant operations under vacuum as its airborne rate of 1 Bq/m^3 is sufficient to infiltrate the target material in an noticeable way. Carbon isotopes can similarly be induced into the scintillator, as it is primarily a carbon chain, when a muon passes through the volume and spallates. C-10 and C-11, in particular, have short half lives ($\mathcal{T}(^{11}\mathrm{C})_{1/2} = 20$ minutes, $\mathcal{T}(^{10}\mathrm{C})_{1/2} = 19.3$ seconds) and relevant $\mathcal{Q}$ values ($\mathcal{Q}(^{11}\mathrm{C}) = 0.96$ MeV, $\mathcal{Q}(^{10}\mathrm{C}) = 3.6$ MeV). The bulk of these events can be eliminated by implementing an veto going up to a minute in length following a muon event in the detector in case spallation occurred. Longer lived ^{11}C isotopes are identified through coincidence tagging between the prompt (muon) and delayed events. Above this threshold of 2.5 MeV however, only ^{208}Tl and ^{214}Bi are of concern. It is customary to take the approach of broadening the cuts applied to ^{212,214}BiPo tagging for solar analyses. The solar ^{8}B flux offers a constant rate of events. It is acceptable to favour rejecting more potential background events which comes with the risk of discrediting signal events as false negatives. Tighter cuts on ^{212,214}BiPo tagging allow for a smaller sample of those backgrounds which entails the likelihood of backgrounds remaining in the signal sample. The efficiency of ^{214}BiPo tagging in SNO+ following the first approach is high at 99.77% and 99.84% for ^{212}BiPo events, with 99.85% of ^{8}B ν_e signal events [73].

Improvements to ^{208}Tl tagging have been achieved via multisite discrimination techniques, which leverages the fact that these γ rays create several energy deposits, as opposed to single solar decay events fully depositing their energy during a single interaction.

The road leading to the potential observation of $0\nu\beta\beta$ decay is wrought with peril. SNO+ was built with that objective in mind; every feature of the detector is designed to maximise resolution and fight undesirable backgrounds. Background mitigation has been explored starting with the broad shielding techniques. Radiopurity requirements were considered and led to the introduction of SNO+'s processing plants. The conversion of a light emitting interaction in liquid scintillator into raw electronic information, and subsequently into physical quantities was provided. The concepts of simulation and calibration were established as crucial to ascertain the accuracy of the detector response so that the surviving backgrounds that cannot be avoided can be effectively identified through analysis techniques. The next chapter dives into the mechanics of how particles interact with liquid scintillator to produce the light picked up by SNO+ PMTs.

Chapter 4

Liquid Scintillator

Mostly Harmless

- D. Adams

In a liquid scintillator, light is produced by two main mechanisms: Cherenkov radiation and scintillation. Cherenkov radiation arises from the refractive index of the scintillator allowing for emitted particles to travel at speeds greater than celerity. A generic liquid scintillator combines a solvent and a fluor with the occasional additional fluor referred to as a wavelength shifter.

This chapter provides an overview of light production and propagation mechanisms, underlines the unique properties of Cherenkov radiation, and describes optical properties of liquid scintillators with particular attention to LAB. Further discussion explores the development and characterisation of the SNO+ liquid scintillator.

4.1 Propagating Light

Liquid scintillator and noble gas neutrino experiments have two handles by which to maximise detectable signal disregarding increasing energy and timing resolution, as

well as augmenting radiopurity as was the focus of chapter 3. These are the mean free path and the interaction cross section. The first is directly correlated with the scale of the detector; the bigger the better. The second is dictated by the choice of active target deployed. While media can be doped with nuclei maximising the cross section of particular neutrino interactions part of a detector's scientific program, the base solvent itself is chosen for its light propagation efficiency. Energy deposits within the active volume emit light captured by the detector hardware. Scintillators are attractive due to their high light yield, which translates to finer energy resolution.

Physically, light is electromagnetic radiation ranging over a broad[a] wavelength spectrum. It is emitted and absorbed during interactions, exciting the atoms involved. Excitation and de-excitation refers to the process in which electrons jump between orbital states; absorbing a photon to reach a more energetic state or releasing one to fall back to a more stable state, respectively.

Free particles traversing matter incur energy loss. The heavier charged particles[b] ionise or excite particles they inelastically collide with depending on the energy transferred. Assuming a constant molecular structure serving as the medium with quantum orbitals involved, charged particle interactions can only be given as a probability over a path length. This idea of a statistical energy loss per unit length is referred to as the stopping power and can be parametrised by the Bethe-Bloch equation which is the quantum expansion on Bohr's classical formulation of the concept [124, 92]

$$\left\langle -\frac{dE}{dx} \right\rangle = K\frac{Z}{A}\frac{z^2}{\beta^2}\left[\ln\frac{2m_e c^2\gamma^2 W_{\max}}{I^2} - 2\beta^2\right], \tag{4.1.1}$$

[a] Gamma rays have wavelengths of the order of 10^{-11} m. Radio waves range from 10^{-3} to 10^{3} m. Light detectable by the human eye populates the $[400, 700]\times10^{-9}$ m region.

[b] "Heavier" here is used to exclude electrons. It therefore refers to muons, protons, α particles, pions, etc..

where K is a constant coefficient ($2\pi N_A r_e^2 m_e c^2 = 0.1535\,\mathrm{MeVcm^2g^{-1}}$) involving the electron mass and radius, z is the charge of the incident particle, Z is the atomic number, A is the atomic mass, $\gamma = 1/\sqrt{1-\beta^2}$, and $W_{\max}$ is the maximum energy transfer to an electron in a single collision. Correction terms can be added to account for the density effect[c] and the shell effect[d]. Other numerical corrections can be applied as the Bethe-Bloch formula is heavily energy dependent. It describes electronic losses though not radiative losses where the relativistic regime takes over, and even then overestimates the probable energy loss. Especially when the medium is not a pure substance, *in situ* measurements are preferable, though an approximation can be formulated by averaging the stopping power of each component weighted by its proportion in the solution.

As for the lighter charged particles, electrons, they are more prone to Coulomb scattering their way through the active volume, losing their energy by ionisation and *Bremsstrahlung*. The accumulation of these small-angle scatters is equivalent to modeling the outgoing particle at an angular deflection from the original direction of the incoming particle at the point of interaction. Low energy[e] electrons are also prone to backscattering which occurs when the deflection angle is wide[f] with respect to the particle direction due to scattering off the nuclei. The probability of backscattering is then dependent on the atomic number of the target nucleus Z.

Regardless of the quantum processes describing the physics of particle interactions in matter, light is emitted and propagated. The processes relevant to the SNO+ target

[c] Denser materials have a lower stopping power for highly relativistic charged particles as they polarize the medium's valence electrons along their path.

[d] When the incoming particle carries a kinetic energy of the same order of magnitude as that of the inner shell electrons.

[e] E_e <1 MeV.

[f] The scattering angle is roughly proportional to the inverse of the incoming electron's momentum.

medium, Cherenkov radiation and scintillation, will be the focus of this chapter.

4.1.1 Cherenkov Radiation

In 1934, Cherenkov noticed the blueish hue emanating from a radioactive source submerged in water [48]. In 1937, Frank and Tamm understood this effect to be due to the radioactive decay daughters surpassing the speed of light in certain media. They parametrised this Cherenkov radiation and all three scientists shared the 1958 Nobel Prize.

When a particle travels faster than the speed of light in that medium[g], it produces a "shockwave" with that characteristic blue tint. The light produced in the wake of these energetic charged particles is emitted in a cone around the direction of the incident particle, as is depicted in figure 4.1. The cone's angle is determined by [124]

$$\cos\theta_\gamma = \frac{1}{n(\lambda)}\frac{c}{v}. \tag{4.1.2}$$

As long as the particle of mass m has a kinetic energy allowing for $v > c/n$, photons will follow a trajectory defining the Cherenkov cone. That energy can be calculated as [124]

$$E_\gamma = m\left(\frac{1}{\sqrt{1-n^{-2}}} - 1\right). \tag{4.1.3}$$

This energy threshold is obviously an inherent hindrance to experimental physics. Scintillators, which are the subject of the rest of this chapter, are a powerful tool

[g]This means that the speed of the charged particle in that medium exceeds that of photons in that medium which can be calculated as $v = c/n$ where c is celerity in vacuum and n the medium's refractive index.

for experiments aiming to probe lower energies and improve energy resolution by boosting the photon yield per unit energy of interactions.

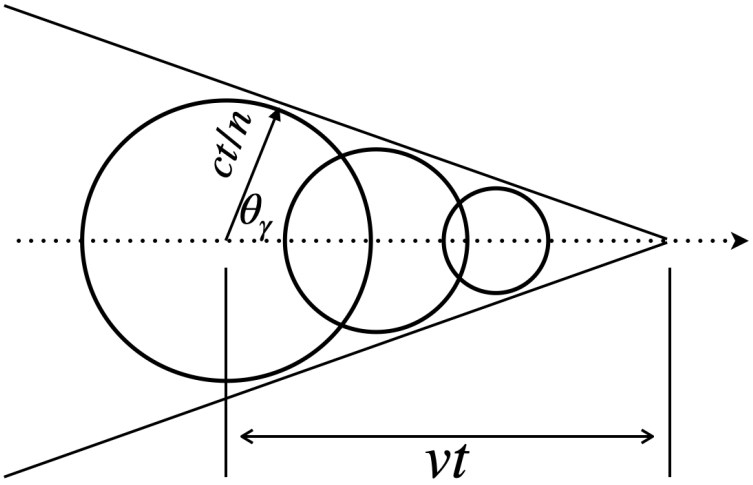


Figure 4.1: A Cherenkov cone forming in the wake of a particle traveling faster than light ($v > c/n$) in a medium of refractive index n. The angle is correlated to the velocity of the particle.

The Frank-Tamm formula determines the number of emitted photons N_γ per distance traveled x and wavelength λ:

$$\frac{d^2N_\gamma}{dxd\lambda} = \frac{2\pi\alpha z^2}{\lambda^2}\left(1 - \frac{1}{\beta^2 n(\lambda)^2}\right) \tag{4.1.4}$$

where α is the fine structure constant (1/137), z is the charge of the particle, β is the ratio of the particle's speed v over the speed of light c and $n(\lambda)$ is the index of refraction of the medium at wavelength λ [105]. Then, practically, the number of radiated photons expected to be captured by PMTs for example, can be determined by integrating over the sensitivity range of those PMTs.

Equation 4.1.4 indicates why the radiation is dominated by shorter wavelengths as the number of emitted Cherenkov photons is inversely proportional to λ^2. While

Cherenkov radiation is technically emitted across the whole UV spectrum, the Frank-Tamm formula explains why the shorter blue wavelengths are preferentially propagated among the visible light spectrum.

The reason Cherenkov light has been so instrumental in major neutrino experimental results is its intrinsic anisotropy. The Cherenkov cone, depicted in figure 4.1, contains the light produced after a neutrino interaction with the target nucleus. This property is particularly exploitable in the case of an energetic directional signal, with the sun being the prime example. For centuries, its position relative to any point on Earth could be tracked and calculated with remarkable accuracy. Conversely, scintillation light, produced by following charged particle interactions in the medium, is isotropic. The Compton scattering and pair production they induce over their long path lengths produce charged leptons that cause scintillation light to be emitted. Furthermore, the Cherenkov ring[h] created along the direction of the event allowed water experiments to extract particle identification. As the lighter particle, the Cherenkov ring created by an electron scatter would be blurrier compared to the defined boundaries and tight ring of a muon event.

Cherenkov light continues to be produced in organic liquid scintillators, though it is not the primary mechanism for scintillation light production. Cherenkov light, or at least the primary fluorescence mechanism that will be elaborated on in section 4.1.2, is said to be instantaneous at a time delay of the order of 10^{-15} s which is indiscernible to the timing resolution of modern day neutrino detectors ($\mathcal{O}(10^{-9})$ s). This is why Cherenkov light will here on out be described as "early" instead of "prompt". This distinction will become apparent in the discussion on selection via time residuals in section 5.3. However, because Cherenkov light is emitted early, it is expected to be

[h] i.e.: The projection of the Cherenkov cone on the walls of a detector.

absorbed by the scintillator solution and reemitted at its emission spectrum rendering it indistinguishable. SNO+ is not the first, or likely last, neutrino experiment hoping to recover early Cherenkov light and directionality.

Though the timing profile of scintillators depends on their chemical components [145], Cherenkov light will be recorded early assuming the detector has the required timing resolution. This instantaneous emission quality, along with the dependence of the Cherenkov cone angle and the light yield on the velocity, or energy, of the incoming particle make this type of radiation a powerful and versatile principle to be used in experimental particle physics. Being relatively affordable, Cherenkov detectors continue to be used in a wide range of physics experiments. For example, ATLAS and CMS employ them as a fast forward particle counter in the shape of an scintillator detector around their main beam axis; the medium being quartz fibers.

4.1.2 Scintillation Light

Scintillation is the process by which an interaction between a charged particle and a scintillator molecule create radiation that fluoresces[i] as the excited molecule emits photons. As a charged particle travels through the scintillator, it excites its molecules directly or causes ionisation.

The sacrifice of directionality is necessary in $0\nu\beta\beta$ searches as scintillation drastically improves the light yield of any interaction. Birks' law [39] describes the total number of produced γs L per distance travelled x as a function of energy loss per

[i]Fluorescence is the (luminous) product of a non-thermal excitation following ionisation.

unit path length $\frac{dE}{dx}$

$$\frac{dL}{dx} = S\frac{\frac{dE}{dx}}{1 + k_{\mathrm{B}}\frac{dE}{dx}} \tag{4.1.5}$$

where S is the scintillation efficiency, otherwise known as its luminescence, and k_B is Birks' constant, both properties of the scintillator that can be measured *ex situ* [40]. Birks' law is a semi-empirical model taking into account increased recombination and quenching effects in denser, more complex molecular structures. In can be thought of as providing a metric for the scintillation saturation. These optical properties, responsible for the empirically observed non-linearity of $\frac{dL}{dx}$, are notoriously difficult to quantify. SNO+, as with all liquid scintillator experiments, is no stranger to wrestling equation 4.1.5 in the develpment of its optical model. Birks' constant itself has a propensity for taking on the role of scapegoat for optical modeling failures across literature.

The dominant scattering mechanism in a large liquid scintillator detector is Rayleigh scattering, where average emission wavelengths are larger than the target's molecular structure. The process is elastic, as interactions do not impact the frequency of radiation such that the incident radiation is propagated at the same frequency until the end of its mean free path. Experiments choose their solvent along with their additives, as well as their detection hardware, to maximise the scintillation processes occurring within a range in line with the capacities of their chosen detection hardware. In the longer wavelengths where absorption and emission do not occur, Rayleigh scattering is the dominating optical process.

Three quantum numbers, intrinsic properties of elements, describe all configuration of orbitals, the probability plane in which an electron or a number of electrons

carrying a discrete quanta of energy orbit around their nucleus. These are the principal or shell, angular momentum and the magnetic quantum numbers. The fourth quantum number, the spin, only comes into play when two electrons populate the same orbit - they must be of opposite spin according to the Pauli exclusion principle.

All the possible particle interactions broached throughout this thesis share one common denominator: an exchange of energy quanta. What this implies on a chemical level is the bumping up or down of electrons on the orbital structures determined by quantum numbers of the molecules making up the active medium. LAB valence electrons can be excited directly or indirectly via ionisation and subsequent recombination. It is the relaxation from the excited state where molecules radiatively de-excite by emitting optical photons, which results in the production of scintillation light.

Linear alkylbenzene is the solvent of the scintillator cocktail developed for SNO+. It is an aromatic hydrocarbon. A chain (9-14 (>95% 9-12)) of carbon attaches [61] to the simplest form of an aromatic hydrocarbon: a phenyl group, in this case, benzene (C_6H_6). The ringlike structure of a benzene molecule can be found in figure 4.2, and it is this bonding formation that defines aromaticity where the free electrons of each carbon not engaged in a bond with a neighboring carbon or hydrogen atom are "shared" by the ring. This formation is referred to as a π bond. Aromatic molecules make for highly stable compounds, which is of interest to a physics experiment concerned with radiopurity and looking to submit its solution through purification processes without risking the break down of its solvent.

The π orbital of the benzene ring is a key optical feature in LAB. These delocalised

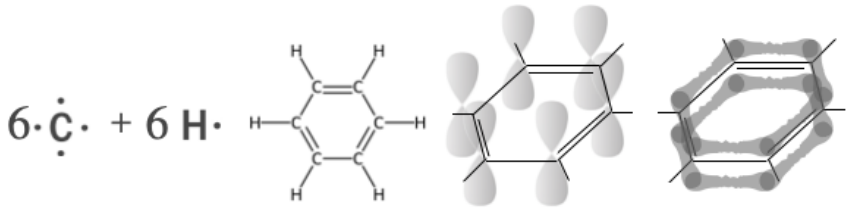


Figure 4.2: Different notations and representations of the benzene ring illustrating how the valence electrons form bonds and how the p orbitals around each carbon form the π molecular orbital ring. The s orbitals of H bonding with C are omitted for clarity.

electrons are likelier to be excited than if they existed in a localised σ orbital[j] closer to the C nucleus.

Transitions between the π orbital excitation states produce the different optical phenomena encompassed by the umbrella term of scintillation. Figure 4.3 summarizes them. The excited electron in the singlet state has a spin orientation that is anti-parallel to the electron in the ground state. In the triplet state, their spins are aligned.

Absorption is the fastest of the processes, the energy transfer occurring on the scale of $10^{-15} - 10^{-9}$ s. Fluorescence and phosphorescence present discernible timing profiles for a detector like SNO+ equipped with a timing resolution of 1 ns. The singlet state relaxes in a matter of a few nanoseconds. Fluorescence is then the prompt timing pulse. The delayed timing pulse corresponds to the de-excitation of a triplet state. Phosphorescence occurs several order of magnitude after excitation. Delayed fluorescence occurs by intersystem crossing where any excited triplet state converts to an excited singlet state that then fluoresces back to ground state. On the emission profile, the slower component of phosphorescence or delayed fluorescence can

[j] If π orbitals are the binding product of p orbitals; σ orbitals arise from sp-hybridization where the electrons in the $2s$ orbital bond with one of the three available p orbitals.

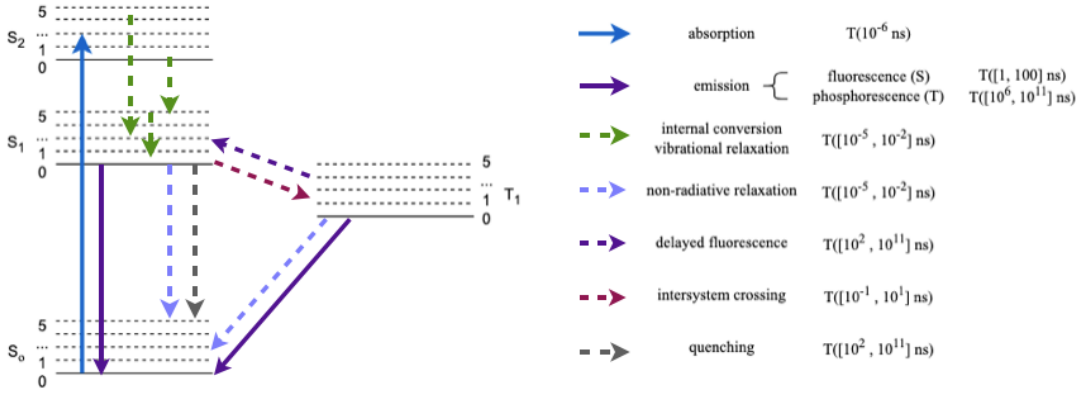


Figure 4.3: Jablonski diagram of π orbitals. S_0, T_0 is the singlet or triplet ground state, $S_{1,2}, T_{1,2}$ are the excited states, while double subscripts $1, ..., 5$ refer to vibrational sublevels. All allowed transition channels between sublevels are omitted for clarity, with only general examples of every process included. Only one excited triplet state is depicted to introduce intersystem crossing which involves a spin flip as an electron crosses between S and T. Timescale ranges are from [132].

be explained by the metastable nature of the triplet state. Heavier ionising particles are more prone to providing sufficient energy for an excitation to this state, which proves useful in particle identification through timing profile studies.

4.1.3 Characterising Light

Organic scintillators present intrinsic optical properties exploited by physics experiments. These are the timing profile - the scintillation intensity as a function of time – including the rise and decay times, as well as the light yield, and the absorption and emission spectra [200]. Pulse shapes of emitted photons along the decay time tail in conjunction with the rise time profiles allows for particle identification, since these two quantities are influenced by the nature of the particle exciting the scintillator molecules. Indeed, decay time can indicate which transition process occurred during

de-excitation such as the longer tails arising from a delayed intersystem crossing. A shorter electron (β) event corresponds to a singlet state de-excitation manifesting as a prompt pulse. A longer α event would imply the lengthier de-excitation of the triplet state. However, there exists no allowed channel to the ground state not involving spin inversion. As a result, longer α events result in a delayed exponential decay tail. In SNO+, the IBD, (α, n) and $\alpha - \beta$ classifiers are built following Log-Likelihood (LL) methods based on the expected pulse shape and timing profile differences [145].

For a multi-component solution, the emission time is empirically taken as the sum of the exponential decay time of each component such that

$$\sum_{i=1}^{n} \frac{N_i}{\tau_i} e^{-t/\tau_i}, \tag{4.1.6}$$

where τ is the decay time constant unique to each component and N is the fractional weight of each i^{th} component in the solution.

Light Yield Fundamentally, the light yield can be understood to be the number of emitted photons per unit of energy deposited during a particle interaction. It is the main metric by which scintillation is assessed and the dominant factor in limiting energy resolution in neutrino detectors.

It is possible that an excited electron returns to the ground state without emitting a photon. This non-radiative relaxation occurs if the vibrational ground energy states overlap with the lowest energy excited state. The higher the probability for this mechanism, the lower the light yield of the scintillator. Quenching, addressed later, is also responsible for de-exciting the scintillator molecules.

The light yield of the SNO+ scintillator cocktail following the addition of 2.2 g/L

PPO was measured by a Hamamatsu PMT to be (11808 ± 630) photons/MeV, scaled and normalized to the previously calculated (11920 ± 630) photons/MeV for the prepared 2.0 g/L PPO concentration sample [61]. Figure 4.4 presents the light yield measurements of the deployed SNO+ liquid scintillator with PPO against prepared LAB+PPO bench top samples as well as published external values. The 2.2 g/L PPO sample from the SNO+ AV following the end of the fill presents a light yield in accordance with the prepared 2.0 g/L PPO sample. The large uncertainties associated with the experimental setup are sufficient to allow for the nominal light yield value of the higher concentration sample to be slightly lower than the prepared 2.0 g/L PPO reference sample.

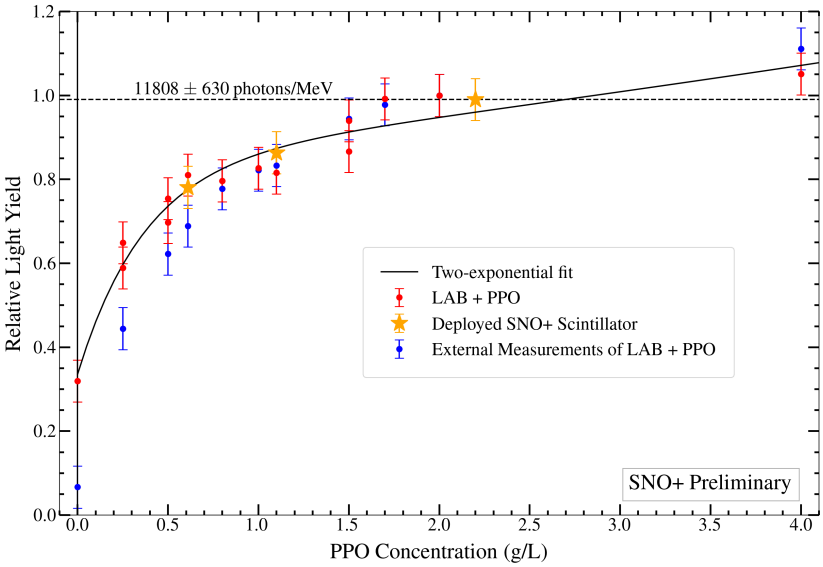


Figure 4.4: Light yield of SNO+ AV (yellow) and bench top (red) LAB+PPO compared to published measurements (blue). The two exponential fit (black) is given by $L_R = ae^{bC_B} + ce^{dC_B}$ where L_R is the relative light yield normalized to a PPO concentration of $C_B = 2.0$ g/L previously measured to have a light yield of 11920 ± 630 photons/MeV. Figure from [22].

Critical concentration of the fluor is defined as the point at which the initial solvent light yield has increased by 50%. [43] Following that point, the increase grows asymptotically until saturation. Though light yield should and would be linearly proportional to the fluor component weight in the solvent, in practice, the non-radiative optical processes of self-absorption or inefficient reemission become more prevalent. This explains the plateauing effect of fluor concentrations with respect to effective light yield. Saturation is reached when light yield begins to decrease due to self-quenching effects [43]. Fundamentally, once the energy transfer efficiency has been maximised, there is no room for it to continue in a linear increase, and so the benefit of adding fluor to the solvent saturates.

Absorption and Attenuation Excitation is the process by which a photon excites an electron on the π orbital of the benzene rings. Essentially, the photon is absorbed by a scintillator molecule or scattered. Because it concerns the excitation process, it is dependent on the scintillaton component. While the type of interaction undergone by a photon is highly correlated to its energy, SNO+ is mainly concerned with Rayleigh scattering as was discussed. In conjunction with an exponential expression dependent on the mean free path, the absorption ratio is given by

$$I(x) = I_0 e^{-\mu x}, \tag{4.1.7}$$

where $I(x)$ is the intensity of the incident photon or photon beam, x is the path length, and μ is the absorption coefficient which is the inverse of the mean free path of the photon. This quantity, also referred to as the attenuation, corresponds to the fraction of photons traveling a distance x before undergoing absorption. In the case

of a compound, Bragg's rule defines the total absorption coefficient as the weighted sum of the molar absorption coefficient of each component:

$$\frac{\mu_{tot}}{\rho_{tot}} = \sum_{i=1}^{n} w_i \frac{\mu_i}{\rho_i}, \tag{4.1.8}$$

where ρ is the density of the i^{th} compound and w is its fractional weight in the solution.

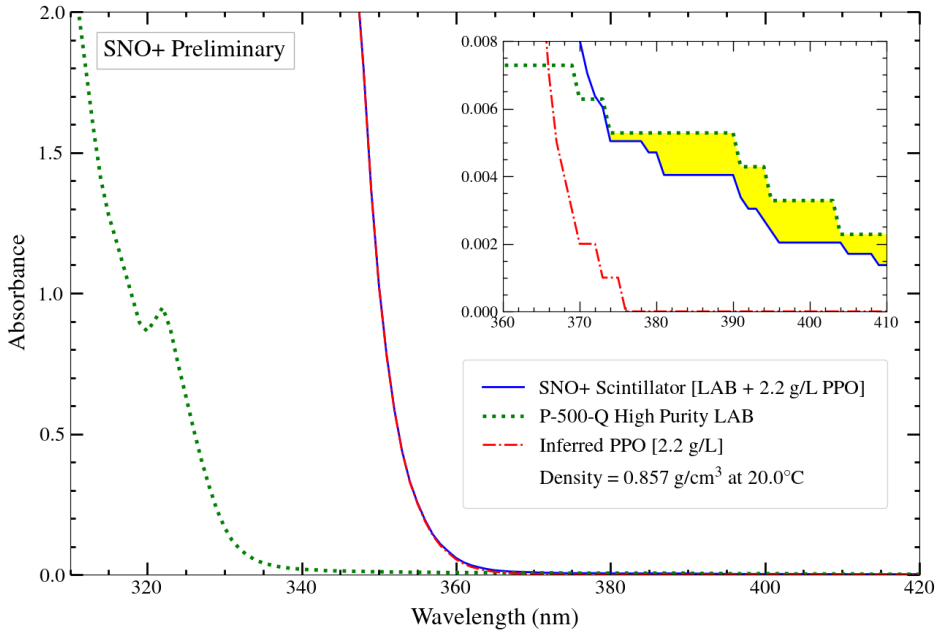


Figure 4.5: Absorption spectra of LAB samples where absorbance is given as the ratio of incident and transmitted photon flux such that $A = \log\frac{I(x)}{I_0}$. Measurements were taken in 1 nm increments at a 1 s frequency. Baseline subtraction was performed using reference cell measurements. Blue and green are SNO+ AV samples with density of 0.857 gcm^{-3}, turbidity of 0.05 NTU and water contents lower than 5 ppm. The inferred PPO absorption spectrum is obtained by using a reference cell filled with pure LAB rather than the standard air filled cuvette for baseline subtraction. Figure from [183].

Absorption length refers to the average distance a photon travels before being absorbed and acts in conjunction with the the mean Rayleigh scattering length to provide the attenuation (or extinction) length as

$$L^{-1}_{\text{attenuation}} = L^{-1}_{\text{absorption}} + L^{-1}_{\text{Rayleigh}}. \tag{4.1.9}$$

Emission This is simply the process by which an absorbed photon is emitted back into the solution at equal or lower energy causing the emission spectrum to live at longer wavelengths than the absorption spectrum with some overlap. It is wavelength dependent with all components of the solution contributing to the final emission spectrum of the scintillator. As was mentioned, the time lapse between absorption and emission is a key feature in particle identification.

Absorption and emission spectra alike can display peaks at different wavelengths as is obvious in figure 4.10. These correspond to the excitation and de-excitation paths taken, respectively, examples of which are depicted in figure 4.3.

Self-Absorption Because absorption and emission occur over a wavelength range instead of sharp values characteristic of elements, there exists a region in which their spectra overlap. Self-absorption occurs when an emitted photon is re-absorbed. The Stokes' shift is defined as the wavelength distance between the absorption and emission peaks. The overlap between the absorption and emission spectra defines the probability of a photon to self-absorb. It is usually a serious consideration for solvents alone going so far as to render some liquid scintillators opaque in the energy range of interest for neutrino experiments. It then stands that choosing a fluor that maximises the Stokes' shift minimises the overlap and opportunity for self-absorption

in the solvent it will be added to.

Re-emission Re-emission is of two types. In resonant fluorescence, the photon is re-emitted with the same energy as it was absorbed foregoing any intermediate vibrational relaxation; this is a feature of single particles and negligible in the context of a complex molecular structure because the resonance occurs only at certain wavelengths. The re-emission that must be considered is that of a molecule to re-absorb and subsequently re-emit from a molecule having just undergone its own fluorescence. In this case, energy loss results in the photon having a longer wavelength. In a solution, this process can happen between two fluors. It can be characterised by different timing profiles. For the SNO+ scintillator composed of LAB+PPO, PPO re-emission where a photon is absorbed and emitted between two PPO molecules is expected to occur following the measured intrinsic PPO exponential decay time constant of 1.6 ns [61]. Re-emission between two LAB molecules where LAB fluoresces and re-emits a photon occurs within the LAB emission spectrum, lower than that of PPO, is suppressed. Finally, re-emission of a photon absorbed by LAB, transferred to a PPO molecule that undergoes re-emission is expected to occur 5.1 ± 0.1 ns after the initial LAB excitation [61].

Energy Transfer and Non-Radiative Transfer Efficiency Another consideration for a binary system is the energy transfer between excited states of fluorescing molecules. An electron excited to a singlet state that undergoes vibrational relaxation is likeliest to simply non-radiatively relax to the ground state, as has been considered thus far. However, in a bonded system, this electron may transfer its energy to an electron on the orbital of another fluor. This is known as Förster (or fluorescence)

Resonance Energy Transfer (FRET). That electron goes through the usual excitation and de-excitation stages. However, upon returning to the ground state, its emission profile will be in line with that of the fluor instead of that of the solvent that has absorbed the incident energy. Because fluors are chosen for their ability to boost the light yield, it stands that FRET is a desirable property. FRET is heavily distance dependent and a naive way to keep solvent and solute close is to increase the concentration. However, self-absorption becomes a hindrance at high concentrations past the saturation point which manifests as a light yield decrease after the plateau. Because the saturation point is difficult to calculate or infer from simulations, benchtop measurements remain the most reliable way to fine-tune liquid scintillator solutions to maximise light yield and are widely conducted by all experiments. According to a quantum extension of FRET, the transition probability of photons between solvent molecules or between solvent and solute molecules goes as $1/R^6$ where R is the distance between molecules [43]. It follows that scintillator properties such as solute concentration and temperature have an effect on R and consequently energy transfer. Density and viscosity may all have an impact. The SNO+ scintillator cocktail is monitored for such values.

Quantum Yield Quantum yield is the counterpart to non-radiative decay processes, because it is the probability an excited state emits a photon through a fluorescent (or delayed fluorescent or phosphorescent) channel. This property is component dependent and one of the main criteria by which the primary fluor is chosen. It measures the efficiency of fluorescence emission relative to all relaxation paths. It can be expressed as the ratio of emitted to absorbed photons. The general formulation of scintillation efficiency S over a path length x that was presented in Birks' law in

equation 4.1.5 is given by

$$\frac{dL}{dx} = S\frac{dE}{dx}, \tag{4.1.10}$$

where $\frac{dE}{dx}$ is still the energy loss of a particle over a distance traveled x, and $\frac{dL}{dx}$ is the light yield. Fluorescence dominates over phosphorescence, and non-radiative processes can result in a light yield reduction. The discussion on the asymptotic behaviour of light yield at limit fluor concentration values can be recalled here. Birks' law for large values of dE/dx, mainly high dE/dx particles such as slow α particles in SNO+, approximates to

$$\frac{dL}{dx} = \frac{S}{k_B}. \tag{4.1.11}$$

Quenching Quenching implies the non-radiative transfer of energy between two molecules or the same molecule. Referring back to Birks' law in equation 4.1.5, it is apparent that quenching effects increase with heavier ionising particles otherwise described as large dE/dx values. It also highlights the non-linearity of scintillation loss or quenching. It encompasses several processes that impinge on the quantum yield of the scintillator and is particle and energy dependent.

The presence of impurities within the scintillator can cause quenching. Large molecular impurities will dissolve within the molecular structure of the scintillator and affect its mean scattering length, or absorb photons and emit them radiatively (or not) following different probabilities, thus hindering the overall light yield. An example of particular interest to SNO+ is oxygen quenching. However, oxygen quenching goes beyond impurity quenching. Oxygen absorbs lower energy electrons, preventing

them from exciting the scintillator. The energy gap between its triplet ground state and singlet first excited state is smaller than in LAB, creating a favoured transition channel between the metastable T_1 LAB state and the O_2 triplet state. This dramatically suppresses delayed fluorescence and phosphorescence, because the triplet transition is energetically favoured [42]. This is without harking back to the degradation oxygenation causes in a hydrocarbon-based scintillator as was discussed in chapter 3.

Ionisation quenching is the most prevalent in liquid scintillator. Correlated to the energy loss dE/dx, it is a common process for heavier α particles and at lower energies at the end of a particle's path through the medium [39]. When these heavier particles come to a stop and deposit a high energy density, the expected light yield from this ionisation process is non-linearly reduced (quenched). This is the effect Birks' law is mainly tasked with accounting for.

Interface effects Refraction and reflection optics at the various interfaces of the SNO+ detector can be modeled by `RAT`. These are the acrylic – LAB and acrylic – water interfaces. Refraction within the AV wall are generally neglected in official MC production sets unless otherwise specified.

4.2 Enhancing the Scintillator

Though it has yielded substantial interesting physics results, the SNO+ scintillator phase is laying the ground work for metal doping through ^{130}Te. Metal loading is wrought with pitfalls. Stably suspending metals in an aromatic solution is challenging. Purifying the dopant to keep the experiment's background levels in check is tedious. Upholding the optical clarity of the scintillator requires controlling an

environment within stringent temperature boundaries. Brief exposure to oxidation and humidity, which can be remedied through purification in an organic scintillator, can prove fatal to a doped scintillator if the dopant precipitates out. Self-quenching becomes dominant with metal loading, thus seriously decreasing the light yield. The nature and concentration of additives aims to maintain light yields aligned with the target energy resolution for $0\nu\beta\beta$ decay searches.

Practical considerations play a determining role in the development of a multi-component liquid scintillator. From accessibility, abundance and cost to safety warnings such as toxicity, corrosiveness and flammability, all of these factor into narrowing down the list of candidates. Beyond the pragmatic criteria, chemical and physical requirements are not to be compromised on: SNO+ can summarise its choice of scintillator cocktail to one that fulfills these requirements:

- All components can be bound in a molecular structure that maintains homogeneity in a liquid phase over a volume of several hundred tonnes within ambient temperature and pressure ranges.

- All components in their individual and combined compositions can undergo purification methods such as distillation, water extraction and gas stripping in order to sustain the stringent optical and radio purity goals of the experiment.

Once a readily available solvent is chosen, compatible solutes are selected to counteract some of its shortcomings in terms of maximising the experiment's energy resolution, in other words its light yield. Primary fluors, added in concentrations of a few g/L, are chosen to increase the scintillation process. Secondary fluors, added in concentrations of a few mg/L, are added to shift the emission wavelengths to the PMT quantum efficiency range and to minimise re-absorption by maximising the Stokes'

shift. The layering of fluors and its effect on scintillation is illustrated in figure 4.6. Other reagents are selected to thwart optical degradation, an example of which is oxi-

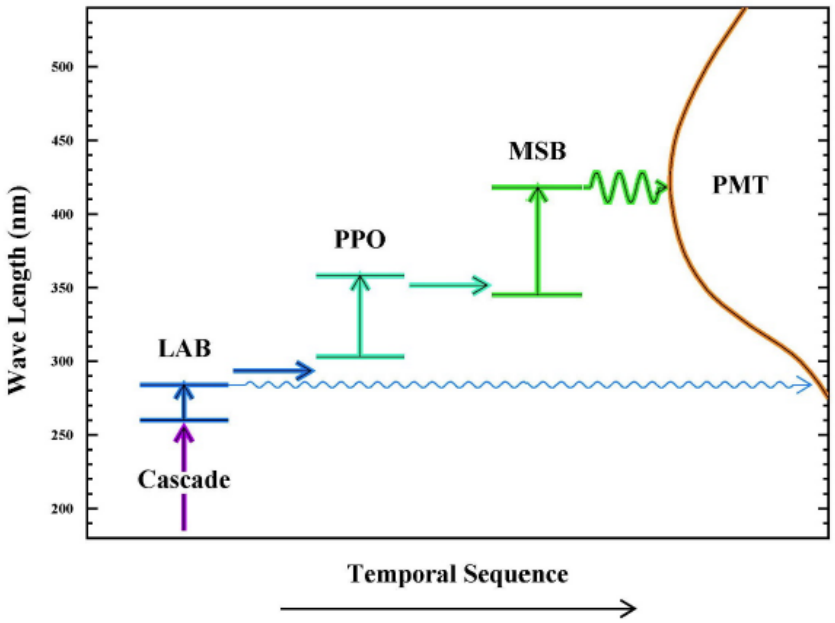


Figure 4.6: Redshift over time of energy transfers between scintillator components to bring emitted photons to the longer wavelengths where they may align with the PMT response curve. Figure from [97].

dation. Finally, the metal dopant's main purpose is to maximise the $0\nu\beta\beta$ event rate. Keeping such a heavy nucleus stably suspended presents several challenges that can be addressed by further complicating the scintillator cocktail. The final three additives, TeA, BD and DDA, are chosen to purify tellurium crystals, synthesize a molecular structure miscible with mineral oil, and neutralize the compound for longevity and stability.

Table 3.2 gives the current concentration of all the components of the SNO+ liquid scintillator. Figure 4.7 presents a timeline of all the experimental phases undergone by SNO+ as they are marked by the medium deployed within the AV.

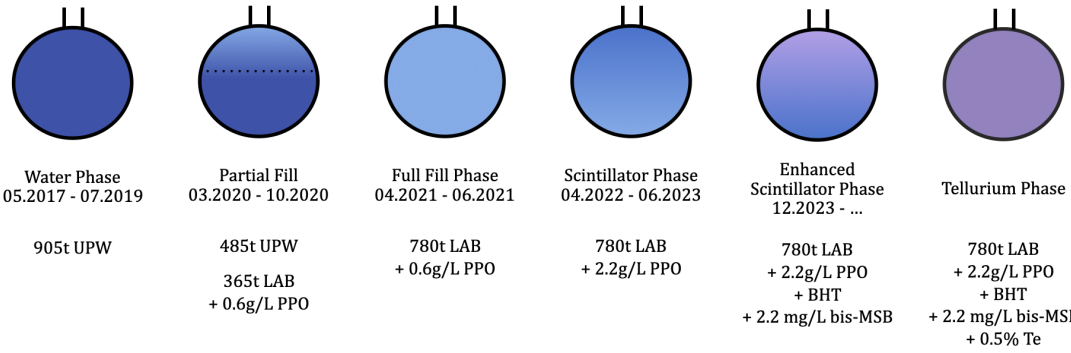


Figure 4.7: The SNO+ experimental phases are presented with their data-taking dates and the composition of the medium deployed within its volume. Time gaps between phases correspond to the fill periods.

4.2.1 LAB

Linear alkylbenzene offers light yields comparable to that of previously tried and tested scintillators such as Pseudocumene (PC) deployed in both KamLAND [196] and Borexino [82]. In addition to its compatibility with acrylic, it boasts a similar refractive index to that of acrylic, thus reducing interface effects. Unlike PC, LAB's Safety Data Sheet (SDS) caution list begins and ends with the risk of choking if swallowed or inhaled[k] [47]. This makes it an especially attractive solvent to be deployed in large quantities 2 km underground. As a mineral oil, it is also very receptive to familiar purification techniques which is the main gateway to achieving high radiopurity. Its Rayleigh scattering lengths average well over the diameter of the AV at > 420 nm. The absorption spectrum range is favoured and localised energy deposits from particle interactions mainly emit light below 400 nm. The molecular structure of LAB is depicted in figure 4.8.

LAB absorbs within the [230, 275] nm range and emits at 278 nm. Spectrophotometry allows the inspection of the absorption spectrum to monitor for purity. An

[k] The turn of phrase employed is far more chilling: "May be fatal if swallowed and enters airways.".

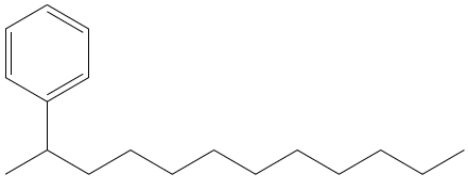


Figure 4.8: Chemical structure of LAB, though the alkyl tail can contain a chain of 10-13 (averaging 11.2) C. Purchased from CEPSA [47].

example of this is provided in figure 4.11 for a plant-distilled sample of LAB, and two control samples[1]. In 2018, a QA program was developed by the collaboration for the specific requirements and restrictions of SNO+. Table 4.1 summarises some of the quantities monitored and how they are tested. Every important scintillator plant operation is monitored through the characterisation of sampled scintillator. During batch addition preparation, QA serves to assess the efficiency of the solute incorporation into the batch volume stored in the mixing vessel V-501; this becomes the master solution. During AV recirculation activities, the performance of the plant in maintaining the optical clarity of the scintillator. This is applicable whether the aim be to distill the scintillator into pure LAB, or load master solution batches to the detector volume. In every case, Rn ingress is mitigated by engaging the stripping column C-300. QA samples are taken throughout to monitor plant malfunctions such as oxygen leaks or excessive humidity. The rest of this section describes standard QA metrics: nephelometry, density, and absorption. The remaining sections in this chapter go over the properties of the additives incorporated in the SNO+ scintillator with a particular focus on BHT and bis-MSB.

[1]The control LAB was drawn from an Surface Transfer Facility (STF) transfer and purified in the surface clean room SNOLAB facility with bench top equipment. The filtered LAB is drawn from a CEPSA shipment and filtered though not purified at Queen's.

	Optical Property	**Instrument**	**Monitored Parameter**
UG	Nephelometry	Hach TL2300 Turbiditimeter	suspended solid or gaseous contaminants
UG	Density	Anton Paar Density Meter DMA35	stability across samples, excessive humidity
UG	Absorption	Aquamate8000 UV-Vis spectrophotometer (1 cm cell)	constituent concentration, dissolved contaminants, oxygenation
AG	Absorption	Lambda800 UV-Vis spectrophotometer (10 cm cell)	constituent concentration, dissolved contaminants, oxygenation
AG	Emission	Fluorescence spectrophotometer	constituent concentration, dissolved contaminants, oxygenation
AG	Humidity	Karl-Fischer SO_2 titration	water content

Table 4.1: Summary table of available QA tests. UG and AG denote if instruments are located in the under or above ground chemistry laboratories.

Nephelometry assesses the cloudiness[m] of a fluid. Turbidity is caused by the presence of suspended insoluble particulate or a heterogenous mixture of the solution in different phases[n]. To measure this, an incident beam is shone through a cuvette of scintillator. Light is then transmitted, absorbed or scattered resulting in the proportional Nephelometric Turbidity Unit (NTU) reading. Pure, filtered and control LAB standards were measured and provide a metric as to the expected turbidity of an optically clear sample. Any sample undergoing QA must return a nephelometry reading within a range set by the standard: $[0.50;\ 0.65]\,\mathrm{NTU}$.

Density is the volumetric mass of a substance. It is dependant on molecular mass and arrangement as well as ambient temperature or pressure. Density, as a characteristic property of a molecule, is a good gauge for dissolved contaminants. For example, the density of pure LAB lies between $[0.8540,\ 0.8560]\,\mathrm{gcm}^{-3}$. An AV LAB sample drawn after PPO loading would read as high as $0.8800\,\mathrm{gcm}^{-3}$. Both of these values are the standardised equivalent at $20\,^{\circ}\mathrm{C}$. The measured density of the SNO+ liquid scintillator after addition of PPO to a $2.2\,\mathrm{g/L}$ concentration is reported in figure 4.9. Figure 4.5 shows the final absorption spectra of the SNO+ cocktail at this loading stage.

Absorption of a sample is measured using UV spectrophotometry. Derived from the same methodology is attenuation or extinction length, which is one of the most direct metrics of scintillator transparency that can be measured. It is highly volatile, being affected by molecular structure that may vary between production batches of the same raw material. Rigorous purification techniques aimed to get consistent attenuation lengths. UV-photospectrometry directs a photon beam from a halogen

[m] The technical, less illustrative, term is turbidity.
[n] The illustrative, less technical, term is bubbles.

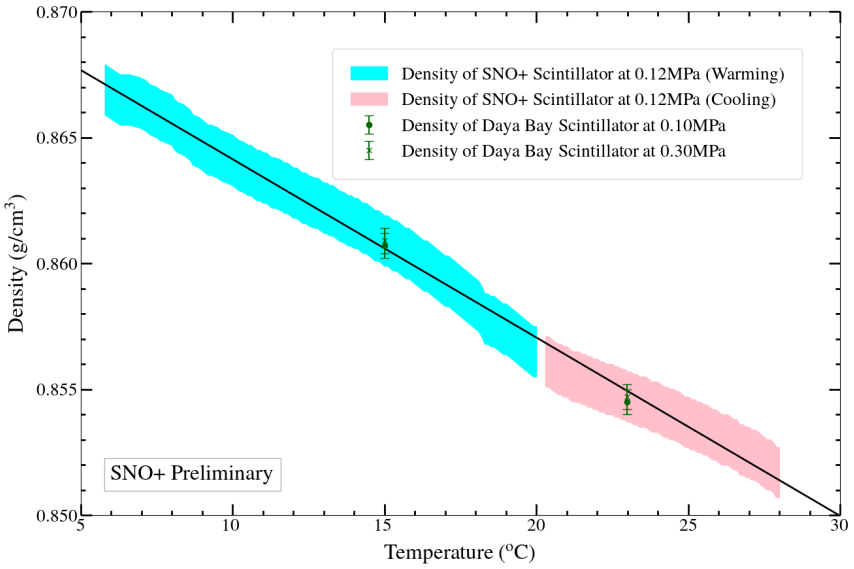


Figure 4.9: Density readings taken at 0.12 MPa ± 5% pressure every 0.1 ° C for a cooled (5.8 ° C) LAB sample as it warmed up to 20.0 ° C with uncertainty bands in blue. Density readings of a heated (28.0 ° C) were taken every 0.1 ° C until the LAB cooled to 20.3 ° C. Also reported are published values of LAB+PPO at specific temperature and pressure values. Figure from [182].

and deuterium[o] lamp of intensity I_0 through quartz cuvettes of 10, 5, 2 and 1 cm path lengths (x). Photons within this beam scatter, undergo absorption or transmission during their journey through the scintillator. The beam intensity upon exiting the cuvette $I(x)$ is taken to calculate the absorption. This is known as the Beer-Lambert law:

$$A(x) = \log_{10} \frac{I_0}{I(x)} \tag{4.2.1}$$

$$= \epsilon c x, \tag{4.2.2}$$

[o]Halogen emits within the [360, 2500] nm range, and deuterium between [190, 360] nm. They are paired to cover the range of interest [200, 800] nm. [20]

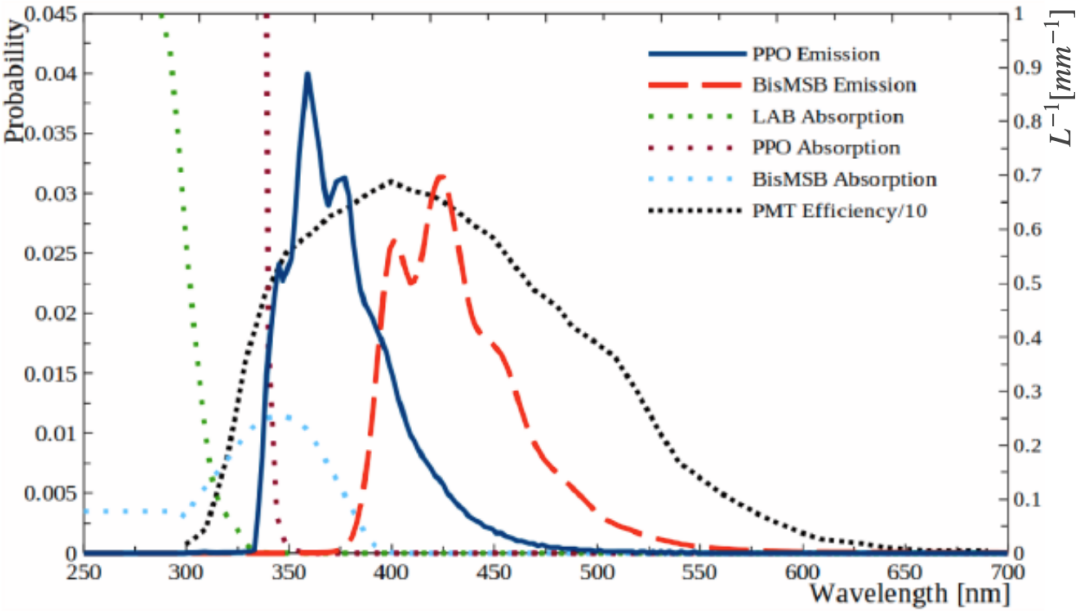


Figure 4.10: Absorption and emission spectra for LAB, PPO and bis-MSB as simulated by `RAT`. Superimposed is the PMT response. Figure adapted from [181].

where c is the concentration of the solute and ϵ is the extinction coefficient. Valid at low fluor concentrations, the Beer-Lambert law parametrises the linearity between absorbance and concentration through the proportionality constant ϵ. This is how calibration curves were created for the QA programs surrounding PPO and bis-MSB additions. Bench top standards were prepared with precisely weighed solutes and solvents. Their spectra were collected via a 1 cm cell to create a calibration curve from which any sample's concentration can be inferred by interpolation.

The Beer-Lambert law can also be written as

$$A(x) = e^{-x/\varepsilon}. \tag{4.2.3}$$

In this form, the attenuation length, ε, can be understood to be the distance it takes

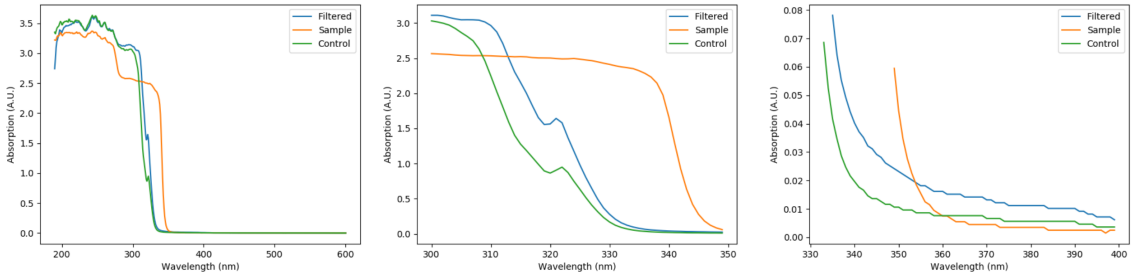
for the intensity to be reduced by a factor of $\frac{1}{e}$. Again, at longer wavelengths, Rayleigh scattering dominates over absorption and measured attenuation lengths in this range lose meaning.

As LAB presents attenuation lengths of ∼10 m, 10 cm cell spectrophotometry is sensitive to optical clarity and any impurities manifesting in the absorption spectrum. However, the 1 cm cell used in underground QA is a valid proxy and informs on general optical impurities of particular danger to SNO+, such as water or oxygen contamination. The latter implies the presence of a leak in the plant which exposes the scintillator to ambient underground laboratory air, rich in Rn, contamination sources discussed at length in chapter 3. A sample taken after mobilising the plant into running primary distillation and stripping after a 23 months hiatus is presented in figure 4.11. The difference in sensitivity a 1 cm and a 10 cm path length offer is noticeable in the difference in absorption range on the y axes. The longer path length can focus on the detail of the shape of the absorption spectrum more closely.

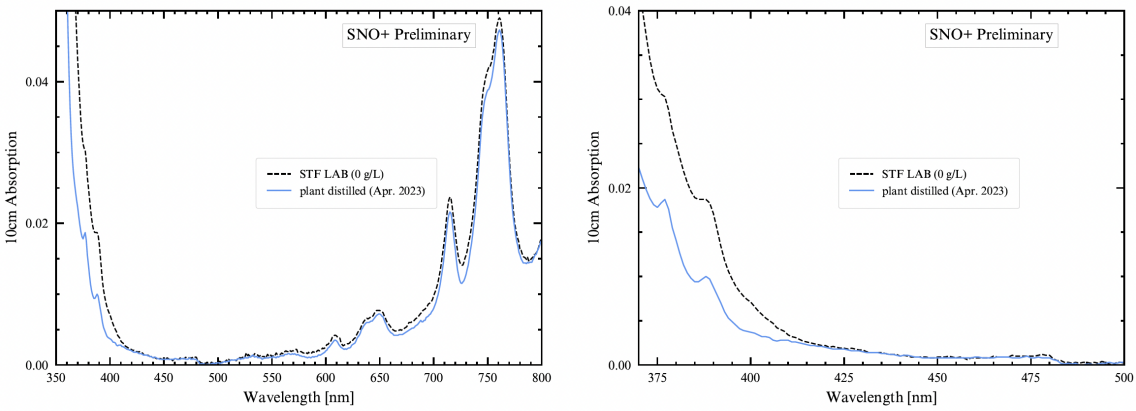
Karl-Fischer titration measures for water content. Humidity constraints on the AV scintillator must be strict due to the degradation in optical clarity and the instability water presents for certain (future) additives. Tests are usually run at the end of a recirculation period and the levels have thus far not surpassed 60 ppm, though they are on average an order of magnitude lower.

4.2.2 PPO

2,5-diphenyhloxazole, shown in figure 4.12, is chosen as the primary fluor. With its phenyl groups increasing the total available π orbitals, PPO is dissolved in LAB



(a)



(b)

Figure 4.11: Figure (a) is an example of the plots produced during plant operations in a 1 cm cuvette focusing on regions of interest. Figure (b) presents two pure LAB samples. The improvement of the plant distilled over the surface transfer obtained from CEPSA is an indication of the efficacy of the scintillator plant at improving the optical clarity of the scintillator.

and reduces the space between molecules which allows for more FRET. Predominantly, charged particles depositing energy excite an LAB molecule, which in turn non-radiatively[P] transfers excitation to one of the PPO rings. Photons fluoresce from the PPO excited states within the emission spectrum of PPO, which ranges from [340, 475] nm, with a peak at 365 nm. PPO absorbs until 303 nm. Since PPO emits below the threshold energy for absorption in LAB, self-absorption by the scintillator is avoided.

[P]Radiative transfer is allowed, though the chosen concentration suppresses this mechanism.

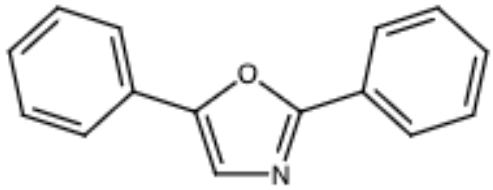


Figure 4.12: Chemical structure of PPO. Purchased from PerkinElmer [153].

As was evidenced in figure 4.5, PPO was added in a concentration that maximises improvements in light yield before reaching the plateau where batch deployments become logistically too costly for the relative diminishing return in quantum yield. The chosen nominal concentration, informed by R&D within the field, lies in a range where PPO self-absorption is less prevalent than non-radiative LAB to PPO transfer.

4.2.3 BHT

Butylated hydroxytoluene was added in a single batch to the detector for its antioxidant properties. As can be seen in 4.13, it presents a linear alkyl chain, its molecular structure further attracts oxygen and peroxyls, thus preventing oxidation degradation – or yellowing – a significant concern for a long lived transparent liquid scintillator experiment. Trapping free oxygen radicals stabilises the solution [188]. BHT has the additional benefit of being highly soluble in LAB[q] [173].

[q]Though it should have been highly soluble at room temperature, batch loading conditions always find a way to complicate things.

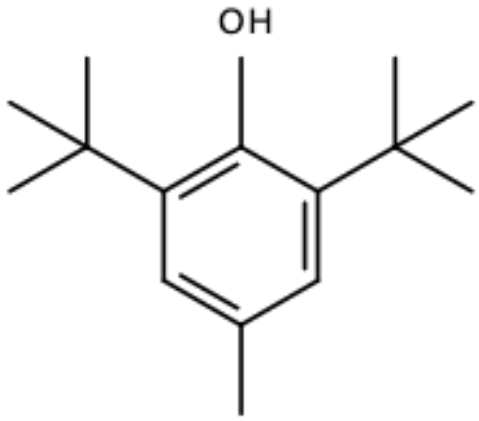


Figure 4.13: Chemical structure of BHT. Purchased from Sigma Aldrich [173].

However, BHT itself is non-scintillating, and adding it to the cocktail has a neutral effect on its light yield; the focus is on improving its long term optical clarity. Proof of BHT's crucial role in preventing degradation lies in studies done by the University of Ottawa [188], where samples collected from the SNO+ AV after its addition and subsequently stored at room temperature were compared to samples freshly taken from the AV consistently cooled to 13° C. Analysis showed that the concentration of BHT in the original sample had fallen over the months as BHT captured free radicals and prevented yellowing.

5.6 kg of BHT were added to the scintillator cocktail in June 2023 which, accounting for a total scintillator volume 780(+12) T of LAB at a density of 0.85 g/L results in a concentration of 5.4 mg/L. The uncertainty in the loss of active material during batch addition along with the lack of method to asses concentration once dissolved explains the decision to not quote BHT concentration in the scintillator cocktail.

4.2.4 Bis-MSB

1,4-bis(2-methylstyryl)-benzene, shown in figure 4.14, was chosen as the secondary fluor. This choice was motivated in part by its impressive quantum yield of 0.98 in cyclohexane [179], as well as for the boost in light yield it can provide in LAB doped with PPO. PPO emission can now be absorbed by bis-MSB for re-emission to occur within the shifted bis-MSB wavelength range. The emission spectrum is effectively pushed to 425 nm, while absorption peaks at 355 nm. From figure 4.10, it can be seen that this is beyond the absorption and re-emission regions of both LAB and PPO. Self-absorption is highly suppressed by widening the Stokes' shift, and the light yield is maximised and concentrated in the ideal optical response wavelength range of the detector's PMTs. This final phase of the cocktail, poised to be doped with tellurium, is dubbed the "enhanced scintillator" phase.

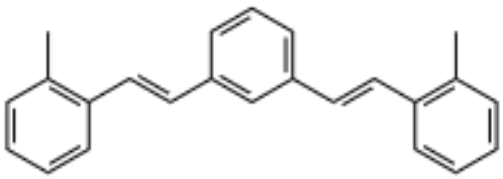


Figure 4.14: Chemical structure of bis-MSB. Purchased from Luxottica Exciton [131].

There are options to estimate the optimal loading concentration for fluors in liquid scintillator, such as relying on simulations or R&D from the astroparticle experimental

physics community. SNO+ decided on a target concentration of 5 mg/L. This was partly informed by the JUNO collaboration's R&D in Daya-Bay reported in figure 4.15, namely the different bis-MSB loading values for a PPO concentration of 2 g/L. It can be seen from the minimal increase in light yield between 1 and 4 mg/L that the critical concentration of bis-MSB is around 2 mg/L. It is hard to interpolate non-linear behaviour given that the known concentration of PPO is at 2.2 g/L, and figure 4.15 suggests a non-negligible gain in light yield between the 2 g/L PPO + 7 mg/L bis-MSB and the 2.5 g/L PPO + 7 mg/L bis-MSB. The optimal concentration of PPO and bis-MSB is highly dependent on the detector. The optical model implemented in `RAT` allows production of MC studies of the effect of different loading permutations to the scintillator properties. These studies were ultimately the basis for determining the target concentration.

The batch size was chosen to be 500 g for a projected 8-12[r] batches required to reach the target concentration and a total mass of 5 kg. In the SNOLAB surface clean room, a glove box was built for this project. It served the dual purpose of further reducing exposure to airborne particulates in the clean room, and reduce radioactive contamination, as well as posing a safety measure to limit the potential of spreading bis-MSB in the clean room itself. As such, 500 g of bis-MSB was mixed into 8 L of distilled LAB to form a slurry. Separated in two 4 L bottles, the slurry was then carried underground.

Referring back to figure 3.9, the preparation tank V-501 was filled with 500 L of LAB, bringing the expected concentration of the master solution to a round

[r]This estimate is based on the uncertainty in the losses of fluor mass associated with the scintillator plant operations necessary to adequately homogenise the master solution and deploy it to the AV volume. No batch loading has a 100% efficiency as plant operations introduce an experimental losses that cannot be preemptively calculated.

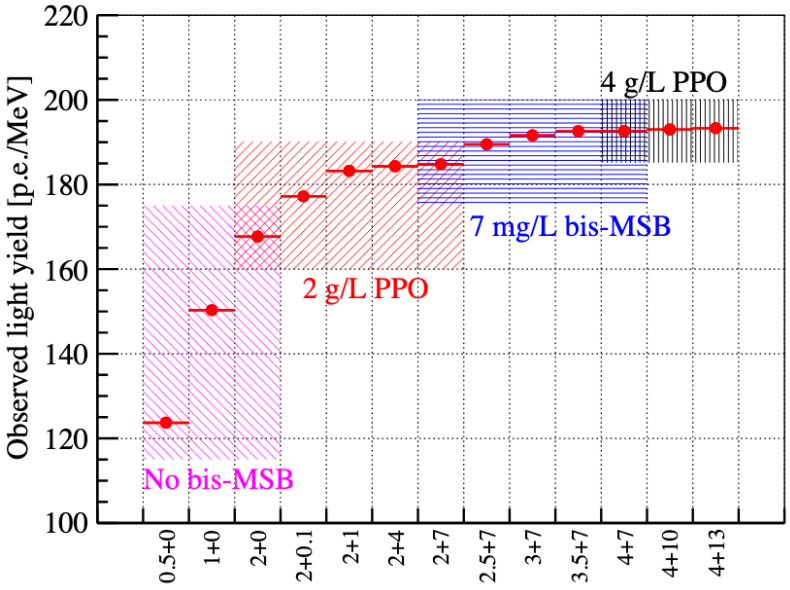


Figure 4.15: Measured observed light yield for various combinations of PPO and bis-MSB in LAB by the JUNO collaboration during the development of their liquid scintillator. Along the x-axis are PPO+Bis-MSB concentrations in g/L and mg/L respectively. Vertical error bars of statistical uncertainties are invisible at 0.2 %. Figure from [29].

1000 mg/L per batch. The mixing vessel V-501 was filled, for the first batch, with LAB distilled by the scintillator plant's primary distillation loop and stored in the 60 tonne tanks from figure 3.8. Subsequent batches used LAB drawn from the AV itself and stored in V-01 to fill V-501.

Each batch underwent the mixing process in V-501, kept at at least 40°C, with the agitator engaged, to increase the solubility of bis-MSB in LAB. The product was submitted to the N_2–UPW–filter loop via a series of nitrogen sparges through pump purges, and water extractions as explained in section 3.3.2.3. This mixing and heating process took up to seven days. The homogenisation of the master solution was tested by sampling it to calculate its concentration. As bis-MSB within these

high concentrations, near saturation[s], of the order of 1 g/L is prone to precipitate out of the LAB solution at ambient temperature, the sampling procedure involved pre-weighing a volume of ≈100 mL of distilled LAB into which a few milliliters of the master solution were immediately diluted directly upon sampling. Even so, the sample diluted by weight was further diluted by a 1:50 ratio with pure LAB in order to determine its concentration to bring it within the order of magnitude of 1 mg/L for which the methodology was developed.

The methodology to measure solute concentration is built on taking the absorption spectra of bench top samples of varying concentrations, in this case of $\mathcal{O}(1-2)$ mg/L. The absorption value at a certain wavelength is taken from each calibration sample in order to create a calibration curve. Concentration of an AV sample can then be interpolated from this curve. The calibration curve for bis-MSB had to be measured in a region free of PPO interference. As can be seen by referring back to figure 4.10, the calibration standard spectra were taken above 375 nm, where bis-MSB absorption is dominating and emission is minimal. Because the target concentrations of the master solution in the batch loading campaign were near saturation, dilutions with pure LAB were necessary to read concentrations. In a 1 cm path length, scattering and absorption on a solute molecule becomes too predominant for the method to maintain validity. The uncertainty of the Aquamate concentration method was evaluated to be at 15 %. This neglects uncertainties arising from the finicky dilution method itself

[s] A larger batch of 1.5 kg was first attempted, but the master solution with a target concentration of 1.5 mg/L never adequately homogenised and heavy material losses were incurred during the mixing process itself. Furthermore, the Polytetrafluoroethylene (PTFE) bottles were found to have been misshapen during their travel underground, thus presenting a risk of having leached chemicals into the slurry. Finally, this slurry had been prepared at the Laurentian University cleanroom which is less closely monitored for airborne particulate levels than the SNOLAB facility, and transported to SNOLAB, a process during which increase of radioactivity is likely. All these reasons led to 'batch 0' being sent to waste rather than deployed to the SNO+ AV.

as described above. Any systematic uncertainties introduced by the dilution method would arise from errors in reading volumes of solute to solvent. As all the reported concentration values were carried out by the same individual in an environment, and with equipment stable over the period, these systematic uncertainties were ignored. Concentration measurements of the master solution in table A.1 are reported with the implied dominating uncertainty of 15%.

Date of batch	Concentration [mg/L]	Turbidity [NTU]	Density [g/cm^3 at 20°C]	Humidity [ppm]	Light Yield
July 20th, 2023	(853) -	0.061	0.8572	6.9	30-55%
October 2nd, 2023	(907) -	0.062	0.8577	7.5	9%
October 12th, 2023	(826) 1.70	0.063	0.8559	7.5	3%
November 29th, 2023	(852) **2.25**	0.055	0.8570	14.2	1%

Table 4.2: Summary table of QA metrics for each bis-MSB loading batch. The concentrations of the master solution are reported in parenthesis. The light yield for the first batch is presented as the increase compared to the measured light yield of the scintillator doped only with PPO which was 11808±630 photons/MeV. The two values indicate the light yield increase with fiducial volume cuts of 3 m or 5 m. Subsequent light yields taken from [112, 113] show the increase compared to the previous batch.

Once the concentration of the master solution stabilised at a value approaching the target concentration of 1000 mg/L, it was passed through filters on its way to the preheated V-41 holding vessel. This was necessary to avoid the same issue of possible precipitation of the solute at this near-saturation concentration. From V-41, the master solution was mixed inline with the plant recirculating in closed loop with the gas stripping column. The batch was then added to the AV over a recirculation of a few tonnes once the optical clarity fulfilled the QA requirements for deployment[t].

[t]The recirculation times in closed loop as well as to the AV and volumes are reported for each batch loading in the appendix A

Table A.1 only lists four batches with a final AV concentration of 2.2 mg/L. There was to attempt to reach the original target concentration of 5 mg/L as the analysis of the data recorded by the detector during this period showed diminishing returns in light yield gains after the first batch addition. ^{210}Po and ^{214}Bi `nHits` distributions were used to tune the optics model and infer light yield measurements. MC peaks are made to agree with the data by modifying the concentration of the bis-MSB, the re-emission probability, Birks' constant, and the scintillation decay time, for example [166, 168, 167]. These studies found that the first batch addition showed a good agreement between the predicted and observed light yield increase, mostly from the Stoke's shift, for the bis-MSB mass deployed in the scintillator. However, the second batch and third batches showed a low increase in `nHits` peak distributions, and therefore no gain in light yield as expected from higher bis-MSB loading. Furthermore, the increase in ^{214}Bi events was concentrated around the base of the neck. It was speculated that differences in the temperature of the volume added from the scintillator plan in comparison to the bulk of the AV caused a batch to "get stuck" within the neck. The AV volume was recirculated in different modes to facilitate homogenization. The effect of this between batches 3 and 4 can be seen in figure 4.16. The concentrations of bis-MSB within the AV which were too low (< 1 mg/L) to be reported by the Aquamate method before the third batch fell in line with the expected values per batch addition. The light yield increased marginally, but continued to plateau with the fourth batch. With the gains to the optical model being evaluated in real time with the data collected during bis-MSB deployment, it was decided that 2.2 mg/L would be sufficient for the purposes of the SNO+ programme.

Figure 4.17 presents the 10 cm absorption spectra of the AV scintillator sampled

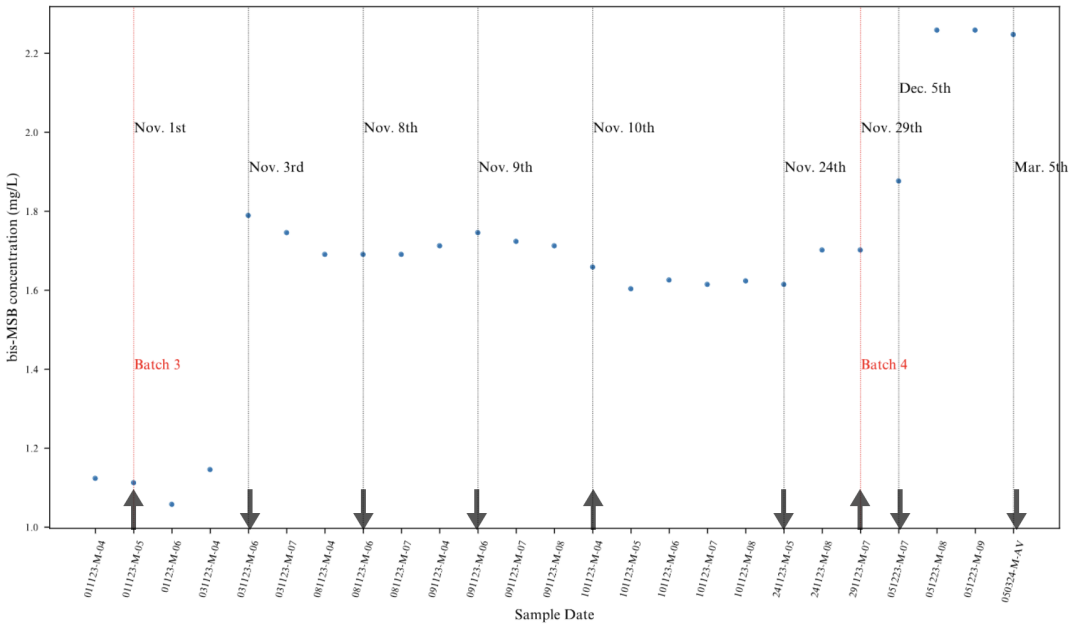


Figure 4.16: AV concentrations of bis-MSB were recorded for every sample taken during recirculation after loading the third batch. The recirculation mode is indicated by an arrow pointing upwards for the bottom to top configuration and pointing downwards for top to bottom. Recirculation shifts were included to speed up the mixing process within the active volume which happens naturally overtime through convection.

after each batch deployment alongside the spectra representative of the optical quality of the scintillator cocktail at each of its stages: unloaded, 2.2 g/L PPO loaded, 2.2 g/L PPO+BHT loaded and 2.2 g/L PPO + BHT + 2.2 mg/L bis-MSB loaded.

Most obvious is the upwards shift in absorption during the second batch which was deployed in two phases. What may have caused this neither worsened or even remained, as the absorption spectra for the third and fourth batches return to the expected absorption levels. The master solution had been mixed in-line in its entirety during the first batch deployment. The second deployment took place ten days later

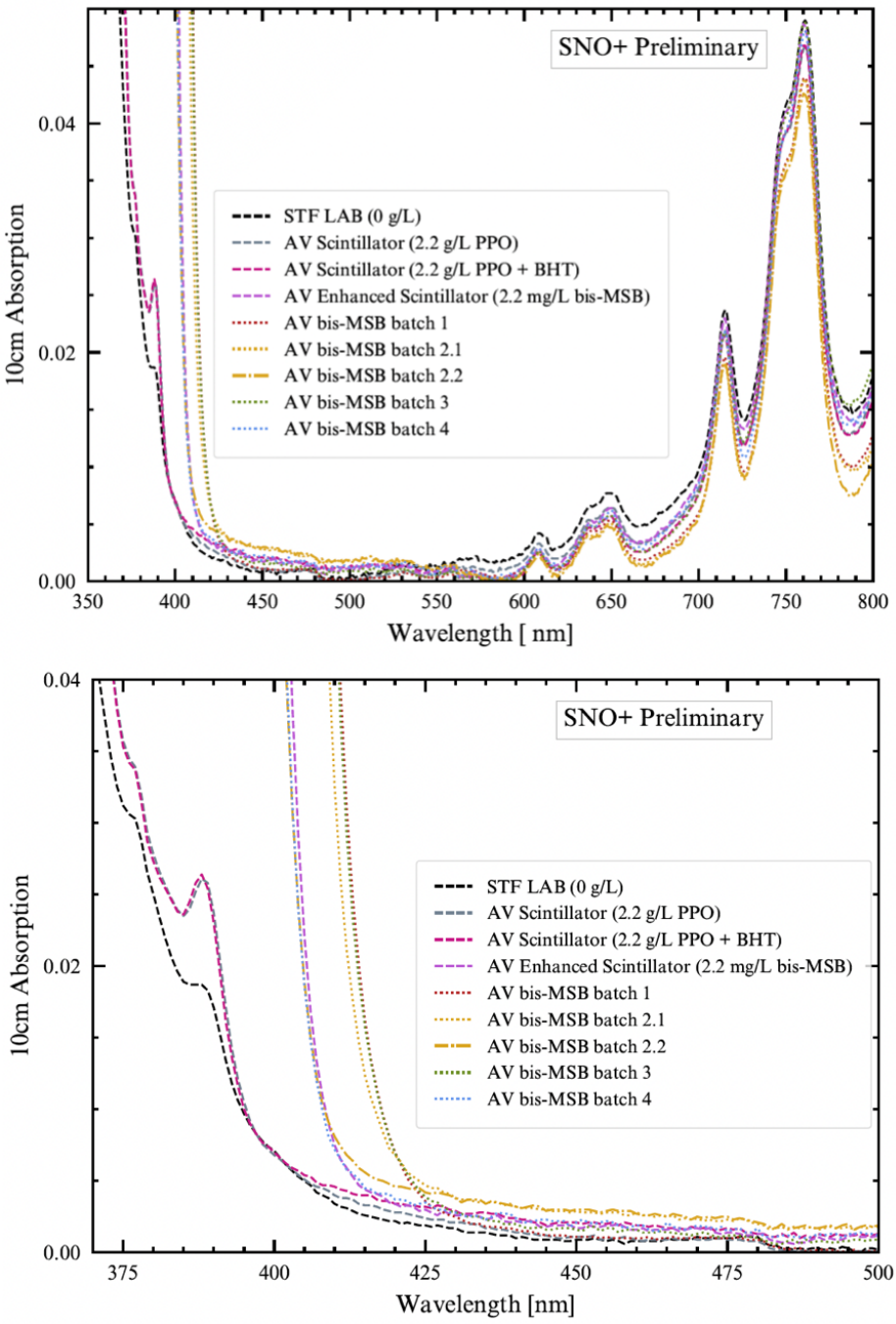


Figure 4.17: AV absorption spectra of following every bis-MSB batch addition (dotted) alongside AV spectra for every scintillator stage (dashed). As a legacy, current samples are plotted alongside the Enhanced Scintillator spectrum for comparison purposes. Baseline subtraction is applied at the minimal value of each spectrum.

following the usual QA approval process in CLR. It is apparent that optical degradation occurred in the material that the 1 cm measurements upon which standard QA approval lies were oblivious to. Figure 4.17 also reflects the unexpected light yield observations reported at that time and reported in table A.1. Figure 4.17 also shows that the concentration measured may have continued to increase with batch additions as expected, but its translation to the absorbance wavelength appears minimal [u]. These observations in the 10 cm absorption spectra and in the light yield measurements are coincidental. There is lacking evidence to suggest causality or even any relation between the two. The optical degradation could be pinned to scattering, and the light yield failing to mirror the increase in concentration could be an indication of a MC modeling failure. Likewise, while comparison to JUNO's modeling and tests is informative, it is in no way directly applicable to SNO+. Finally, as has been discussed in the chapter 3, the bis-MSB loading program suffered from a fatal flaw in the switch from shipped N_2 dewars to SNOLAB-supplied N_2. This introduced contamination levels of Ar so unacceptable [190] that a full turnover of the AV volume to be stripped through the scintillator plant is planned before the tellurium loading operations.

In situ measurement of the attenuation length of the SNO+ liquid scintillator at its two loading stages is presented in figure 4.18. Referring back to equation 4.1.9, $A(x)$ takes into account both absorption and scattering processes. In a similar manner, it is the sum of contributions of individual scintillator components. Equation 4.2.3 indicates the logarithmic relation between absorption and path length. In practice, it is customary to submit a sample to absorption $A(x)$ spectrophotometry over several

[u] It is important to note that the dotted lines in 4.17 are taken as batch deployment closes, at which point the AV volume has not remotely been turned over. The shift between batches 2.1 and 2.2 is simply due to convection currents during the 10 day interval effectively mixing the AV.

path lengths (x), recursively reduce them to a single centimeter path length following

$$\frac{(A(x_i) - A(x_j))}{x_i - x_j}, \tag{4.2.4}$$

for as many x_i, x_j options available[v]. The Lambda-800 spectrophotometer used at the SNOLAB surface clean room laboratory has 10, 5, 2 and 1 cm quartz cuvettes. All the subtracted equivalent "1 cm" spectra are then summed and averaged before being converted to attenuation length.

$$L_{\text{attenuation}} = \frac{1}{A(x_{\text{1cm avg}})\ln(10)}. \tag{4.2.5}$$

Baseline subtraction is applied to each individual spectra before subtraction and averaging as well as to the resulting averaged spectra before the conversion to extinction length. While this subtraction method should effectively reduce systematic uncertainties from air-quartz surface reflections or defects, other factors that may vary between measurements should be considered. This could be as simple as the unstable focusing of the light beam even with a warmed up lamp, for example. Light is fickle and [84] cites uncertainties up to 31% for such measurements. Figure 4.18 presents absorption lengths from cells remeasured in March 2024. Subfigure (d) specifically sheds light on the impact of baseline subtraction methods on the final attenuation length measurement. Three data manipulation options were compared. The baseline was chosen to be either the minimum value of each individual spectrum, the absorption value at a fixed wavelength of 600 nm, or the average absorption taken over the flattest portion of the spectrum which was found to be around [560, 590] nm for most measurements.

[v] The case where $i = j$ is equivalent to dividing the absorption by the path length.

Baseline subtraction was applied either before, after or before and after spectral subtraction. This led to drawing the conclusion that baseline subtraction has an effect on final attenuation lengths only when applied after spectral subtraction and averaging. The shaded regions in subfigure (d) is taken to be the standard deviation of the average of the methods listed in parentheses for each attenuation length spectrum.

The light absorption spectrum of the cocktail at 2.2 g/L PPO + 2.2 mg/L bis-MSB was extracted for each component following the dilution method in cyclohexane. Cyclohexane, optically and chemically inert, was the solvent used in order to extract the characteristic emission spectrum of LAB and both fluors. The AV Scintillator at 2 g/L PPO and the Enhanced AV Scintillator were used as solutes. Dilutions of 1:50, 1:100, 1:1000, 1:2500, 1:10,000 and 1:125,000 LS to cyclohexane were performed for each standard. Absorption over a 10 cm path length was measured for each of these. The spectra were then superimposed and spliced to recreate the full absorption spectrum of the cocktail. This dilution method brings the otherwise unattainable shorter wavelengths where LAB absorbs into range. The result of these dilutions for the SNO+ enhanced liquid scintillator is compared to the JUNO/Daya-Bay measurement in figure 4.19.

The `RAT` framework [168] uses *ex situ* measurements of absorption length, scintillation decay times, light yield and the Birks' constant, and the *in situ* spectra taken during QA operations, in particular the attenuation lengths from 4.18 and full absorption spectra from 4.19, in conjunction with published values for optical properties such as the re-emission probability for the cocktail's components to develop an optical model unique to SNO+. Figure 4.20 shows the optical model in use by `RAT` for analyses during the enhanced scintillator phase.

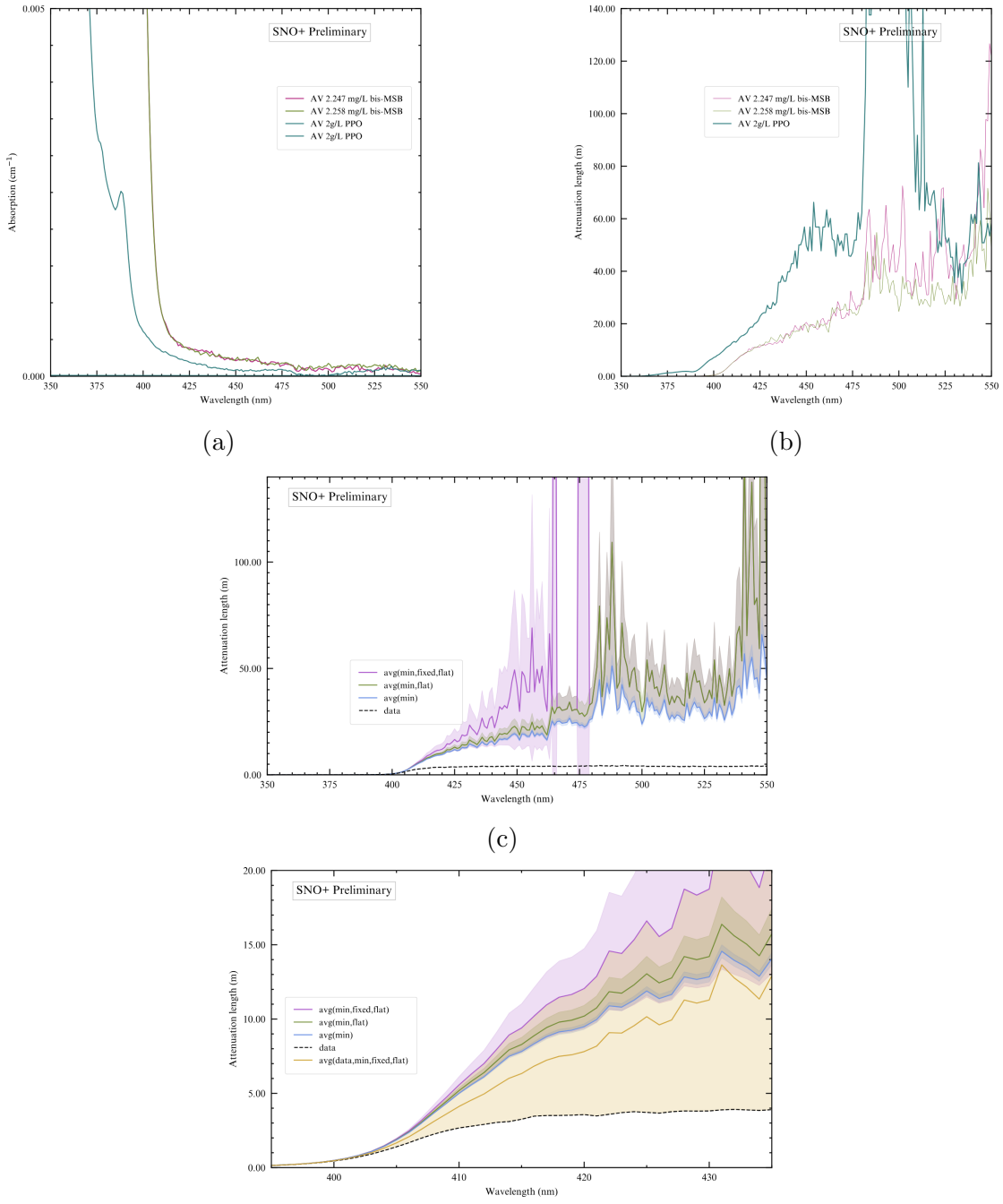
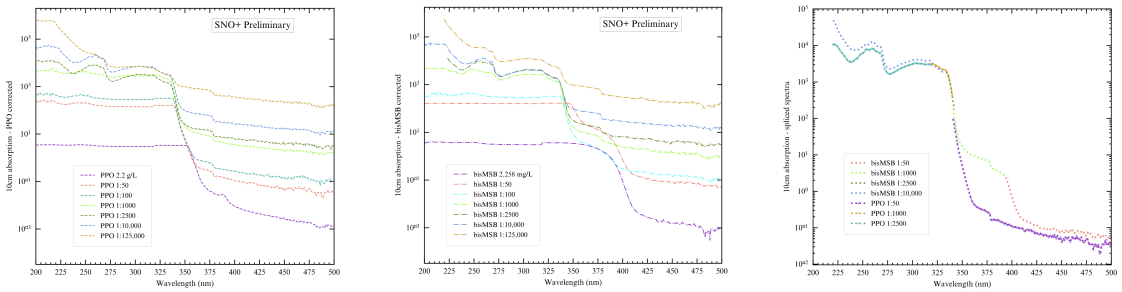
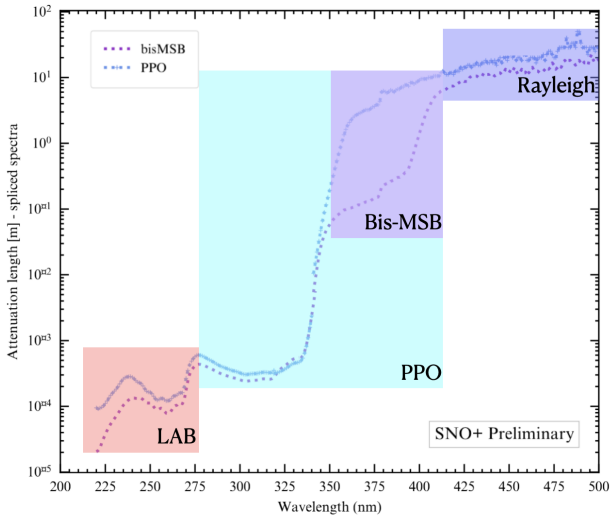


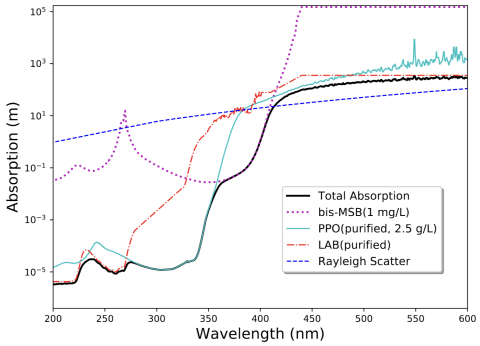
Figure 4.18: Plotted are the absorption (a) and attenuation lengths (b) for the 2.2 g/L PPO and 2.2 g/L PPO + BHT + 2.2 mg/L bis-MSB (samples from December 2023 and March 2024) SNO+ scintillator cocktails. The error bands in (c) and (d) represent the contribution of the choice of baseline subtraction method to the uncertainties. The raw spectrum without data manipulation is in black. All samples use an air-no cuvette instrumental baseline.



(a) (b) (c)



(d)



(e)

Figure 4.19: Absorption spectra with applied baseline subtraction for cyclohexane dilutions of the AV scintillator from April 2022 (2.2 g/L PPO) (a) and from December 2023 (2.2 g/L PPO + 2.2 mg/L bis-MSB) (b). Selected dilutions are amalgamated into a reconstructed "spliced" spectra in (c). The attenuation length is calculated from (c) in (d) and compared to the JUNO/Daya-Bay measurement from 2020 in (e) which is taken from [199].

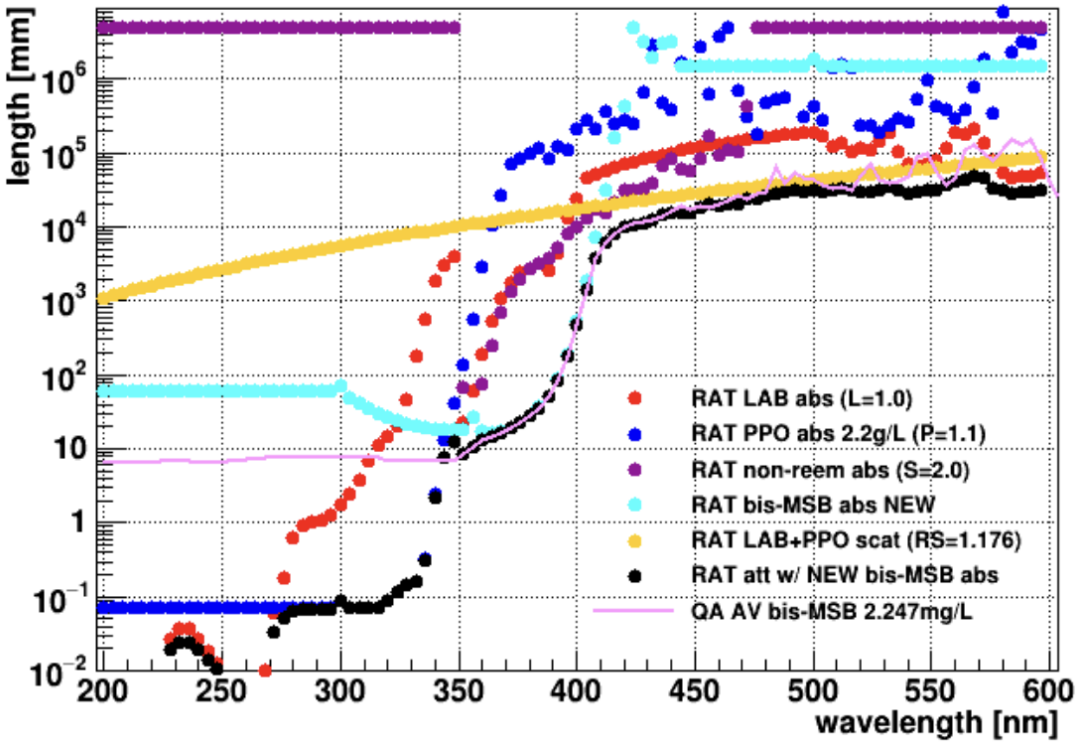


Figure 4.20: The RAT optical model for the enhanced scintillator phase LAB + 2.2 g/L PPO + BHT + 2.2 mg/L bis-MSB. Figure from [168].

4.2.5 Te&co

Metal loading unlocks new energy transfer paths between the metal compound and the solvent or fluors. These compete with the energy transfer mechanisms between the solvent and the reagents that were added to place the emission spectrum at the ideal PMT quantum efficiency. These new energy transfer paths are usually non-radiative, resulting in significant fluorescence loss (quenching) of the scintillator.

As a neutrino detector following a $0\nu\beta\beta$ decay detection programme, it would be beneficial to load ^{130}Te until saturation. Unfortunately, quenching effects grow with concentration. Loss of energy resolution is fatal to discerning the $0\nu\beta\beta$ decay signal from the overwhelming $2\nu\beta\beta$ decay continuum and all other background sources

discussed in chapter 2. This is the main factor in determining the loading ceiling.

Referring back to section 3.3.2.4, it was alluded to that telluric acid and 1,2-butanediol were reactants essential to stable TeBD synthesis. TeBD is the form in which tellurium will be introduced to the enhanced liquid scintillator cocktail. TeA is the molecule formed by a Te atom bonded with six hydroxyl groups. In this form, Te becomes a water-based solution readily rinsed and purified, ridding it as much as possible of residual cosmogenically activated radioactivity. BD is an organic diol with two hydroxyl groups linked to a short carbon chain which allows it to dissolve easily in the organic solvent once the exposed hydroxyl groups is condensed.

The resulting polymer, TeBD, does not present absorption lines within the sensitive emission wavelength range of LAB+PPO+bis-MSB. As a transparent fluid at these concentrations, it only minimally affects the scattering and absorption properties of the solution.

Extensive stability testing has been conducted in the R&D for tellurium deployment. Samples are still being monitored for different loading scenarios. Susceptible to hydrolisis upon exposure to water, TeBD is at risk of precipitating out of a humid liquid scintillator.

N,N-dimethyldodecylamine provides a solution to both concerns. A long carbon chain tertiary amine, DDA is compatible with LAB, has been shown to improve the light yield by 15-20% [115], and has kept TeBD samples stable across torture tests[w] by binding with a TeBD hydroxyl group and halting further polymerisation potentially leading to recrystallisation and precipitation.

[w]Stability, if no other obvious defects make themselves known by visual inspection, should be assessed through a light yield measurement though spectrophotometry is often preferred for its ease.

In this chapter, the light production mechanisms of Cherenkov radiation and scintillation were explored. The development and characterisation of the SNO+ liquid scintillator was reviewed over the course of its various loading phases. Its scintillation properties were reported. Now remains to be seen if what was lost can be reclaimed; can directional Cherenkov radiation pierce through isotropic scintillation light?

Chapter 5

Directionality in Liquid Scintillator

What If?

-R. Munroe

What sets apart the ^{8}B solar neutrino elastic scattering background from others crowding the $0\nu\beta\beta$ ROI is its source. The direction of a solar event is always in line with the Sun's position at the time of the event. Even 2 km underground, a solar neutrino interaction within a Cherenkov detector can tell the time of day[a]. This property was sacrificed in the large scale liquid scintillator experiment that is SNO+ in order to gain the energy resolution and light yield necessary to $0\nu\beta\beta$ decay searches. This directional signature is a unique discriminant for identifying ^{8}B ν_e at low energies for solar neutrino oscillation analyses or in the $0\nu\beta\beta$ ROI. Working against prompt, luminous scintillation, characteristics that make this medium so desirable, via timing resolution and analysis methods is a challenge for those wanting to have their cake and eat it too.

SNO+ and Borexino can be considered sister experiments in many ways. As was previously mentioned, the scintillator plant was not only inspired by Borexino's

[a] A modern day, overly engineered Sun dial.

success in the extremely high radiopurity of its scintillator, but designed by the same company. The liquid scintillator cocktail itself is a PC base doped with 1.5 g/L of PPO; in contrast to SNO+'s LAB base with PPO as the sole fluor during the solar and backgrounds characterization phase of the experiment. If Borexino could extract directionality, why not SNO+?

5.1 Directionality

Directionality is the property by which a point-like source produces an interaction vertex by colliding with a target particle and producing electrons and photons at kinematic energies high enough for them to be detected at an angle in line with the emission direction. While the Sun is an obvious candidate for producing a directional signal, deployed calibration sources are another such example. This intrinsic anisotropy tied to the neutrino source's nature distinguishes solar neutrinos from internal backgrounds.

Equation 4.1.2 was the smoking gun in the experimental difference between scintillation and Cherenkov light. If an event's direction is known, Cherenkov light stands to be detected at an angle dependent on the travel medium from the site of the particle interaction. In SNO+'s scintillator phase $\cos(\theta_\gamma) \approx 0.67$ for an ultrarelativistic ($v/c \approx 1$) particle traveling through LAB having a refractive index of 1.48 [61] at the relevant wavelength range of [200, 800] nm and $\sim 15°$ C.

5.2 Correlated Integrated Directionality

The Borexino collaboration developed [9] and applied [28] the Correlated and Integrated Directionality (CID) method to sub-MeV solar event measurements. As a

statistical method, CID correlates and integrates the PMT hit patterns to the position of the Sun over a large number of events. Solar events are taken to correspond to the hit PMTs in the correct $\cos\theta_{\odot}$[b] value range. By contrast, interactions independent of a directional source, such as radioactive backgrounds, will present a flat distribution across $\cos\theta_{\odot}$.

It then becomes apparent that flat distributions of $\cos\theta_{\odot}$ are incurred both by late scintillation light which is inherently isotropic as well as by directional early Cherenkov light from background events uncorrelated to the Sun. Keeping in mind that liquid scintillator experiments were designed to increase energy resolution by maximising the light yield of the smallest energy interaction, scintillation for any given event will overwhelm any Cherenkov radiation. Addition of fluors vastly reduces the emission time for the scintillation light, rendering timing separation between the two light mechanism more challenging to distinguish. Borexino additionally highlights the case in which a solar event occurring near the inner vessel walls may register early PMT hits associated with scintillation light in the case where Cherenkov photons produced alongside the forward scattering recoil electron must travel the length of the vessel. The fraction of $\cos\theta_{\gamma} = \cos\theta_{\odot}$ events is related to the expected flux of solar interactions with respect to all other detected processes[c], the proportion of Cherenkov to scintillation light and the position of the solar interaction in the case where $path(\gamma_{Cherenkov})/v(\gamma_{Cherenkov}) > time(\gamma_{Scintillation})$. Borexino's MC simulations report a vanishingly small 0.4% Cherenkov to scintillation hits in their target [0.85, 1.29] MeV energy range.

[b] Cherenkov cones of solar events will be henceforth distinguished from Cherenkov cones produced by all other events uncorrelated to the sun by denoting the first as $\cos\theta_{\odot}$ and the second as $\cos\theta_{\gamma}$.

[c] Radioactive background decays, inverse β decays from reactor neutrinos, neutron capture, $2\nu\beta\beta$ and even $0\nu\beta\beta$.

Borexino also makes the point that the $\cos\theta_{\odot}$ distribution offers no insight on distinguishing between the solar neutrino sources. It is solely designed as a statistical tool to extract solar signal at lower energies where other traditional classifiers fail. Boxerino combined all three phases of data collection[d] culminating in a whopping 3104.2 days of livetime[e].

The Borexino collaboration MC PDFs were simulated event by event using a ^{7}Be solar neutrino signal and ^{210}Bi radioactive background. The default MC generation method uniformly fills the volume with events of either ^{7}Be or ^{210}Bi following their energy spectrum. A set of 200 MC events were simulated within a 30 cm sphere of a data event occurring at a set Sun position. This MC set then correctly simulates the patterns of PMTs across the detector by accounting for position reconstruction of events and the PMT coverage at the time of the event. This set is generated once assuming the event is a ^{7}Be solar neutrino or ^{210}Bi background event. This method provides a more comprehensive MC set that fully represents the detector response to solar events around the clock.

Each event is mapped through its hit PMTs which are then sorted in time with respect to the reconstructed start time of the event and taking into account their time-of-flight. This is the same metric SNO+ refers to as time residuals. This is a selection criteria more robust to time reconstruction fluctuations and inconsistencies between data and MC than an absolute time cut. Careful calibration made use of the ^{214}Po peak to fine tune the position and energy reconstruction algorithms, and

[d] Phase I (May 2007–May 2010) [28], Phase II (December 2011–May 2016) [141], [10] and Phase III (July 2016–October 2021) [184]

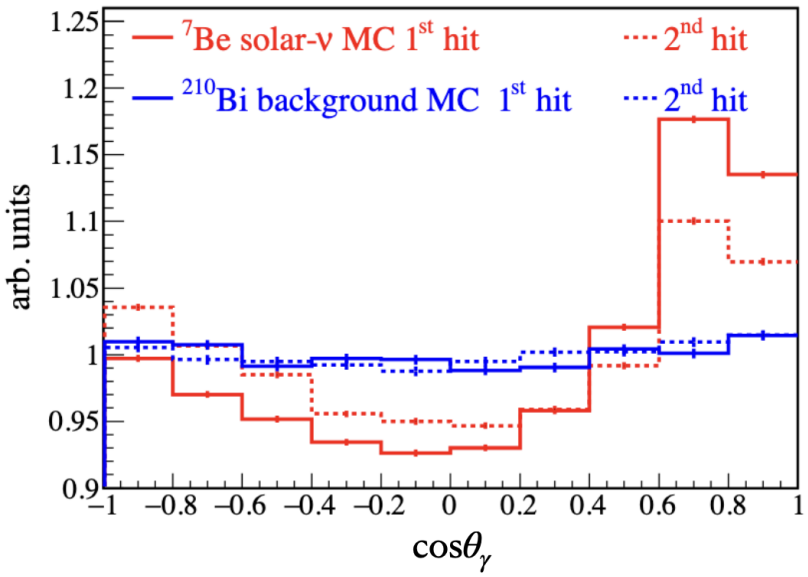
[e] SNO+'s PPO phase has 163.6 days of livetime, placing Borexino's statistical advantage at 1800% over SNO+. This is a misleading metric as volume, coverage, light yield or radiopurity, which all play a role, are not accounted for in this comparison; an omission that doesn't necessarily bode well for SNO+'s hopes.

determined the effective refractive index of Borexino's PC's to be (1.6631±0.0005) for data and (1.6531±0.0003) for MC. Systematic uncertainties were mitigated through a screening process of PMT response time accuracy. A χ^2 fit between simulated signal and background angular distributions indicated that the first two hits carried the most directional information for Borexino in the energy region of interest as can be seen in figure 5.1.

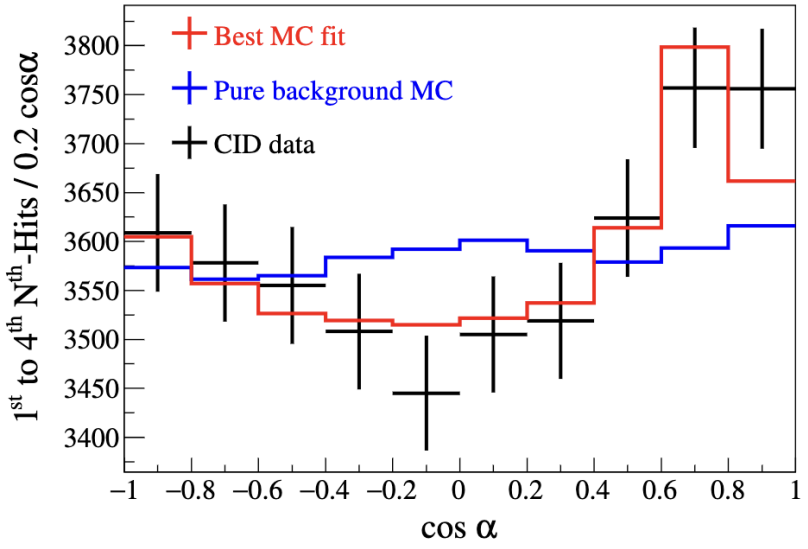
In [28], Borexino reports a measurement of CNO neutrinos through a CID analysis strategy where a χ^2 fit on the $\cos\theta_\gamma$ distribution of the first two PMT hits of all events occurring during the three phases worth of data using directional (^{7}Be) and background (^{210}Bi) MC PDFs. Recalling the flux rates of these low energy processes from figure 2.4, the sheer amount of events collected may well near a singular Large Hadron Collider (LHC) proton-proton beam collision.

Despite prior success during the partial fill phase with event-by-event directionality techniques, SNO+ has yet to successfully extract directional signal in the loaded scintillator phase despite a few internal attempts. This thesis builds on the statistical approach developed by the Borexino collaboration. Its methodology hinges on timing resolution to distinguish the first few hit PMTs of each triggered event as well as the efficiency of the position reconstruction from which the event direction can be inferred. Event direction refers to the direction of the photon from the event to the PMT it hit. Therefore, each event has as many directions as PMTs that detected it. Event direction is entirely dependent on the accuracy of the event vertex position reconstruction algorithm as it is taken to be

$$\vec{event} = (x, y, z)_{\text{PMT}} - (x, y, z)_{\text{event}}. \tag{5.2.1}$$



(a)



(b)

Figure 5.1: (a) Angular distribution for MC events of ^{7}Be (red) and ^{210}Bi (blue) showing a clear peak in the solar signal. The first hit (solid line) carries more directional information than the second hit (dotted line). Histograms are normalized to have the same area. (b) The CID data (black), best fit results (red) and the background MC (blue) scaled to the same total number of events for the combined analysis of data from Phases I, II and III of Borexino. Figures from [9].

The variable of interest, $\cos\theta_\odot$ is defined as the cosine of the angle between the Sun and event direction as is illustrated in figure 5.2.

$$\cos\theta_\odot = -(\vec{sun} \cdot \vec{event}). \tag{5.2.2}$$

Because the Sun direction is classically taken pointing towards the Sun, equation 5.2.2 takes the inverse of the scalar product.

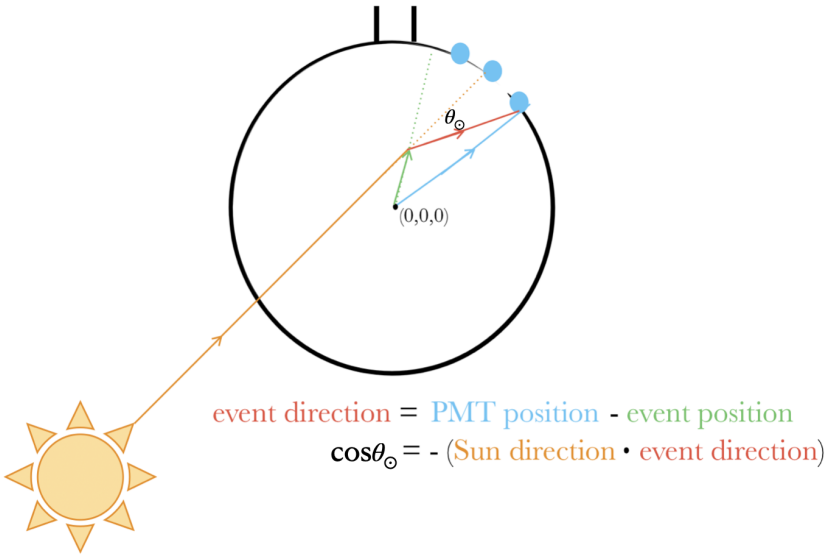


Figure 5.2: Schematic of a solar event interaction in the detector. PMTs are represented along the walls of the AV instead of embedded in the PSUP and therefore refraction at the acrylic interface is omitted from this depiction for simplicity.

The following section describes preliminary studies on the three variables CID is built upon: Sun direction, event position and the hit PMT time.

5.3 Designing the methodology

While the SNO+ collaboration produces official MC sets for common background and signal processes, this analysis additionally required sister sets with only Cherenkov or scintillation processes simulated. The final simulation files also include physics processes such as lower level optical effects at the boundaries. From a computational standpoint, these official MC sets mimic `RAT nTuples` and process simulations to the point of reconstructing position and energy. For this analysis however, the upstream hit PMT times are crucial. Weightier MC sets were simulated with all the calibrated PMT information factoring in the reflections, scattering, absorption and re-emission a photon may incur during its path to a PMT. These sets were produced in the run-by-run regime reckoning with detector status and configuration throughout the period to keep track of channels online and open to registering solar signal. The period chosen corresponds to the full fill PPO phase and only runs passing the criteria for Gold run selection are generated. The Gold criteria requires the detector state to be operating with all crates at high voltage, have at least 80% PMT coverage, at least 80% panel coverage, for OWL PMTs to be on, and runs to be of a minimum of 30 minutes in duration. This corresponds to a physics livetime of 163.6 days. MC sets for signal (^{8}B, ^{7}Be, *pep* and *pp* ν_e) and background (internal ^{208}Tl) were produced with Cherenkov and scintillation light processes toggled in turn and simultaneously. The Cherenkov mechanism was tuned in `Geant4` for SNO+ with calibration data from the ^{16}N and Laserball deployments during the water phase. Their emission intensity is modeled after the Frank-Tamm formula 4.1.4. Their wavelength dependent timing spectrum was never measured *in situ* during the liquid scintillator phase. Table 5.1 summarizes MC sets produced for this analysis.

Source	Cherenkov	Scintillation	Cherenkov + Scintillation
^{8}B ν_e	✓	✓	✓
^{208}Tl	✓	✓	✓
^{7}Be ν_e	-	-	✓
pep ν_e	-	-	✓
pp ν_e	-	-	✓

Table 5.1: Summary table of MC sets produced. Cherenkov and scintillation processes were isolated in dedicated sets in order to investigate signature variables.

5.3.1 Sun Direction

The detector's internal clock is set to January 1st, 2010 Coordinated Universal Time (UTC). The method to calculate the sun direction with respect to the static detector is inherited from SNO though time zero t_0 for astronomical constants was pushed up from 1975 to 2010. The Sun Utility [99] described in this section fetches the universal clock's time to the nanosecond level precision to infer the exact time of year and day. With the Sun's orbit having been studied and parameterised for centuries, its direction can be calculated extremely precisely in detector coordinates. The number of days since t_0 allow a direct calculation of the obliquity of the ecliptic (ϵ) which refers to the projection of the Earth's axis 23° tilt on the orbital plane,

$$\epsilon(t_{\text{days}}) = \text{tilt} - \Delta\text{tilt} * t_{\text{days}}, \tag{5.3.1}$$

which is gradually decreasing over time due to gravitational perturbations to the Earth's orbit. The argument of perihelion (ω) which is the point along a planet's

orbit closest to the Sun is given by

$$\omega(t_{\text{days}}) = \omega_0 + \Delta\omega * t_{\text{days}}. \tag{5.3.2}$$

The eccentricity (e) of the Earth's orbit is

$$e(t_{\text{days}}) = e_0 + \Delta e * t_{\text{days}}. \tag{5.3.3}$$

The mean anomaly

$$a_m = a_0 + \Delta a * t_{\text{days}} \tag{5.3.4}$$

represents the Sun's position along its orbit assuming circularity which is corrected via a second order solution to Kepler's equation to the eccentric anomaly for an elliptic by

$$a_e = a_m + e\sin(a_e) \tag{5.3.5}$$

$$\approx a_m + e\sin(a_m)(1 + e\cos(a_m)). \tag{5.3.6}$$

The true anomaly is the angle between the position of Earth along its orbit and its perihelion and is computed with the projection of x and y on the elliptical orbit such that

$$a_{\text{true}} = \tan^{-1}\big(\frac{\sqrt{1-e^2}\sin(a_e)}{\cos(a_e) - e}\big). \tag{5.3.7}$$

The Sun direction vector is then corrected with the argument of perihilion and calculated from its position on its orbit with respect to the detector's position (0,0,0).

$$s\vec{u}n = (\sin(a_{\text{true}} + \omega)\cos(\epsilon)\hat{x}, \sin(a_{\text{true}} + \omega)\sin(\epsilon)\hat{y}, \cos(a_{\text{true}} + \omega)\hat{z}) \tag{5.3.8}$$

Finally, the precise time of day is needed to account for the Earth's rotation about its axis. The spin angle between $[0, 4\pi]$ is applied to the latitude and longitude of the detector and transposed on the vector to give the final sun direction at any time of day. Thankfully, this was worked out for SNO and is now packaged as a convenient callable utility accessible in the `RAT` framework.

No uncertainties are associated with the Sun direction vector for this analysis.

5.3.2 Timing

Referring back to equation 3.8.1, time residuals take into account the registered PMT hit time, the reconstructed event time and the time of flight of the photons. `RAT` offers two calculators for this purpose. The slightly antiquated `LightPathCalculator` was opted for because it allows user definitions of the light path. In this case, no approximations were employed and simulated photons were made to travel through scintillator and cavity water including optical effects such as refraction or reflection upon crossing the AV threshold until reaching the PSUP PMTs. Correctly reconstructed event vertices yield timing profiles sharply peaked after the event trigger time with a late tail representing other delayed scintillation processes such as re-emission discussed in the previous chapter. Figures 5.3 and 5.4 show time residual and event or PMT hit time distributions for the ^{8}B MC sets simulated with Cherenkov and scintillation light toggled independently.

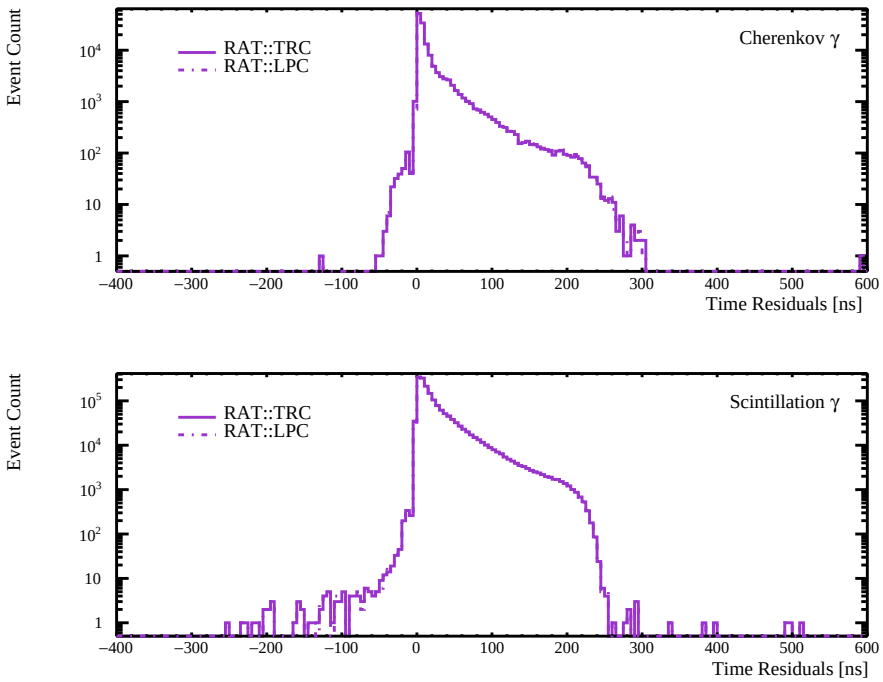


Figure 5.3: Time residuals distributions of signal MC for all hit PMTs in every triggered event. Differences between the `RAT::TimeResidualCalculator` and the manual calculation using `RAT::LightPathCalculator` are minimal.

Figure 5.4 provides a visual understanding of the value of time residuals in the endeavor of ordering early PMT hits per event. Figure 5.5 illustrates the effect of event interaction vertices reconstructing near the AV wall. The first 5 PMT hits per triggered event and their respective time residual value are reported. It can be seen that the earliest hit registers at unphysically early time residuals compared to the subsequent ones when the whole FV is considered, an effect that is dampened by imposing a 2 m radius fiducial volume to select events reconstructing near the center of the vessel.

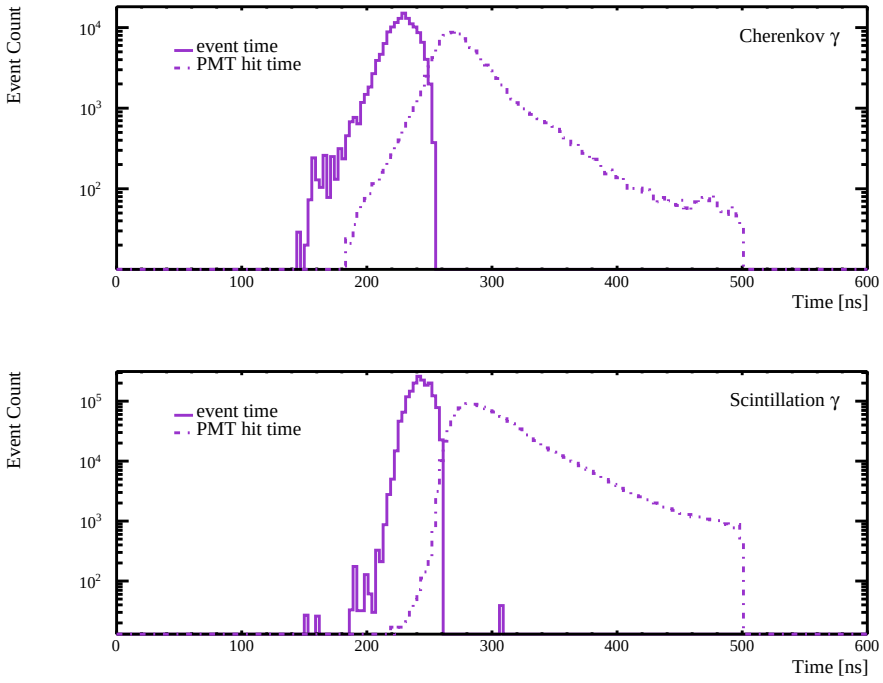
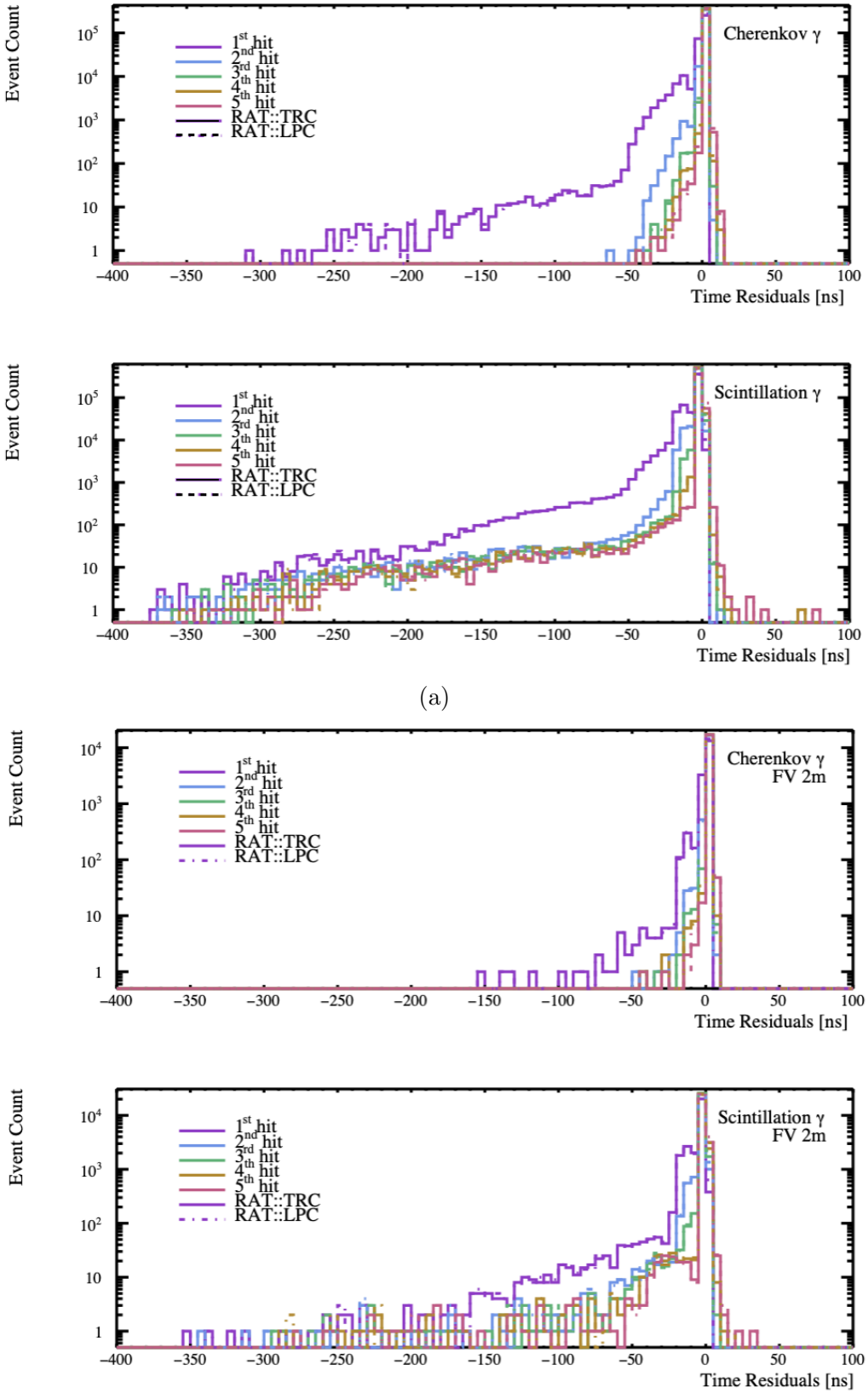


Figure 5.4: Timing profiles of all hit PMTs (dotted line) and the reconstructed timing distribution of their corresponding event vertex (solid line).

5.3.3 Position Reconstruction

What careful timing calibration of the PMTs response time and understanding of the optical properties of the scintillator lead to is event vertex reconstruction. `RAT`'s reconstruction algorithms and fitters are all iterations of varying accuracy of the `PositionTimeLikelihood` method. Nanosecond precision time residual PDFs of point-like electrons of 3 and 6 MeV are generated at every point in the AV in the run-by-run regime accounting for detector state. Each event registers many PMT hit times. Knowledge of their position on the PSUP in conjunction with scintillator propagation effective velocity leads to inferring the time of flight assuming a straight travel path from the vertex energy deposition [147]. Any four hit PMTs provide an



(a)

(b)

Figure 5.5: Five first hit PMTs for every simulated ^{8}B MC event with Cherenkov or

equation system sufficient to solve for the vertex origin via

$$|\vec{\mathrm{x}_{\mathrm{PMT}}} - \vec{\mathrm{x}_{\mathrm{event}}}| = v_{\mathrm{eff}}(t_{\mathrm{PMT}} - t_{\mathrm{event}}) \tag{5.3.9}$$

The profile of the time residual distribution for each event is then compared and fitted to the PDFs following a likelihood minimisation algorithm. It converges on the best fit position and the inner AV coordinates for which that PDF was produced are assigned to the event. `MultiPDF` was designed as an improvement to mitigate the effect of poor position reconstruction near the walls of the AV due to optical effects at the boundary [148]. Fiducial volume cuts have the added benefit of reducing the occurrence of external backgrounds.

The position reconstruction algorithms were recoordinated for the full fill PPO phase with an improved optical model for effective velocities and the `MultiPDF` algorithm [149].

MC simulations offer a handle on position reconstruction biases. The `TruthEvent` branch can be compared to its fitter reconstructed counterpart one to one for every variable. $\mathrm{Cos}\theta_{\odot}$ angular distributions can be made with both and the effect of systematic misreconstructions observed in figure 5.6 for Cherenkov or scinitllation only light propagation mechanisms of the ^{8}B ν_e solar signal. Of note is the "upturn" at $\cos\theta_{\odot} = -1$ that was not aforementioned though it is noticeable in Borexino's results in figure 5.1. Its persistence which cannot be ignored throughout the distributions presented in this chapter suggest this must be an explainable optical or physical effect. The fact the bias's height relative to the signal peak is lessened, though not eliminated, by using the `True` position points towards it being the relics of an optical effect. This upturn is most pronounced in early light as the region flattens gradually

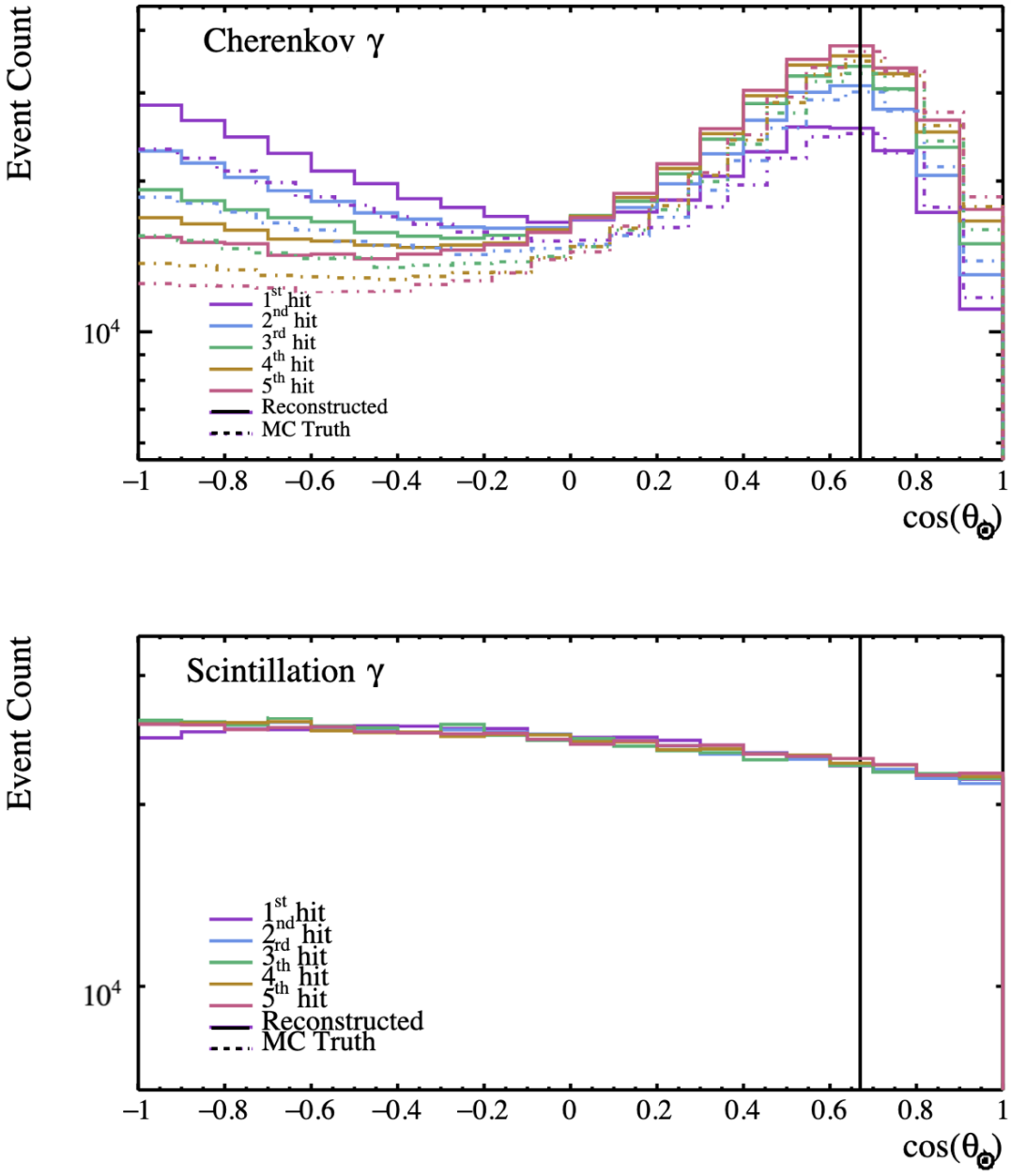


Figure 5.6: Five first hit PMTs for every simulated ^{8}B MC event with Cherenkov or scintillation processes enabled; full detector volume considered. The angular distribution of every individual hit from 1 through 5 is reported using the `Truth` (dotted line) and fitter positions (solid line). A solid vertical black line is drawn at $\cos\theta_\odot = 0.67$.

with later hits. The signal peak is better centered around the nominal $\cos\theta_{\odot} = 0.67$ value. Interestingly, reconstruction bias, which was shown to be most prevalent in Cherenkov only sets in figure 5.7, is not sufficient to explain the backwards peak as it is also present in the scintillation only set.

`ScintFitter` and `MultiPDF`'s performance accuracy's strong radial dependence in conjunction with the heightened probability of scintillation light hitting PMTs before Cherenkov photons for directional events interacting near the AV wall they entered from, strengthens the argument of applying a fiducial volume cut to the method. The group velocity in a medium is dependent on its refractive index such that

$$v(\lambda) = \frac{c}{n(\lambda)}\left(1 - \frac{\lambda}{n(\lambda)}\frac{dn(\lambda)}{d\lambda}\right)^{-1}. \tag{5.3.10}$$

As has been assumed in the calculation of $\cos\theta_{\odot}$, the refractive index in the [200, 800] nm range is dominated by the LAB with PPO having no measurable influence [197]. As usual, assuming a straight path L with minimal scattering, the transit time t_{transit} can be taken to be

$$t_{\text{transit}} = \frac{n(\lambda)L}{c}. \tag{5.3.11}$$

The emission time is instantaneous for Cherenkov light. The mechanism of scintillation, as explored in chapter 4, results in an emission time spectrum affected by added fluors. However, the rise time is of the order of sub-nanoseconds, with the prompt decay occurring within 2-3 ns [46]. For a refractive index of 1.49 in scintillator and 1.33 in UPW, the time residual profile of a photon in UPW during the 2 m separating the AV and PSUP as the shortest distance for the opposite Sun direction lies between

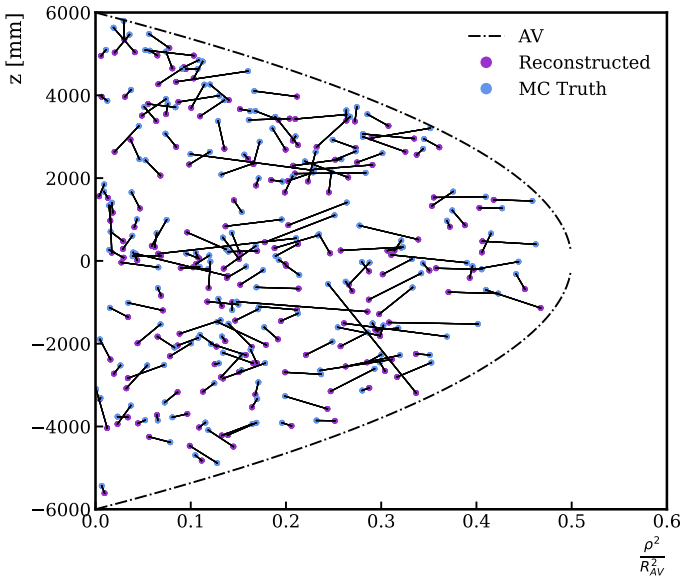
[0.3, 1.5] ns. The Cherenkov photon emitted in the direction of the Sun and having to traverse 12 m of scintillator and 2 m of water should then register a time residual distribution as early as 0 ns and no later than 2 ns. While a scintillation photon travelling 12+2 m would present a time residual profile distinguishable from Cherenkov radiation with a travel time of about 86 ns, it becomes apparent that events occurring near the AV wall may produce scintillation photons having to travel short enough distance for their hit PMT times to be confused with that of the directional ones on the opposite end of the detector.

Imposing a fiducial volume cut of 5 m therefore serves the purpose of removing external backgrounds near the AV walls as well as reducing the effect of radial bias in position reconstruction.

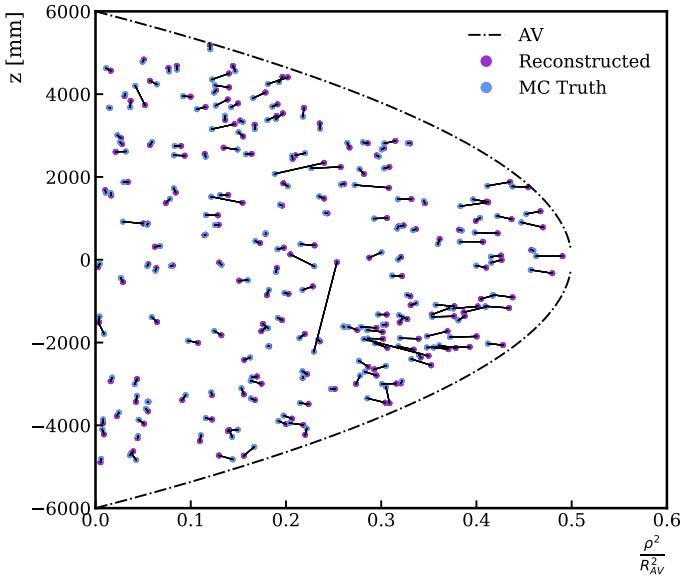
Figure 5.7 illustrates `Truth` and fitted vertex positions for a subset of the Cherenkov and scintillation signal MC sets. The position as given by the `Truth` and `ScintFitter` reconstructed vertex are presented as a pair joined by a line for every event within a projection of the AV. These pair are further apart for Cherenkov only light as it is more prone to poor position reconstruction due to its lower luminosity.

5.3.4 Energy Reconstruction

Energy reconstruction, that is the mapping of number of hit PMTs to an energy scale, also presents a radial dependence. Event interactions near the AV walls are likelier to be detected by close PMTs and more likely to receive multiple photoelectrons when hit. This effect is apparent at high energy values where the linear mapping between `nHits` and energy starts to register misalignment. A multiphoton correction



(a)



(b)

Figure 5.7: `Truth` and fitted vertex positions for a few events within the Cherenkov (a) and scintillation (b) ^{8}B MC sets.

factor H for multiple `nHits` (photoelectrons) per PMT is built into `ScintFitter` as

$$H = -\sum_{i=1}^{S} N^i_{\text{PMT}} \log\left(1 - \frac{N^i_{\text{hits}}}{N^i_{\text{PMT}}}\right) \tag{5.3.12}$$

in which the detector is segmented into S regions of PMTs with equivalent solid angles with respect to the simulated event position. The ratio of hits PMTs N_{hits} to PMTs in S N_{PMTs} partially corrects for non linearity and radial dependence. It also takes into account the randomness of offline PMTs throughout data taking periods, meaning that an interaction's number of triggered PMTs is affected by the distribution of offline PMTs particularly in the case where they are concentrated in a particular S region. Much like position reconstruction, the data is compared to PDFs from 2.2 MeV events from tagged ^{214}Bi decays at points throughout the AV. Figure 5.8 shows energy and `nHits` distributions alongside the correction algorithm results for the ^{8}B ν_e and ^{208}Tl MC sets. [72]

By definition, `nHits` are the number of hit PMTs registered during a triggered event window. As a raw variable encoded by the detector hardware, it undergoes basic data cleaning protocols including filtering out information from uncalibrated PMTs. The remaining `nHits` are referred to as cleaned, and are passed on to the detector state correction utility. This energy variable is that obtained by the reconstruction algorithm using the cleaned `nHits`.

To improve the resolution by accounting for the effect of offline channels on energy reconstruction, the equivalent variables of `nHits` and energy are corrected by applying the detector state correction to these values. The detector state correction tool calculates a scaling factor dependent on the channel status of a given run. The utility accepts event position as well as the number of channels and average channel

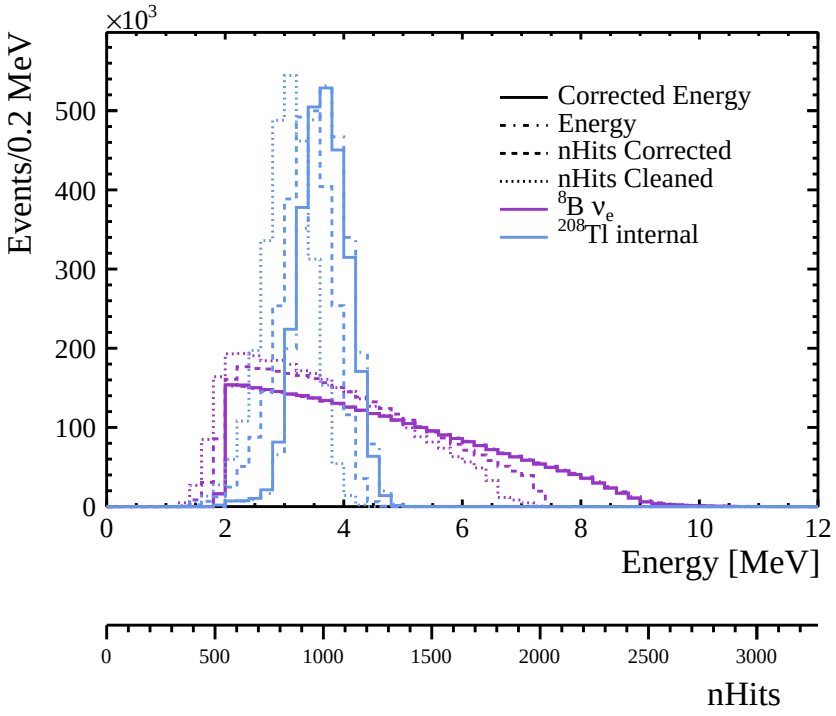


Figure 5.8: Mapping between corrected energy (solid line), energy (dash dotted line), corrected `nHits` (dashed line) and cleaned `nHits` (dotted line) for ^{8}B ν_e (violet) and ^{208}Tl (blue) MC sets. In the PPO phase, 1 MeV corresponds to 273 `nHits`.

efficiency as arguments. The event position is relevant in that the correction depends on the proximity of the event relative to clusters of unused channels. It takes into account the distance to the hit PMTs and the angle of incidence of the incoming photons. If they are not specified, the scaling factor is calculated relative to default values taken at the first run of the full PPO fill period. In this analysis, the event position is passed as an argument which prompts the utility to perform the correction relative to the perfect detector state. [121]

Beyond the radial and PMT coverage dependence, other factors affect the accuracy of the reconstruction algorithm. While these can and should be mitigated by

regular and careful calibration campaigns, they must be absorbed into systematic uncertainties. The angular response of the PMT concentrators as well as their physical dulling over time has not been monitored since the ^{16}N and Laserball directional calibrations for the water phase. Boundary effects such as absorption by the AV acrylic, heightened refraction and reflection for photons produced near the AV walls with more acute incidence angles require heavy MC simulation and *in situ* calibration.

$\cos\theta_{\odot}$ is not energy dependent, this analysis will calculate the angular distribution of events across the full [2, 14] MeV energy spectrum, as well as use energy for event identification during background tagging.

5.3.5 Building the Probability Density Functions

This analysis is conducted on physics data collected over the full LAB + 2.2 g/L PPO period. Run selection criteria were for the Gold standard. All crates were required to be online with a mininum of channels live for all crates online as maximal detector coverage is required for directionality studies. The Gold list for the full fill scintillator phase between April 22$^{\text{nd}}$, 2022 and March 10$^{\text{th}}$, 2023[f] amounts to 163 days, 15 hours, 33 minutes and 12 seconds of physics livetime. The 20 days accumulated during April and May 2022 were sacrificed as the detector cooled down from recirculation following PPO top up operations and ingressed Rn daughters decayed away. ^{212,214}BiPo levels fell back within acceptable radiopurity levels by June 2022.

As a statistical rather than event-by-event angled analysis, no physical selection cuts beyond data cleanliness checks are applied in the initial MC study. Prompt light, as defined by a time residual window, from any event without any attempt at

[f]Though loading and preparation for the enhanced scintillator phase only began in June of that year a rather igniting incident brought the detector into a forced shutdown and halted operations for a while.

particle identification is considered. Data quality requisites are valid fit parameters; `ScintFitter` must have converged on a valid vertex position, timing and energy for the triggered event. For MC, retriggers are handled by the `MCPE noise` flag that ensures unique photoelectron counts per PMT. In data, retriggers are eliminated by disregarding any triggered events past the initial one having launched the 400 ns event time window. Corrections to `nHits` and energy branches are applied before imposing energy cuts focused on data cleaning, which include a muon veto and energy > 2 MeV. Figure 5.9 shows the simulated solar fluxes of the ^{7}Be, *pep* and *pp* processes. While their flux is high, the rate of backgrounds in SNO+ dominates in this region. An additional consideration is the smearing effect of kinematics at lower energies on the $\cos\theta_{\odot}$ directional peak. While this low energy cut at 2 MeV implies sacrificing solar signal from ^{7}Be, *pep* and *pp*, it has the added benefit of eliminating a significant portion of low energy background events.

Final MC PDFs were chosen to be the ^{8}B solar neutrino signal and the ^{208}Tl internal background. These were produced to match the expected flux and production rate for the livetime of the PPO phase, as well as the detector configuration during this data collection period. These will constitute the PDFs used to create the model.

5.3.6 Modeling the Fit

With MC PDFs produced run-by-run alongside data processed for the PPO loaded scintillator phase with matching selection cuts, a model must be produced from the background and signal MC processes to be fit to the $\cos\theta_{\odot}$ distribution in data. Broadly, the model is to be constructed with an array of parameters consisting of

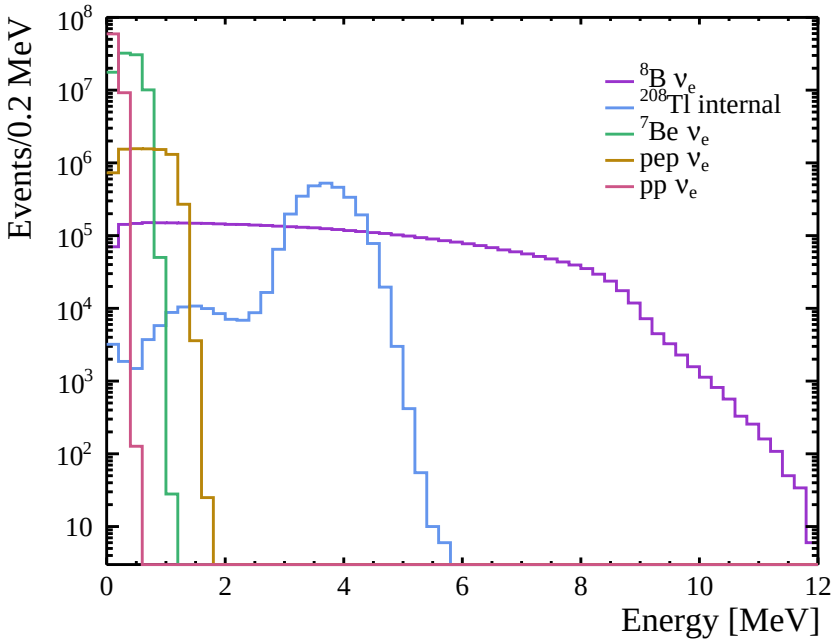


Figure 5.9: Energy distributions for the MC simulation sets of four solar neutrino channels and the ^{208}Tl background.

physics observables as well as shape altering factors absorbing the systematic uncertainties of the fit.

The final fitting strategy is twofold. Instead of a simultaneous two dimensional fit over energy and $\cos\theta_{\odot}$, a simple LL fit is performed over the energy distributions of ^{8}B and ^{208}Tl MC sets to determine three fitting regions with varying signal ratio purity.

$$\mathcal{L} = \sum_{i} (N_{\text{data}}(x_i) \log(f_{\text{model}}(x_i))). \tag{5.3.13}$$

Here, i = signal, background, and so the model is simply

$$f_{\text{model}} = \frac{N_{\text{signal}}}{N_{\text{signal}} + N_{\text{background}}} * \text{PDF}_{\text{signal}} + \frac{N_{\text{background}}}{N_{\text{signal}} + N_{\text{background}}} * \text{PDF}_{\text{background}}. \tag{5.3.14}$$

The only constraint applied on the model is for $N_{\text{signal}} + N_{\text{background}} = N_{\text{data}}$. The LL in this extended formalism is constrained to

$$\mathcal{L} = \sum_{\text{data}} \log(f_{\text{model}}(x_i)) - \log_{\text{Poisson}}(N_{\text{data}}, N_{\text{observed}}) \tag{5.3.15}$$

indicating that the uncertainty on the fit coefficients is Poissonian as the last term is referred to as the Poisson penalty[g].

Two sets of cuts based on signal efficiency and background rejection are inferred from the LL fit results. Referring back to figure 5.8 for the energy distributions of the ^{8}B and ^{208}Tl MC sets, the ^{208}Tl peak was excluded following a Log-Likelihood Ratio (LLR) of 0.7 or 0.9 based on maximising signal efficiency and background rejection while avoiding false positives and negatives[h]. The LLR of a variable x, which would refer to energy or $\cos\theta_{\odot}$ in this analysis, is often written as

$$LLR(x) = \frac{\text{PDF}_{\text{signal}}(x)}{\text{PDF}_{\text{signal}}(x) + \text{PDF}_{\text{background}}(x)} \tag{5.3.16}$$

LLR values of 0.7 and 0.9 indicate highly signal dominated regions, and correspond to excluding the [2.8, 4.6] or [2.6, 4.8] MeV regions respectively. Alternatively, as was

[g] A perfect fit, the maximum LL solution, would land at the constraint $N_{\text{signal}} + N_{\text{background}} = N_{\text{data}}$.

[h] Statistically, false positives are background events identified as signal, and false negatives are signal events classified as background.

done in the 2D fit, the $\cos\theta_\odot$ model can be fit over low, peak and high energy regions, a nomenclature that is defined in table 5.2.

LLR value	**lowE** [MeV]	**peak** [MeV]	**highE** [MeV]
0.7	2.0-2.8	2.8-4.6	4.6-12.0
0.9	2.0-2.6	2.6-4.8	4.8-12.0

Table 5.2: Low (lowE), ^{208}Tl peak (peak) and high (highE) energy regions as determined by the LLR obtained from an extended LL fit over the energy distributions of ^{8}B and ^{208}Tl MC sets with toy data generated as 30, 50 or 70% signal and 70, 50, or 30% background.

The choice of this method was informed by considering the results of the 2D fit over energy and $\cos\theta_\odot$. Fit results on toy data sampled from ^{8}B and ^{208}Tl MC sets indicated that performance was driven by the energy. The accuracy of the 2D fit only ever matched the accuracy of the 1D fit over energy; $\cos\theta_\odot$ providing no additional information. To see if this behavior changed in energy regions less populated with background ^{208}Tl events, simultaneous extended LL fits were applied over the three energy regions defined in table 5.2. Toy data was generated from the combined model in a 70% to 30% signal to background ratio. An extended LL fit was performed on this full dataset as divided over the three energy ranges. The result of these three separate fits are presented in figure 5.10. The shape of the $\cos\theta_\odot$ projection in each energy region seem to indicate that between [2.0, 2.8] MeV the ^{8}B PDF loses the Cherenkov $\cos\theta_\odot$ peak at 0.67.

Dividing the fitting strategy into two sequential one dimensional fits renders error handling and uncertainty estimation more transparent without compromising the sanity of the fit. The 2D fit per energy region described above was therefore put aside. As was explored in section 5.3.4, energy and $\cos\theta_\odot$ are uncorrelated in the

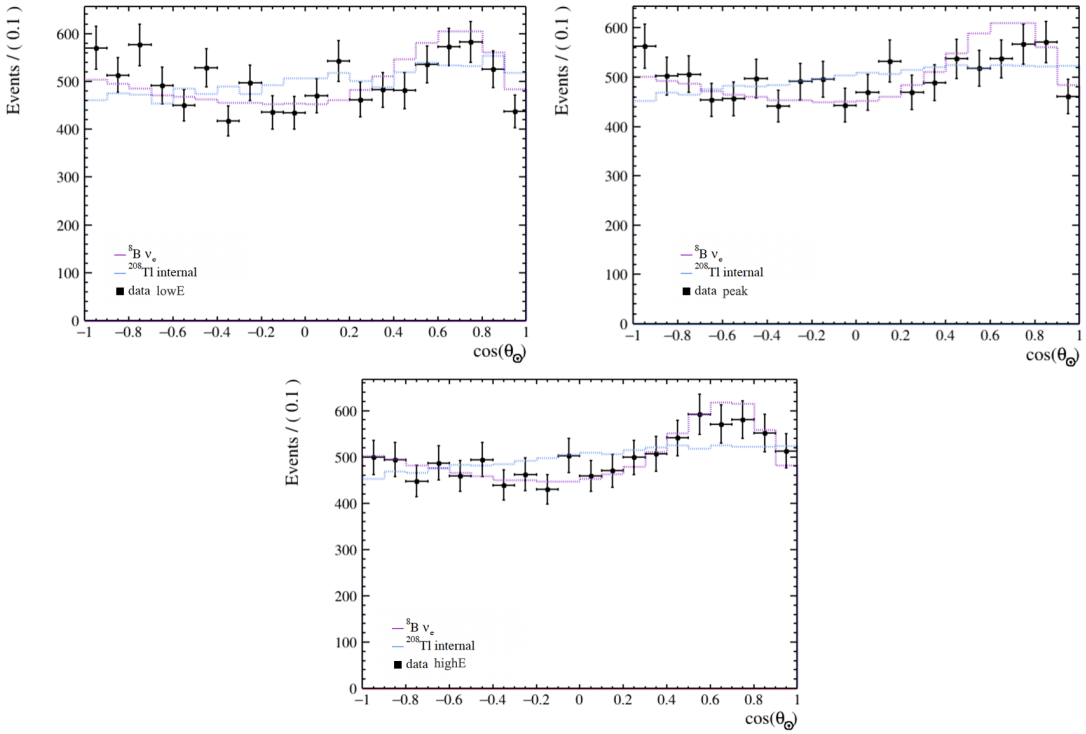


Figure 5.10: Fit results for all three energy regions from 0.7 LLR as defined in table 5.2 where the 2D PDFs are constructed as products in `RooFit`. As an example, a toy dataset distributed as 798 signal events to 27 background events fits to 583 ± 78 signal events in the lowE region; 751 signal events to 964 background events fits to 398 ± 11 signal events in the peak region; and 602 signal events to 2 background events fits to 602 ± 29 signal events in the highE region where, due to low statistics, the background PDF is taken to be the standard flat background of the lower energy regions containing ^{208}Tl.

region selected.

The model for the $\cos\theta_{\odot}$ distributions is built in a similar manner to that of the energy distributions. The main difference lies in the fact that the number of events, the yield parameter, is not allowed to float as the PDFs were normalised. Therefore, the likelihood fit is not an extended one but one that employs fractional contributions

of signal and background PDFs such that equation 5.3.14 becomes

$$f_{\text{model}} = f_{\text{signal}} * \text{PDF}_{\text{signal}} + (1 - f_{\text{signal}}) * \text{PDF}_{\text{background}}. \tag{5.3.17}$$

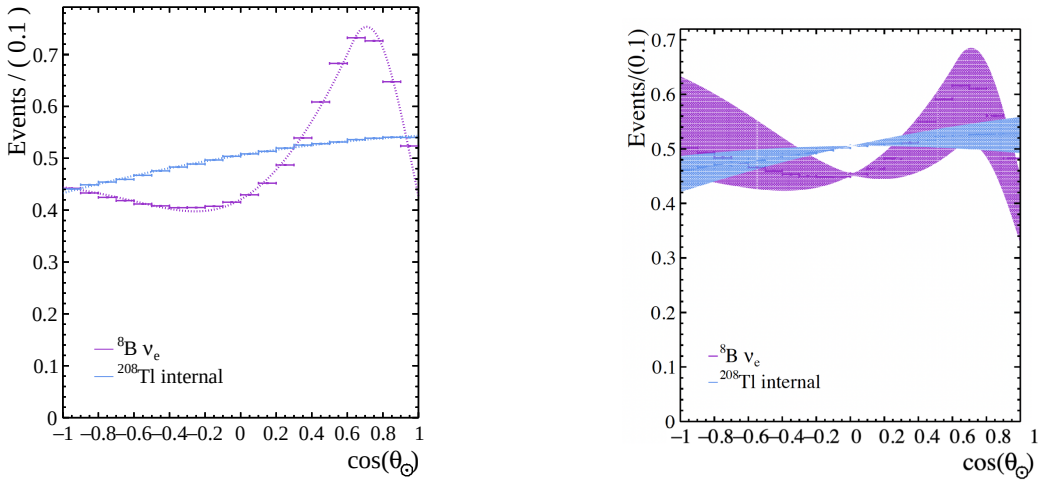
The shape of the normalised $\cos\theta_{\odot}$ distributions cannot be parametrised by a standard function. However, the parameters making up the modeling function encompass the systematic uncertainties associated with the fit. Those strictly related to the shape of the PDFs are allowed to float within a set of constraints without contributing to the total systematic uncertainties. Those carrying physical weight can. The detail of how these were determined will be addressed at the close of this section. Figure 5.11 shows the parametrised fit functions overlaid with the PDF shape they model for ^{8}B and ^{208}Tl MC sets.

Firstly, functions must be built to match the shape of the PDF histograms of ^{8}B and ^{208}Tl. The signal function $s(x)$ is comprised of a decreasing exponential function for what should be the flat component in the negative region of $\cos\theta_{\odot}$

$$s_{\text{flat}}(x) = e^{(i_s + r_s x)}, \tag{5.3.18}$$

and a modified Gaussian function with an asymmetric tail and sharp peak for the scintillator Cherenkov angle.

$$s_{\text{peak}}(x) = \begin{cases} e^{\left(-\frac{1}{2}\left(\frac{x-p_s}{w_s}\right)^2\right)} & \text{if } \left(\frac{x-p_s}{w_s}\right) \leq a_s \\ A\left(\frac{u_s}{a_s}\right)^{a_s} e^{\left(-\frac{1}{2}a_s^2\right)} & \text{if } \left(\frac{x-p_s}{w_s}\right) > a_s \end{cases} \tag{5.3.19}$$



(a) (b)

Figure 5.11: (a) Normalised $\cos\theta_\odot$ distributions for ^{8}B and ^{208}Tl MC sets with their parametrised function (dotted) fitted to best match the shape of the binned PDFs. (b) Visualisation of the constraints set on the shape parameters described in table 5.3 for the signal and background PDFs individually.

They are blended together by a logistic function.

$$s_{\text{bridge}}(x) = \left(1 + e^{-(x-p_t)/r_t}\right)^{-1}. \tag{5.3.20}$$

The final signal is a weighted sum of these components

$$s_{\text{total}}(x) = s_{\text{flat}}(x)\left(1 - s_{\text{bridge}}(x)\right) + s_{\text{peak}}(x)\, s_{\text{bridge}}(x) \tag{5.3.21}$$

$$s_{\text{total}}(x) = \left(1 + e^{-(x-p_t)/r_t}\right)^{-1} s_{\text{peak}}(x) + \left[1 - \left(1 + e^{-(x-p_t)/r_t}\right)^{-1}\right] s_{\text{flat}}(x). \tag{5.3.22}$$

The background function $b(x)$ is simpler, and given by a second order polynomial

taking into account the slight slope where a completely flat PDF was expected.

$$b_{\text{tot}}(x) = 1 + r_b \cdot x + c_b \cdot x^2. \tag{5.3.23}$$

The parameters for both fitted functions are introduced in table 5.3. This table also includes the next step of the modeling process in the last two columns. Once the PDFs were adjusted to form their respective functions, the value of the parameters on which the fit converged are passed to the next phase. This consists of choosing which shape parameters are allowed to float and within which constraints to build a sound uncertainty model. Therefore, the parameters are presented alongside the range allowed during the fit to the PDF histogram bins. The value on which they converge is passed onto the constrained model and their flexibility tested. As such, the fourth and fifth columns present the results of these model sanity tests. Parameters contributing tho the final systematics are listed with the allowed flexibility of their constraints. The constraints are applied as Gaussian constraints based on the error on the first fit. Parameters not contributing are set to the fit value from the PDF shape modeling and are listed as constant.

The final model underwent typical statistical tests to decide the number of degrees of freedom it is allowed. Ensemble tests on the fit to the shape of the PDFs to build the model function converge as expected around bias (0.0102 ± 0.0042) and pull (1.1014 ± 0.2017) values indicating fit sanity. The numbers quoted are for the 1:1 signal to background ratio toy data generated and presented in figure 5.12.

Only the mean p_s, width w_s and slope r_b parameters are treated as nuisance parameters in the fit uncertainty. Physically, the mean represents the $\cos\theta_\odot$ peak center and is indicative of angular bias which is typically corrected using calibration

parameter	definition	range	systematics	constraints
i_s	intercept	0.40	-	constant
r_s	slope (flat region)	-0.04	-	constant
p_s	mean	[0.62, 0.67]	✓	±30∗error
w_s	width	[0.15, 0.40]	✓	±30∗error
a_s	asymmetry parameter	[0.05, 2.00]	-	constant
u_s	tail parameter	[0.5, 5.0]	-	constant
p_t	transition point	-0.15	-	constant
r_t	"smoothness" of transition region	[0.05, 1.0]	-	constant
f_t	signal contribution at transition point	[0, 1]	-	[0.3, 0.6]
r_b	slope	[0.0, 0.5]	✓	±30∗error
c_b	curvature	[-0.5, 0.0]	-	constant

Table 5.3: Summary of the parameters making up the signal and background PDF models. If the *constraint* column lists "constant" when a range was provided, the parameter value is fixed at that at which the model was fit to match the shape of the PDF. Similarly, the "error" value is that of the same fit result.

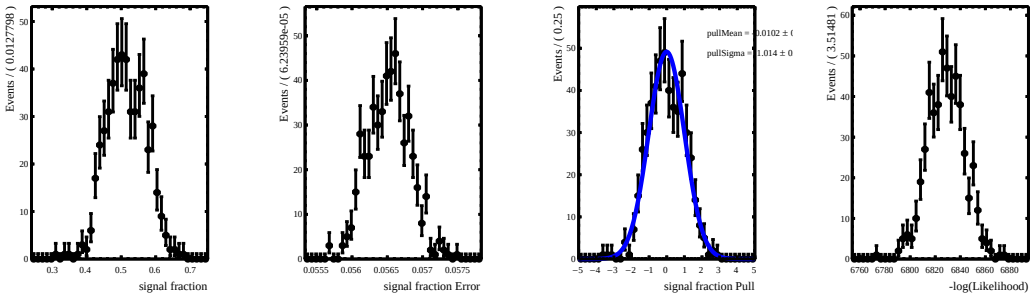


Figure 5.12: An example of the ensemble test results for the model function determination obtained by fitting functions to the ^{8}B and ^{208}Tl MC sets.

data. The width is a measure of detector angular and timing resolution. The more precise these quantities are, the narrower the peak would be around the expected Cherenkov angle. The remaining shape regularisation parameters are either set as constants except for f_t which is allowed to float within a predefined range. It was found that f_t has significant impact on the shape of the PDF function without carrying physical value as it is strongly correlated to the signal fraction. Systematic nuisance parameters are incorporated into the likelihood via Gaussian constraints centered on the values obtained from the converged Hesse fit. This corresponds to a profile LL treatment of shape uncertainties.

The performance and validity of the model were evaluated through ensemble pull and bias tests with generated toy data as 30:70, 50:50, 70:30 % signal-to-background ratios. The inclusion of the asymmetry a_s and curvature c_b parameters, both jointly and individually, as nuisance parameters introduced strong correlations with the signal fraction and resulted in biased profile LL estimates of the signal fraction. They were therefore excluded from the systematic treatment. Even when constrained with Gaussian priors, allowing these parameters to float caused the signal fraction distribution to become heavily skewed towards 1. In this regime, the signal PDF gained excess flexibility relative to the background, leading the LL to preferentially populate the signal component. This behaviour is indicative of parameter degeneracy as the model tends to absorb any shape variations into the signal distribution while fitting to data. Restricting the systematic treatment to the physically motivated signal peak position p_s, width w_s, and background slope r_b countered this degeneracy and produced signal fraction distributions centered around 0.3, 0.5, or 0.7, consistent with the true signal content of the toy ensembles.

The pull widths traditionally defined as

$$pull(f_{\text{signal}}) = \frac{f_{\text{signal}}^{\text{fit}} - f_{\text{signal}}^{\text{true}}}{\sigma_n^{\text{fit}}} \tag{5.3.24}$$

where σ_n^{fit} denotes the statistical uncertainty returned by the fit, were found to inflate when strongly correlated shape parameters were included. This does not point to a true statistical variance, but rather to systematic underestimation of the fitted uncertainty caused by poorly applied constraints.

Residuals from ensemble tests exhibited a signal-like shape, indicating that highly correlated and weakly identifiable shape parameters were absorbing shape and normalisation fluctuations. To mitigate this effect, the tail u_s and asymmetry a_s parameters, converging with elevated error in the PDF modeling, were fixed in the constrained model to the values obtained from the signal-only shape fit, thereby reducing degeneracies in the profile LL manifesting as overly large pull widths mentioned above.

Fits performed separately in background dominated [-1, 0] $\cos\theta_\odot$ and signal dominated [0, 1] $\cos\theta_\odot$ regions confirmed the necessity of retaining the background slope parameter r_b as a nuisance parameter. It serves to absorb background shape variations as the sign of the slope is not physically motivated and should not be penalized in the fit through underfitting. These studies also demonstrated the need to fix the transition region parameters, whose large uncertainties and strong correlations significantly increased the rate of bad fits, boundary effects, vanishing errors, and inflated pull widths. While the transition region is required for continuity of the PDF, its p_t and slope parameters carry no direct physical interpretation and are weakly constrained by the data. They are therefore fixed after convergence to stabilise the

constrained LL model. To avoid overfitting, only the f_t parameter is allowed to float within a constrained range. It cannot be set as a constant as it must carry the shape modeling of the transition region. However, as it was found to be strongly correlated to the signal fraction, it is not set as a nuisance parameter, but only as a tightly constrained one.

Gaussian constraints were preferred over log-normal, Bayesian or χ^2 constraints, as they provided a stable quadratic approximation to the likelihood near its maximum, minimised the occurrence of non-convergent fits and boundary errors, and yielded well-defined Hessian matrices.

The final model therefore freezes or applies Gaussian constraints to the parameters from table 5.3 centered around the value they converged on following the model determination from the fit to the signal and background PDF shapes. As the mean p_s and width w_s of the signal peak are correlated, a penalty term is applied if both vary. As the width is expected to carry most of the weight in the systematics due to the detector's resolution direct influence on it, w_s is preferentially allowed to float within loose Gaussian constraints. An additional Gaussian constraint on the signal fraction, the only yield parameter among shape nuisances, is included in the final constrained model as it vastly improved the model stability.

With the floating shape parameters showing negligible correlations and properly constrained, signal-only and background-only hypotheses were tested by fitting the data separately with the corresponding pure PDF. The result of these tests was compared to the full constrained model using a LLR statistic following

$$q = 2(\mathrm{NLL} * \mathrm{sig,bkg} - \mathrm{NLL} * \mathrm{full}), \tag{5.3.25}$$

where NLL refers to the negative log likelihood. Applied to datasets that will be covered in section 5.4.2, the q value for signal and background hypotheses consistently returned equal values with significant σ thus indicating that neither component alone was sufficient in describing the data's angular distribution.

Uncertainties calculated by a Hesse fit have a tendency to return large symmetric uncertainties due to the boundary constraints on the signal fraction. Its estimate assumes a Gaussian likelihood that is bound to fail near boundaries where it becomes unphysical. A Minos profile LL evaluation reports asymmetric uncertainties more aptly describing the edge cases when the best fit lies where the data is predominantly background or signal. Again, correlations show negligible couplings between the signal fraction, that is the amplitude of the fit, to the floating nuisance parameters p_s and w_s. Only f_t, the internal signal contribution at the transition point, causes a slight anticorrelation. It is however not the cause for the broad uncertainties of the fit which are due to boundary effects as opposed to degeneracy against which the model has been safeguarded by various statistical verifications.

For the final model configuration, the systematic ensemble for the 50% signal-to-background toy dataset returns a pull mean of 0.261 and a pull width of 1.39. This indicates a small but noteworthy residual bias in the signal fraction estimator and an inflation of the uncertainty relative to the ideal unit-width pull, consistent with the presence of systematic shape uncertainties propagated through the profile LL. The resulting systematic uncertainty on the signal fraction is characterised through quantiles by a median value of $0.510^{+0.098}_{-0.088}$. These asymmetric systematic uncertainties obtained from a Minos instead of a Hesse fit on the final constrained model are at the $\mathcal{O}(10\%)$ level.

In contrast, the statistical ensemble yields a pull mean of 0.099 ± 0.046 and a pull width of 0.966 ± 0.033, consistent with an unbiased estimator and correct statistical coverage. The comparison demonstrates that while the statistical component of the fit is well behaved, systematic shape uncertainties dominate the total uncertainty budget on the signal fraction and constitute the limiting factor in the precision of the measurement.

5.4 What If

Now that the 'how to' has been covered, 'what if' becomes the predominant question.

The solar flux $\phi(\nu)$ is calculated by the SSM for every solar process. With knowledge of the detector geometry and target medium chemistry, the expected rate of solar events R can be calculated as a function of energy E from the oscillation probability $P_{ee}, (1 - P_{ee})$ as given by equation 2.2.15 and cross section $\sigma_{\nu_{e,\mu,\tau}}(E)$. The integral over energy giving the rate is then

$$R = \phi(\nu) N_e \int_{E_{\min}}^{E_{\max}} S_\nu(E)(P_{ee}(E)\sigma_{\nu_e}(E) + (1 - P_{ee}(E))\sigma_{\nu_{\mu,\tau}}(E))dE \tag{5.4.1}$$

where $S_\nu(E)$ is a simplification in the form of a normalised spectrum of the emitted solar neutrino given the solar process studied. The number of electron targets requires the fractional proportions $f_{\text{LAB,PPO}}$ of PPO and LAB in the cocktail as well as the carbon chain proportional composition. It further requires the absolute mass M of scintillator as well as the density of its components to infer the molecular weight m.

It is expressed as

$$N_e = \frac{f_{\mathrm{LAB}} n_{\mathrm{LAB}} + f_{\mathrm{PPO}} n_{\mathrm{PPO}} N_A M_{\mathrm{LAB}}}{m}. \tag{5.4.2}$$

For a livetime of 365 days, a fiducial volume of 6 m of LAB + 2.2 g/L PPO, and a solar flux of $5.03 \times 10^6\,\mathrm{cm}^{-2}\cdot\mathrm{s}^{-1}$ [8], the ^{8}B ν_e solar flux can be calculated to lie at 862.65 events [104]. This number can be scaled back to match energy, fiducial volume and other analysis specific cuts, as well as the total livetime of 143 days of the scintillator Gold list used for this analysis[i]. For example, with the specific cuts from table 5.5, 86 events are expected. This is in line with the number of solar ^{8}B ν_e events tagged by [103] in the set used to tune the time residual ordering window for the CID method. The expected signal events in various regions are detailed in table 5.9 which compares this number to the events tagged by the fitting algorithm.

Background events can be counted in a similar manner. The number of expected events is of particular importance, because the statistical significance of the signal is almost entirely dependent on the radiopurity of the medium. This is due to the fact that the CID method is by design a statistical approach that weakly relies on standard tagging and selection cuts. While this may have yielded excellent results for the Borexino collaboration, the radiopurity levels achieved by SNO+ require this application of the CID method to remove ^{212,214}BiPo and ^{208}Tl events via coincidence tagging. The background levels achieved during the PPO phase contribute to the

[i]The total run time is 171 days including 9 days of dead time. April and May are also excluded, removing an additional 20 days.

expected rate of

$$R = \sigma_{\text{bkg}} \times C_{g/g} \times M \frac{ln(2)}{m_A \tau_{1/2}} t \tag{5.4.3}$$

where σ_{bkg} is the branching ratio of the isotope of atomic mass m_A and half-life $\tau_{1/2}$ considered, $C_{g/g}$ its concentration in mass M of scintillator over a livetime t. With the concentrations from table 3.1, the expected number of solar events, within both fiducial volumes and across the whole energy range, would still be discernible via the statistical CID method.

5.4.1 Validating the algorithm

The performance of the CID algorithm and fitting model will first be evaluated against a subset of data from the PPO scintillator phase that is expected to show directionality. Specifically, a set of 83 solar event candidates was obtained from Ana Sofia Inacio [103] by standard analysis means, the details of which are compiled in table 5.5.

Figure 5.13 illustrates the CID algorithm's workflow. The first data selection stage consists of standard data cleanliness checks, the removal of the low energy [0, 2] MeV region, the removal of external backgrounds via a fiducial volume cut of 1 m, the removal of instrumental backgrounds via a muon follower and a retrigger cut, and the removal of known radioactive backgrounds via coincidence tagging. All surviving calibrated PMTs within this pruned dataset are then ordered by time residuals. The earliest hit PMTs are kept and their $\cos\theta_{\odot}$ is computed to contribute to the final distribution.

Though the only energy cuts applied are a low energy noise threshold and a high

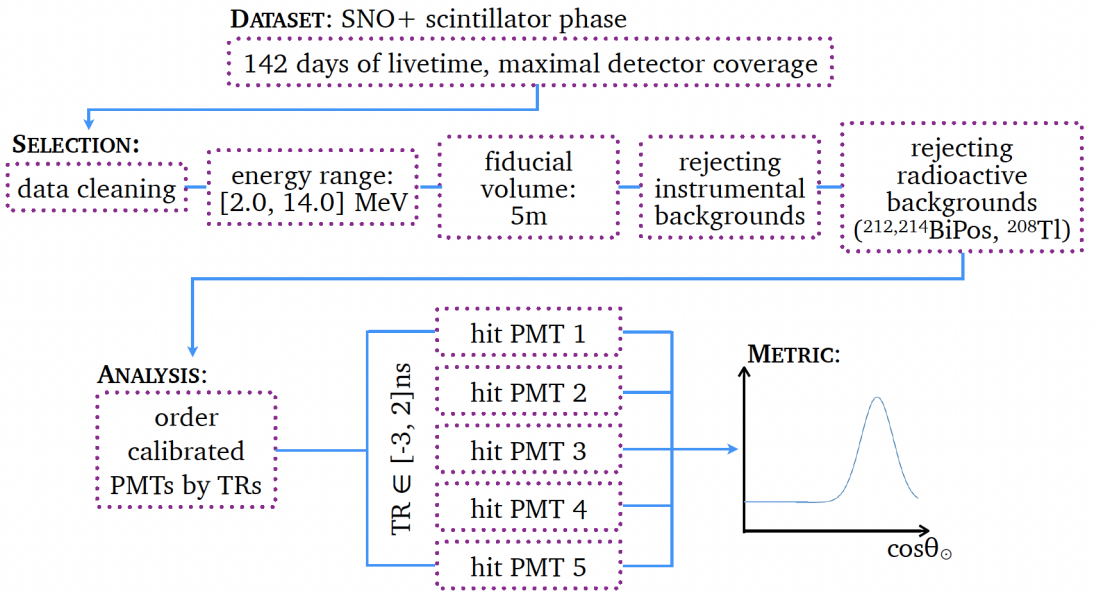


Figure 5.13: Flowchart of the broad stages of the analysis workflow for the CID

energy missed muon veto, event energy distributions are compiled to be used as an additional observable or dimension in the fit. While the data cleaning mask handles most noise and muon events, the 20 s follower cut for high energy events and keeping only the first event having triggered the event window are common additional cuts across most analyses to account for instrumental backgrounds.

A fiducial volume cut at 5 m is applied to remove the bulk of external backgrounds. An additional set of MC PDFs and data distributions is produced in parallel for the $0\nu\beta\beta$ fiducial volume cut at 3.3 m.

During data analysis, energy cuts are used for coincidence tagging of the dominant background sources ^{212,214}BiPo and ^{208}Tl. A tagged set for which the selection criteria are listed in table 3.3 is created. All pairs are saved as their unique combination of runID and GTID. These sets are compared against the GTID of all triggered events during the main analysis loop and skipped if a match is found. The analysis proceeds if

the triggered event is not associated to a tagged background event and will contribute to the final data distributions.

The RATDB table of calibrated PMTs for the run under analysis is then accessed to calculate the time residuals of every and all hit PMTs during that run. Time residuals are calculated as

$$t_{res} = t_{PMT} - t_{flight} - t_{event}, \tag{5.4.4}$$

from equation 3.8.1 where the time of flight uses RAT's LightPathCalculator

$$t_{flight} = \text{group velocity}(d_{\text{LS}} - d_{\text{AV}} - d_{\text{water}}), \tag{5.4.5}$$

thus accounting for the photon's path through scintillator within the inner AV, the acrylic as it refracts through the wall, and the water as it travels through the cavity to the PSUP.

The ordering and quantity of PMT hits to include in the analysis are of paramount importance. Fundamentally, Cherenkov radiation is expected to be discernible in the rise time before the event scintillates. With the inclusion of PPO in the scintillator cocktail, the separation between timing profiles is incredibly narrow, or possibly even smeared, with a scintillation emission time of 2.6 ns. While in MC simulations, the Cherenkov window is concentrated in a steep rise at and before t_0 as in figure 5.5, uncertainty in the optical model justified tuning the analysis time residual window on a subset of data.

The distributions obtained by applying the CID algorithm to the 83 selected events making up the solar dataset, the main additional selection cut being a high energy

cut at 5 MeV, served to fine tune the final selection cuts before applying the method to the broader Gold data period. Figure 5.14 shows the time residuals of the first 50 hit PMTs of every solar event. The time residuals were sorted with a preference for negatives in a decreasing order then for positives in an increasing order in a series of windows and sample sizes. Setting the time residual window to [-8, 2] ns rejects unphysically early hits that could be explained by the dark rate. The separation of Cherenkov light is lost beyond 2 ns.

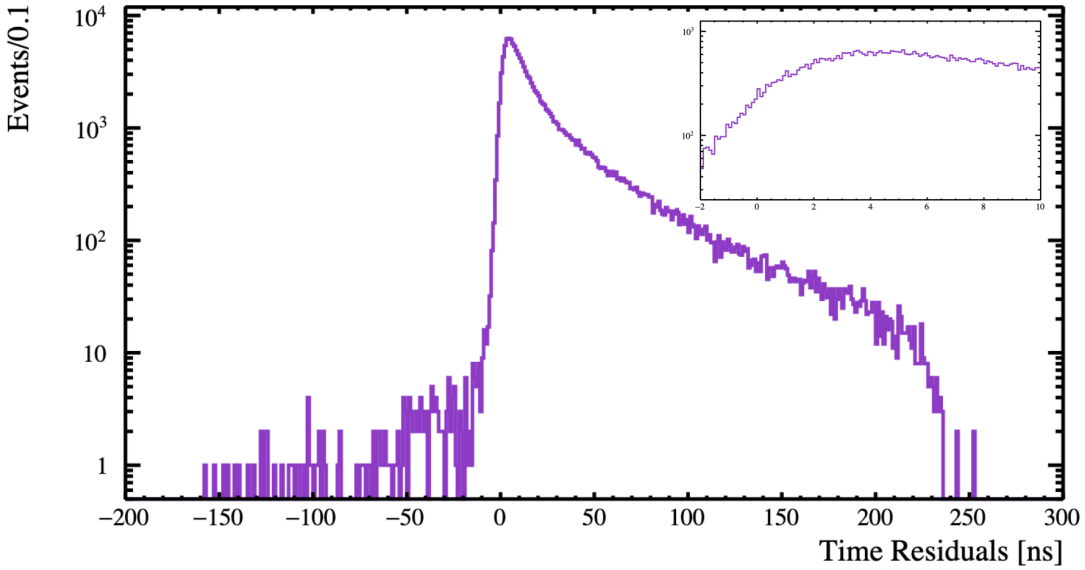


Figure 5.14: Time residual profile of all the hit PMTs of all 83 events in the solar set. The inset focuses on the [-2, 10] ns region where the rising edge evens out as scintillation light starts emitting.

The effect of the time residual window is negligible on directional events, implying that fine tuning its upper and lower bounds is secondary to optimising the number of hit PMTs to consider, if at all relevant. This is due to the ordering strategy that favours early events closest to t_0. This time residual window is therefore set in data as a safeguard to PMT noise registering as early PMT hits.

The number of hit PMTs to consider was optimised by evaluating both the relative height of the $\cos\theta_{\odot}$ peak at 0.67 to the flat valley across the rest of the angular distribution in addition to comparing the area under the signal peak which is referred to as the 'integral' method in table 5.4. This was done in MC for the PDFs of individual hits as well as summed hits one through five. The results of the best fit

$$\sigma = \frac{\sqrt{\sum_i^{\text{bins}} \text{peak}_i^2 - \sum_i^{\text{bins}} \text{flat}_i^2}}{\sum_i^{\text{bins}} \text{peak}_i^2 + \sum_i^{\text{bins}} \text{flat}_i^2} \tag{5.4.6}$$

are compiled in table 5.4.

Because only 83 events survive the cuts from table 5.5 to make up the solar set, the integral method to determining the most statistically significant hit number is preferred. The results are reported in table 5.6.

In conclusion, the CID method adapted for SNO+ similarly builds its foundation on the time residual observable. Events are ordered by shortest to longest time residuals centered around 0 ns with a preference for negatives. While the topology of all 20 first hit PMTs was studied, it was found that directional information is lost past 5. Only this subset will be selected to pass into the final PDFs. For these earliest PMT hits, the direction of the event is obtained with the knowledge of the PMT coordinates and the reconstructed event position as such

$$\vec{d}_{\text{event}} = \text{PMT}(\hat{x}, \hat{y}, \hat{z}) - \text{event}(\hat{x}, \hat{y}, \hat{z}). \tag{5.4.7}$$

Applying the Sun direction utility described in section 5.3.1, the angular distribution

Hit PMTs	height		integral	
	combined	*individual*	*combined*	*individual*
1	0.311	0.311	0.273	0.273
2	0.352	0.388	0.310	0.342
3	0.372	**0.410**	0.325	**0.353**
4	0.379	0.399	0.329	0.342
5	**0.380**	0.384	**0.330**	0.334
6	0.375	0.379	0.326	0.330
7	0.376	0.364	0.324	0.301
10	0.362	0.307	0.310	0.262
15	0.344	0.284	0.290	0.227
20	0.330	0.268	0.273	0.208

Table 5.4: Summary table of fit results of the optimisation of number of hit PMTs to include in final PDFs. Best fits are reported in bold. The *individual* columns represent the fit values for a single time ordered hit by contrast with the *combined* column representing the fit values for the summed distribution of the same hits. The first hit having the worst results and the methodology decreasing in efficiency past 5 hits are noteworthy.

of early Cherenkov light is reconstructed following

$$\cos\theta_{\odot} = -\vec{d}_{\text{sun}} \cdot \vec{d}_{\text{event}}. \tag{5.4.8}$$

PDFs are populated with the angular distribution of $\cos\theta_{\odot}$ for all events passing the selection cuts grouped in table 5.7.

When applied to the 83 event dataset comprised of the $\cos\theta_{\odot}$ distribution of the 5 first PMT hits as ordered by their time residual value, the model fits the expected

Variable	Cut Value
FV	R<5 m
Energy	>5 MeV
Fit Vertex Validity	`(Energy, Position, Time) valid`
Clean	DC mask `0x2100000042C2`
muon followers	`(dcFlagged&0x4000)!=0x4000`
	`nHits`>5000 or `(dcFlagged&0x80)!=0x80`
multiplicity	ΔT>500 ns
PMT noise	$0.2 < \text{ITR} < 3$

Table 5.5: Summary table of solar selection cuts used by [103].

83 signal events to 81 ± 4 events as can be seen in figure 5.15 which overlays the normalised ^{8}B ν_e signal-only and ^{208}Tl background-only PDFs to the data. The results of applying these selection cuts on these 83 solar events can also be seen in figure 5.15.

Figure 5.16 provides a visual interpretation of the methodology applied by presenting a projection of event positions within the AV and their corresponding hit PMTs selected as the early directional beacons. This is introduced as the data driven equivalent of the schematic used in figure 5.2.

5.4.2 Fitting the Model

The CID methodology successfully extracted directionality from a subset of data identified as solar events via other classic tagging cuts, most importantly a severe energy cut at 5 MeV. This is sufficient to state that the CID methodology can be applied to SNO+ to separate early Cherenkov radiation from scintillation light even

Hit PMTs	*combined*	*individual*
1	0.2925	0.2925
2	0.2188	0.1511
3	0.3327	0.5709
4	**0.4163**	**0.6805**
5	0.3999	0.2643
6	0.3796	0.2500
7	0.3735	0.3164
8	0.3626	0.2912
9	0.3578	0.2953
10	0.3563	0.3408
20	0.3182	-
30	0.2039	-
40	0.2016	-
50	0.1848	-

Table 5.6: Summary table of fit results of the optimisation of number of hit PMTs taken from the solar set. Best fits are reported in bold. The *individual* columns represent the fit values for a single time ordered hit by contrast with the *combined* column representing the fit values for the summed distribution of the same hits. The fourth hit carries the most directionality in this set.

on the low statistics offered by the PPO scintillator phase. With this proof of concept achieved, it remains to see how far this method can be pushed in extracting directional information across wider energy regions.

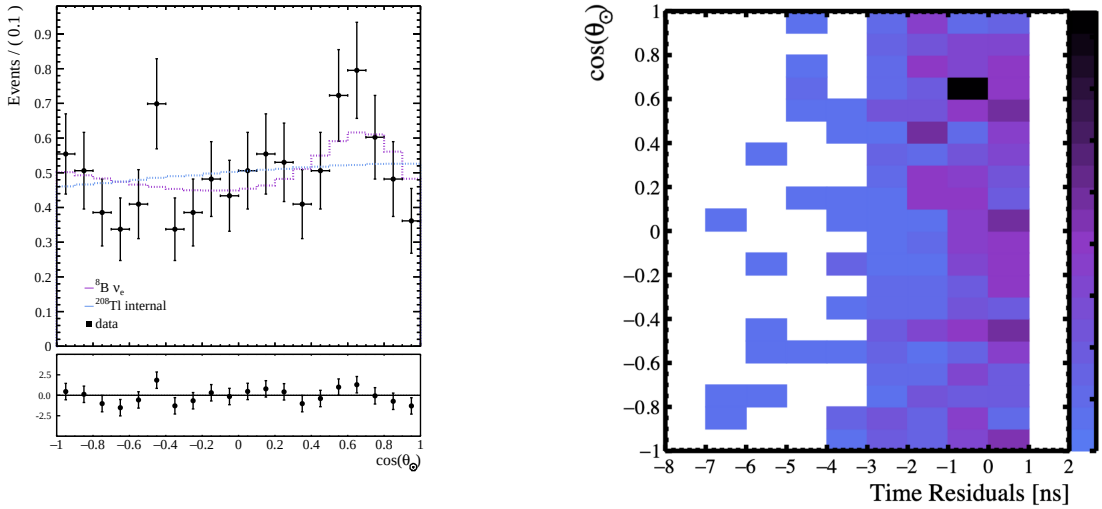
As has been expressed throughout this thesis, one such region lies in the lower energies where solar analyses suffer from high decay rates from the U and Th chains.

Variable	Cut Value	
	MC	Data
FV	R<5 m	R<5 m
Energy	<2000 `nHits` & >2 MeV	
Noise	`MCPE(noise) false`	`evIndex==0`
Fit Vertex Validity	`(Energy, Position, Time) valid`	
Time Residual	[-3, 2] ns	
Universal Time	<50 ys	
Clean		DC mask `0xD82100000162C6`

Table 5.7: Summary table of selection cuts applied to MC distributions and datasets. The cut on the universal time utility accounts for an erratic jump in `UTDays` noticed by the collaboration during a data reprocessing campaign.

The other is specific to the $0\nu\beta\beta$ search in the ROI defined as [-0.5,1.5] σ around $Q_{\beta\beta}(^{130}\text{Te}) = 2.53\,\text{MeV}$ which places it at [2.42, 2.56] MeV where ^{8}B ν_e is the main background. It should be reiterated that energies lower than 2 MeV have been excluded early in MC studies due to directionality smearing and high background levels.

The main concern at low energies, to all SNO+ analyses, is the '2.2 MeV excess'. A peak at 2.2 MeV has consistently been reported by the collaboration as early as the partial fill period. It does not naturally fit any of the extended background models proposed to explain it. Therefore, it is unaccounted for in the expected background rates. In solar searches, it vastly overwhelms the signal in its region and renders low energy solar analyses impractical. Even with backgrounds rejected via the classic selection cuts outlined in table 3.3, the '2.2 MeV excess' events statistically drown ^{8}B ν_e events at low energies. The predominance of this peak can be seen in the



(a) (b)

Figure 5.15: (a) Constrained fit result of the cos$\theta_\odot$ distribution of the 5 first PMT hits of the solar set as ordered by their time residual value (black) overlaid with the background (blue) and signal (violet) normalised MC distributions. Residuals are reported in the band beneath the main plot. The relationship between time residuals and cos$\theta_\odot$ is shown as a density plot in (b) that shows how directional information predominantly lied in the rise time between -1 and 0 ns. Because there is no gain in directional information by including time residuals earlier than -3 ns, the window was further restrained to [-3, 2] ns.

energy spectra of all triggered events passing basic cleanliness cuts occurring within the PPO phase from June 2022 till March 2023 displayed in figure 5.17. This figure also indicates that additional instrumental backgrounds survive the cleanliness cuts applied in table 5.7, even at higher energies past 4.5 MeV where the ^{8}B solar neutrino flux should dominate. These background rise up to some 3 orders of magnitude above the expected ^{8}B solar neutrino flux when extending down to the '2.2 MeV excess' energy region. A density distribution of the event positions projected onto the AV in figure 5.18 further confirms the data is dominated by background events. Were the selection cuts fully effective, solar events would be distributed evenly throughout the

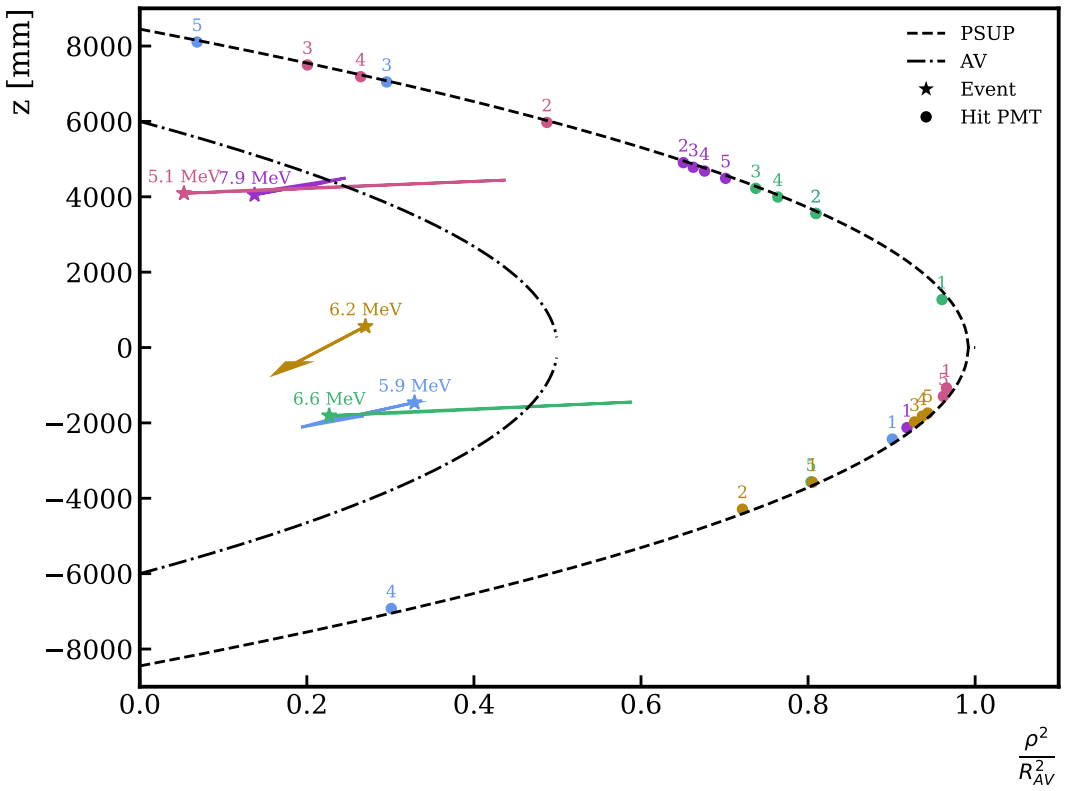


Figure 5.16: Visual representation of the designed algorithm. Five events were selected at random from the solar set and plotted on a normalised (ρ, z) projection of the detector with their associated energy. ρ is normalised to the radius of the AV R_{AV} such that $\sqrt{\frac{x^2+y^2}{2R_{\text{AV}}}}$. The hit PMTs line the contour of the projection at the radius of the PSUP and are numbered. The arrow represents the Sun direction at the time the event was triggered, $\vec{s}$,is projected onto xy plane in the ρ direction as $d\rho = \frac{x \cdot s_x + y \cdot x_y}{\sqrt{x^2+y^2}} \times \frac{1}{\sqrt{R_{\text{AV}}^2}}$. The 5.9 MeV event depicted in blue is the only one to not carry any directional information in the five PMTs it triggered first as they are not arranged in any semblance of a Cherenkov cone.

active volume.

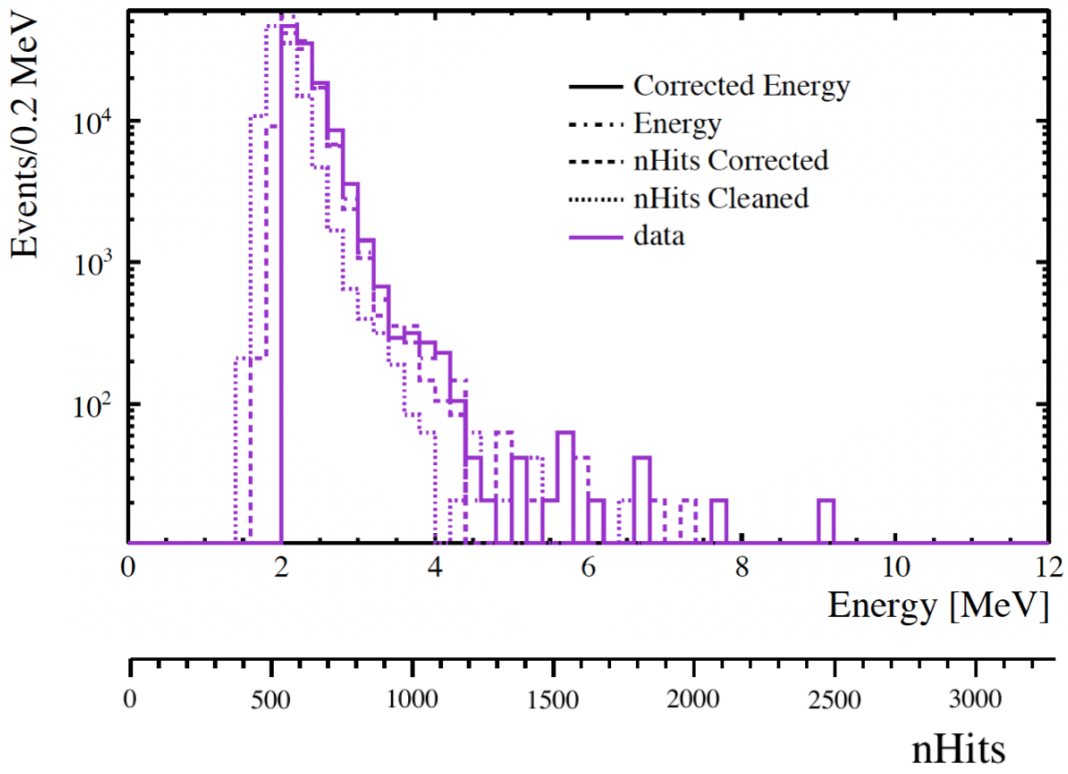


Figure 5.17: Energy spectrum of all triggered events within the PPO phase for the basic selection cuts.

Obstacles notwithstanding, the CID algorithm was fit in the lower energy region. The result of the fit between 2.0 and 2.8 MeV is presented in figure 5.19. As expected, the $\cos\theta_\odot$ distribution is flat. In some way, the lack of directional peak is a reassuring, though anticipated, corroboration that the '2.2 MeV excess' is not the result of unforeseen nuclear activities in the Sun's core. The CID method is not the tool that will help reject these events. It is therefore neither the technique that will assist solar analyses in probing such low energy ranges.

Though it problematically overlaps with the tail of the '2.2 MeV excess', the next

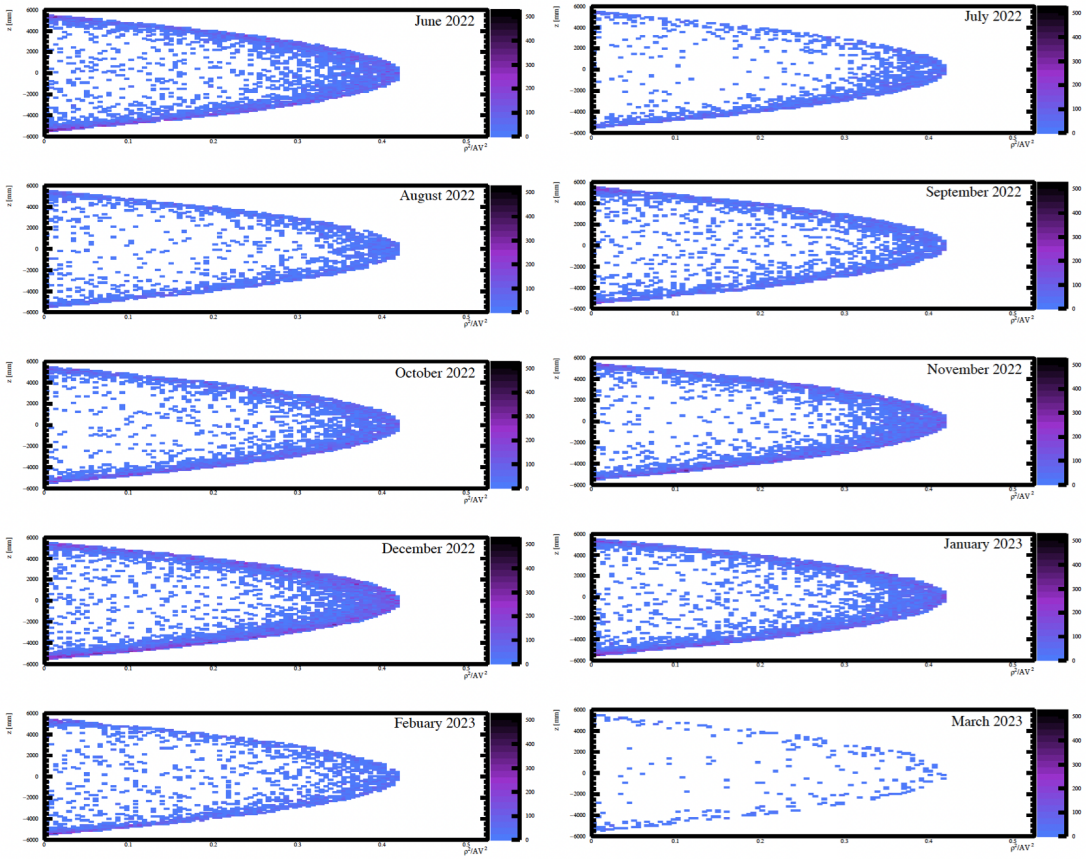


Figure 5.18: Event position on a normalised (ρ, z) projection of the AV for all triggered events within the PPO phase for the basic selection cuts.

region to apply the CID method to is the $0\nu\beta\beta$ ROI. If any directionality is extracted, there would be value in expanding this technique to the optics of the tellurium doped cocktail in order to correctly identify the ^{8}B solar background events. Figure 5.20 displays the fit result of 9^{+27}_{-9}(stat.) $\pm$ 7(syst.) out of an expected 5 events in that region. 116 events are recorded in this region. Again, with such low statistics due to energy bin width and short livetime, the CID methodology struggles to provide meaningful results. While the fit result itself agrees with the prediction, referring back to figure 5.11(b), it is likely that the events in the negative $\cos\theta_{\odot}$ bins are fit to

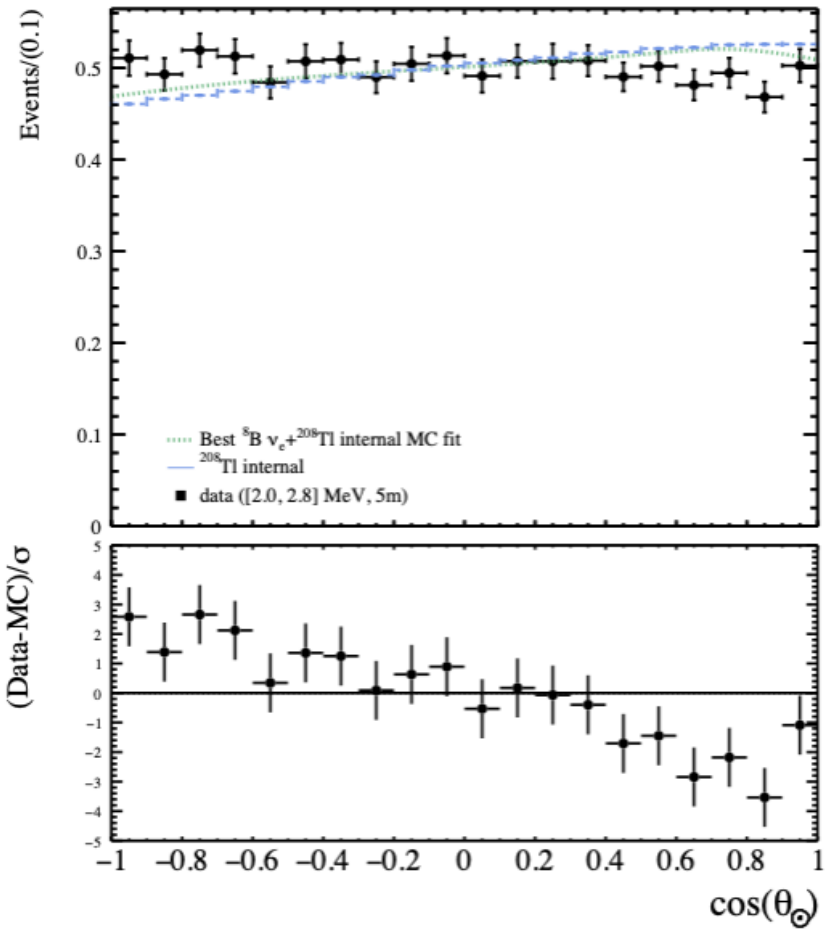


Figure 5.19: Constrained fit result of the $\cos\theta_\odot$ distribution of the 5 first PMT hits as ordered by their time residual value (black) from the PPO dataset for events in the low energy region defined as [2.0, 2.8] MeV overlaid with the best fit, ^{8}B ν_e signal + ^{208}Tl background, (green) and background MC (blue) normalised distributions. Residuals are reported in the band beneath the main plot.

signal when in reality the PDFs should be almost indiscernible in this region.

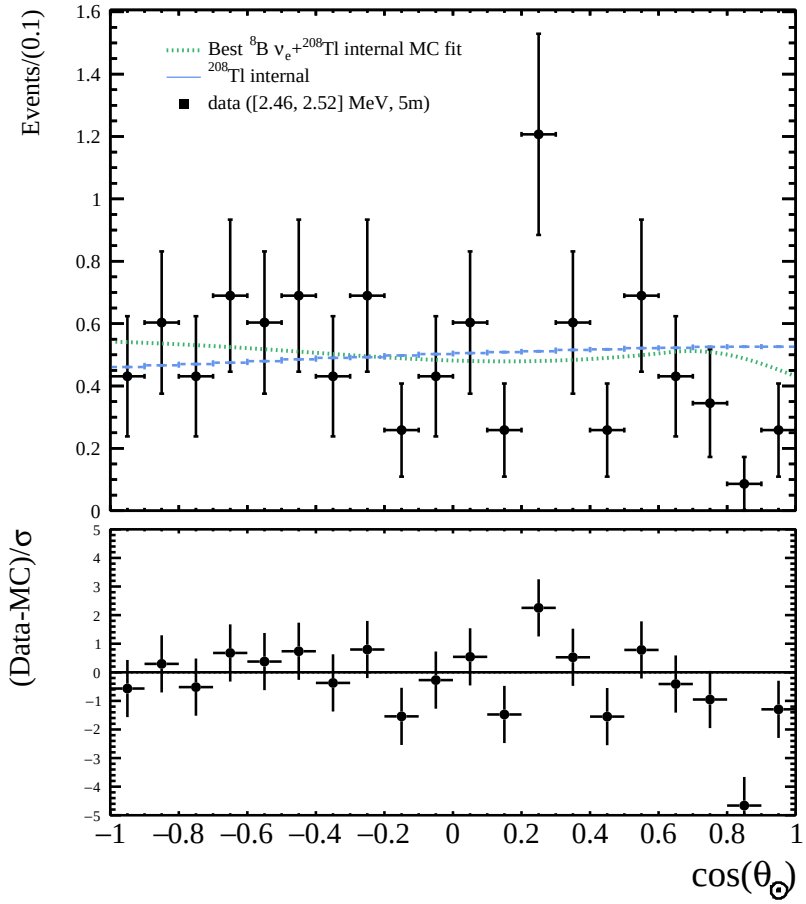


Figure 5.20: Constrained fit result of the $\cos\theta_\odot$ distribution of the 5 first PMT hits as ordered by their time residual value (black) from the PPO dataset for events for the $0\nu\beta\beta$ ROI overlaid with the best fit, ^{8}B ν_e signal + ^{208}Tl background, (green) and background MC (blue) normalised distributions. Residuals are reported in the band beneath the main plot.

The number of events in all regions is two orders of magnitude higher than the expected number of solar events. This even applies to the 0.7 and 0.9 LLR regions defined in table 5.2 which were designed to reject the energy region dominated by the ^{208}Tl peak. The limitations of the CID method were highlighted in figures 5.19 and

5.20. In a region where the solar signal is drowned in backgrounds, the $\cos\theta_\odot$ distribution is flat and the model cannot extract directionality. In the narrow $0\nu\beta\beta$ region, statistical limitations hindering the fitting algorithm still come with overwhelming backgrounds.

Figure 5.17 points to the obvious; additional background suppression methods will need to be applied. Directionality cannot be extracted when the background rate overwhelms the signal by several orders of magnitude. Before applying selection cuts characteristic of low energy solar analyses, a few distributions relevant to the CID method are presented. Figure 5.21 serves to show that the time residual window optimised using the solar dataset does not present any unforeseen correlation with $\cos\theta_\odot$ throughout the year for a dataset dominated by backgrounds.

Detector coverage has been a recurrent concern throughout this study. Figure 5.22 presents the compilation of the PMT occupancy of the first 20 PMTs to receive a photon when a global trigger is recorded. The maps are presented per month over the PPO data taking period to prove that in the runs selected for the Gold list, the detector coverage is uniform with all crates at high voltage. It can also be seen, specifically in the last panel that is allotted to the PMT hits for the solar subset, that early light does not "prefer" any crate or detector region. This would not necessarily have been obvious in the other panels given that recorded triggered events have been shown to overwhelmingly be radioactive and instrumental backgrounds.

These distributions seem to rule out any obvious detector effects related to directional early light. This applies both for the $\cos\theta_\odot$ peak at 0.67 as well as the upturn at $\cos\theta_\odot = -1$ in signal and the forward bias in backgrounds. No cuts based on detector regions would benefit a preferential selection of solar events.

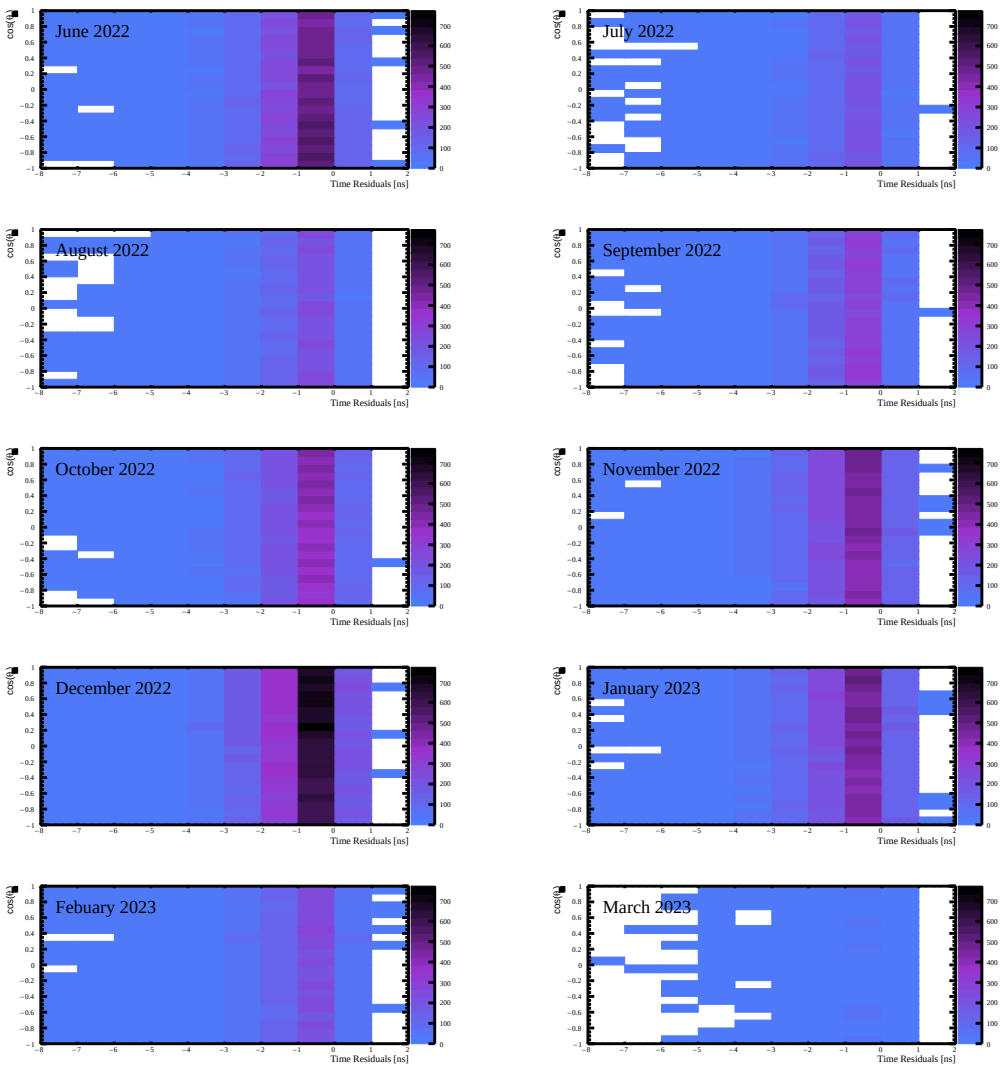


Figure 5.21: $\cos\theta_{\odot}$ and time residuals density plots of all triggered events within the PPO phase for the basic selection cuts and presented for every month.

5.4.3 Improving the Selection

The CID method's performance on the PPO data period has been considered over the previous section. The $\cos\theta_{\odot}$ distributions have been produced for different configurations of energy regions and fiducial volume. Any possible dependence of the

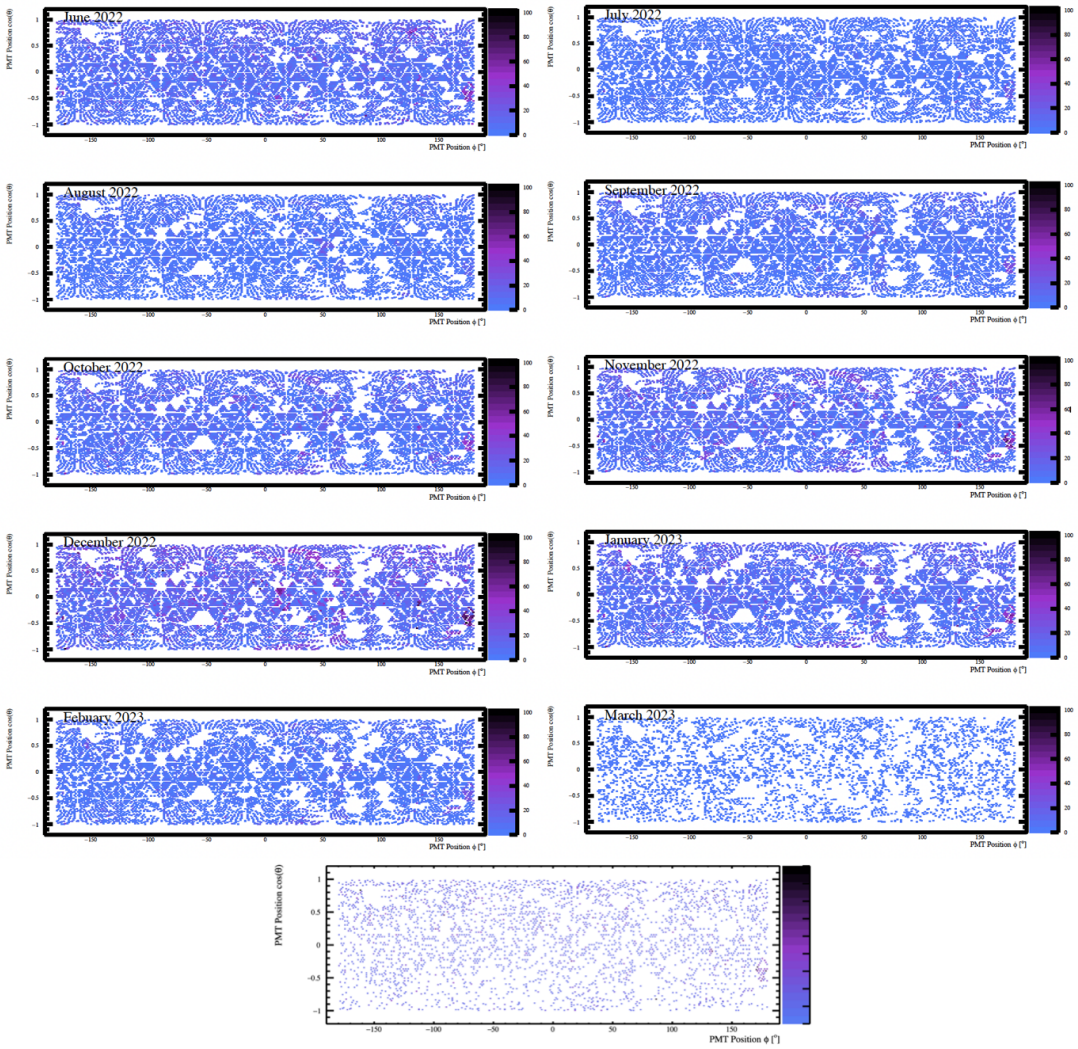


Figure 5.22: PMT occupancy flat maps of the first 20 hit PMTs of every triggered event in the PPO gold period. The geodesic PSUP structure is projected onto a flat map in the ϕ, $\cos(\theta)$ space. Every point represents a single PMT. The bottom panel is of the solar data.

results to sun direction or detector coverage have been rejected. The background levels in SNO+ proved too high to extract any statistically significant solar directionality without analysis specific cuts. Therefore, in addition to the cuts on time residuals

and low energy, developed for the CID methodology specifically, more stringent background suppressing cuts will now be applied to the PPO period. The set of cuts to be added was developed for the ^{8}B solar oscillation analysis by Daniel Cookman, and are therefore most appropriate for the aim of this analysis.

The missed muon veto that was previously implemented as a 20 s veto following a high energy event at `nHits`$>$ 2000 was replaced by a more precise combination of cuts aimed to recuperate high energy ^{8}B candidates past 2000 `nHits` which corresponds to about 8 MeV. In combination with the data cleaning mask that filters out muons, missed muons will now be identified as any events recording above 750 `nHits` and over 4 OWL PMT hits. The 20 s veto window is applied following events fitting these cuts.

The collaboration has been reporting a high rate of backgrounds from two localised positions [135]. As they are situated near the junction between the base of the neck and the AV, they are known as the "neck hotspots". A 1 s follower cut is implemented for any event reconstructing within their respective positions for which the coordinates can be found in table 5.8.

An ITR cut is also added to reduce any possible instrumental noise in the distributions.

In addition to the standard coincidence tagging of ^{212,214}BiPo pairs and ^{208}Tl, the `alphaBeta212` classifier taking advantage of the separation in the timing profiles of alpha and beta decays is applied to reduce the number of remaining in-window events surviving the out-of-window coincidence tagging. [74] found this cut to have substantial impact on low energy events within a tighter fiducial volume.

Owing to their resistance to background tagging along with the impossibility of

constraining their flux to a predictable limit due to their unknown origin, the [2.0, 2.5] MeV region will be excluded from the CID method. The '2.2 MeV excess' tail will still be visible at 2.5 MeV. A summary of the final set of cuts including these more specific background cuts is presented in table 5.8.

Variable	Cut Value
FV	R<5 m
Energy	2.5 MeV < E < 14.0 MeV
Missed Muons	`nHits`≥750, `OWLs`>4
Neck Hotspot 1	x∈[0.1, 0.38] m, y∈[-1.2, -0.85] m, z∈[5.55, 5.98] m
Neck Hotspot 2	x∈[0.51, 0.72] m, y∈[-0.83, -0.56] m, z∈[5.64, 5.98] m
Instrumentals	0.1≤`ITR`≤0.35
In-Window ^{212}BiPos	`alphabeta212`<-20
Time Residual	[-3, 2] ns
Universal Time	<50 ys
Noise, Retriggers	`evIndex`==0
Fit Vertex Validity	`(Energy, Position, Time) valid`
Clean	DC mask `0xD82100000162C6`

Table 5.8: Summary table of updated selection cuts by [74] applied to the PPO Gold dataset with the aim of improving background rejection.

The majority of these cuts, namely the ITR, neck hotspot and potentially even the low energy cut to avoid the bulk of the '2.2 MeV excess', target instrumental backgrounds. This implies that, though the radiopurity was improved with the removal of in-window BiPo events, the overwhelming number of events observed in the initial data selection can be attributed to instrumental backgrounds in the detector.

The energy profile of figure 5.23 distinctly show both the ^{208}Tl peak and the tail

of the '2.2 MeV excess' peak indicating that these are the main sources of irreducible backgrounds in this set. Referring back to figure 5.17, it is apparent that the set of cuts focused on instrumental backgrounds and in-window BiPos had a significant impact on the <5 MeV region.

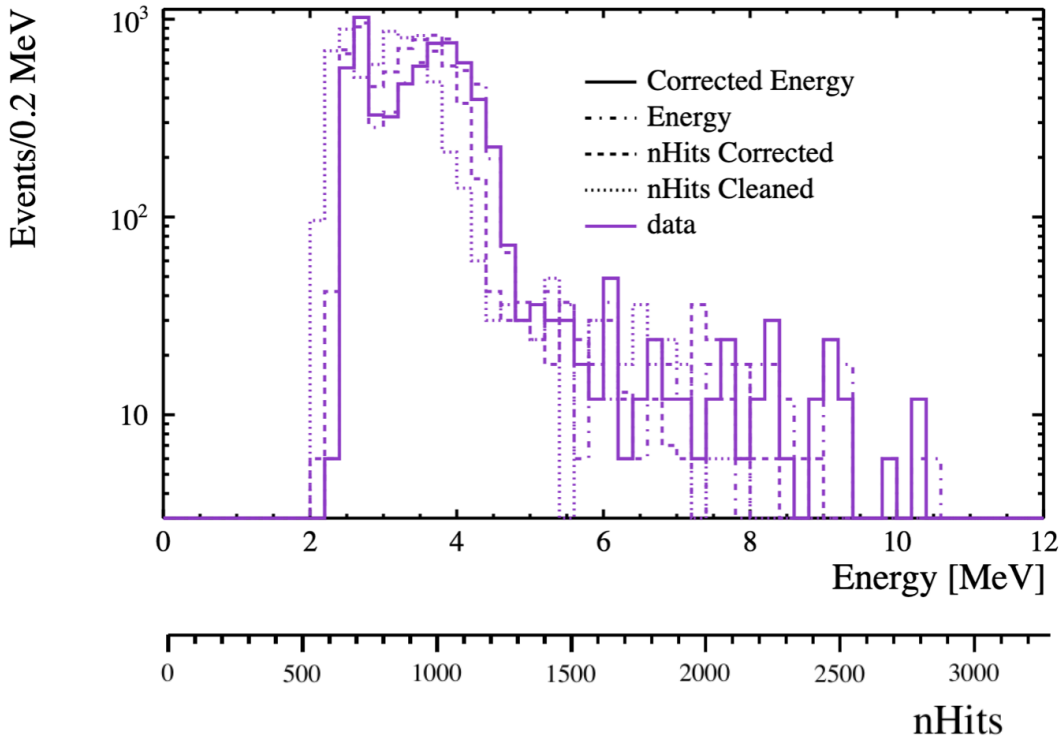


Figure 5.23: Energy profile of the full [2.5, 14] MeV region. Additional cuts revealed the distinctive '2.2 MeV excess' tail and ^{208}Tl peak features which were indiscernible in figure 5.17.

The fit will be performed over the 'lowE', 'highE', 0.7 LLR, ^{208}Tl peak and full energy regions. The expected events per region alongside the number events surviving the selection cuts are tabulated in table 5.9 with the fit results. Figure 5.24 presents the fit over all 1303 events passing the background cuts detailed in table 5.8. The number of expected ^{8}B ν_e events only makes up ~10% of the reconstructed events in

this region. However, The best fit, ^{8}B ν_e signal + ^{208}Tl background, in green does show the 0.67 cos$\theta_\odot$ peak structure from the ^{8}B MC. The model fits to 175^{+43}_{-56}(stat.) ± 76(syst.) signal events to 1128^{+276}_{-361}(stat.) ± 489(syst.) background events, confirming that the data is not fully compatible with the background-only hypothesis in blue.

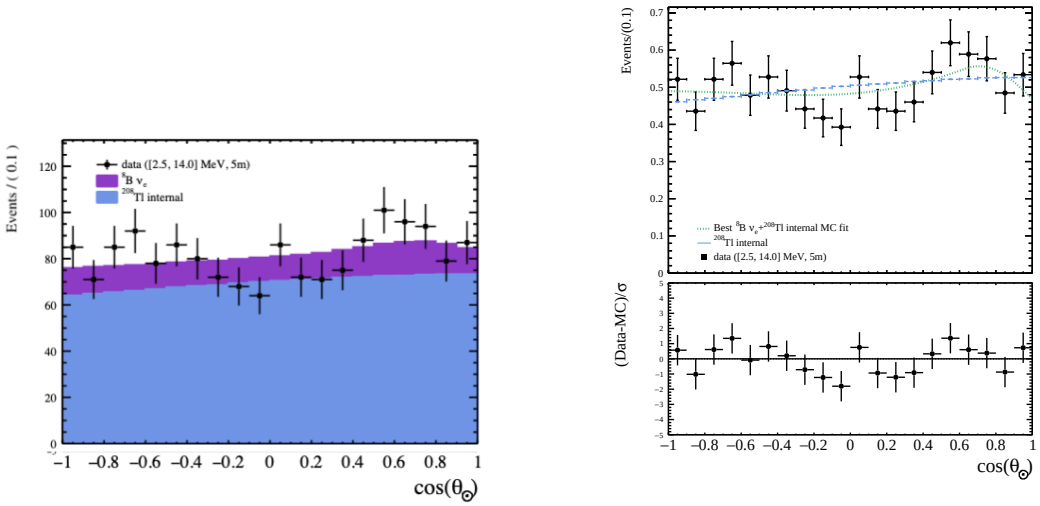
Cut Region	Expected Events	Events in Region	Fit Events
E>2.5 MeV, 5 m	103	1303	175^{+43}_{-56}(stat.) ± 76(syst.)
2.5<E<2.8 MeV, 5 m	9	90	12^{+16}_{-8}(stat.) ± 17(syst.)
E∈ [2.5, 2.8] & [4.6, 14.0] MeV (0.7 LLR), 5 m	85	507	111^{+23}_{-25}(stat.) ± 34(syst.)
E>5 MeV, 5 m	83	88	86^{+3}_{-11}(stat.) ± 7(syst.)
2.8<E<4.6 MeV, 5 m	18	793	66^{+31}_{-57}(stat.) ± 53(syst.)

Table 5.9: Expected and fitted events for different energy and fiducial volume regions with lesser backgrounds.

As a sanity check, the high energy region above 5 MeV which was obtained from a different set of cuts and used to tune the CID methodology will be isolated in this dataset. The data from figure 5.25 can be directly compared to that of figure 5.15. The previous dataset yielded a fit of 81 ± 4 to the expected 83 events in this region, this new dataset converges on a 86^{+3}_{-11}(stat.) ± 7(syst.) result.

Using the 0.7 LLR range to avoid the ^{208}Tl peak, figure 5.26 excludes events having an energy within the [2.8, 4.6] MeV region from the distribution. However, it still includes the high background levels present in the lower [2.5, 2.8] MeV range. In doing so, the fit result slightly improves to 111^{+23}_{-25}(stat.) ± 34(syst.) though with lower statistics, the model tends to overfitting with wide statistical and systematic uncertainties.

As a better test of the efficacy of the model in extracting directional solar events in



(a) (b)

Figure 5.24: (a) $\cos\theta_\odot$ distribution of the 5 first PMT hits as ordered by their time residual value (black) from the PPO dataset for events for the full energy spectrum ranging from 2.5 to 14.0 MeV compared to the stacked background (blue) and signal (violet) MC distributions. (b) Constrained fit result of the same dataset with the best fit (green) and background MC (blue) normalised distributions. Residuals are reported in the band beneath (b).

a high background region, the [2.8, 4.6] MeV region corresponding to the ^{208}Tl peak is fit. This is more relevant to analyses as this is a region where radioactive backgrounds and instrumental backgrounds are maximally reduced by other selection cuts. The fit result of 66^{+31}_{-57}(stat.) $\pm$ 53(syst.) solar events in a region where 18 were expected could at first glance suggest that the CID method can extract the few ^{8}B solar events within the ^{208}Tl peak. Upon closer inspection of figure 5.27, the residuals as well as the errors on the fit result, it is clear that the model is overfitting. It is possible that it struggles in differentiating a distribution trending in an upwards slope at positive values of $\cos\theta_\odot$ compared to the Cherenkov peak. Perhaps higher statistics would further flatten the distribution as is expected in this background dominated region.

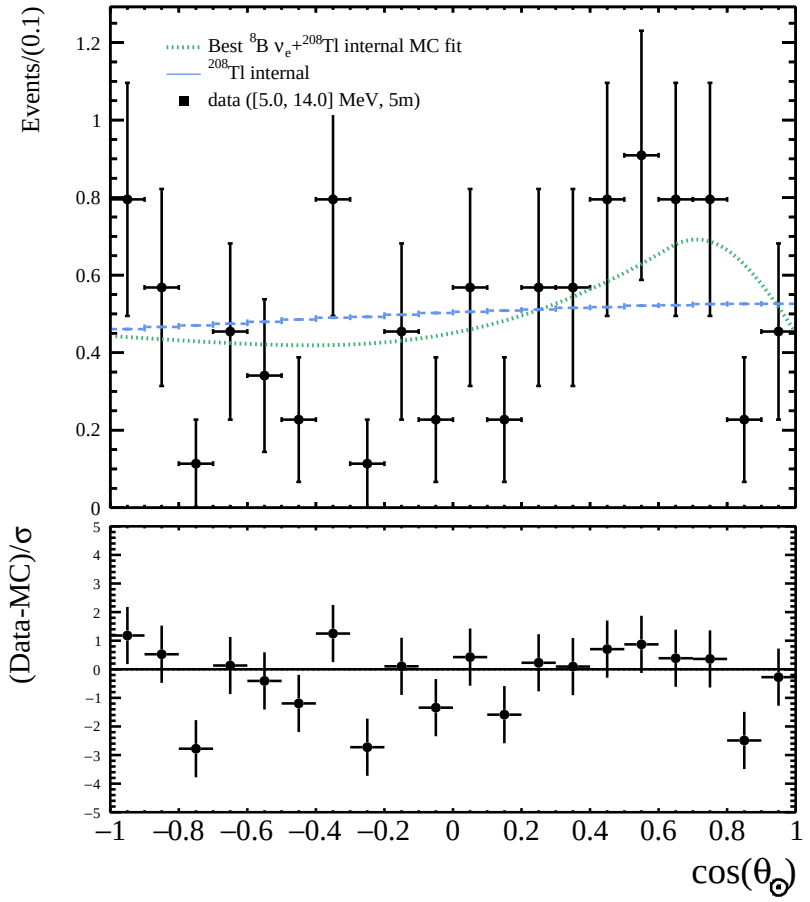


Figure 5.25: Constrained fit result of the $\cos\theta_\odot$ distribution of the 5 first PMT hits as ordered by their time residual value (black) from the PPO dataset for events for the energy region corresponding to [5.0, 14.0] MeV overlaid with the best fit (green) and background MC (blue) normalised distributions. Residuals are reported in the band beneath the main plot.

Finally, as solar analyses try to push the lower energy limit ever further, the [2.5, 2.8] MeV energy band was isolated. Despite this region being populated with the tail of the '2.2 MeV excess', it avoids the ^{208}Tl peak. The distribution of these events is presented in figure 5.28. While a directional peak remains visible, the model converges on a fit that is, similar to the $0\nu\beta\beta$ fit in the previous section, prone to both statistical

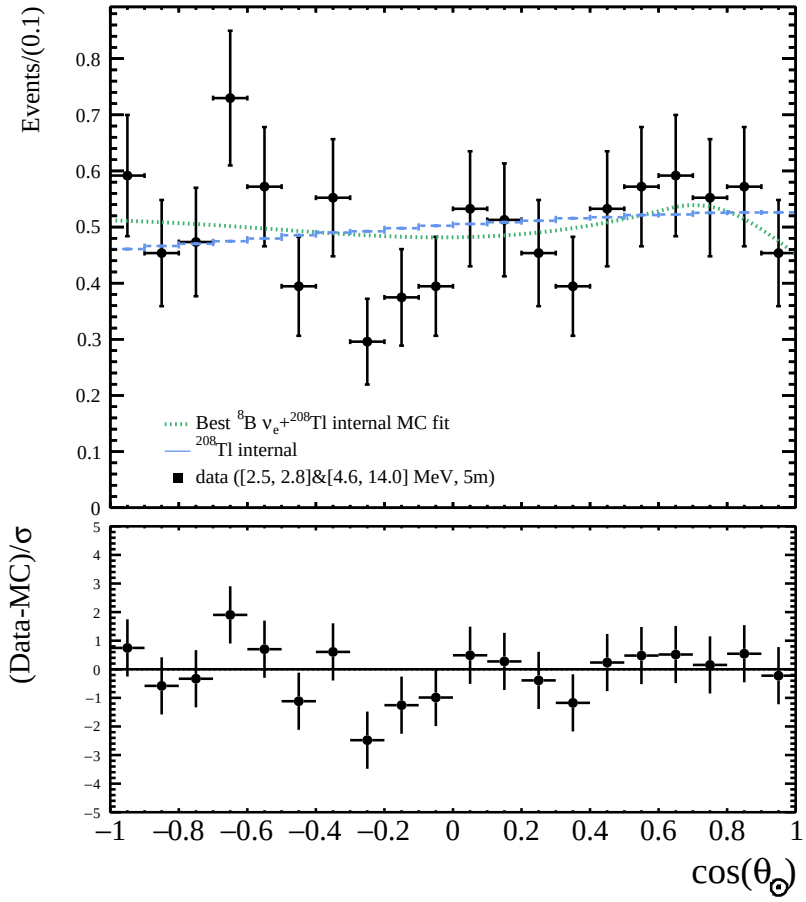


Figure 5.26: Constrained fit result of the $\cos\theta_\odot$ distribution of the 5 first PMT hits as ordered by their time residual value (black) from the PPO dataset for events for the energy region corresponding to [2.5, 2.8] MeV and [4.6, 14.0] MeV overlaid with the best fit (green) and background MC (blue) normalised distributions. Residuals are reported in the band beneath the main plot.

limitations and overfitting from the signal PDF shape parameters absorbing much of the fluctuations. Nine expected events in this region are fit as $12^{+16}_{-8}(\text{stat.}) \pm 17(\text{syst.})$.

The largeness of the uncertainties returned by the model are a symptom of the statistical limitations of a method relying on accumulating large statistics. As has

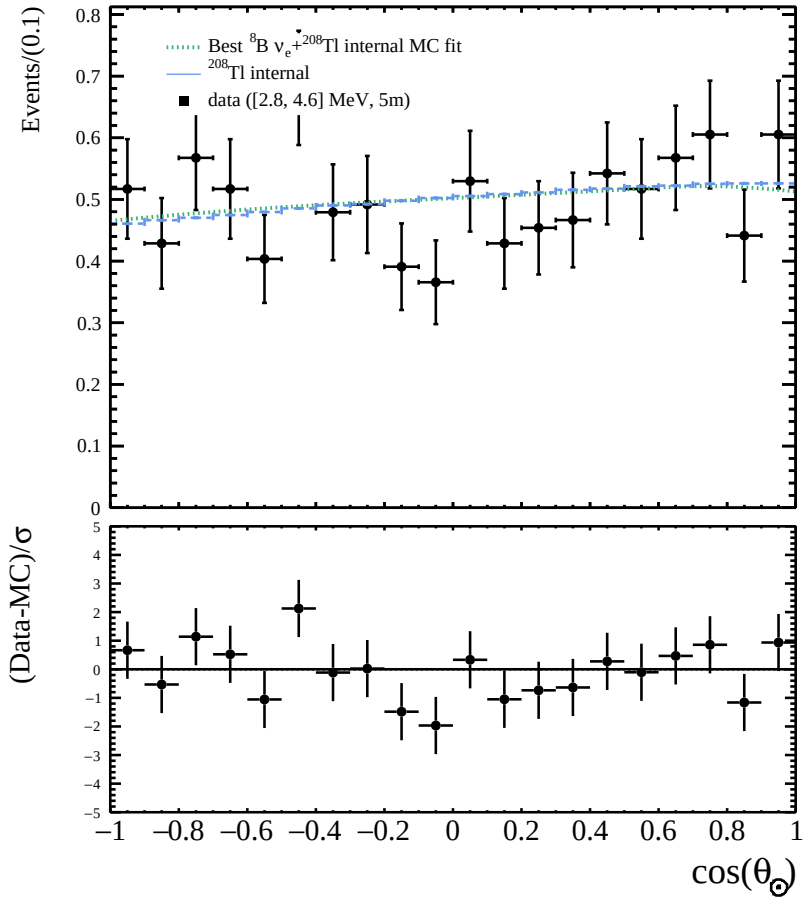


Figure 5.27: Constrained fit result of the $\cos\theta_\odot$ distribution of the 5 first PMT hits as ordered by their time residual value (black) from the PPO dataset for events for the energy region corresponding to ^{208}Tl peak between [2.8, 4.6] MeV overlaid with the best fit (green) and background MC (blue) normalised distributions. Residuals are reported in the band beneath the main plot.

been repeatedly emphasized, the LAB+PPO scintillator phase only ran for a total of 142 days of usable physics livetime with maximal detector coverage. The expected solar events in this time period within a fiducial volume of 5 m is therefore quite limited, and even more so when only certain energy bins are considered. Specifically,

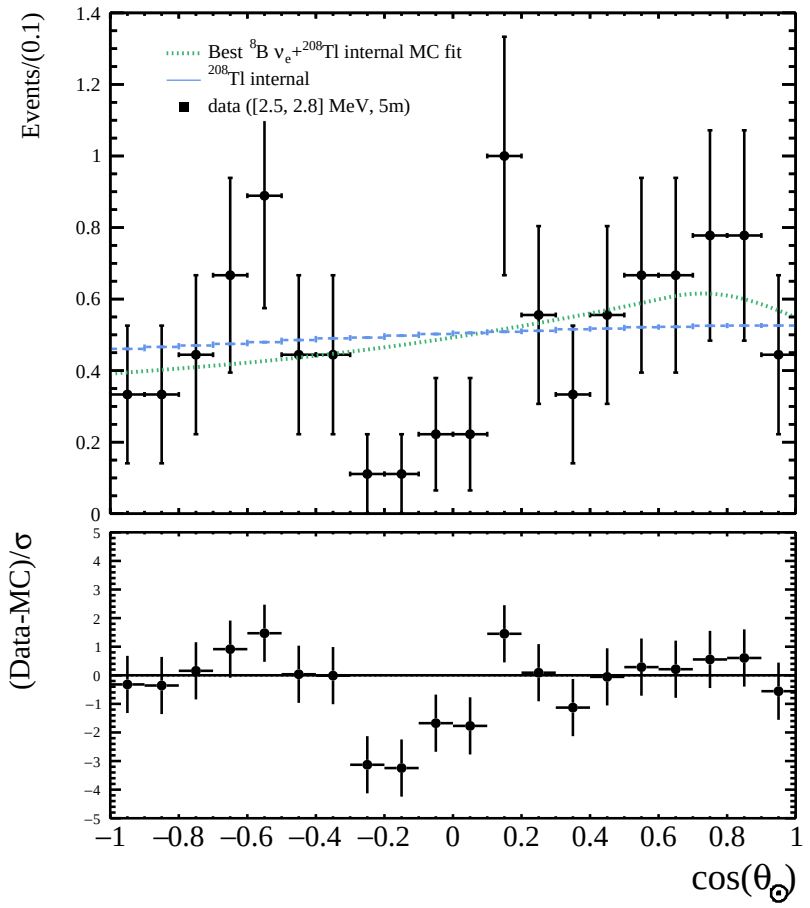


Figure 5.28: Constrained fit result of the $\cos\theta_\odot$ distribution of the 5 first PMT hits as ordered by their time residual value (black) from the PPO dataset for events for the [2.5, 2.8] MeV energy band overlaid with the best fit (green) and background MC (blue) normalised distributions. Residuals are reported in the band beneath the main plot.

in the region where the ^{8}B solar neutrino flux is dominated by the ^{208}Tl background, between 2.8 and 4.6 MeV, the CID method was not effective in definitively resolving the two event classes without large statistical and systematic uncertainties. The systematics were modeled as flexible shape parameters that were meant to absorb unkowns concerning the detector response that may affect the position and width

of the $\cos\theta_\odot$ peak. This analysis was performed on the LAB+PPO phase rather than the Enhanced Scintillator phase for the simple fact that, at the time of carrying out this analysis, the bis-MSB optical model was still being developed. At the time of writing, many clarifying calibration campaigns that have a minimal though non-negligible effect on the reconstruction resolution of the detector response as well as on the optical model itself were being carried through. Time residual ordering and event direction reconstruction through PMT position rely on accurate modeling of the angular response of the PMTs. The deployment of the AmBe source and the Laserball occurred during the enhanced scintillator fill, leaving a gap during the data period chosen. More importantly, the aging of the PMT concentrators is neither modeled or accounted for. The uncertainty associated with these metrics is included in the large systematic uncertainty bars.

Though the CID methodology was not effective in the narrow lower energy region both for solar and $0\nu\beta\beta$ analyses, it has been proven to successfully identify solar events through a directional $\cos\theta_\odot$ signature to energies as low as 2.5 MeV. SNO+ can retrieve early directional Cherenkov light in a medium developed to maximise isotropic scintillation light.

Chapter 6

Conclusion

The Remains of the Day

K. Ishiguro

In its quest to probe the phase space where an interaction holding the key likely to unlock physics beyond the Standard Model, the international astroparticle physics community has commissioned the next generation of large scale neutrino detectors. SNO+ and KamLAND-Zen have been in the foreground of the road leading to neutrinoless double beta decay detection. Other large scale water-based experiments such as Super-Kamiokande and soon-to-be Hyper-K have ongoing solar neutrino physics programs. JUNO, the large liquid scintillator based experiment only recently going online is focused on solving neutrino mass ordering. While usually commissioned for one specific physics goal, these detectors are versatile. In its current scintillator stage, SNO+ was focused on solar neutrinos and background characterisation. Directionality, the subject of this thesis, dwells in the narrow space where this distinct combination of scintillation light and directional neutrino sources overlap.

This thesis has shown that the methodology of Cherenkov timing separation is possible in the SNO+ LAB+PPO phase. The earliest light to reach the PMTs is

selected by ordering these registered hits by their time residual value; a value that takes into account the PMT hit time, the event time and the travel time of the photons through the detector. This is expected to be Cherenkov light as its propagation mecanism is instantaneous. Scintillation light, though increasingly fast with the addition of fluors in the liquid scintillator, propagates in an isotropic manner with predictable timing profiles dependent on the scintillation process. The Correlated Integrated Directionality method therefore selects these early hits for each event interacting within the detector volume and relates it to the Sun direction at the time of the event. This is the $\cos\theta_{\odot}$ variable. The algorithm fits a model composed of the probability density functions of the $\cos\theta_{\odot}$ distributions of a ^{8}B solar neutrino signal and ^{208}Tl flat background to the $\cos\theta_{\odot}$ distributions of the selected early hits in the PPO phase data, thus discerning directional light within a medium developed to maximise isotropic light propagation. This result is applicable across the ^{8}B energy range extending down to 2.5 MeV for a dataset having undergone selection cuts to reject radioactive and instrumental backgrounds. The energy range was divided into regions of interest relevant to different physics analyses. The Correlated Integrated Directionality methodology was tested on the low energy region below the ^{208}Tl peak for low energy solar analyses, on the narrow $0\nu\beta\beta$ region, on the ^{208}Tl peak itself as a potential background rejection classifier, and on the high energy region dominated by solar signal. It was found that directionality can be recovered throughout these regions; the performance of the model being strongly tied to the statistical significance of the expected solar signal with respect to the background events counted in the detector. As such, the high energy region naturally provides the best fit result.

This thesis has also focused on characterising the SNO+ enhanced scintillator

phase through the addition of bis-MSB. The current state of the optical properties of the scintillator cocktail through *in* and *ex situ* measurements in parallel with the deployment strategy were reported. While the experiment has been collecting data in this phase over the past 3 years, the gain in statistics requires the new optical model, currently in use for the Enhanced Scintillator phase. The methodology would need to be tested and adjusted in light of the changes induced by the addition of this wavelength shifting secondary fluor; the physics and chemistry of which were the subject of chapter 4.

Though SNO+ has demonstrated it can apply Borexino's Correlated Integrated Directionality methodology to its dataset, limited livetime and large background rates were the main obstacles in applying it to the low energy regions of interest either to low energy ^{8}B solar analyses or the $0\nu\beta\beta$ search for the specific time period chosen for this thesis. Nonetheless, this thesis has shown that the timing resolution of the SNO+ PMTs is precise enough for Cherenkov light to be perceived before scintillation – a recovery of directionality via the Correlated Integrated Directionality method in a liquid scintillator experiment.

Bibliography

[1] J. N. Abdurashitov et al. "Solar Neutrino Flux Measurements by the Soviet-American Gallium Experiment (SAGE) for Half the 22-Year Solar Cycle". In: *Journal of Experimental and Theoretical Physics* 95.2 (Aug. 2002), pp. 181–193. ISSN: 1090-6509. DOI: 10.1134/1.1506424.

[2] JN Abdurashitov et al. "The Russian-American gallium experiment (SAGE) Cr neutrino source measurement". In: *Physical Review Letters* 77.23 (1996), p. 4708.

[3] K. Abe et al. "Measurement of Neutrino and Antineutrino Oscillations by the T2K Experiment Including a New Additional Sample of ν_e Interactions at the Far Detector". In: *Physical Review D* 96.9 (Nov. 2017), p. 092006. ISSN: 2470-0010, 2470-0029. DOI: 10.1103/PhysRevD.96.092006. arXiv: 1707.01048 [hep-ex].

[4] Shingo Abe et al. "Precision measurement of neutrino oscillation parameters with KamLAND". In: *Physical review letters* 100.22 (2008), p. 221803.

[5] M. Abreu et al. *Measurement of Reactor Antineutrino Oscillations with 1.46 Ktonne-Years of Data at SNO+*. Nov. 2025. DOI: 10.48550/arXiv.2511.11856. arXiv: 2511.11856 [hep-ex].

[6] Angel Abusleme et al. *First Measurement of Reactor Neutrino Oscillations at JUNO*. Nov. 2025. DOI: 10.48550/arXiv.2511.14593. arXiv: 2511.14593 [hep-ex].

[7] M. A. Acero et al. "An Improved Measurement of Neutrino Oscillation Parameters by the NOvA Experiment". In: *Physical Review D* 106.3 (Aug. 2022), p. 032004. ISSN: 2470-0010, 2470-0029. DOI: 10.1103/PhysRevD.106.032004. arXiv: 2108.08219 [hep-ex].

[8] B Acharya et al. "Solar fusion III: New data and theory for hydrogen-burning stars". In: *Reviews of Modern Physics* 97.3 (2025), p. 035002.

[9] M. Agostini et al. "Correlated and Integrated Directionality for Sub-MeV Solar Neutrinos in Borexino". In: *Physical Review D* 105.5 (Mar. 2022), p. 052002. ISSN: 2470-0010, 2470-0029. DOI: 10.1103/PhysRevD.105.052002. arXiv: 2109.04770 [hep-ex, physics:physics].

[10] M. Agostini et al. "Simultaneous Precision Spectroscopy of *pp*, ^{7}Be, and *pep* Solar Neutrinos with Borexino Phase-II". In: *Physical Review D* 100.8 (Oct. 2019), p. 082004. ISSN: 2470-0010, 2470-0029. DOI: 10.1103/PhysRevD.100.082004. arXiv: 1707.09279 [hep-ex].

[11] Q.R. Ahmad. "Muon Correlated Background at the Sudbury Neutrino Observatory". PhD thesis. Brown University, 2002.

[12] A. Allega et al. "Event-by-Event Direction Reconstruction of Solar Neutrinos in a High Light-Yield Liquid Scintillator". In: *Physical Review D* 109.7 (Apr. 2024), p. 072002. ISSN: 2470-0010, 2470-0029. DOI: 10.1103/PhysRevD.109.072002. arXiv: 2309.06341 [hep-ex].

[13] R. Alves et al. "The Calibration System for the Photomultiplier Array of the SNO+ Experiment". In: *Journal of Instrumentation* 10.03 (Mar. 2015), P03002–P03002. ISSN: 1748-0221. DOI: 10.1088/1748-0221/10/03/P03002. arXiv: 1411.4830 [physics].

[14] J. F. Amsbaugh et al. "An Array of Low-Background ^3He Proportional Counters for the Sudbury Neutrino Observatory". In: *Nuclear Instruments and Methods in Physics Research Section A: Accelerators, Spectrometers, Detectors and Associated Equipment* 579.3 (Sept. 2007), pp. 1054–1080. ISSN: 01689002. DOI: 10.1016/j.nima.2007.05.321. arXiv: 0705.3665 [nucl-ex].

[15] Amsler, P. and et al. (Particle Data Group). "Leptons". In: *Particle Data Group (PDG)* PL B667, 1. (2019). URL: https://pdg.lbl.gov/2019/tables/rpp2019-sum-leptons.pdf.

[16] Luis Anchordoqui et al. "Ultrahigh Energy Cosmic Rays: The State of the Art before the Auger Observatory". In: *International Journal of Modern Physics A* 18.13 (May 2003), pp. 2229–2366. ISSN: 0217-751X, 1793-656X. DOI: 10.1142/S0217751X03013879. arXiv: hep-ph/0206072.

[17] M. Anderson. "Studies of Machine Learning for Event Reconstruction in the SNO+ Detector and Electronic Noise Removal in P-Type Point Contact High Purity Germanium Detectors". PhD thesis. July 2024.

[18] *Are Neutrinos Their Own Antiparticles?* URL: https://next-experiment.org/experiment/neutrinoless-double-beta-decay/.

[19] D. J. Auty et al. "A Method to Load Tellurium in Liquid Scintillator for the Study of Neutrinoless Double Beta Decay". In: *Nuclear Instruments and*

Methods in Physics Research Section A: Accelerators, Spectrometers, Detectors and Associated Equipment 1051 (June 2023), p. 168204. ISSN: 01689002. DOI: 10.1016/j.nima.2023.168204. arXiv: 2212.12444 [physics].

[20] *AvaLight-D(H)-S*. URL: https://www.avantes.com/products/light-sources/halogen-and-deuterium-halogen/avalight-dh-s/.

[21] Frank T. Avignone, Steven R. Elliott, and Jonathan Engel. "Double Beta Decay, Majorana Neutrinos, and Neutrino Mass". In: *Reviews of Modern Physics* 80.2 (Apr. 2008), pp. 481–516. ISSN: 0034-6861, 1539-0756. DOI: 10.1103/RevModPhys.80.481. arXiv: 0708.1033 [nucl-ex].

[22] Bacon, A. and Tam, B. *SNO+ Scintillator (LAB+2.2g/L PPO) Light Yield*. Tech. rep. SNO+ Internal Document, June 2022. URL: DocDB:7506-v1.

[23] John N Bahcall and Carlos Pena-Garay. "Solar Models and Solar Neutrino Oscillations". In: *New Journal of Physics* 6 (June 2004), pp. 63–63. ISSN: 1367-2630. DOI: 10.1088/1367-2630/6/1/063.

[24] John N. Bahcall and M. H. Pinsonneault. "What Do We (Not) Know Theoretically about Solar Neutrino Fluxes?" In: *Physical Review Letters* 92.12 (Mar. 2004), p. 121301. ISSN: 0031-9007, 1079-7114. DOI: 10.1103/PhysRevLett.92.121301. arXiv: astro-ph/0402114.

[25] John N. Bahcall and Roger K. Ulrich. "Solar Models, Neutrino Experiments, and Helioseismology". In: *Reviews of Modern Physics* 60.2 (Apr. 1988), pp. 297–372. DOI: 10.1103/RevModPhys.60.297.

[26] Bahcall, J. N. "Solar Models: An Historical Overview". In: *Nuclear Physics B* Proceedings Supplements.118 (2003) 77-86 ().

[27] J. Barea and F. Iachello. "Neutrinoless Double-Beta Decay in the Microscopic Interacting Boson Model". In: *Physical Review C* 79.4 (Apr. 2009), p. 044301. ISSN: 0556-2813, 1089-490X. DOI: 10.1103/PhysRevC.79.044301.

[28] D. Basilico et al. "Final Results of Borexino on CNO Solar Neutrinos". In: *Physical Review D* 108.10 (Nov. 2023), p. 102005. ISSN: 2470-0010, 2470-0029. DOI: 10.1103/PhysRevD.108.102005. arXiv: 2307.14636 [hep-ex].

[29] Daya Bay et al. *Optimization of the JUNO Liquid Scintillator Composition Using a Daya Bay Antineutrino Detector*. July 2020. DOI: 10.48550/arXiv.2007.00314. arXiv: 2007.00314 [physics].

[30] J.J. Beatty, J. Matthews, and S.P. Wakely. "Cosmic Rays". In: *Particle Data Group Reviews* (2019), p. 21. URL: https://pdg.lbl.gov/2019/reviews/rpp2019-rev-cosmic-rays.pdf.

[31] Alain Bellerive. "Review of Solar Neutrino Experiments". In: *International Journal of Modern Physics A* 19.08 (Mar. 2004), pp. 1167–1179. ISSN: 0217-751X, 1793-656X. DOI: 10.1142/S0217751X04019093. arXiv: hep-ex/0312045.

[32] Giovanni Benato. "Effective Majorana Mass and Neutrinoless Double Beta Decay". In: *The European Physical Journal C* 75.11 (Nov. 2015), p. 563. ISSN: 1434-6044, 1434-6052. DOI: 10.1140/epjc/s10052-015-3802-1. arXiv: 1510.01089 [hep-ph].

[33] H.A. Bethe. *Elementary Nuclear Theory*. 1st ed. Hoboken (N. J.): J. Wiley & Sons, 1947.

[34] A. Bialek et al. "A Rope-Net Support System for the Liquid Scintillator Detector for the SNO+ Experiment". In: *Nuclear Instruments and Methods in*

Physics Research Section A: Accelerators, Spectrometers, Detectors and Associated Equipment 827 (Aug. 2016), pp. 152–160. ISSN: 01689002. DOI: 10.1016/j.nima.2016.04.114.

[35] S. M. Bilenky. "Neutrino. History of a Unique Particle". In: *The European Physical Journal H* 38.3 (Apr. 2013), pp. 345–404. ISSN: 2102-6459, 2102-6467. DOI: 10.1140/epjh/e2012-20068-9. arXiv: 1210.3065 [hep-ph].

[36] S. M. Bilenky and C. Giunti. "Neutrinoless Double-Beta Decay. A Brief Review". In: *Modern Physics Letters A* 27.13 (Apr. 2012), p. 1230015. ISSN: 0217-7323, 1793-6632. DOI: 10.1142/S0217732312300157. arXiv: 1203.5250 [hep-ph].

[37] S.D Biller et al. "Measurements of Photomultiplier Single Photon Counting Efficiency for the Sudbury Neutrino Observatory". In: *Nuclear Instruments and Methods in Physics Research Section A: Accelerators, Spectrometers, Detectors and Associated Equipment* 432.2-3 (Aug. 1999), pp. 364–373. ISSN: 01689002. DOI: 10.1016/S0168-9002(99)00500-8.

[38] Steven D. Biller. "Combined Constraints on Majorana Masses from Neutrinoless Double Beta Decay Experiments". In: *Physical Review D* 104.1 (July 2021), p. 012002. ISSN: 2470-0010, 2470-0029. DOI: 10.1103/PhysRevD.104.012002. arXiv: 2103.06036 [hep-ex].

[39] J B Birks. *The Theory and Practice of Scintillation Counting*. London: Pergamon Press, 1964.

[40] J. B. Birks. "Theory of the Response of Organic Scintillation Crystals to Short-Range Particles". In: *Physical Review* 86.4 (May 1952), pp. 569–569. ISSN: 0031-899X. DOI: 10.1103/PhysRev.86.569.

[41] A. Bobyk, W. A. Kaminski, and F. Simkovic. "Neutrinoless Double Beta Decay within Self-consistent Renormalized Quasiparticle Random Phase Approximation and Inclusion of Induced Nucleon Currents". In: *Physical Review C* 63.5 (Apr. 2001), p. 051301. ISSN: 0556-2813, 1089-490X. DOI: 10.1103/PhysRevC.63.051301. arXiv: nucl-th/0012010.

[42] E. J. Bowen and A. Norton. "The Quenching of Fluorescence in Solution". In: *Transactions of the Faraday Society* 35 (1939), p. 44. ISSN: 0014-7672. DOI: 10.1039/tf9393500044.

[43] Christian Buck and Minfang Yeh. "Metal-Loaded Organic Scintillators for Neutrino Physics". In: *Journal of Physics G: Nuclear and Particle Physics* 43.9 (Sept. 2016), p. 093001. ISSN: 0954-3899, 1361-6471. DOI: 10.1088/0954-3899/43/9/093001. arXiv: 1608.04897 [physics].

[44] Adam Burrows, Klein Klein, and Raj Gandhi. "The Future of Supernova Neutrino Detection". In: *Physical Review D* 45.10 (May 1992), pp. 3361–3385. DOI: 10.1103/PhysRevD.45.3361.

[45] Cameron, J. "The Photomultiplier Tube Calibration of the Sudbury Neutrino Observatory". PhD thesis. 2001.

[46] J. Caravaca et al. "Characterization of Water-Based Liquid Scintillator for Cherenkov and Scintillation Separation". In: *The European Physical Journal*

C 80.9 (Sept. 2020), p. 867. ISSN: 1434-6044, 1434-6052. DOI: 10.1140/epjc/s10052-020-8418-4.

[47] CEPSA Quimica Becancour Inc. *CEPSA PetreLAB 500-Q Safety Data Sheet*.

[48] P. A. Čerenkov. "Visible Radiation Produced by Electrons Moving in a Medium with Velocities Exceeding That of Light". In: *Physical Review* 52.4 (Aug. 1937), pp. 378–379. DOI: 10.1103/PhysRev.52.378.

[49] WU Yu-Cheng et al. "Measurement of Cosmic Ray Flux in China JinPing Underground Laboratory". In: ().

[50] BT Cleveland et al. "Update on the measurement of the solar neutrino flux with the Homestake chlorine detector". In: *Nuclear Physics B Proceedings Supplements* 38 (1995), p. 47.

[51] Cleveland, B. et al. "Results from the Homestake Solar Neutrino Observatory". In: *The Astrophysical Journal* (1998), pp. 496, 505.

[52] Daya Bay Collaboration et al. "Measurement of Electron Antineutrino Oscillation with 1958 Days of Operation at Daya Bay". In: *Physical Review Letters* 121.24 (Dec. 2018), p. 241805. ISSN: 0031-9007, 1079-7114. DOI: 10.1103/PhysRevLett.121.241805. arXiv: 1809.02261 [hep-ex].

[53] Double Chooz Collaboration et al. "Reactor Rate Modulation Oscillation Analysis with Two Detectors in Double Chooz". In: *Journal of High Energy Physics* 2021.1 (Jan. 2021), p. 190. ISSN: 1029-8479. DOI: 10.1007/JHEP01(2021)190. arXiv: 2007.13431 [hep-ex].

[54] DUNE Collaboration et al. "Long-Baseline Neutrino Oscillation Physics Potential of the DUNE Experiment". In: *The European Physical Journal C* 80.10 (Oct. 2020), p. 978. ISSN: 1434-6044, 1434-6052. DOI: 10.1140/epjc/s10052-020-08456-z. arXiv: 2006.16043 [hep-ex].

[55] IceCube Collaboration et al. "Measurement of Atmospheric Neutrino Oscillations at 6-56 GeV with IceCube DeepCore". In: *Physical Review Letters* 120.7 (Feb. 2018), p. 071801. ISSN: 0031-9007, 1079-7114. DOI: 10.1103/PhysRevLett.120.071801. arXiv: 1707.07081 [hep-ex].

[56] MINOS+ Collaboration et al. "Precision Constraints for Three-Flavor Neutrino Oscillations from the Full MINOS+ and MINOS Data Set". In: *Physical Review Letters* 125.13 (Sept. 2020), p. 131802. ISSN: 0031-9007, 1079-7114. DOI: 10.1103/PhysRevLett.125.131802. arXiv: 2006.15208 [hep-ex].

[57] S. N. O. Collaboration et al. "Combined Analysis of All Three Phases of Solar Neutrino Data from the Sudbury Neutrino Observatory". In: *Physical Review C* 88.2 (Aug. 2013), p. 025501. ISSN: 0556-2813, 1089-490X. DOI: 10.1103/PhysRevC.88.025501. arXiv: 1109.0763 [nucl-ex].

[58] SAGE Collaboration et al. "Measurement of the Solar Neutrino Capture Rate with Gallium Metal. III: Results for the 2002–2007 Data-Taking Period". In: *Physical Review C* 80.1 (July 2009), p. 015807. ISSN: 0556-2813, 1089-490X. DOI: 10.1103/PhysRevC.80.015807. arXiv: 0901.2200 [nucl-ex].

[59] SNO+ Collaboration et al. *Cosmogenic Neutron Production in Water at SNO+*. Nov. 2025. DOI: 10.48550/arXiv.2511.04600. arXiv: 2511.04600 [hep-ex].

[60] SNO+ Collaboration et al. "Current Status and Future Prospects of the SNO+ Experiment". In: *Advances in High Energy Physics* 2016 (2016), pp. 1–21. ISSN: 1687-7357, 1687-7365. DOI: 10.1155/2016/6194250. arXiv: 1508.05759 [physics].

[61] SNO+ Collaboration et al. "Development, Characterisation, and Deployment of the SNO+ Liquid Scintillator". In: *Journal of Instrumentation* 16.05 (May 2021), P05009. ISSN: 1748-0221. DOI: 10.1088/1748-0221/16/05/P05009. arXiv: 2011.12924 [physics].

[62] SNO+ Collaboration et al. *First Evidence of Solar Neutrino Interactions on* ^{13}C. Oct. 2025. DOI: 10.48550/arXiv.2508.20844. arXiv: 2508.20844 [nucl-ex].

[63] SNO+ Collaboration et al. "Measurement of Reactor Antineutrino Oscillation at SNO+". In: *Physical Review Letters* 135.12 (Sept. 2025), p. 121801. ISSN: 0031-9007, 1079-7114. DOI: 10.1103/gypt-lc9v. arXiv: 2505.04469 [hep-ex].

[64] SNO+ Collaboration et al. "Optical Calibration of the SNO+ Detector in the Water Phase with Deployed Sources". In: *Journal of Instrumentation* 16.10 (Oct. 2021), P10021. ISSN: 1748-0221. DOI: 10.1088/1748-0221/16/10/P10021. arXiv: 2106.03951 [physics].

[65] SNO+ Collaboration et al. "The SNO+ Experiment". In: *Journal of Instrumentation* 16.08 (Aug. 2021), P08059. ISSN: 1748-0221. DOI: 10.1088/1748-0221/16/08/P08059. arXiv: 2104.11687 [physics].

[66] Super-Kamiokande Collaboration et al. "Atmospheric Neutrino Oscillation Analysis with External Constraints in Super-Kamiokande I-IV". In: *Physical Review D* 97.7 (Apr. 2018), p. 072001. ISSN: 2470-0010, 2470-0029. DOI: 10.1103/PhysRevD.97.072001. arXiv: 1710.09126 [hep-ex].

[67] Super-Kamiokande Collaboration et al. "Solar Neutrino Measurements in Super-Kamiokande-IV". In: *Physical Review D* 94.5 (Sept. 2016), p. 052010. ISSN: 2470-0010, 2470-0029. DOI: 10.1103/PhysRevD.94.052010. arXiv: 1606.07538 [hep-ex].

[68] T2K Collaboration et al. "Improved Constraints on Neutrino Mixing from the T2K Experiment with 3.13×10^{21} Protons on Target". In: *Physical Review D* 103.11 (June 2021), p. 112008. ISSN: 2470-0010, 2470-0029. DOI: 10.1103/PhysRevD.103.112008. arXiv: 2101.03779 [hep-ex].

[69] The Borexino Collaboration. "Precision Measurement of the 7Be Solar Neutrino Interaction Rate in Borexino". In: *Physical Review Letters* 107.14 (Sept. 2011), p. 141302. ISSN: 0031-9007, 1079-7114. DOI: 10.1103/PhysRevLett.107.141302. arXiv: 1104.1816 [hep-ex].

[70] The KamLAND Collaboration. "Precision Measurement of Neutrino Oscillation Parameters with KamLAND". In: *Physical Review Letters* 100.22 (June 2008), p. 221803. ISSN: 0031-9007, 1079-7114. DOI: 10.1103/PhysRevLett.100.221803. arXiv: 0801.4589 [hep-ex].

[71] The SNO Collaboration. "The Sudbury Neutrino Observatory". In: *Nuclear Instruments and Methods in Physics Research Section A: Accelerators, Spectrometers, Detectors and Associated Equipment* 449.1-2 (July 2000), pp. 172–

207. ISSN: 01689002. DOI: 10.1016/S0168-9002(99)01469-2. arXiv: nucl-ex/9910016.

[72] The SNO+ Collaboration. *RAT scripts: Energy Reconstruction*. June 2023. URL: https://github.com/snoplus/rat/blob/master/src/fit/methods/EnergyRThetaFunctional.cc.

[73] Cookman, D. "Measurement of Oscillations in Solar Boron-8 Neutrinos and Studies of Optical Scattering in the SNO+ Detector". PhD thesis. University of Oxford, 2023.

[74] Cookman, D. *Scintillator Solar Analysis Update for March CM*. Tech. rep. SNO+ Internal Document, Mar. 2026. URL: DocDB:9026-v1.

[75] Cookman, D. *The Position-Dependent Residual Energy Calibration of the SNO+ Detector in the BisMSB Phase*. Tech. rep. SNO+ Internal Document, Mar. 2025. URL: DocDB:8651-v2.

[76] G. Danby et al. "Observation of High-Energy Neutrino Reactions and the Existence of Two Kinds of Neutrinos". In: *Physical Review Letters* 9.1 (July 1962), pp. 36–44. DOI: 10.1103/PhysRevLett.9.36.

[77] Raymond Davis. "A Review of the Homestake Solar Neutrino Experiment". In: *Progress in Particle and Nuclear Physics* 32 (Jan. 1994), pp. 13–32. ISSN: 0146-6410. DOI: 10.1016/0146-6410(94)90004-3.

[78] Raymond Davis, Don S. Harmer, and Kenneth C. Hoffman. "Search for Neutrinos from the Sun". In: *Physical Review Letters* 20.21 (May 1968), pp. 1205–1209. DOI: 10.1103/PhysRevLett.20.1205.

[79] Stefano Dell'Oro et al. "Neutrinoless Double Beta Decay: 2015 Review". In: *Advances in High Energy Physics* 2016.1 (2016), p. 2162659. ISSN: 1687-7365. DOI: 10.1155/2016/2162659.

[80] "Direct neutrino-mass measurement with sub-electronvolt sensitivity". In: *Nature Physics* 18.2 (2022), pp. 160–166.

[81] Michelle J. Dolinski, Alan W. P. Poon, and Werner Rodejohann. "Neutrinoless Double-Beta Decay: Status and Prospects". In: *Annual Review of Nuclear and Particle Science* 69.1 (Oct. 2019), pp. 219–251. ISSN: 0163-8998, 1545-4134. DOI: 10.1146/annurev-nucl-101918-023407. arXiv: 1902.04097 [nucl-ex].

[82] F. Elisei et al. "Measurements of Liquid Scintillator Properties for the Borexino Detector". In: *Nuclear Instruments and Methods in Physics Research Section A: Accelerators, Spectrometers, Detectors and Associated Equipment* 400.1 (Nov. 1997), pp. 53–68. ISSN: 01689002. DOI: 10.1016/S0168-9002(97)00933-9.

[83] Fazzini, T. et al. "Electron Decay of the Pion". In: *Physical Review Letters* 1.7 (Oct. 1958). DOI: PhysRevLett.1.247.

[84] Ding Xue Feng et al. "Measurement of the Fluorescence Quantum Yield of Bis-MSB". In: *Chinese Physics C* 39.12 (Dec. 2015), p. 126001. ISSN: 1674-1137. DOI: 10.1088/1674-1137/39/12/126001. arXiv: 1506.00240 [physics].

[85] E. Fermi. "Versuch einer Theorie der Strahlen. I". In: *Zeitschrift fur Physik* 88.3-4 (Mar. 1934), pp. 161–177. ISSN: 1434-6001, 1434-601X. DOI: 10.1007/BF01351864.

[86] R. P. Feynman and M. Gell-Mann. "Theory of the Fermi Interaction". In: *Physical Review* 109.1 (Jan. 1958), pp. 193–198. DOI: 10.1103/PhysRev.109.193.

[87] Gianni Fiorentini et al. "Geo-Neutrinos: A Short Review". In: *Nuclear Physics B - Proceedings Supplements* 143 (June 2005), pp. 53–59. ISSN: 09205632. DOI: 10.1016/j.nuclphysbps.2005.01.087. arXiv: hep-ph/0409152.

[88] G.L Fogli et al. "A Global Analysis of the Atmospheric Neutrino Data". In: *Nuclear Instruments and Methods in Physics Research Section A: Accelerators, Spectrometers, Detectors and Associated Equipment* 451.1 (Aug. 2000), pp. 10–15. ISSN: 01689002. DOI: 10.1016/S0168-9002(00)00367-3.

[89] Ford, R. "A Scintillator Purification Plant and Fluid Handling System for SNO+". In: *LOW RADIOACTIVITY TECHNIQUES 2015 (LRT 2015): Proceedings of the 5th International Workshop in Low Radioactivity Techniques*. Seattle, WA, USA, 2015, p. 080003. DOI: 10.1063/1.4927998.

[90] Giunti, C. and Chung, W. K. *Neutrino Physics and Astrophysics*. Oxford University Press, 2007. ISBN: 978-0-19-850871-7.

[91] M. Goeppert-Mayer. "Double Beta-Disintegration". In: *Physical Review* 48.6 (Sept. 1935), pp. 512–516. DOI: 10.1103/PhysRev.48.512.

[92] D. E. Groom and S. R. Klein. "Passage of Particles through Matter". In: *The European Physical Journal C* 15.1-4 (Mar. 2000), pp. 163–173. ISSN: 1434-6044, 1434-6052. DOI: 10.1007/BF02683419.

[93] Thomas D. Gutierrez. *Standard Model Lagrangian*.

[94] E.D. Hallman. *Sudbury Neutrino Observatory Underground Spray Testing Urylon Plyurethane Coatings*. Tech. rep. SNO STR 93-010. Creighton Mine: Laurentian University, Jan. 1993.

[95] W. Hampel et al. "GALLEX Solar Neutrino Observations: Results for GALLEX IV". In: *Physics Letters B* 447.1 (Feb. 1999), pp. 127–133. ISSN: 0370-2693. DOI: 10.1016/S0370-2693(98)01579-2.

[96] Wolfgang Hampel et al. "GALLEX solar neutrino observations: Results for GALLEX IV". In: *Physics Letters B* 447.1-2 (1999), pp. 127–133.

[97] S. Hans et al. "Light Yield Quenching and Quenching Remediation in Liquid Scintillator Detectors". In: *Journal of Instrumentation* 15.12 (Dec. 2020), P12020–P12020. ISSN: 1748-0221. DOI: 10.1088/1748-0221/15/12/P12020.

[98] S. Hans et al. "Purification of Telluric Acid for SNO+ Neutrinoless Double-Beta Decay Search". In: *Nuclear Instruments and Methods in Physics Research Section A: Accelerators, Spectrometers, Detectors and Associated Equipment* 795 (Sept. 2015), pp. 132–139. ISSN: 01689002. DOI: 10.1016/j.nima.2015.05.045.

[99] P. Harvey and N. Barros. *RAT scripts: Sun Utility*. June 2000. URL: https://github.com/snoplus/rat/blob/master/src/util/SunUtil.cc.

[100] K. S. Hirata et al. "Search for Correlation of Neutrino Events with Solar Flares in Kamiokande". In: *Physical Review Letters* 61.23 (Dec. 1988), pp. 2653–2656. ISSN: 0031-9007. DOI: 10.1103/PhysRevLett.61.2653.

[101] A. K. Ichikawa. *Latest Results from the K2K Experiment*. June 2002. DOI: 10.48550/arXiv.hep-ex/0206037. arXiv: hep-ex/0206037.

[102] Inacio, A.S. "Data Analysis of the Water and Scintillator Phases of SNO+ from Solar Neutrino Measurements to Double Beta Decay Sensitivity Studies". PhD thesis. Universidade de Lisboa, 2022.

[103] Inacio, A.S. *Directionality Summary*. Tech. rep. SNO+ Internal Document, Mar. 2024. URL: DocDB:8151-v1.

[104] Inacio, A.S. and Kladnik, J. *Update on the Solar Neutrino Event Rate in SNO+*. Tech. rep. SNO+ Internal Document, Dec. 2025. URL: DocDB:8913-v1.

[105] John David Jackson. *Classical Electrodynamics*. 3. ed., [Nachdr.] Hoboken, NY: Wiley, 2009. ISBN: 978-0-471-30932-1.

[106] R. E. Jewett. "Characteristics of Physician's Assistant Programs". In: *Journal of Medical Education* 50.12 pt 2 (Dec. 1975), pp. 92–96. ISSN: 0022-2577. DOI: 10.1097/00001888-197512000-00013.

[107] C.J Jillings et al. "The Photomultiplier Tube Testing Facility for the Sudbury Neutrino Observatory". In: *Nuclear Instruments and Methods in Physics Research Section A: Accelerators, Spectrometers, Detectors and Associated Equipment* 373.3 (May 1996), pp. 421–429. ISSN: 01689002. DOI: 10.1016/0168-9002(96)00067-8.

[108] *John Bahcall Home Page -Institute for Advanced Study*. URL: https://www.sns.ias.edu/~jnb/.

[109] B. J. P. Jones. *The Physics of Neutrinoless Double Beta Decay: A Primer*. Feb. 2022. DOI: 10.48550/arXiv.2108.09364. arXiv: 2108.09364.

[110] F. Kaether et al. "Reanalysis of the Gallex Solar Neutrino Flux and Source Experiments". In: *Physics Letters B* 685.1 (Feb. 2010), pp. 47–54. ISSN: 0370-2693. DOI: 10.1016/j.physletb.2010.01.030.

[111] Takaaki Kajita et al. "Establishing atmospheric neutrino oscillations with Super-Kamiokande". In: *Nuclear Physics B* 908 (2016), pp. 14–29.

[112] Kaptanoglu, T. *Energy & Optics Overview*. Tech. rep. SNO+ Internal Document, Mar. 2024. URL: DocDB:8215-v1.

[113] Kaptanoglu, T. *Energy&Optics Update*. Tech. rep. SNO+ Internal Document, July 2023. URL: DocDB:7875-v1.

[114] Kaptanoglu, T. "Reactor Antineutrinos in the SNO+ Water Phase and Detector R&D For Large-Scale Neutrino Detectors". PhD thesis. University of Pennsylvania, 2020.

[115] Kaptanoglu, T. and Galban, K. *Light Yields with DDA*. Tech. rep. SNO+ Internal Document, 2018. URL: DocDB:5732.

[116] Soo-Bong Kim. *New Results from RENO and Prospects with RENO-50*. Dec. 2014. DOI: 10.48550/arXiv.1412.2199. arXiv: 1412.2199 [hep-ex].

[117] K. Kodama et al. "Observation of Tau Neutrino Interactions". In: *Physics Letters B* 504.3 (Apr. 2001), pp. 218–224. ISSN: 03702693. DOI: 10.1016/S0370-2693(01)00307-0.

[118] T. Kroupová. "Improving the Sensitivity to Neutrinoless Double Beta Decay in SNO+". PhD thesis. University of Oxford, 2020.

[119] I. Lam. "Search For Invisible Nucleon Decay in SNO+ With Improved Sensitivity". PhD thesis. Oct. 2020.

[120] L. Landau. "On the Conservation Laws for Weak Interactions". In: *Nuclear Physics* 3.1 (Mar. 1957), pp. 127–131. ISSN: 0029-5582. DOI: 10.1016/0029-5582(57)90061-5.

[121] Lebanowski, L. *Position-Dependant Detector State Correction*. Tech. rep. SNO+ Internal Document, Mar. 2024. URL: DocDB:7730-v3.

[122] T. D. Lee and C. N. Yang. "Parity Nonconservation and a Two-Component Theory of the Neutrino". In: *Physical Review* 105.5 (Mar. 1957), pp. 1671–1675. DOI: 10.1103/PhysRev.105.1671.

[123] Tsung-Dao Lee and Chen Ning Yang. "Question of parity conservation in weak interactions". In: *Physical Review* 104.1 (1956), p. 254.

[124] William R. Leo. *Techniques for Nuclear and Particle Physics Experiments: A How-to Approach*. Berlin, Heidelberg: Springer Berlin Heidelberg, 1994. ISBN: 978-3-540-57280-0 978-3-642-57920-2. DOI: 10.1007/978-3-642-57920-2.

[125] Julien Lesgourgues and Sergio Pastor. "Neutrino mass from Cosmology". In: *Advances in High Energy Physics* 2012.1 (2012), p. 608515.

[126] A. Lesov. *The Weak Force: From Fermi to Feynman*. Oct. 2009. DOI: 10.48550/arXiv.0911.0058. arXiv: 0911.0058 [physics].

[127] Andrew J. Long, Cecilia Lunardini, and Eray Sabancilar. "Detecting Non-Relativistic Cosmic Neutrinos by Capture on Tritium: Phenomenology and Physics Potential". In: *Journal of Cosmology and Astroparticle Physics* 2014.08 (Aug. 2014), pp. 038–038. ISSN: 1475-7516. DOI: 10.1088/1475-7516/2014/08/038. arXiv: 1405.7654 [hep-ph].

[128] V. Lozza and J. Petzoldt. "Cosmogenic Activation of a Natural Tellurium Target". In: *Astroparticle Physics* 61 (Feb. 2015), pp. 62–71. ISSN: 09276505. DOI: 10.1016/j.astropartphys.2014.06.008. arXiv: 1411.5947 [physics].

[129] Valentina Lozza. *backgroundsTable*. Tech. rep. SNO+ Internal Document, Nov. 2025. URL: DocDB:507-v44.

[130] C. Lunardini and A. Yu Smirnov. "Neutrinos from SN1987A: Flavor Conversion and Interpretation of Results". In: *Astroparticle Physics* 21.6 (Sept. 2004), pp. 703–720. ISSN: 09276505. DOI: 10.1016/j.astropartphys.2004.05.005. arXiv: hep-ph/0402128.

[131] Luxottica Exciton. *Luxottica Exciton Bis-MSB Safety Data Sheet*. Mar. 2017.

[132] M.W. Davidson. *Molecular Expressions Microscopy Primer: Specialized Microscopy Techniques - Fluorescence - Basic Concepts in Fluorescence*.

[133] Ziro Maki, Masami Nakagawa, and Shoichi Sakata. "Remarks on the Unified Model of Elementary Particles". In: *Prog. Theor. Phys.* 28 (1962), pp. 870–880. DOI: 10.1143/PTP.28.870.

[134] Manecki, S and Tam, B. "The SNO+ Tellurium Deployment Programme". In: *XXXI International Conference on Neutrino Physics and Astrophysics*. Milan, Italy: SNO+ Internal Document, June 2024.

[135] Matt Marzano. *Neck Hotspots Summary Report*. Tech. rep. SNO+ Internal Document, Aug. 2022. URL: DocDB:7576-v1.

[136] Javier Menéndez. "Shell Model Progress on Neutrinoless Double Beta Decay: Nuclear Matrix Element Uncertainties, Neutrino Exchange Mechanism in See-saw Models". In: *Journal of Physics: Conference Series* 312.7 (Sept. 2011), p. 072012. ISSN: 1742-6596. DOI: 10.1088/1742-6596/312/7/072012.

[137] S. P. Mikheev and A. Iu. Smirnov. "Resonant Amplification of ν Oscillations in Matter and Solar-Neutrino Spectroscopy." In: *Nuovo Cimento C Geophysics Space Physics C* 9 (Feb. 1986), pp. 17–26. ISSN: 0390-5551. DOI: 10.1007/BF02508049.

[138] Stanislav P. Mikheev and A. Yu Smirnov. "Neutrino Oscillations in a Medium with Variable Density". In: *Soviet Physics Uspekhi* 29.12 (Dec. 1986), p. 1155. ISSN: 0038-5670. DOI: 10.1070/PU1986v029n12ABEH003628.

[139] Miller, C., Singh, K. *TeA purification efficiency and cosmogenic backgrounds.* Tech. rep. SNO+ Internal Document, Mar. 2024. URL: DocDB:3879-v3.

[140] Mills, C. "Improved Sensitivity to Δm^2_{21} by Classification of the $^{13}C(\alpha, n)^{16}O$ Background in the SNO+ Antineutrino Analysis". PhD thesis. University of Sussex, 2022.

[141] Lino Miramonti. *Recent Results on Pp-Chain Solar Neutrinos with the Borexino Detector*. Jan. 2019. DOI: 10.48550/arXiv.1901.09965. arXiv: 1901.09965 [hep-ex].

[142] R. N. Mohapatra and A. Y. Smirnov. "Neutrino Mass and New Physics". In: *Journal of Physics: Conference Series* 53 (Nov. 2006), pp. 44–82. ISSN: 1742-6588, 1742-6596. DOI: 10.1088/1742-6596/53/1/003. arXiv: hep-ph/0603118.

[143] Samuel Naugle. *Te 0.5% Plots for Approval*. Tech. rep. SNO+ Internal Document, Nov. 2025. URL: DocDB:8816-v7.

[144] S Navas and et al. (Particle Data Group). "Neutrino Mixing". In: *Phys. Rev. D* 110, 030001 (2024). Updated 2025.

[145] H. M. O'Keeffe, E. O'Sullivan, and M. C. Chen. "Scintillation Decay Time and Pulse Shape Discrimination in Oxygenated and Deoxygenated Solutions of Linear Alkylbenzene for the SNO+ Experiment". In: *Nuclear Instruments and Methods in Physics Research Section A: Accelerators, Spectrometers, Detectors and Associated Equipment* 640.1 (June 2011), pp. 119–122. ISSN: 01689002. DOI: 10.1016/j.nima.2011.03.027. arXiv: 1102.0797 [physics].

[146] Pages, J. "Reactor Antineutrino Oscillation Detection in Liquid Scintillator at SNO+". PhD thesis. University of Sussex, 2024.

[147] Parker, W. *MulitPDF Method for Position Reconstruction*. Tech. rep. SNO+ Internal Document, Aug. 2021. URL: DocDB:7257-v2.

[148] Parker, W. *Radial Shells for MultiPDF and ScintEffectiveVelocity*. Tech. rep. SNO+ Internal Document, Jan. 2024. URL: DocDB:7257-v2.

[149] Parker, W. *Recoordinating ScintEffectiveSpeed and MultiPDF with Updated 2.2g/L Optics*. Tech. rep. Nov. 2022. URL: DocDB:7636-v2.

[150] Particle Data Group et al. "Review of Particle Physics". In: *Physical Review D* 98.3 (2025), p. 030001. DOI: 10.1103/PhysRevD.98.030001. URL: https://pdg.lbl.gov/2025/tables/contents_tables.html.

[151] Paton, J. "Directional Reconstruction in Liquid Scintillator Neutrino Detectors". PhD thesis. University of Oxford, 2023.

[152] Pauli, W. *Dear Radioactive Ladies and Gentlemen*. Dec. 1930. URL: https://www.math.utah.edu/~beebe/talks/2015/qtm/pdf/pauli-1930-ltc.pdf.

[153] Perkin Elmer. *2,5-Diphenyloxazole (PPO) Safety Data Sheet*. Dec. 2020.

[154] ST Petcov. "The nature of massive neutrinos". In: *Advances in High Energy Physics* 2013.1 (2013), p. 852987.

[155] W. J. Peterson et al. "The Late Effects of Selected Immunosuppressants on Immunocompetence, Disease Incidence, and Mean Life-Span. II. Cell-mediated Immune Activity". In: *Mechanisms of Ageing and Development* 4.3-4 (1975), pp. 241–249. ISSN: 0047-6374. DOI: 10.1016/0047-6374(75)90026-3.

[156] A Pich. "The Standard Model of Electroweak Interactions". In: ().

[157] Piepke, A et al. "Double Beta Decay". In: *Particle Data Group (PDG)*. Prog.Theor.Exp.Phys. 083C01 (2022).

[158] Pontecorvo, B. *Inverse Beta Process*. Chalk River Laboratories. 1946.

[159] Pontecorvo, B. "Inverse Beta Processes and Nonconservation of Lepton Charge". In: *J. Exptl. Theoret. Phys. (U.S.S.R.)* 34 (Jan. 1958), pp. 247–249.

[160] A. W. P. Poon. "Neutrino Observations from the Sudbury Neutrino Observatory". In: *AIP Conference Proceedings*. Vol. 610. 2002, pp. 218–230. DOI: 10.1063/1.1469931. arXiv: nucl-ex/0110005.

[161] Hyper-Kamiokande Proto-Collaboration et al. "Hyper-Kamiokande Design Report". In: arXiv:1805.04163 (Nov. 2018). DOI: 10.48550/arXiv.1805.04163. arXiv: 1805.04163 [physics].

[162] X. Qian and P. Vogel. "Neutrino Mass Hierarchy". In: *Progress in Particle and Nuclear Physics* 83 (July 2015), pp. 1–30. ISSN: 01466410. DOI: 10.1016/j.ppnp.2015.05.002. arXiv: 1505.01891 [hep-ex].

[163] P. K. Rath et al. "Uncertainties in Nuclear Transition Matrix Elements for Neutrinoless $\beta\beta$ Decay within the PHFB Model". In: *Physical Review C* 82.6 (Dec. 2010), p. 064310. ISSN: 0556-2813, 1089-490X. DOI: 10.1103/PhysRevC.82.064310. arXiv: 1104.3965 [nucl-th].

[164] F. Reines and Cowan, C. "The Neutrino: From Poltergeist to Particle". In: *Reviews of Modern Physics* 68.2 (Apr. 1996), pp. 317–327. ISSN: 0034-6861, 1539-0756. DOI: 10.1103/RevModPhys.68.317.

[165] F. Reines, H. S. Gurr, and H. W. Sobel. "Detection of $\bar{\nu}_e - e$ Scattering". In: *Physical Review Letters* 37.6 (Aug. 1976), pp. 315–318. DOI: 10.1103/PhysRevLett.37.315.

[166] Ricetto, S. *Bis-MSB Data vs MC CM-March2024*. Tech. rep. SNO+ Internal Document, Mar. 2024. URL: DocDB:8164-v1.

[167] Ricetto, S. *RAT Optics Bis-MSB 2.2mg/L after CM March 2024*. Tech. rep. SNO+ Internal Document, June 2024. URL: DocDB:8298-v1.

[168] Ricetto, S. *RAT Optics Bis-MSB 2p2mg/L Summary and Proton Discussion*. Tech. rep. SNO+ Internal Document, July 2024. URL: DocDB:8376-v1.

[169] Tomas R. Rodriguez and G. Martinez-Pinedo. "Energy Density Functional Study of Nuclear Matrix Elements for Neutrinoless $\beta\beta$ Decay". In: *Physical Review Letters* 105.25 (Dec. 2010), p. 252503. ISSN: 0031-9007, 1079-7114. DOI: 10.1103/PhysRevLett.105.252503. arXiv: 1008.5260 [nucl-th].

[170] Tomas R. Rodriguez and Gabriel Martinez-Pinedo. "Neutrinoless Double Beta Decay Studied with Configuration Mixing Methods". In: *Progress in Particle and Nuclear Physics* 66.2 (Apr. 2011), pp. 436–440. ISSN: 01466410. DOI: 10.1016/j.ppnp.2011.01.047. arXiv: 1012.1783 [nucl-th].

[171] Abdus Salam. "On Parity Conservation and Neutrino Mass". In: *Il Nuovo Cimento (1955-1965)* 5.1 (Jan. 1957), pp. 299–301. ISSN: 1827-6121. DOI: 10.1007/BF02812841.

[172] J. D. Seader and Ernest J. Henley. *Separation Process Principles*. 2nd ed. Hoboken (N. J.): J. Wiley & Sons, 2006. ISBN: 978-0-471-46480-8.

[173] Sigma-Aldrich. *Butylated Hydroxytoluene Safety Data Sheet*. Apr. 2022.

[174] F. Šimkovic. "Neutrinoless Double-Beta Decay and Related Topics". In: *Physics of Particles and Nuclei* 42.4 (July 2011), pp. 598–612. ISSN: 1063-7796, 1531-8559. DOI: 10.1134/S1063779611040137.

[175] Singh, K. *PSUP Camera Pictures*. Tech. rep. SNO+ Internal Document, Apr. 2017. URL: DocDB:4161-v3.

[176] *SNEWS – SuperNova Early Warning System*. URL: https://snews2.org/.

[177] Sonzogni, A. "NuDat3.0". In: *National Nuclear Data Center* (). URL: https://www.nndc.bnl.gov/nudat3/.

[178] E. C. G. Sudarshan and R. E. Marshak. "Chirality Invariance and the Universal Fermi Interaction". In: *Physical Review* 109.5 (Mar. 1958), pp. 1860–1862. DOI: 10.1103/PhysRev.109.1860.2.

[179] J. Sujatha and A.K. Mishra. "Bis-MSB, a Laser Dye as a Polarization Probe for Microheterogeneous Media". In: *Journal of Photochemistry and Photobiology A: Chemistry* 101.2-3 (Dec. 1996), pp. 245–250. ISSN: 10106030. DOI: 10.1016/S1010-6030(96)04301-8.

[180] Tam, B. "Enabling Neutrinoless Double Beta Decay in the SNO+ Experiment through the Deployment and Study of Liquid Scintillator". PhD thesis.

[181] Tam, B. *QA Overview for bisMSB Addition and Enhanced Scintillator Cocktail*. Tech. rep. Internal SNO+ Document, Apr. 2023.

[182] Tam, B. *SNO+ Scintillator (LAB+2.2g/L PPO) Density Plot*. Tech. rep. SNO+ Internal Document, Aug. 2022. URL: DocDB:7405-v2.

[183] Tam, B. *SNO+ Scintillator (LAB+2.2g/L PPO) UV-Vis Absorption Plot*. Tech. rep. SNO+ Internal Document, June 2022. URL: DocDB:7378-v3.

[184] The Borexino Collaboration. "Experimental Evidence of Neutrinos Produced in the CNO Fusion Cycle in the Sun". In: *Nature* 587.7835 (Nov. 2020), pp. 577–582. ISSN: 0028-0836, 1476-4687. DOI: 10.1038/s41586-020-2934-0.

[185] The SNO+ Isotope working group. *Tellurium Loading for the SNO+ Collaboration*. Tech. rep. SNO+ Internal Document, Apr. 2019. URL: DocDB:5718-v2.

[186] ThermaFisher Scientific. *Cyclohexane Safety Data Sheet*. Oct. 2009.

[187] Thomson, M. *Modern Particle Physics*. 1st ed. Vol. 1. Cambridge University Press, 2013. ISBN: 978-1-107-03426-6.

[188] A. Upadhyay. *SNO+ Liquid Scintillator Oxidation Stability Studies*. Tech. rep. SNO+ Internal Document, 2023. URL: DocDB:7778-v1.

[189] J.R. Wilson et al. "Background Analysis for the SNO+ Experiment". In: *Journal of Physics: Conference Series* 888 (Sept. 2017), p. 012246. ISSN: 1742-6588, 1742-6596. DOI: 10.1088/1742-6596/888/1/012246.

[190] Wilson, J.D. *Krypton-85 in the SNO+ Neutrino Detector to Late 2024*. Tech. rep. SNO+ Internal Document, July 2025. URL: DocDB:8815-v1.

[191] Wilson, J.D. et al. *Validation of Radioactive Decay Simulations*. Tech. rep. SNO+ Internal Document, Oct. 2013. URL: DocDB:2188-v3.

[192] Julia Woithe, Gerfried J Wiener, and Frederik F Van Der Veken. "Let's Have a Coffee with the Standard Model of Particle Physics!" In: *Physics Education* 52.3 (May 2017), p. 034001. ISSN: 0031-9120, 1361-6552. DOI: 10.1088/1361-6552/aa5b25. URL: https://iopscience.iop.org/article/10.1088/1361-6552/aa5b25 (visited on 09/29/2024).

[193] L. Wolfenstein. "Neutrino Oscillations in Matter". In: *Physical Review D* 17.9 (May 1978), pp. 2369–2374. DOI: 10.1103/PhysRevD.17.2369.

[194] Workman, R.L. and et al. (Particle Data Group). "Neutrino Mixing". In: *Particle Data Group Reviews* 083C01 (2022). URL: https://pdg.lbl.gov/2022/listings/rpp2022-list-neutrino-mixing.pdf.

[195] C. S. Wu et al. "Experimental Test of Parity Conservation in Beta Decay". In: *Physical Review* 105.4 (Feb. 1957), pp. 1413–1415. ISSN: 0031-899X. DOI: 10.1103/PhysRev.105.1413.

[196] S. Yoshida et al. "Light Output Response of KamLAND Liquid Scintillator for Protons and 12C Nuclei". In: *Nuclear Instruments and Methods in Physics Research Section A: Accelerators, Spectrometers, Detectors and Associated Equipment* 622.3 (Oct. 2010), pp. 574–582. ISSN: 01689002. DOI: 10.1016/j.nima.2010.07.087.

[197] H. S. Zhang et al. "Refractive Index in the JUNO Liquid Scintillator". In: *Nuclear Instruments and Methods in Physics Research Section A: Accelerators, Spectrometers, Detectors and Associated Equipment* 1068 (Nov. 2024), p. 169730. ISSN: 01689002. DOI: 10.1016/j.nima.2024.169730. arXiv: 2405.19879 [physics].

[198] Pengpeng Zhang et al. "Single-Photon Elimination in Liquid Scintillation Counting with Pulse Shape Discrimination and Delayed Coincidence". In: *Radiation Measurements* 178 (Nov. 2024), p. 107299. ISSN: 13504487. DOI: 10.1016/j.radmeas.2024.107299.

[199] Yan Zhang et al. "A Complete Optical Model for Liquid-Scintillator Detectors". In: *Nuclear Instruments and Methods in Physics Research Section A: Accelerators, Spectrometers, Detectors and Associated Equipment* 967 (July 2020), p. 163860. ISSN: 01689002. DOI: 10.1016/j.nima.2020.163860. arXiv: 2003.12212 [physics].

[200] P. A. Zyla, et al., and (Particle Data Group). "Particle Detectors at Accelerators". In: *Prog.Theor.Exp.Phys.* 083C01 (June 2020), p. 87.

Appendix A

Bis-MSB deployment campaign

This table compiles the most noteworthy samples taken during the bis-MSB deployment campaign. Samples are identified by their OSA shift number (ddmmyy-S) and sample number (-xx). The recirculation mode indicates whether the sampled product was taken from the master solution holding vessel V-41, the plant while running stripping in closed loop, or the plant during deployment to the AV. The concnetrations are reported when taken. Shifts where the AV volume was recirculated are tabulated alongside batch loading operations in chronological order. Samples in bold have 10 cm spectra taken in addition to the array of underground QA tests.

Shift goal	**Shift OSA**	**Sample**	**Mode**	**Time**	**Conc. [mg/L]**
batch 1	210723-M	-02, -04	V41	6:34	671.4
		-06	CLR	9:17	
		-07	AV start	9:50	
		-09	AV end	15:00	
batch 2.1	290923-M	-02	V41	9:56	856.5
		-05	CLR	13:26 (1.5h)	
		-06	AV start	13:57	
		-08	AV end	14:55 (4T)	
batch 2.2	021023-M	-01	V41	7:56	
		-04	CLR	13:36 (3.5hs)	
		-06	AV start	14:05	
		-07	AV end	14:50 (3T)	
batch 3	121023-M	-03	V41	9:50	826
		-06	CLR	12:55 (1h)	
		-07	AV start	13:18	
		-08	AV end	15:15 (7.7T)	
recirc	011123-M	-03	CLR	12:37 (1h)	
		-04	AV start	13:07	1.123
		-06	AV end	14:55 (7.3)	1.057
recirc	031123-M	-03	CLR	11:05 (40mins)	
		-04	AV start	11:27	1.145
		-07	AV end	14:52 (17.7T)	1.745
recirc	081123-M	-03	CLR	12:10 (45mins)	
		-05	AV start (F-01)	12:42	1.690
		-07	AV end	14:53 (10.2T)	1.690
recirc "bypass"	091123-M	-03	CLR	9:05 (40mins)	
		-04	AV start	9:31	1.712
		-08	AV end	12:30 (12.1T)	1.712
recirc	101123-M	-03	CLR	9:50 (40mins)	
		-04	AV start	10:23	1.658
		-08	AV end	14:36 (17.5T)	1.645
recirc	241123-M	-03	CLR	11:15 (40mins)	
		-05	AV start	11:53	1.614
		-08	AV end	14:56 (12.3T)	1.701
batch 4	281123-M	-02	V41	12:00	852
	291123-M	-03	CLR	9:55 (40mins)	
		-04	AV start	10:28	
		-07	AV end	14:50 (17.6T)	1.701
recirc	051223-M	-05	CLR	10:35 (45mins)	
		-06	AV start	11:04	
		-09	AV end	14:50 (13.1T)	2.268
recirc	050324-M	-03	CLR	11:10 (50mins)	
		-04	"AV scintillator"	11:56-14:09 (13.3T)	2.247

Table A.1: Reference table for Bis-MSB loading metrics as reported during underground activities.